Doctoral Dissertation

Behavior of Ground Displacement Caused by Groundwater Seepage Force

MENG LINGYU

Graduate School for International Development and Cooperation
Hiroshima University

September 2014

Behavior of Ground Displacement Caused by Groundwater Seepage Force

D116041

MENG LINGYU

A Dissertation Submitted to
the Graduate School for International Development and Cooperation
of Hiroshima University in Partial Fulfillment
of the Requirement for the Degree of
Doctor of Engineering

September 2014

We hereby recommend that the dissertation by Mr. MENG LINGYU entitled "Behavior of Ground Displacement Caused by Groundwater Seepage Force" be accepted in partial fulfillment of the requirements for the degree of DOCTOR OF ENGINEERING.

Committee on Final Examination:

H. Yamamoto.

Haruyuki YAMAMOTO, Professor
Chairperson

Y. Higo

Yasushi HIGO, Professor

Takao Yamashita

Takao YAMASHITA, Professor

M. Yamazaki

Masahiro YAMAZAKI, Professor
Faculty of Engineering, Okayama University of Science

Koji Ichii

Koji ICHII, Associate Professor
Graduate School of Engineering, Hiroshima University

Date: July 25, 2014

Approved:

FUJIWARA Akimasa, Professor
Dean

Date: September 5, 2014

Graduate School for International Development and Cooperation
Hiroshima University

Abstract

Underground stores, basement parking and subways are concentrated in the downtown of the city because the underground space is very commonly exploited to optimize high land cost in urban development. Constructions are often accompanied with dewatering engineering, which causes ground deformation in a large affected area. Roads, structures, underground pipelines and etc. are usually crowded around the excavation pit, therefore, the environment conditions around sites are growing severe. In view of the recent catastrophes associated with ground subsidence due to dewatering project, there is an urgent need to provide vital guidelines on the design of the construction processes.

It is hard to estimate the ground behaviors around the construction sites due to complex situations of construction and many influencing factors in the crowded cities. In consequence of ground behaviors due to groundwater remain a challenging geotechnical engineering problem with difficulties.

In addition to the effect of underwater, the influence of maintenance structures and interaction between structure and soil are key points, as well as difficulties in the practical engineering.

Simulating the ground behaviors due to seepage by considering structure interaction with soil and maintenance structures could provide insight understanding of deformation process around construction sites. The numerical results will make valuable to disaster predication in practical engineering.

To investigate the mechanical behaviors around the dewatering projects, numerical research of single pumping well and dewatering of foundation pit are conducted respectively. An unsteady saturated-unsaturated model for seepage and a non-linear model for deformation are employed to represent the mechanical behavior of ground in numerical analysis. The finite element method and finite different method are used to study the space problem and time dimension respectively, and the numerical simulation code implemented by FORTRAN is applied to predict the flow velocity distribution and the results of ground displacement.

This study presents a hydro-mechanical model to analysis ground behaviors around the dewatering projects incorporating excavating theory and spring element. The interaction between the structure and the soil was characterized with the Goodman's zero thickness elements. It is found that the settlement of ground will become larger if the effect of unsaturated zone is considered, which is encouraging that the effect of capillary zone should be considerable in both seepage and displacement field. The numerical values of displacement in excavation case are compared with the field observed data. Three numerical cases have been compared, the prediction accuracy by the external load and joint element is more agreeable with the field observed data. It is found that external load has a great impact on the deformation behind the SMW, but it has small influence on the heave inner pit. Relative movements between the SMW and soil mass should not be ignored in displacement analysis.

Consequently, it is vital to integrate various factors in numerical analysis to model as closely as possible the true ground behaviors in the field and hydro-mechanical model analysis is necessary to present useful reference to the excavation stability and excavation disaster predication

ACKNOWLEDGMENT

First of all, I would like to express my most sincere gratitude to my supervisor Professor Haruyuki YAMAMOTO. With his encouragement, understanding and guidance in the past five years, I am able to complete my work. His continuous encouragement throughout my research, especially in hard times, is much appreciated. The dissertation could not be completed without his support.

I also express my sincere gratitude to my vice-supervisors, Professor Yasushi HIGO and Professor Takao YAMASHITA, for their thorough review of my dissertation and their valuable suggestions and comments in revising the dissertation.

Special thanks go to the members of my Dissertation Committee, Professor Masahiro YAMAZAKI of Faculty of Engineering, Okayama University of Science and Associate Professor Koji ICHII of Graduate School of Engineering, Hiroshima University. Their innovative ideas and unique insights into the research impressed me a lot and made me progress faster.

I would like to particular thank Professor Wei LI, Shenyang Jianzhu University, who take me into the geotechnical field when I study in China. Specifically, I would like to thank Professor Dean SUN, Shanghai University for his support and encouragement when he was in Hiroshima University as visiting professor.

I would not have been able to finish this work without the financial support from Japan government for providing the MEXT scholarship for five years. During this period, I can completely focus my time on research.

I also want to express my sincere grateful to all the other members of the laboratory, Dr. Shaohong JIN, Dr. He HUANG and Dr. Hongyang CHENG for their technical help and care in dairy life.

At last, I would like to give my sincere words for my family for their love and bearing of me for the past years. Thank them for giving me a wonderful life.

MENG Lingyu

Table of contents

CHAPER 1

CHAPTER 2

CHAPER 3

CHAPTER 4

CHAPTER 5

CHAPTER 6

Chapter 7

List of figures

List of tables

CHAPER 1

INTRODUCTION

1.1 Research backgrounds

With the increase of economy and development of industry, the underground space is very commonly exploited to optimize high land cost in urban development. Recently, many excavation works, especially deep excavation engineering have been carried out to construct multifarious types of underground infrastructure such as underground stores, deep basements, service tunnels and subways. Generally speaking, during the deep excavation construction, dewatering project is an essential part to lower water and control underground water level. The purposes of lowering the groundwater level are to keep the excavation bottom dry, to avoid upheaval failure or sand boiling, and to forestall the occurrence of floating basements, as explained in the following:

(1) To keep the excavation bottom dry:

With the higher flow velocity of groundwater in sand or gravel, groundwater may flow into the excavation pit, which could cause inconvenience for construction work. To keep the excavation bottom dry, the groundwater level is generally lowered to 0.5-1.0 m below the excavation surface, which is shown in Figure 1-1.

(2) To forestall the upheaval failure:

There exists a permeable layer underlying the clayey layer in Figure 1-2. The water pressure from the permeable layer will generate an upheaving force against the clayey layer. When the water pressure acting on the bottom of the clayey layer is larger than the total weights of the clayey layers, the upheaval failure will occur. One of the methods to prevent the occurrence of upheaval failure is to lower the piezometric pressure of the permeable layer by pumping.

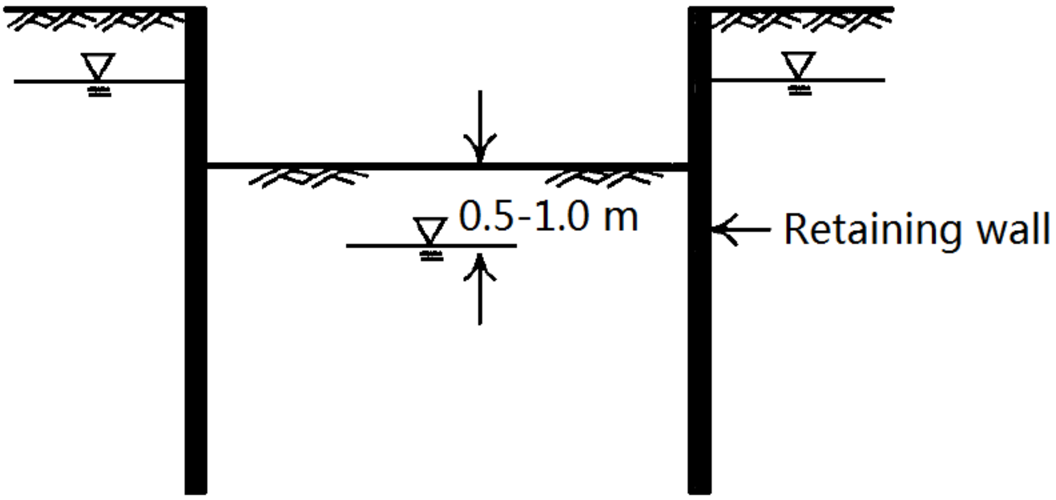

Figure 1-1 Keeping the excavation bottom dry by lowering
the groundwater level inner pit

(3) To avoid sand boil:

While excavation proceeds, the difference between the groundwater levels within and outside the excavation pit becomes larger and larger. When the hydraulic gradient around the excavation bottom grows equals or larger the critical hydraulic gradient of soils, sand boiling will occur. There are many methods are available to avoid sand boiling. The most common one is to lower the groundwater level outside the excavation pit.

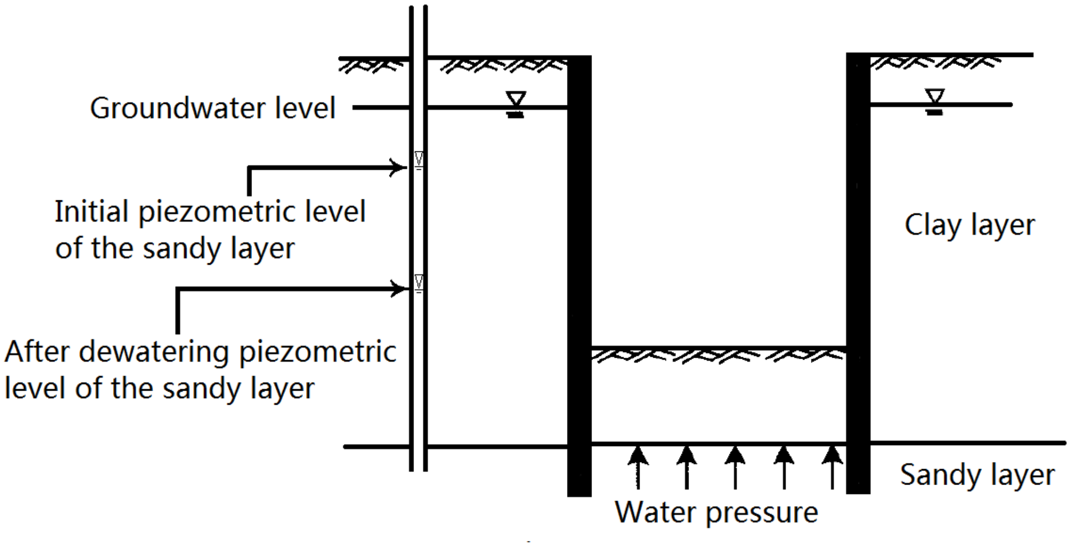

Figure 1-2 Lowering the piezometric level in sandy soils to avoid upheaval failure

4. To keep the basement from floating:

With the completion of the excavation, one starts the construction of basements. In sandy soils, with the light weight of structure during the stage of basement construction, the phenomenon of the floating of the basement is likely to happen if the weight of structures is smaller than the water pressure acting on the foundation base. Once the floating phenomenon has happened, with the differential heaves of the foundation, the floated basement will not necessarily sink back to the original elevation while building construction proceeds, which may lead to damage of the structures, which is shown in Figure 1-3. In the worst condition, the basement may need to be demolished or reconstructed. Therefore, dewatering is usually required at the stage of basement construction to keep the upheaving force on foundation bottoms smaller than the weight of structures during construction.

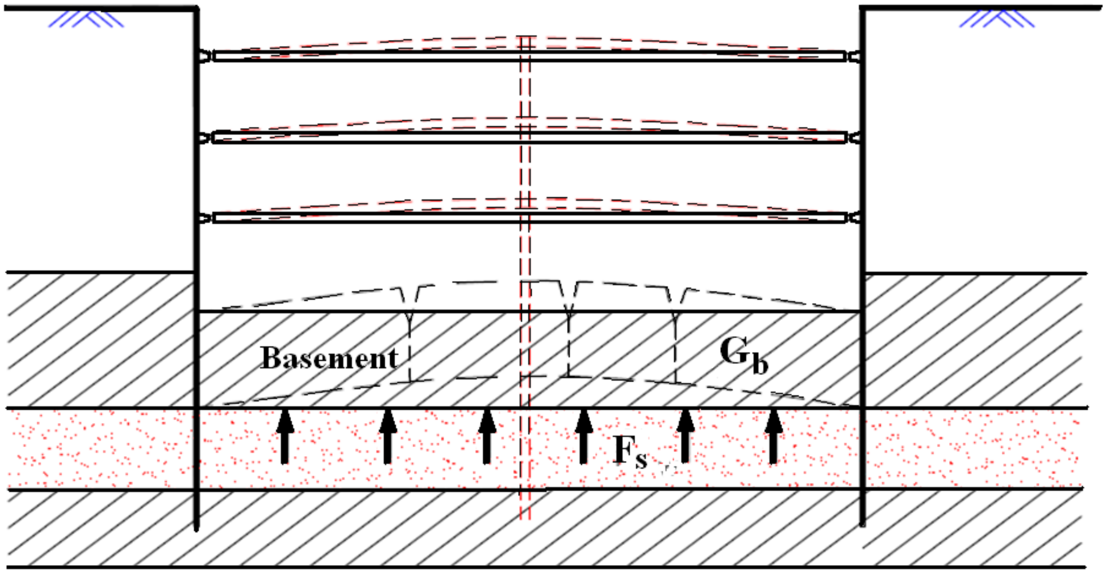

Figure 1-3 Floating phenomenon of basement

Ground water level draw down leads to the ground deformation and can cause serious damage to structures in a large affected area. In China, continuous over pumping of groundwater for engineering construction have resulted in severe ground deformations and have caused serious damages of road and structural. Many other places in the world such as San Joaquin Valley, Taiwan and Mexico City have also experienced similar problems. In the last two decades, since tall buildings, underground stores and subways are concentrated in the downtown of the city. Roads, structures, underground pipelines and etc. are crowded around the excavation work, therefore, the environment conditions of deep excavation are growing severe. As a result, deep excavation engineering remains a challenging geotechnical engineering problem with high risks and difficulties.

The finite element method (FEM) is a numerical technique method that gives approximate solutions to differential equations that model problems arising in engineering and physics. It is a general tool enables in identifying a numerical solution to any problems which can be described by using a group of partial derivative equations over a finite area. A variety of methods serve to take account of spatial or temporal discontinuities in the targeted solutions, etc. This method provides the possibility of incorporating of highly-sophisticated behavioral models, which are more realistic than conventional methods, therefore, the finite element method has incited considerable interest on the part of civil engineers. While the FEM has been used in many fields of engineering practice for over forty years, it is only relatively recently that the geotechnical problems have begun to be widely used for analysis. This is probably because that there are many complicated questions which are specific to geotechnical engineering. With the development of the finite element method, the ability to numerically model complicated soil structures has become possible relatively recently.

During the excavation of foundation pit, due to the great variation of groundwater level, the huge head fall could result in drastic seepage flow of the ground water, which will bring about a full influence on the deformation on the surrounding structures in a large-scale rang, therefore, it is very important to determines the location of phreatic surface. The history of research relevant to dewatering can be traced back to the 1860s, the analytical solutions of single well pumping have been proposed by researchers such as Dupuit 1) and Theis 2). Most of the solutions used the Dupuit assumption, which simply assumes that the phreatic surface is connecting to the water level in the pumping well. Therefore, there is no leaching face on the boundary of the pumping well. However, under the condition of unconfined aquifer, the leaching face does exist, the height of which depends on the permeability of the soil. If the height of the leaching face is large, the leaching face can't be ignored. The Figure 1-4 shows the actual drawdown level of the groundwater and the Dupuit's assumption surface.

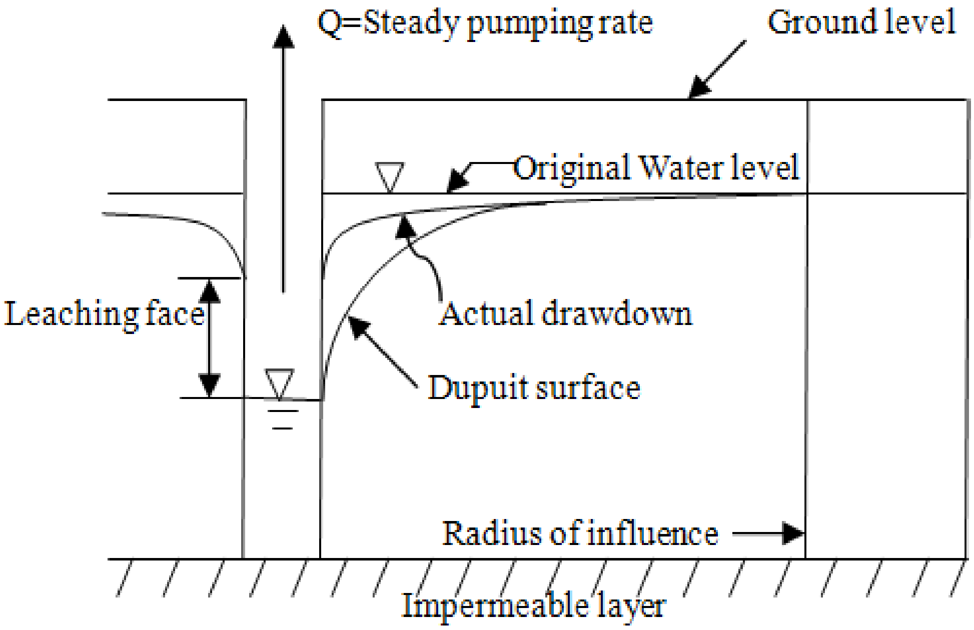

Figure 1-4 Actual drawdown level and Dupuit's assumption surface

For unconfined flow, actual flow path and the location of the leaching face are difficulties in the numerical prediction. At first, they calculate the phreatic surface by Altered Mesh Method which is adjusting the shape of the mesh for the phreatic surface boundary until the results converge. But mesh iteration have many weakness, for instance, it will causes mesh deformity if the change of mesh is very large, and the same mesh can't be used when stress and strain are calculated.

In 1970, the first Fixed Mesh Method which named Galerkin method was made by Neuman 3). The ground deformation calculation also had been solved by considering body force from Brown and Borges 4) in 1973.

So far, there are four principal Fixed Mesh Methods for calculating the actual flow path:

(1) Residual Flow Procedure by Desai (1983) 5)

(2) The Element Conducting Matrix Adjustment Method by Bathe (1979) 6)

(3) Imaginary Element Method by WU Mengxi (1994) 7)

(4) Initial Flow Method by ZHANG Youtian (1988) 8)

In recent years, unsteady model, especially saturate-unsaturated model has been more emphasized heavily 9)-14). The effect of the capillary zone has been taken into account, which is much more realistic manner to simulate the groundwater seepage flow. Figure 1-5 shows the schematic of saturated-unsaturated seepage model.

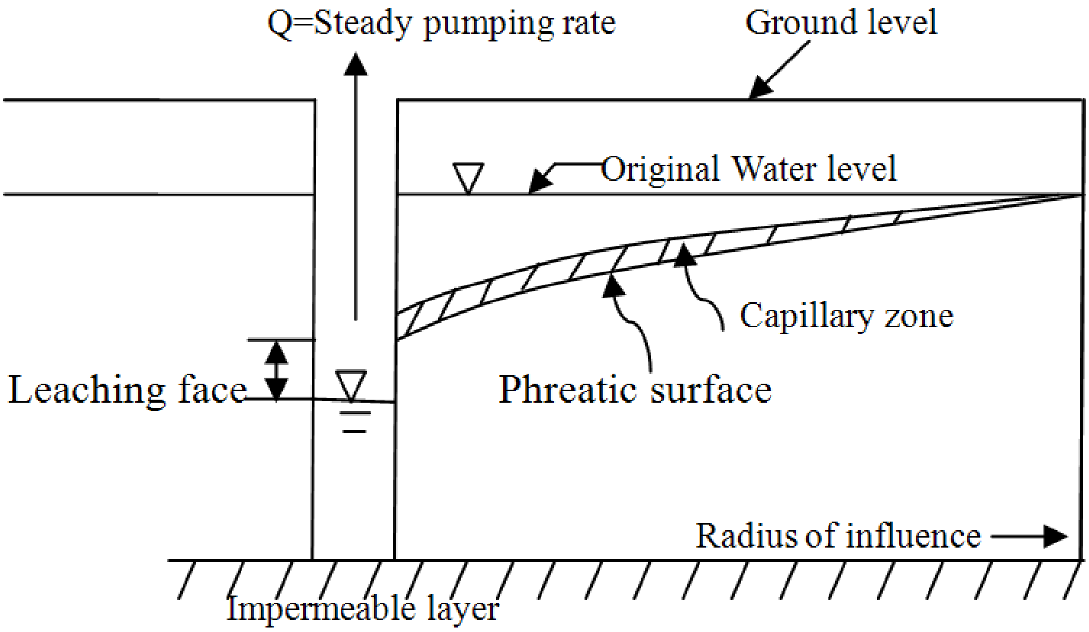

Figure 1-5 Schematic of saturate-unsaturated seepage model

After the initial applications to dams, excavations and retaining walls 15)-17), the use of the FEM for computing diaphragm walls began during the 1970's [18)-21)]. In subsequent research, a number of papers have addressed the problem of sequential soil excavation. For example Hsi and Small [22)] simulated a fully coupled elastic porous material, and Borja et al [23)] presented drained analyses that the results were independent of the number of excavation stages. Borja [24)] later extended these analyses to include pore pressures by considering both undrained and drained conditions.

Most of these procedures modeled steady conditions, and unsaturated soil is rarely considered, however it is well known that the stability of an excavation is a time dependent process. This was recognised by researchers [25)-27)], and they developed a coupled analysis with the inclusion of a sequential construction sequence. In subsequent research, new methods have been applied in coupled analysis more and more deeply [28)-38)]. With the development of computer science and elevation of computing rate recently, three-dimensional model have been gradually regarded [39)-42)].

1.2 Objective of studies

As with all numerical modeling, the aim is to model as closely as possible the true "in the field" behavior. This research aims to improve the current understanding of the effect of deep excavation and to develop a practical decision making tool for excavation design. In order to achieve this goal, the following objectives were identified:

For unconfined flow, actual flow path and the location of the leaching face under unsteady seepage condition were studied. The saturate-unsaturated method was carried to simulate dewatering construction. Simplified ground deformation mechanisms due to dewatering of single well were discussed.

Based on the saturated-unsaturated medium's theory, a three-dimensional coupling model of soil and water was studied for behaviors around the excavation due to unsteady seepage. The finite element method and finite different method were employed to study the space problem and time dimension, respectively.

1.3 Outline of thesis

This thesis contains 7 chapters. Chapter 1 describes the background, objectives and scope of the work. Chapter 2 introduces basic theory of seepage flow and ground behaviors. This includes an overview of the empirical methods. Chapter 3 discusses finite element method theory. The history and basic concepts of FEM are described. Results of the model tests including ground movements for steady state and unsteady state due to single pumping well are presented in Chapter 4. Chapter 5 gives a numerical prediction for excavation. In this chapter, both elastic deformation model and non-linear deformation model are given for discussion. Chapter 6 introduces general situation of the excavation project of the Zhujiang Road station and other application case. The finite element analysis model for simulation is applied to predict deformation around the excavation due to seepage. Chapter 7 summarizes the contributions of each chapter and suggests a context for future research.

Reference

1) Li Guangxin, Advanced Soil Mechanics, Tsinghua University press, 2009, pp. 220-226 (In Chinese)

2) Theis CV, The relation between lowering of the pizeometric surface and the rate and duration of discharge of a well using groundwater storage. Tans. Am. Geophys.Un., Vol..16 annual meeting, 1935, pp.519-524

3) Neuman SP, Witherspoon PA, Finite element method of analyzing steady seepage with a free surface, Water Resource Research, Vol.6, 1970, pp. 889-897

4) Brown C.B., Borges S.J., Steady stage ground motions caused by single-well pumping, Water Resource Research, Vol.9, 1973, pp. 1420-1427.

5) Desai CS, A residual flow procedure and application for free surface flow in porous media, Advances in Water Resources, Vol.6, 1983, pp.27-35

6) Bathe KT, Finite element free surface seepage analysis without mesh iteration, International Journal for Numerical and Analytical Methods in Geomechanics, Vol.3, 1979, pp.13-22.

7) WU Mengxi, Imaginary element method for numerical analysis of seepage with free surface, Journal of Hydraulic Engineering, Vol. 8, 1994, pp.67-71. (In Chinese)

8) ZHANG Youtian, Initial flow method for seepage with free surface problem, Journal of Hydraulic Engineering, Vol. 8, 1988, pp.18-26. (In Chinese)

9) WU Mengxi, Saturated-unsaturated unsteady seepage numerical analysis, Journal of Hydraulic Engineering, Vol. 12, 1999, pp.38-42. (In Chinese)

10) FU Jun-feng, JIN Sheng, A study on unsteady seepage flow through dam, Journal of Hydrodynamics, 2009, Vol.21, pp. 499-504.

11) SHENG Zhen-zhong, Numerical simulation of composite geomembrane defect leakage experiment based on saturated-unsaturated seepage theory, SHUILI XUEBAO, 2009, Vol. 40, pp. 1091-1095. (In Chinese)

12) FU Yan-ling, Improved adjustment method of compound element conductivity matrix for calculating 3D seepage field with free surface, Chinese Journal of Geotechnical Engineering, Vol. 31, 2009, pp.1434-1439. (In Chinese)

13) Karamouzis D, Computation of unsteady two-dimensional free surface of groundwater by the finite-element method, Journal of Hydrology, Vol. 74, 1984, pp. 53-65.

14) J. P. HIS, Surface subsidence and drawdown of the water table due to pumping, Geotechnique, Vol. 44, 1994, pp.381-396

15) Tan X., etc., Saturated-unsaturated Seepage Analysis of Slope under Rainfall, Rock and Soil Mechanics, Vol.24, No.3, 2003, pp.381-384. (In Chinese)

16) Li Y., etc., Saturated-unsaturated Seepage Analysis Based on FLAC3D, Rock and Soil Mechanics, Vol.33, N0.2, 2012, pp.617-622. (In Chinese)

17) Chang C.Y., Duncan J.M., Analysis of soil movement around a deep excavation, Proc, ASCE, J. of the Soil Mechanics and Foundations Division, Vol.96, SM5, 1970, pp. 1655-1681

18) Clough G.W., Woodward R. J., Analysis of embankment stresses and deformations, Proc. ASCE, J. of the Soil Mechanics and Foundations Division, Vol.93, SM4, 1967, pp. 529-549

19) Clough G.W., Duncan J.M., Finite element analysis of retaining wall behavior, Proc. ASCE, J. of the Soil Mechanics and Foundations Division, Vol.97, SM12, 1971, pp. 1657-1673

20) Bjerrum L., Frimann Clausen C.J., Duncan J.M., Earth pressure on flexible structures, A state of the art report, Comptes-rendus du Ve CEMSTF (Madrid), ed. SEMSC, Vol. 2, 1972, pp. 169-196

21) Egger P., Influence of wall stiffness and anchor prestressing on earth pressure diaphragms (cut-off walls) in Italy, Ve CIMSTF (Paris), Vol. 2, 1972, pp. 403-411.

22) Hsi J. P. and Small J. C., Simulation of excavation in a poro-elastic material, International Journal for Numerical and Analytical Methods in Geomechanics, Vol 16,1992, pp. 25-43.

23) Borja R. I., Lee S. R. and Seed R. B., Numerical simulation of excavation in elasto-plastic soils, International Journal for Numerical and Analytical Methods in Geomechanics, Vol 13, 1989, pp.231-249.

24) Borjar. I, Analysis of incremental excavation based on critical state theory, J. Geotech. Eng. Div., ASCE vol. 116, no. 6, 1990, pp. 964-985.

25) Osaimi A. E. and Clough G. W., Pore-pressure Dissipation During Excavation, Journal of the Geotechnical Division, ASCE Vol. 105, 1979, pp.481-498.

26) Holt D. A. and Griffiths D. V., Transient Analysis of Excavations in Soil, Computers and Geotechnics 13, 1992, pp.159-174

27) Banerjee P. K. and Kumbhojar A. S., Finite Element Analysis of the Stability of a Cut using an Isotropic Soil Model, Canadian Geotechnicai Journal 25, 1988, pp.119-127.

28) Clough G.W., Weber P.R., Lamont J., Design and observation of a tied-back wall, Proc. ASCE Special Conf., New York, ASCE, Vol. 1, 1972, pp. 1367-1389.

29) Palmer J.H.L., Kenney T.C., Analytical study of a braced excavation in weak clay, Revue Canadienne de Géotechnique, Vol 9, 1972, pp. 145-164.

30) Mehmet M. B., Investigation of Stability of Slopes under Drawdown Conditions,

Computers and Geotechnics 34, 2007, pp.81-91

31) Tian D. F., Coupling numerical analysis of unsaturated seepage and stress fields for soil slope, Rock and Soil Mechanics, Vol.30, No.3, 2009, pp.810-814. (In Chinese)

32) Chen L. Q., etc., 2D Numerical Simulation of Considering K0 Consolidation and Coupling of Deformation and Seepage in Soft Soil Excavation Engineering, Vol.8 No.1, 2011, pp. 39-47. (In Chinese)

33) Zhu W. B., etc., Forming and Development Process of Soil Landslide during Rainfall, Chinese Journal of Rock Mechanics and Engineering, Vol.21 No.4, 2002, pp. 509-512. (In Chinese)

34) Dehasis R., Keith K.R., Surface settlements at a soft site due to bedrock dewatering, Engineering Geology, Vol. 107, 2009, pp.109-117.

35) Cao X.S., Yin Z.Z., Simplified Computation of Two-dimensional Consolidation of Unsaturated Soils, Rock and Soil Mechanics,Vol.30, No.9, 2009, pp.2575-2580. (In Chinese)

36) Reto S., etc., Effect of Rising Water Table in an Unsaturated Slope, Engineering Geology, Vol. 114, 2010, pp.71-83.

37) Niu W., etc., Limit Analysis of a Soil Slope Considering Saturated-unsaturated Seepage, Rock and Soil Mechanics, Vol.30, No.8, 2009, pp. 2477-2482.

38) Chen Y.F., etc., Modeling Coupled Processes of Non-steady Seepage Flow and Non-linear Deformation for a Concrete-faced Rockfill Dam, Computers and Structures, Vol 89, 2011, pp.1333-1351.

39) Luo Z.J., etc., Numerical Simulation Based on the Three-dimensional Full Coupling Model between Deep Foundation Pit Dewatering and Land-subsidence, Journal of Hydrodynamics, Vol. 21, No. 4, 2006, pp. 479-485. (In Chinese)

40) XU Y. S., etc., Three-dimensional Analysis of Land Subsidence Based on Groundwater Flow Model, Rock and Soil Mechanics, Vol.26, 2005, pp.109-112. (In Chinese)

41) Luo Z. J., etc., Three-dimensional Coupled Numerical Model between Deep Foundation Pit Dewatering and Land-subsidence, Journal of Jiangsu University, Vol.27, No. 4, 2006, pp. 356-359. (In Chinese)

42) Lin C., Zhou D. and Cao L., 3D Numerical Analysis on Dewatering of Foundation Pit in Soft Considering Seepage-consolidation Coupling, Tunnel Construction, Vol.30, pp.187-193. (In Chinese)

CHAPTER 2

BASIC THEORY OF SEEPAGE FLOW AND GROUND BEHAVIORS

2.1 Introduction

Water often exists in the materials which constitute the earth's crust. In addition to its physico-chemical effects, its influence on the mechanical behaviour of soil or rock masses is of utmost importance. The water flow induces hydrostatic pressures and seepage forces which have to be taken into consideration in order to solve geotechnical problems.

The presence of water in the pores as well as in the joints and cracks of soil or rock masses affects the intergranular state of equilibrium. A close interaction exists between mechanical and hydraulic phenomena: the flow influences the state of stress, which in turn determines the hydraulic characteristics of the media. Generally speaking，the state of stress governs the variations in the intergranular spaces in soil or porous media.

Underground water also plays an active role in seismo-tectonic phenomena, especially earthquakes. Evans (1966) 1) pointed out that the observed seismic activity in Denver from 1962 to 1966 was directly related to industrial liquid waste-injections in deep layers through the Rocky Mountains deep wells, close to Denver. The pore pressure increase, induced by the injections reduced the normal stresses on discontinuity planes. The consequence was a decrease of shear strength along the rock discontinuities, and sudden displacements under the pre-existing tectonic stresses. Permeability tests generally show that higher permeability values are obtained when measured by injection than by pumping $^{2)}$.

In order to accurately simulate the seepage flow and ground behaviors due to well pumping, we should be familiar with the soil mechanics. This chapter attempts to review and summarize the basic theory of seepage flow and ground behaviors.

2.2 Seepage

A material is said to be permeable if it contains continuous voids. Since such voids are contained in all soils including the stiffest clays, and in all nonmetallic construction materials including sound granite and neat cement, all these materials are permeable. Furthermore, the flow of water through all of them obeys approximately the same laws. Hence the difference between the flow of water through clean sand and through sound granite is merely one of degree.

The permeability of soils has a decisive effect on the cost and the difficulty of many construction operations, such as the excavation of open cuts in water-bearing sand, or on the rate at which a soft clay stratum consolidation under the influence of the weight of a superimposed fill. Even the permeability of dense concrete or rock may have important practical implications, because water exerts a pressure on the porous material through which it percolates. This pressure, which is known as seepage pressure, can be very high.

Actually, water flow in the soil or rock mass is very complicated which is quite different from the surface water, because the size and shape of cracks or voids are irregular which is shown in Figure 2-1. It is difficult to obtain the real distribution and flow situation of seepage in the soil or rock, so we research the seepage generally as an average distribution system using statistics method.

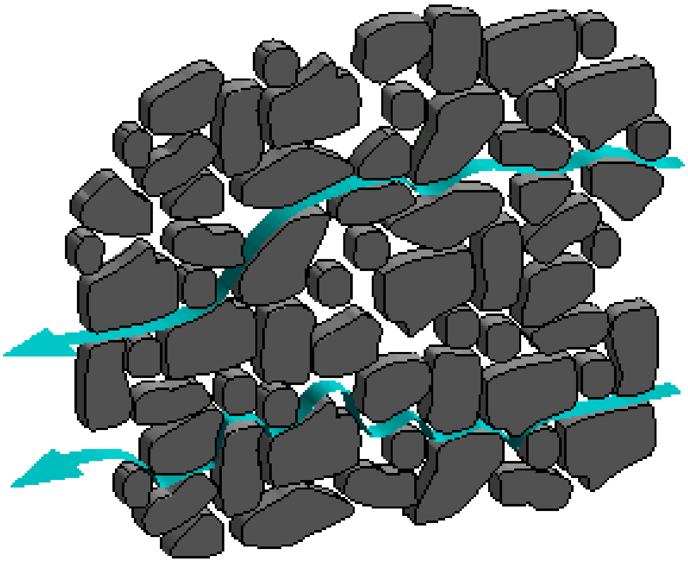

Figure 2-1 True flow paths of the seepage

2.2.1 Concept

By using statistics method, we can assume the imaginary water flow instead of real flow. We consider the imaginary water flow fills the whole medium domain, including the space which is occupied by the skeleton of the soil. In addition, the imaginary flow should obey the following properties:

(1) The flow rate of the imaginary water flow through arbitrary cross-section should equal to the real flow rate through the same cross-section, which is shown in Figure 2-2 and Figure 2-3.

(2) The water head of the imaginary water flow on arbitrary cross-section should equal to the real water head.

(3) The resistance force which the water flow gets in the soil or rock mass should equal to the real resistance force.

The seepage has two characteristic quantities: velocity of flow and water head, both of which are varying with time.

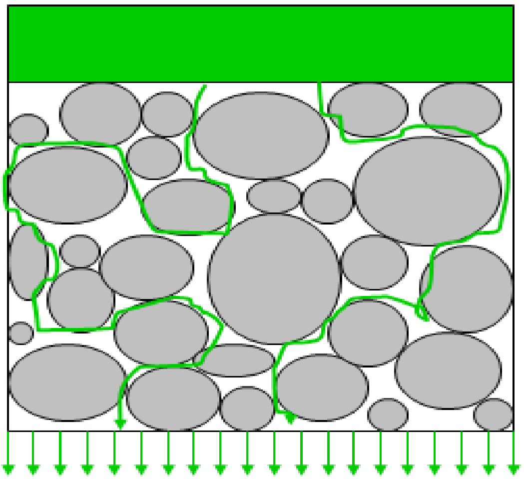

Figure 2-2 Real flow rate through arbitrary cross-section

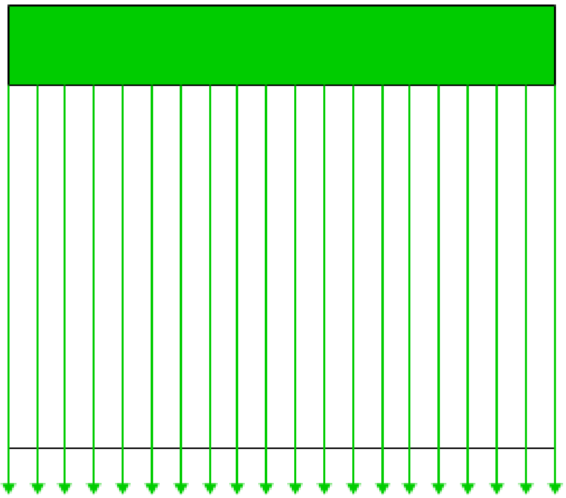

Figure 2-3 Imaginary flow rate through arbitrary cross-section

2.2.1.1 Total head

The total head h of arbitrary point in the seepage field can be expressed as:

$$h = \frac{P}{\gamma_w} + z + \frac{v^2}{2g} \qquad (2\text{-}1)$$

Where, $\frac{P}{\gamma_w}$ is pressure head

z is position head

$\frac{v^2}{2g}$ is velocity head

Generally speaking, the velocity of seepage in the soil or rock mass is very small relatively, so the velocity head can be ignored, and the Equation (2-1) can be shown as:

$$h = \frac{P}{\gamma_w} + z \qquad (2\text{-}2)$$

Total head is a fundamental physical quantity which is a function of space coordinates x, y, z and time t.

2.2.1.2 Seepage velocity

Seepage velocity is the average flow rate through the cross-section. The relationship between seepage velocity and real flow is shown below:

$$V = n \cdot u \qquad (2\text{-}3)$$

Where, V is seepage velocity

n is porosity of the soil or rock mass

u is real flow velocity

Seepage velocity is also a fundamental physical quantity which is a function of space coordinates x, y, z and time t, however, seepage velocity is vector, and total head is scalar.

2.2.2 Fundamental law of seepage

2.2.2.1 Darcy's law

As water percolates through a permeable material, the individual water particles move along paths which deviate erratically but only slightly from smooth curves known as flow lines. If adjacent flow lines are straight and parallel, the flow is said to be linear.

Henri Darcy, a French hydraulic engineer interested in purifying water supplies using sand filters, conducted experiments to determine the flow rate of water through the filters. He established empirically that the flux of water through a permeable formation is proportional to the distance between top and bottom of the soil column, which is shown in Figure 2-4.

Darcy's law provides an accurate description of the flow of ground water in almost all hydro-geologic environments and the equation is expressed as:

$$V = -K J = -K \frac{dh}{dL} \tag{2-4}$$

$$\begin{cases} Vx = -Kx\frac{\partial h}{\partial x} \\ Vy = -Ky\frac{\partial h}{\partial y} \\ Vz = -Kz\frac{\partial h}{\partial z} \end{cases} \tag{2-5}$$

where, K is hydraulic conductivity

J is hydraulic gradient

h is total head

L is the length

The hydraulic conductivity represents a measure of the ability for flow through porous media.

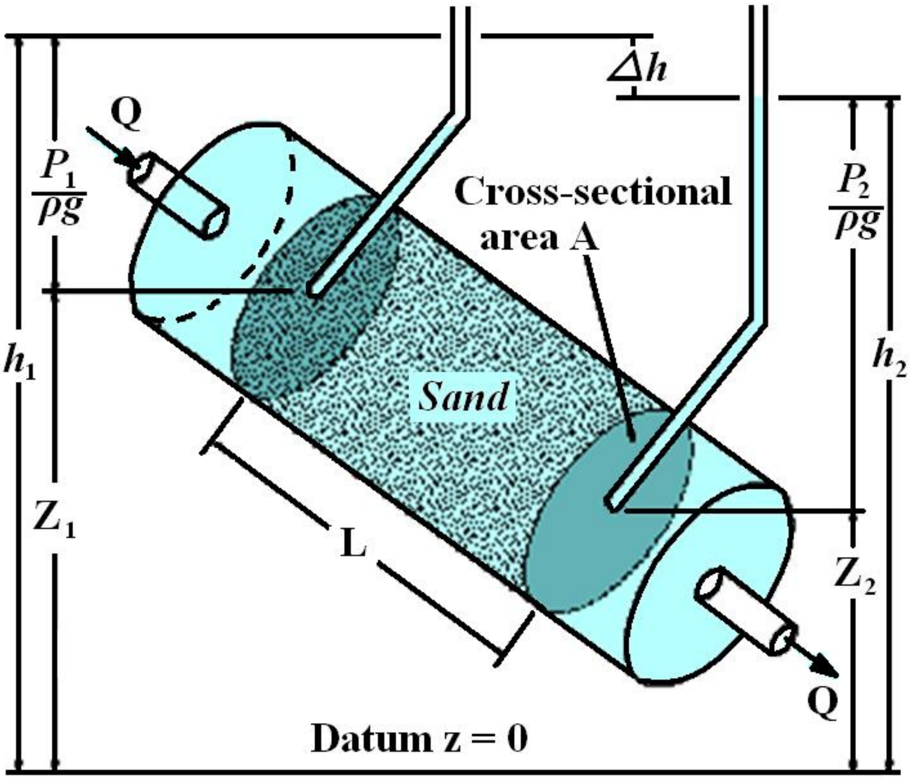

Figure 2-4 Generalization of Darcy's column

2.2.2.2 Applicable Conditions of Darcy's law

Darcy's law holds for:

(1) Saturated flow and unsaturated flow.

(2) Steady-state and transient flow.

(3) Flow in aquifers and aquitards.

(4) Flow in homogeneous and heterogeneous systems.

(5) Flow in isotropic or anisotropic media.

(6) Flow in rocks and granular media.

(7) Raynolds number is under 10.

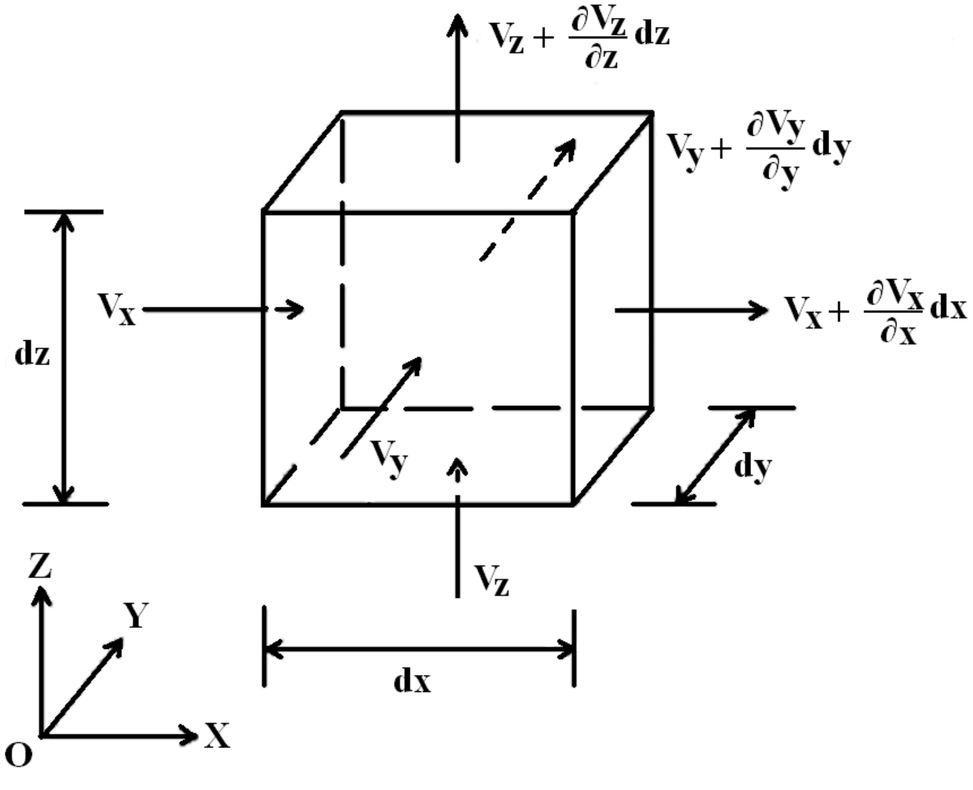

Figure 2-5 Representative elementary volume

2.2.3 Continuum equation of seepage in 3D seepage field

Continuum equation of seepage describes conservation of fluid mass during flow through a porous medium, and results in a partial differential equation of flow. Figure

2-5 shows the seepage flow pass through the representative elementary volume in 3D seepage field.

Table 2-1 Inflow and outflow of representative elementary volume

Direction	Inflow	Outflow
x	$\rho_w V_x dydzdt$	$\left[\rho_w V_x + \frac{\partial(\rho_w V_x)}{\partial x} dx\right] dydzdt$
y	$\rho_w V_y dxdzdt$	$\left[\rho_w V_y + \frac{\partial(\rho_w V_y)}{\partial y} dy\right] dzdxdt$
z	$\rho_w V_z dxdydt$	$\left[\rho_w V_z + \frac{\partial(\rho_w V_z)}{\partial z} dz\right] dxdydt$

As we can see, in the Table 2-1, the inflow and outflow of representative elementary volume in 3D seepage field are shown.

According to the law of mass balance: Outflow – Inflow = Change in storage, we get the continuum equation of seepage which is given by Equation (2-6) by considering the discharge volume Q.[3)]

$$-\left(\frac{\partial V_x}{\partial x} + \frac{\partial V_y}{\partial y} + \frac{\partial V_z}{\partial z}\right)\rho_w + Q\rho_w = \frac{\Delta V}{\Delta t} = \frac{\partial}{\partial t}(\rho_w Sw\, n) \tag{2-6}$$

Where, Sw is saturation

n is porosity

ρ_w is density of water

A change in h will produce change in ρ_w and n, replaced with specific storage Ss and specific capacity Cs and the right hand side of the Equation (2-6) can be changed to [3)]

$$\frac{\partial}{\partial t}(\rho_w Sw\, n) = \rho_w \frac{\partial}{\partial t}(Sw\, n) + Sw\, n\, \frac{\partial \rho_w}{\partial t}$$

$$= \left[\rho_w Sw \frac{\partial}{\partial h}(\, n) + \rho_w n\, \frac{\partial Sw}{\partial h}\right] \frac{dh}{dt} + Sw\, n\, \frac{\partial \rho_w}{\partial t}$$

$$\fallingdotseq \rho_w(\beta\, Ss + Cs)\frac{dh}{dt} \tag{2-7}$$

Where, Ss is specific storage

Cs is specific capacity

$$\beta = \begin{cases} 0 : \text{unsaturated} \\ 1 : \text{saturated} \end{cases}$$

$$\beta\, Ss = Sw \frac{\partial}{\partial h}(\, n)$$

$$Cs = n\, \frac{\partial Sw}{\partial h}$$

$$Sw\, n\, \frac{\partial \rho_w}{\partial t} \fallingdotseq 0$$

2.2.4 Basic differential equations of seepage

According to Equation (2-5), Equation (2-6) and Equation (2-7), we can get the basic differential equation of seepage in 3D seepage field. 3)

$$\frac{\partial}{\partial x}\left(K_x \frac{\partial h}{\partial x}\right) + \frac{\partial}{\partial y}\left(K_y \frac{\partial h}{\partial y}\right) + \frac{\partial}{\partial z}\left(K_z \frac{\partial h}{\partial z}\right) + Q = (\beta\, Ss + Cs)\frac{dh}{dt} \tag{2-8}$$

Under the steady flow state, the potential head doesn't vary with respect to time, so Equation (2-8) can be reduced to 3)

$$\frac{\partial}{\partial x}\left(K_x\frac{\partial h}{\partial x}\right)+\frac{\partial}{\partial y}\left(K_y\frac{\partial h}{\partial y}\right)+\frac{\partial}{\partial z}\left(K_z\frac{\partial h}{\partial z}\right)+Q=0 \tag{2-9}$$

2.2.5 Definite condition for basic differential equations

For seepage flow problem, the definite conditions include boundary conditions and initial conditions.

2.2.5.1 Boundary conditions

Boundary conditions mean the status (total head, flow velocity etc.) of hydraulic elements on the boundary, and boundary conditions include the first boundary condition and the second boundary condition.

The first boundary condition which is also called Dirichlet boundary condition means that the variation law of total head with time on the boundary is known, it can be shown as

$$h(x,y,z,t)=\overline{h}(x,y,z,t) \quad \text{on S1} \tag{2-10}$$

where, $\overline{h}(x,y,z)$ is known function

S1 is known boundary

The second boundary condition which is also called Neumann Boundary condition means the variation law of flow rate with time on the boundary is known, this kind of boundary conditions can be shown as

$$K\frac{\partial h}{\partial n}=\overline{V}\,(x,y,z,t) \quad \text{on S2} \tag{2-11}$$

where, $\overline{\mathrm{V}}\,(\mathrm{x,y,z,t})$ is known flow rate function

S2 is known boundary

On the impervious boundary, $\overline{\mathrm{V}} = 0$ Equation (2-11) reduced to

$$\mathrm{K}\frac{\partial \mathrm{h}}{\partial \mathrm{n}} = 0 \tag{2-12}$$

2.2.6 Axisymmetric seepage field theory

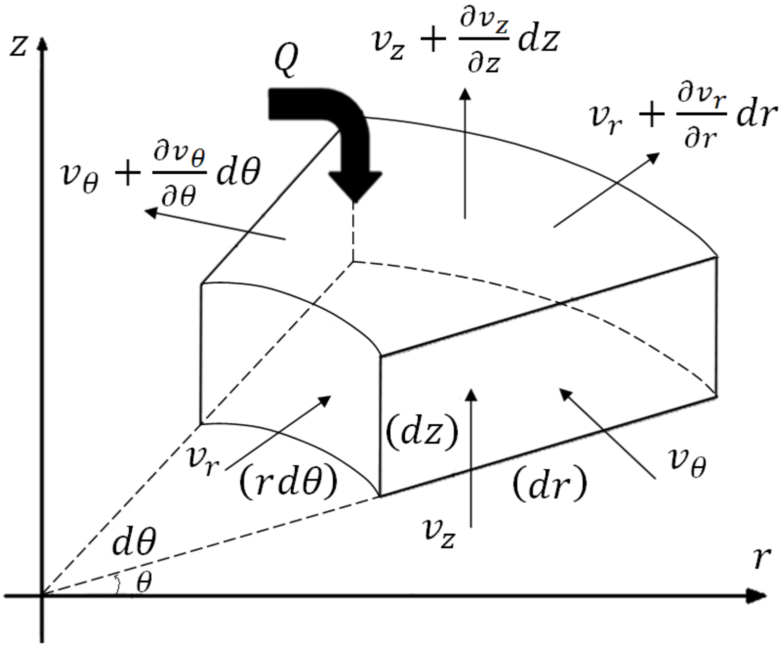

Figure 2-6 Representative elementary volume in cylindrical coordinate

The simulation of water flow in 3D seepage field is tedious, so when the single pumping well problem was considered, the axisymmetrical method can be used. In this way, the behaviors around the pumping well are assumed to be axisymmetrical, therefore, cylindrical coordinates can be used, and the problem can be considered as a 2D one. Figure 2-6 shows the representative elementary volume (REV) in cylindrical coordinate.

Table 2-2 Inflow and outflow of REV in cylindrical coordinate

Direction	Inflow	Outflow
r	$\rho v_x r d\theta dz dt$	$\left(v_r + \frac{\partial v_r}{\partial r} dr\right)(r + dr) d\theta dz dt$
θ	$\rho v_\theta dr dz dt$	$\left(v_\theta + \frac{\partial v_\theta}{\partial \theta} d\theta\right) dr dz dt$
z	$\rho v_z (r + \frac{dr}{2}) d\theta dr dt$	$\left(v_z + \frac{\partial v_z}{\partial z} dz\right)\left(r + \frac{dr}{2}\right) d\theta dr dt$

Table 2-2 shows the inflow and outflow of REV in cylindrical coordinate seepage field.

2.2.6.1 Continuum equation of seepage in axisymmetric seepage field

According to the law of mass balance: Outflow – Inflow = Change in storage, the continuum equation of seepage is given by Equation (2-13) by considering the discharge volume Q. 3), 4)

$$-(\frac{\partial v_r}{\partial r} + \frac{1}{r} v_r + \frac{1}{r}\frac{\partial v_\theta}{\partial \theta} + \frac{\partial v_z}{\partial z})\rho + Q\rho = \frac{\Delta V}{\Delta t} = \frac{\partial}{\partial t}(\rho Sw\, n) \qquad (2\text{-}13)$$

2.2.6.2 Basic differential equation of seepage in axisymmetric seepage field

Darcy’s law in axisymmetric seepage field can be written as

$$\begin{cases} V_r = -K_{rr}\frac{\partial h}{\partial x} \\ V_\theta = -\frac{1}{r}K_{\theta\theta}\frac{\partial h}{\partial \theta} \\ V_z = -K_{zz}\frac{\partial h}{\partial z} \end{cases} \tag{2-14}$$

According to Equation (2-7), Equation (2-13) and Equation (2-14), the basic differential equation of seepage in axisymmetric seepage field is shown in Equation (2-15)$^{3)}$

$$\frac{\partial}{\partial r}\left(k_{rr}\frac{\partial h}{\partial r}\right)+\frac{1}{r}k_{rr}\frac{\partial h}{\partial r}+\frac{\partial}{\partial z}\left(k_{zz}\frac{\partial h}{\partial z}\right)+Q=(\beta\,Ss\ +Cs)\frac{dh}{dt} \tag{2-15}$$

The first term and the second term on the left hand side of the equation can be combined, and the Equation (2-13) can be shown as

$$\frac{1}{r}\frac{\partial}{\partial r}\left(rk_{rr}\frac{\partial h}{\partial r}\right)+\frac{\partial}{\partial z}\left(k_{zz}\frac{\partial h}{\partial z}\right)+Q=(\beta\,Ss\ +Cs)\frac{dh}{dt} \tag{2-16}$$

By multiplying $2\pi r$ to the both sides of the equation, Equation (2-14) can be transformed to$^{3)}$

$$\frac{\partial}{\partial r}\left(K_{Haxis}\frac{\partial h}{\partial r}\right)+\frac{\partial}{\partial z}\left(K_{Vaxis}\frac{\partial h}{\partial z}\right)+Q_{axis}=C_{axis}\frac{dh}{dt} \tag{2-17}$$

where, $Q_{axis}=2\pi rQ$, $K_{Vaxis}=2\pi rk_{zz}$, $K_{Haxis}=2\pi rk_{rr}$, $C_{axis}=2\pi r(\beta\,Ss\ +Cs)$

k_{rr} is coefficient of permeability in horizontal direction

k_{zz} is coefficient of permeability in vertical direction

Q is discharge volume

h: total head

t: time

Ss is specific storage

Cs is specific capacity

$$\beta = \begin{cases} 0 : \text{unsaturated} \\ 1 : \text{saturated} \end{cases}$$

Under the steady flow state, the potential head doesn't vary with respect to time, so Equation (2-17) can be reduced to [3), 4)]

$$\frac{\partial}{\partial r}\left(K_{Haxis}\frac{\partial h}{\partial r}\right) + \frac{\partial}{\partial z}\left(K_{Vaxis}\frac{\partial h}{\partial z}\right) + Q_{axis} = 0 \qquad (2\text{-}18)$$

2.2.7 Saturated-unsaturated seepage theory

The saturated-unsaturated theory has been considered in recently. The effect of the capillary zone has been taken into account, which is much more realistic manner to simulate the groundwater seepage flow. According to unsteady seepage theory, the position of free surface of underground water and overflow boundaries are also changed with time.

The Saturated-unsaturated theory divides the whole domain by phreatic surface into two parts, saturated region and unsaturated region. Because the phreatic surface and leaking face are both unknown at first, an iteration process for locating the phreatic surface and leading face is needed on each time step. The saturated-unsaturated seepage theory will be discussed in the detail in section (4.3.3)

2.3 Ground behaviors

To understand the ground behavious, it is necessary to understand how normal stresses and shear stresses are shared by the different phases. Neither gas nor liquid provide significant resistance to shear stress. The shear resistance of soil is provided by friction and interlocking of the particles. The friction depends on the intergranular contact stresses between solid particles. The normal stresses are shared by the fluid and the particles. Although the pore air is relatively compressible, and hence takes little normal stress in most geotechnical engineering problems, liquid water is relatively incompressible and if the voids are saturated with water, the pore water must be squeezed out in order to pack the particles closer together.

2.3.1 Concept

2.3.1.1 Effective stress

The principle of effective stress, introduced by Karl Terzaghi, states that the effective stress σ' (the average intergranular stress between solid particles) may be calculated by a simple subtraction of the pore pressure from the total stress which is shown in Equation (2-19).

$$\sigma' = \sigma - u \tag{2-19}$$

where, σ is the total stress

u is the pore pressure.

It is not practical to measure σ' directly, so in practice the vertical effective stress is calculated from the pore pressure and vertical total stress.

2.3.1.2 Total stress

For level ground conditions, the total vertical stress σ at a point, on average, is the weight of everything above that point per unit area. The vertical stress beneath a uniform surface layer with mass density ρ, and thickness H is:

$$\sigma = \rho g H \; = \; \gamma H \tag{2-20}$$

where, g is the acceleration due to gravity

γ is the unit weight of the overlying layer

If there are multiple layers of soil or water above the point, the vertical stress may be calculated by summing the product of the unit weight and thickness of all of the overlying layers. Total stress increases with increasing depth in proportion to the density of the overlying soil.

2.3.1.3 Pore water pressure

Pore water pressure refers to the pressure of groundwater held within a soil or rock, in gaps between particles or pores. Pore water pressures in below the phreatic level are measured in piezometers. The vertical pore water pressure distribution in aquifers can generally be assumed to be close to hydrostatic. Pore water pressure is vital in calculating the stress state in the ground soil mechanics, from Terzaghi's expression for the effective stress of a soil.

2.3.1.4 Ground behaviors due to seepage

The act of pumping can draw down the free surface of the groundwater table, and can affect a large region which is shown in Figure 2-7.

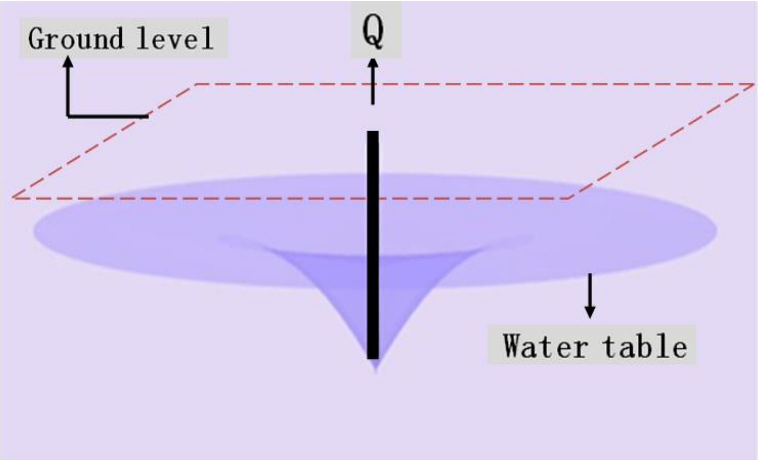

Figure 2-7 The act of pumping

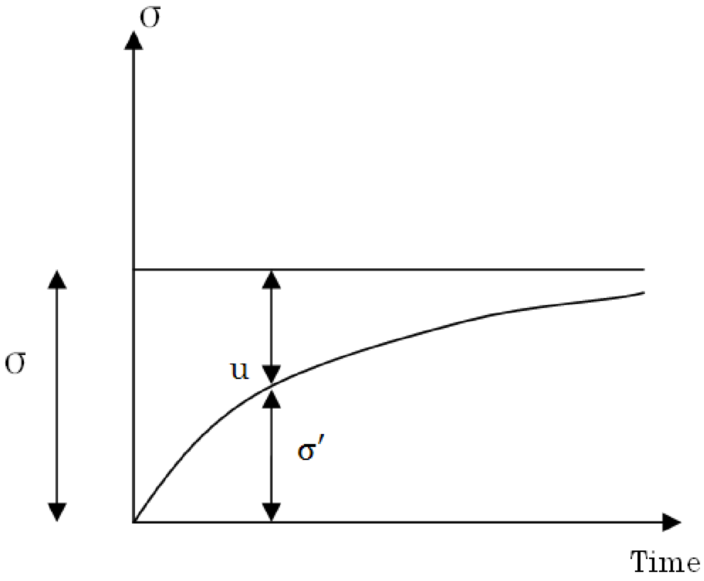

Figure 2-8 The relationship of effective stress and pore pressure

In the area which is saturated before pumping and unsaturated after pumping, the pore pressure will be decreased. From the Equation (2-19), when total stress σ is constant, effective stress σ' will increase if pore pressure decreases. The relationship of effective stress and pore pressure is shown in Figure 2-8.

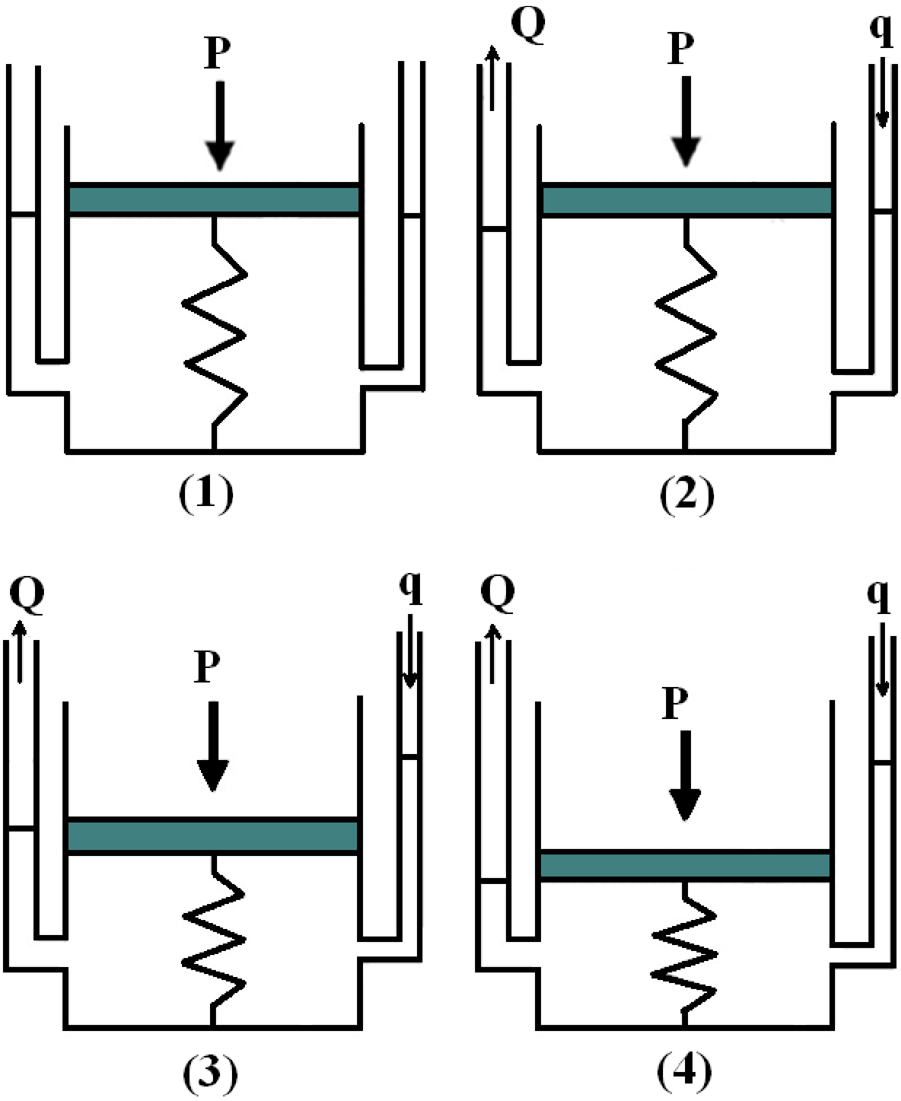

Figure 2-9 Deformation spring analogy

The effective stress in the soil will be increased by lowering the ground water level, which causes subsequent ground deformation. Figure 2-9 shows the deformation spring analogy. The process of soil deformation due to well pumping can be explained with an idealized system composed of a spring, and a container with water. In this system, the spring represents the compressibility or the structure itself of the soil, and the water which fills the container represents the pore water in the soil.

(1) The container is completely filled with water. At this stage, external force P is resisted by both water and spring.

(2) Drain the water off as a pumping rate Q and supply the water as a feed water rate q. Pumping rate Q represents the pumping well effect and the feed water rate q stands for the water supply effect from the surrounding areas.

(3) When pumping rate Q is larger than feed water rate q, the volume of water in the container begins to decrease and the spring shortens. (The effective stress in the soil is increased by lowering the ground water level, which causes subsequent ground deformation).

(4) After some time, the feed water rate q becomes larger and larger until q equal to the pumping rate Q. At this stage, the volume of water in the container is constant and the spring will no longer become shorter. (Steady state and the phreatic surface is no longer changed)

2.3.2 Factors affecting the ground behaviors due to seepage

Generally speaking, pumping rate Q and seepage force are very important factors, which can affect the ground behaviors.

On one hand, if the pumping rate Q is larger, the phreatic surface will be drawn down lower, and the unsaturated area will be relatively larger, which causes larger vertical deformation of soil due to the increasing effective stress.

On the other hand, seepage force due to seepage flow can also cause deformation of soil, which is shown in Equation (2-21). 5)

$$\mathrm{F} = -\frac{\partial \mathrm{h}}{\partial \mathrm{L}}\gamma_{\mathrm{w}} \tag{2-21}$$

where, h is the total head

L is the length

γ_{w} is unit weight of water

The direction of seepage force is in accordance with the direction of seepage flow, so it can cause both vertical and horizontal deformations. There is no direct relationship between the seepage force and coefficient of permeability. But soil is anisotropic material and natural soil is formed hierarchically. The permeability of different soils varies greatly, which affects the value and direction of seepage force apparently. Therefore, in actual project, the influence of permeability of soils about displacement distribution is significant.

2.3.3 Three-dimensional deformation theory

First of all, the basic equation of solid mechanics should be reviewed. As we know, in numerical analysis, soil is a three-phase body, which naturally mixed by granular, water and air. For simplicity, the soil is generally considered as continuum materials. Generally speaking, three requirements termed as equilibrium, compatibility and constitutive relation should be strictly demanded. Moreover, the initial and boundary conditions on the forces and displacement must be satisfied. The three dimensional case equations are given below.

2.3.3.1 Equations of equilibrium

The discussion scope is limited to the statics problem. The correlation among stress components, body force and external force in Figure 2-10 should be satisfied and the equilibrium equations which considers the seepage force is shown in Equation (2-22)$^{5)}$

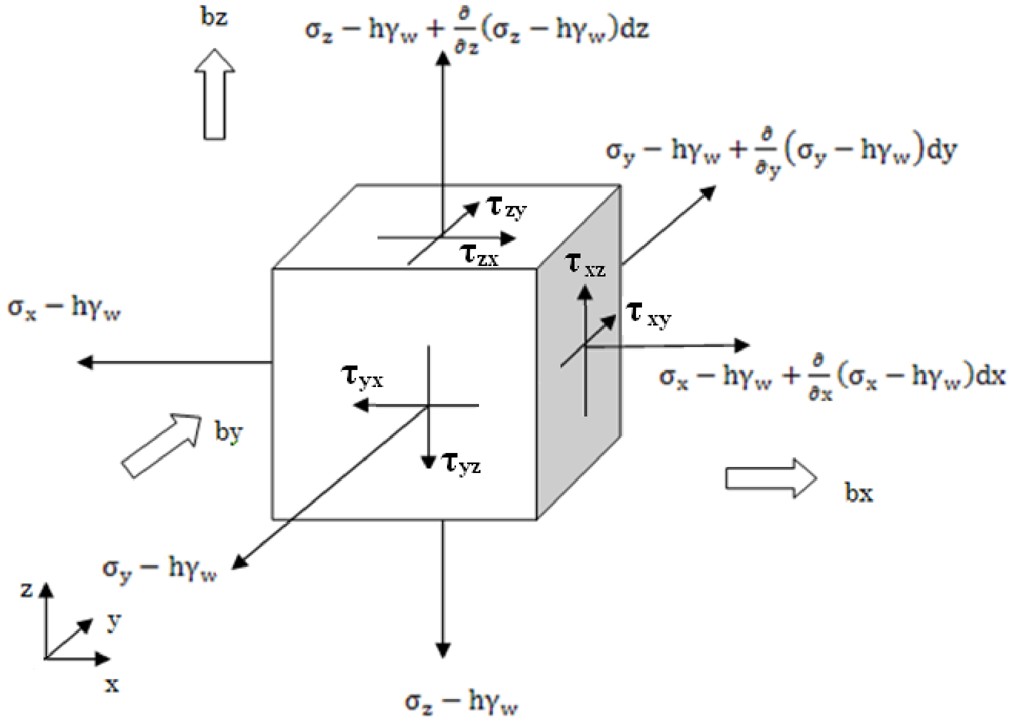

Figure 2-10 Stresses in the element component

$$\begin{cases} \frac{\partial \sigma_x}{\partial x} + \frac{\partial \tau_{yx}}{\partial y} + \frac{\partial \tau_{zx}}{\partial z} + bx - \frac{\partial h}{\partial x}\gamma_w = 0 \\ \frac{\partial \tau_{xy}}{\partial x} + \frac{\partial \sigma_y}{\partial y} + \frac{\partial \tau_{zy}}{\partial z} + by - \frac{\partial h}{\partial y}\gamma_w = 0 \\ \frac{\partial \tau_{xz}}{\partial x} + \frac{\partial \tau_{yz}}{\partial y} + \frac{\partial \sigma_z}{\partial z} + bz - \frac{\partial h}{\partial z}\gamma_w = 0 \end{cases} \qquad (2\text{-}22)$$

where, b_x, b_y, b_z are respectively denote body forces in three directions. $\frac{\partial h}{\partial x}\gamma_w$, $\frac{\partial h}{\partial y}\gamma_w$, $\frac{\partial h}{\partial z}\gamma_w$ are respectively stand for seepage forces in three directions

2.3.3.2 Equation of compatibility

Compatibility condition is regarded as relation between the strain components and displacement components, and the Equation (2-23) give the equation of compatibility in 3D stress field.

$$\begin{cases} \varepsilon_x = \frac{\partial u}{\partial x} \\ \varepsilon_y = \frac{\partial v}{\partial y} \\ \varepsilon_z = \frac{\partial w}{\partial z} \\ \gamma_{xy} = \frac{\partial u}{\partial y} + \frac{\partial v}{\partial x} \\ \gamma_{yz} = \frac{\partial v}{\partial z} + \frac{\partial w}{\partial y} \\ \gamma_{xz} = \frac{\partial w}{\partial x} + \frac{\partial u}{\partial z} \end{cases} \tag{2-23}$$

The u, v, w denotes the displacement and the six strain components are not independent.

2.3.3.3 Constitutive equation

This relation is to describe material behavior. In simple terms, it is the stress-strain behavior of the soil body. It also provides the link between equilibrium and compatibility. Here 3D form is given in Equation (2-24).

$$\{\sigma\} = \begin{Bmatrix} \sigma_x \\ \sigma_y \\ \sigma_z \\ \tau_{xy} \\ \tau_{yz} \\ \tau_{zx} \end{Bmatrix} = \frac{E(1-\nu)}{(1+\nu)(1-2\nu)} \begin{bmatrix} \mathbf{1} & & & & \mathbf{(sym)} & \\ \frac{\nu}{1-\nu} & \mathbf{1} & & & & \\ \frac{\nu}{1-\nu} & \frac{\nu}{1-\nu} & \mathbf{1} & & & \\ & & & \frac{1-2\nu}{2(1-\nu)} & & \\ & \mathbf{0} & & & \frac{1-2\nu}{2(1-\nu)} & \\ & & & & & \frac{1-2\nu}{2(1-\nu)} \end{bmatrix} \begin{Bmatrix} \varepsilon_x \\ \varepsilon_y \\ \varepsilon_z \\ \gamma_{xy} \\ \gamma_{yz} \\ \gamma_{zx} \end{Bmatrix} \qquad (2\text{-}24)$$

where, ν is Poisson's ratio

E is Young's elastic Modulus

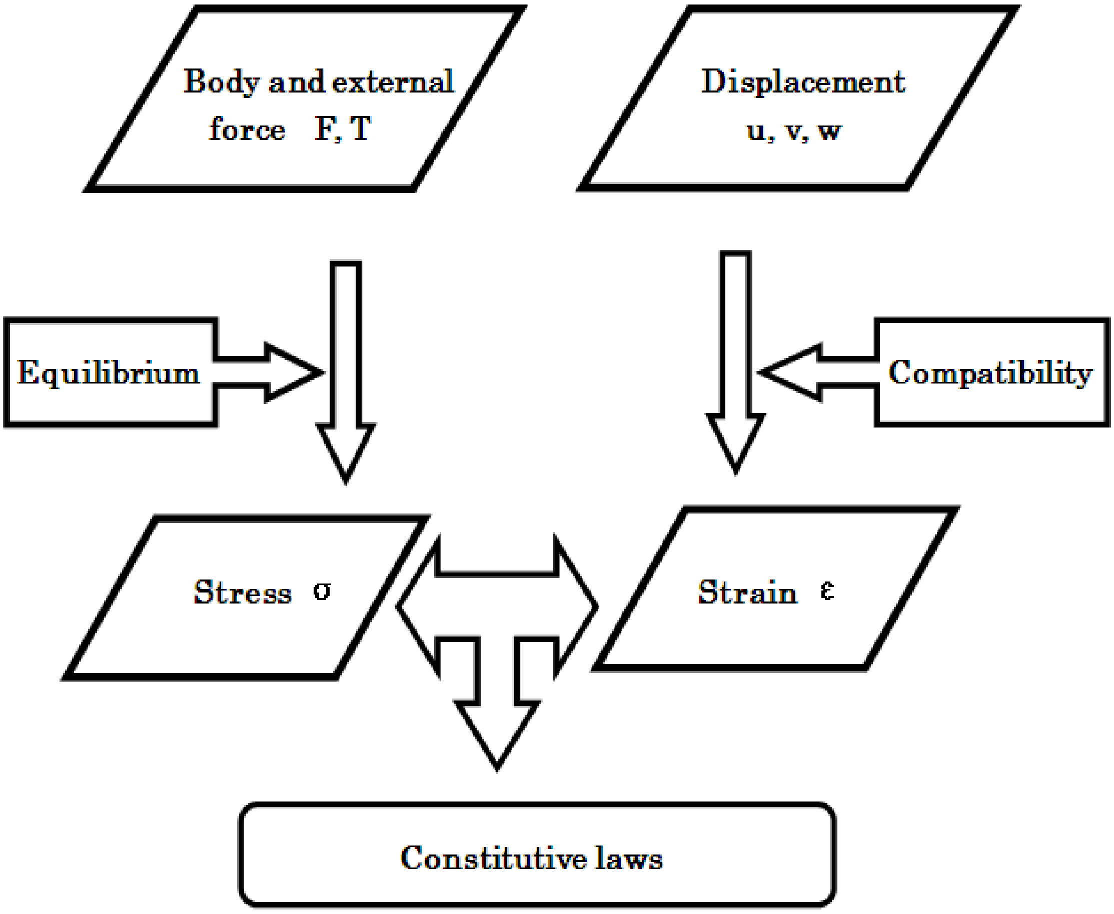

Figure 2-11 Interrelationship of variables

If the material constitutive law is established, the general formulation for the solution of a solid mechanics can be completed. The above three equations interrelationship can be summarized in Figure 2-11.

2.3.4 Axisymmetric deformation theory

According to the axisymmetrical problem, totally, there are four stress and four strain components and two displacement components. In the axisymmetrical coordinate, r and z stand for respectively the radial and axial coordinates, and the u and v denote the corresponding displacements. Moreover, θ represents angle direction.

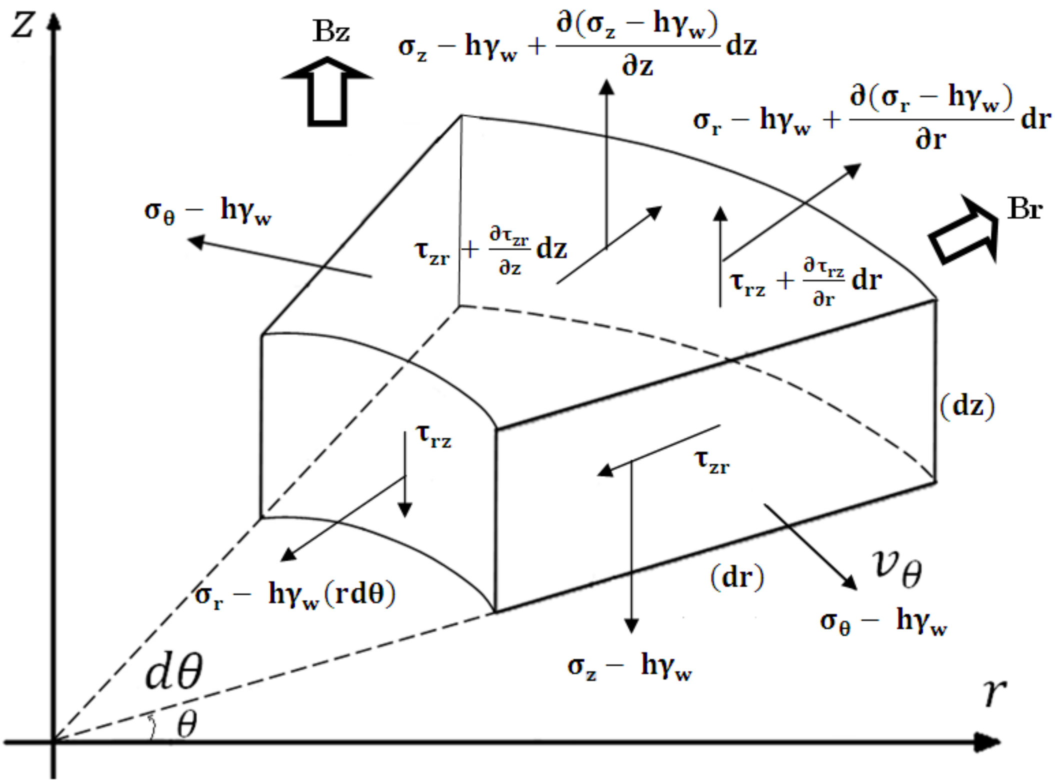

Figure 2-12 Stresses in axisymmetric element component

2.3.4.1 Equations of equilibrium

Stresses in axisymmetric element component are shown in the Figure 2-12. The correlation among stress components, body force and external force in Figure 2-12 should be satisfied and the equilibrium equations which considers the seepage force in axisymmetric stress field is shown in Equation (2-25)

$$\begin{cases} \frac{\partial \sigma_r}{\partial r} + \frac{\partial \tau_{zr}}{\partial z} + \frac{\sigma_r - \sigma_\theta}{r} + \mathrm{br} - \frac{\partial h}{\partial r}\gamma_w = 0 \\ \frac{\partial \tau_{rz}}{\partial r} + \frac{\partial\, \sigma_z}{\partial z} + \frac{\tau_{rz}}{r} + b_z - \frac{\partial h}{\partial z}\gamma_w = 0 \end{cases} \tag{2-25}$$

2.3.4.2 Equation of compatibility

Refer to axisymmetrical problem, totally, there are four strain components, and the equation of compatibility in axisymmetrical stress field is given in Equation (2-26).

$$\begin{cases} \varepsilon_r = \frac{\partial u}{\partial r} \\ \varepsilon_z = \frac{\partial v}{\partial z} \\ \varepsilon_\theta = \frac{u}{r} \\ \gamma_{rz} = \frac{\partial u}{\partial z} + \frac{\partial v}{\partial r} \end{cases} \tag{2-26}$$

2.3.4.3 Constitutive equation

Similar with Equation (2-24), there are four components of stress and strain in axisymmetrical field. And the constitutive equation is given in Equation (2-27).

$$\{\sigma\} = \begin{Bmatrix} \sigma_r \\ \sigma_z \\ \sigma_\theta \\ \tau_{rz} \end{Bmatrix} = \frac{E(1-\nu)}{(1+\nu)(1-2\nu)} \begin{bmatrix} 1 & \frac{1}{1-\nu} & \frac{1}{1-\nu} & 0 \\ \frac{1}{1-\nu} & 1 & \frac{1}{1-\nu} & 0 \\ \frac{1}{1-\nu} & \frac{1}{1-\nu} & 1 & 0 \\ 0 & 0 & 0 & \frac{1-2\nu}{2(1-\nu)} \end{bmatrix} \begin{Bmatrix} \varepsilon_r \\ \varepsilon_z \\ \varepsilon_\theta \\ \gamma_{rz} \end{Bmatrix} \tag{2-27}$$

2.3.5 Non-linear deformation theory

Duncan-chang model 6) is a nonlinear elastic model, which has been establishing based on Mohr-Coulomb strength criterion and bulk strain assuming to be hyperbola in generalized which is shown in Figure 2-13.

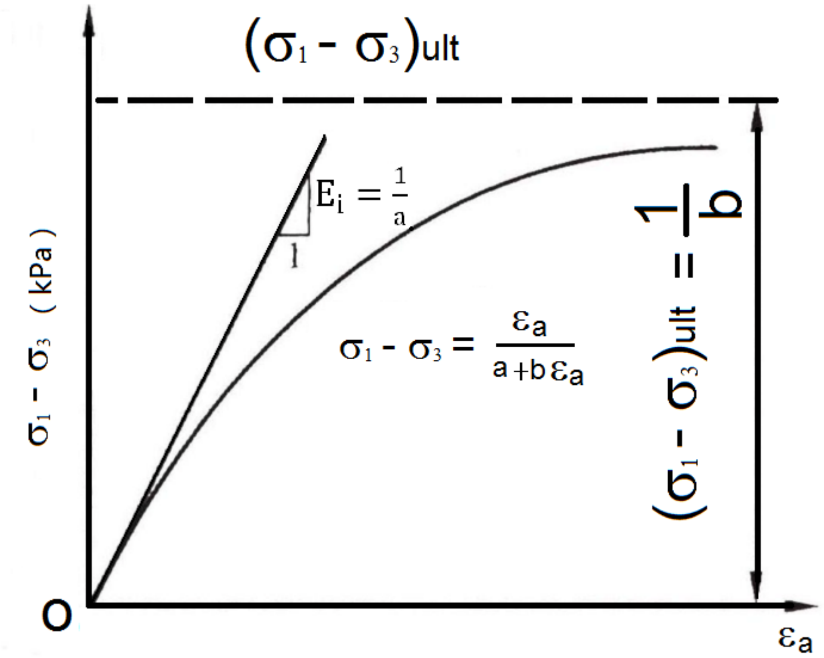

Figure 2-13 Duncan-Chang model

$$E_t = \left[1 - \frac{R_f(1-\sin\varphi)(\sigma_1-\sigma_3)}{2c\cos\varphi + 2\sigma_3\sin\varphi}\right]^2 Kp_a\left(\frac{\sigma_3}{p_a}\right)^n \tag{2-28}$$

$$E_{ur} = K_{ur}p_a\left(\frac{\sigma_3}{p_a}\right)^n \tag{2-29}$$

This approach can be used in both loading and unloading conditions, as well as reloading problem, and the model parameters could be obtain directly from the tri-axial compression test, therefore, Duncan-Chang model is well known in the field of geotechnical engineering as one of the most popular constitutive model 7)-10) and widely used in geotechnical engineering.

The expression for Young's modulus E_t under loading condition can be expressed in Equation (2-28). Soil is an elasto-plastic material in the sense that strains induced upon primary loading are only partially recoverable upon unloading, and when reloaded it behaves nearly elastically. The modulus value of unloading-reloading with confining pressure for D-C model E_{ur} may be represented in Equation (2-29).

2.4 Summary

This chapter introduces basic theory of seepage flow and ground behaviors, respectively. The seepage and the deformation theory has been introduces in detail. The finite element method theory for seepage and deformation will be discussed in next chapter.

Reference

1) D. M. Evans, The Denver area earthquakes and the rocky mountain arsenal disposal well, Mr. Geol., 3(1), 1966, pp. 23-36.

2) G.Gudehus: Finite elements in geomechanics, John wiley & sons, 1977, pp.478-511.

3) Makoto NISHIGAKI, Simulation of groundwater flow and solute transport, Gihodo press, 2010, pp. 31-55. (In Japanese)

4) Haruyuki YAMAMOTO, Koji TOMINAGA and Mamoru SAHARA, Experimental Research on controlling the effective stress in sand by means of seepage force, Research report of faculty of engineering Hiroshima University, 1987, pp. 33-41. (In Japanese)

5) Miau-Bin Su, Cheng-Lung Su, Chi-Jeh Chang, Yuh-Jyh Chen: A numerical model of ground deformation in induced by single well pumping, Compurers and Geotechnics 23, 1998, pp. 39-60.

6) J. M., Duncan, C. Y. Chang, Nonliear analysis of stress and strain in soil, SMFE ASCE, Vol. 96, 1970, pp. 1629-1653.

7) D.A. Sun, H. matsuoka, Estimate of initial modulus of hyperbolic stress-strain relation from result of consolidation tests, Thirteenth southeast Asian geotechnical conference, Taipei, 1998, pp.171-176.

8) C. F. Zhao, etc., An improved Duncan-Chang model considering effect of intermediate principal stress and shear dilatancy, Journal of Tongji University, Vol. 39, 2011, pp. 309-313. (In Chinese)

9) Z. H. Dai, etc., Noticeable problems of Duncan-Chang model applied in engineering of

foundation pit, Journal of Fuzhou University, Vol. 38, 2010, pp.120-126. (In Chinese)

10) L. H. Cheng, etc., Comprehensive illustration on improvement methods for Duncan-Chang model, Shanxi architecture, 2010, pp. 121-122. (In Chinese)

CHAPER 3

FINITE ELEMENT METHOD FORMULATION

3.1 Introduction

3.1.1 History

The development of FEM can be traced back to the work by Alexander Hrennikoff (1941) 1) and Richard Courant (1943) 2). The finite element method originated from the need for solving complex elasticity and structural analysis problems in civil and aeronautical engineering. Although the approaches used by these pioneers are different, they share one essential viewpoint: the continuous domain can be discretized into a set of discrete subdomains, which are usually called elements. The finite element method is a good choice for solving partial differential equations over complicated domains.

3.1.2 Basic concepts

The finite element method (FEM), or finite element analysis (FEA), is a numerical technique, which can be used for finding approximate solutions of partial differential equations as well as of integral equations. While the FEM has been used in many fields of engineering practice extensively for over forty years, it is only relatively recently that the geotechnical problems have begun to be widely used for analysis 3)-4). This is probably because that there are many complicated questions which are specific to geotechnical engineering. With the development of the finite element method, the ability to numerically model complicated soil structures has become possible recently.

3.2 Basic theory of finite element method

3.2.1 Available elements

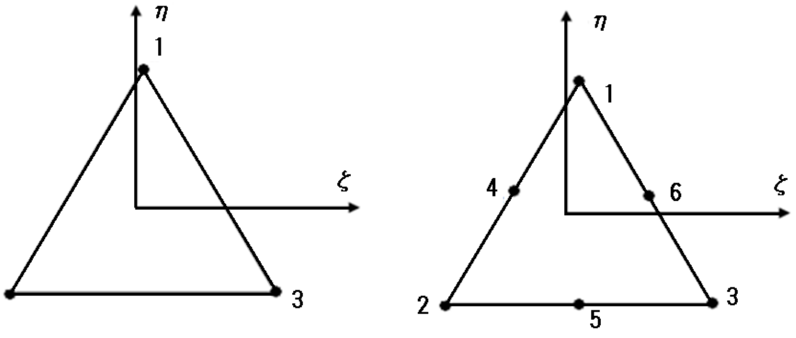

(a) 3- nodal triangular element (b) 6- nodal triangular element

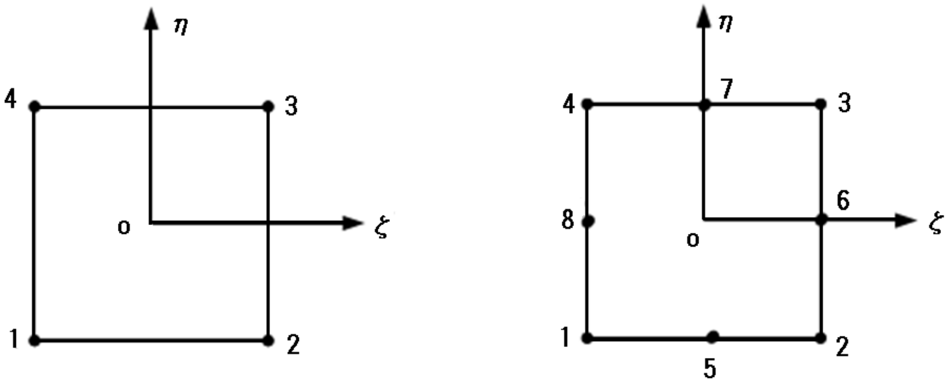

(c) 4-nodal quadrilateral element (d) 8- nodal quadrilateral element

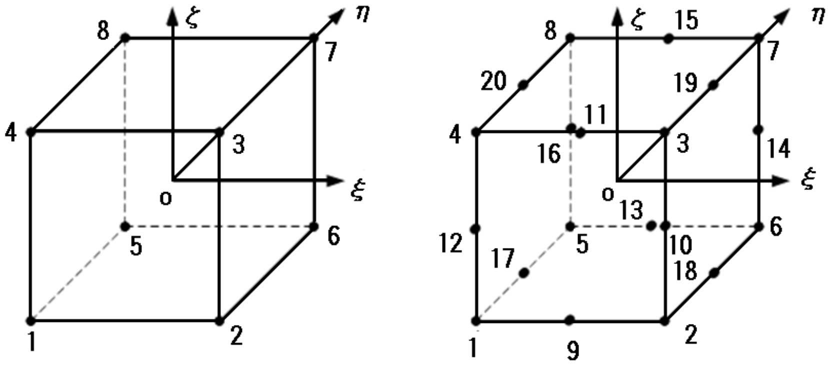

(e) 8-nodal hexahedron element (f) 20- nodal hexahedron element

Figure 3-1 Common elements for finite element analysis

There are many kinds of elements，which are available for finite element analysis. The most common elements are triangular element, quadrilateral element and hexahedron element, some of which are given in Figure 3-1

Generally speaking, triangular element and quadrilateral element are used for 2D and axisymmetric calculation while hexahedron element is for 3D calculation.3.2.2 Variational principle and functional

3.2.2 Variational principle and functional

A variational principle is a scientific principle used within the calculus of variations, which develops general methods for finding functions which minimize or maximize the value of quantities that depends upon those functions.

Functional is the function that the independent variable of the function is another function.

For example, A is a function of Φ and Φ is a function of x, and A is a functional. The variational formulations are shown in Equation (3-1), (3-2) and (3-3).

$$\frac{d\emptyset}{dx} = A \tag{3-1}$$

$$\delta\left[\frac{1}{2}(A)^2\right] = A\delta A \tag{3-2}$$

$$\delta A = \delta\left(\frac{d\emptyset}{dx}\right) = \frac{d\delta\emptyset}{dx} \tag{3-3}$$

3.2.2.1 Functional for axisymmetric seepage field

Here the functional was defined for axisymmetric seepage field which is given in Equation (3-4)

$$V = \int_A \frac{1}{2}\left\{\left[K_{Haxis}\left(\frac{\partial h}{\partial r}\right)^2 + K_{Vaxis}\left(\frac{\partial h}{\partial z}\right)^2\right] - 2Q_{axis}h + 2C_{axis}h\frac{dh}{dt}\right\} dA + \int_{L_2} \bar{v}_{axis}hdL \tag{3-4}$$

Where, $K_{Haxis} = 2\pi r k_{rr}$

$$K_{Vaxis} = 2\pi r k_{zz}$$

$$Q_{axis} = 2\pi r Q$$

$$\bar{v}_{axis} = 2\pi r\bar{v}$$

$$C_{axis} = 2\pi r(\beta\, Ss + Cs)$$

Cs is specific capacity

Ss is specific storage

$\bar{v}$ is velocity of the water on the boundary conditions

If variational operations were made to Equation (3-4) according to variational principle, the equation was shown below

$$\delta V = \int_A \left[K_{Haxis}\frac{\partial h}{\partial r}\frac{\partial}{\partial r}(\delta h) + K_{Vaxis}\frac{\partial h}{\partial z}\frac{\partial}{\partial z}(\delta h) - Q_{axis}\delta h + C_{axis}\frac{dh}{dt}\delta h\right] dA + \int_{L_2} \bar{v}_{axis}\delta hdL \tag{3-5}$$

The first term on the right hand side of the Equation (3-5) can be transformed to

$$\int_A \left[K_{Haxis}\frac{\partial h}{\partial r}\frac{\partial}{\partial r}(\delta h)\right]dA$$
$$=\int_A \left[\frac{\partial}{\partial r}\left(K_{Haxis}\frac{\partial h}{\partial r}\delta h\right)-\frac{\partial}{\partial r}\left(K_{Haxis}\frac{\partial h}{\partial r}\right)\delta h\right]dA \qquad (3\text{-}6)$$

According to Gaussian divergent theorem, the first term on the right hand side of the Equation (3-6) is transformed as below

$$\int_A \left[\frac{\partial}{\partial r}\left(K_{Haxis}\frac{\partial h}{\partial r}\delta h\right)\right]dA=\int_{L_2} \ell_r K_{Haxis}\frac{\partial h}{\partial r}\delta h dL$$

where, ℓ_r is direction cosine in the r direction on the boundary surface.

In this way, Equation (3-6) can be given as

$$\int_A \left[K_{Haxis}\frac{\partial h}{\partial r}\frac{\partial}{\partial r}(\delta h)\right]dA$$
$$=\int_L \ell_r K_{Haxis}\frac{\partial h}{\partial r}\delta h dL-\int_A \frac{\partial}{\partial r}\left(K_{Haxis}\frac{\partial h}{\partial r}\right)\delta h dA$$

In the same way, the second item on the right hand side of the Equation (3-5) can be transformed to

$$\int_A \left[K_{Vaxis}\frac{\partial h}{\partial z}\frac{\partial}{\partial z}(\delta h)\right]dA$$
$$=\int_{L_2} \ell_z K_{Vaxis}\frac{\partial h}{\partial z}\delta h dL-\int_A \frac{\partial}{\partial z}\left(K_{Vaxis}\frac{\partial h}{\partial z}\right)\delta h dA$$

where, ℓ_z is direction cosine in the z direction on the boundary surface.

From the above, Equation (3-5) can be written as Equation (3-7), which is shown as below

$$\delta V = \int_A -\left[\frac{\partial}{\partial r}\left(K_{Haxis}\frac{\partial h}{\partial r}\right) + \frac{\partial}{\partial z}\left(K_{Vaxis}\frac{\partial h}{\partial z}\right) + Q_{axis} - C_{axis}\frac{dh}{dt}\right]\delta h dA$$

$$+ \int_{L_2} 2\pi r\left[\bar{v} + k_{rr}\frac{\partial h}{\partial r}\ell_r + k_{zz}\frac{\partial h}{\partial z}\ell_z\right]\delta h dL \qquad (3\text{-}7)$$

Here, the boundary conditions $\bar{v}$ were introduced, as it is introduced in chapter 2, there are two kinds of boundary conditions for seepage.

(1) The first boundary condition (total head is known)

On the first boundary $h = \bar{h}$

(2) The second boundary condition (flow velocity is known)

On the second boundary

$$-k_r\frac{\partial h}{\partial r} - k_z\frac{\partial h}{\partial z} = \bar{v}$$

Figure 3-2 shows the coordinate transformation, ℓ_r and ℓ_z stand for the direction cosine respectively in r and z direction on the boundary surface.

Equation (3-8) gives the vector transformation in two dimensional seepage field.

$$\begin{Bmatrix} v'_r \\ v'_z \end{Bmatrix} = \begin{bmatrix} \ell_r & \ell_z \\ -\ell_z & \ell_r \end{bmatrix}\begin{Bmatrix} v_r \\ v_z \end{Bmatrix} \qquad (3\text{-}8)$$

Here, $\bar{v} = v'_r$ and the expression was shown as below

$$\bar{v} = -k_{rr}\frac{\partial h}{\partial r}\ell_r - k_{zz}\frac{\partial h}{\partial z}\ell_z$$

On the impervious boundary, $\bar{v} = 0$, so from the above, the expression of boundary conditions can be written as below

$$\left.\begin{array}{l} k_{rr}\frac{\partial h}{\partial r}\ell_r + k_{zz}\frac{\partial h}{\partial z}\ell_z + \bar{v} = 0 \\ \bar{v} = 0 \text{ (On the impervious boundary)} \end{array}\right\} \tag{3-9}$$

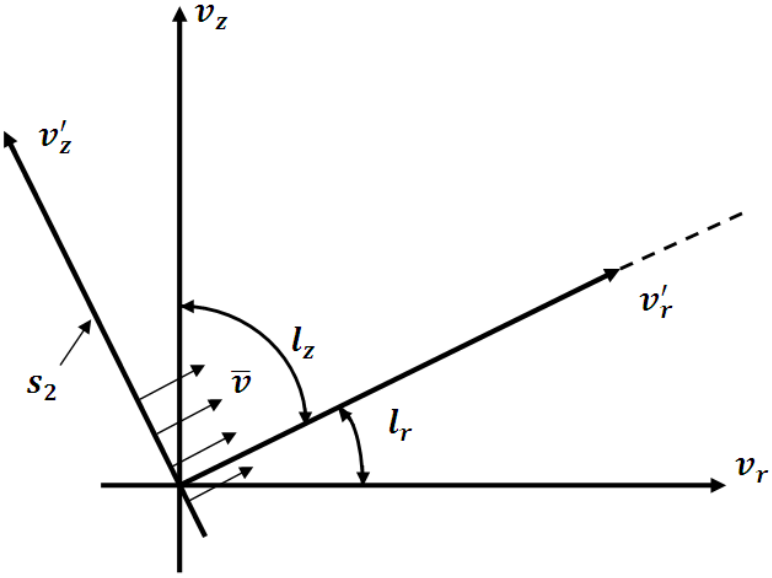

Figure 3-2 Coordinate transformation

As it is shown in the Equation (3-7), the first term on the right hand side of the equation involves the Equation (2-17) and the second term involves the Equation (3-9).

If δV=0 in Equation (3-7), it is tenable and the stationary exists, the Equation (2-17) and Equation (3-9) are valid. And according to this stationary, the value of h (r, z, t) can be given, which satisfies the both of Equation (2-17) and Equation (3-9).

3.2.2.2 Functional for 3D seepage field

The functional for 3D seepage field under steady state is defined as below

$$V = \int_V \frac{1}{2}\left\{\left[k_x\left(\frac{\partial h}{\partial x}\right)^2 + k_y\left(\frac{\partial h}{\partial y}\right)^2 + k_z\left(\frac{\partial h}{\partial z}\right)^2\right] - 2Qh\right\} dV + \int_{S_2} \bar{v}hdS \qquad (3\text{-}10)$$

If variational operation is made to Equation (3-10) according to variational principle, the equation can be shown as below

$$\delta V = \int_V \left[k_x \frac{\partial h}{\partial x}\frac{\partial}{\partial x}(\delta h) + k_y \frac{\partial h}{\partial y}\frac{\partial}{\partial y}(\delta h) + k_z \frac{\partial h}{\partial z}\frac{\partial}{\partial z}(\delta h) - Q\delta h\right] dV$$

$$+ \int_{S_2} v\delta hdS \qquad (3\text{-}11)$$

According to Gaussian divergent theorem, the Equation (3-11) can be transformed as below

$$\delta V = \int_V -\left[\frac{\partial}{\partial x}\left(k_x \frac{\partial h}{\partial x}\right) + \frac{\partial}{\partial y}\left(k_y \frac{\partial h}{\partial y}\right) + \frac{\partial}{\partial z}\left(k_z \frac{\partial h}{\partial z}\right) + Q\right] \delta hdV$$

$$+ \int_{S_2} \left[\bar{v} + k_x \frac{\partial h}{\partial x}\ell_x + k_y \frac{\partial h}{\partial y}\ell_y + k_z \frac{\partial h}{\partial z}\ell_z\right] \delta hdS \qquad (3\text{-}12)$$

In the 3D seepage field, the boundary conditions $\bar{v}$ can be shown in Equation (3-13)

$$\left.\begin{array}{l} k_x \frac{\partial h}{\partial x}\ell_x + k_y \frac{\partial h}{\partial y}\ell_y + k_z \frac{\partial h}{\partial z}\ell_z + \bar{v} = 0 \\ \bar{v} = 0 \text{ (On the impervious boundary)} \end{array}\right\} \qquad (3\text{-}13)$$

As it is shown in the Equation (3-12), the first term on the right hand side of the equation involves the Equation (2-9) and the second term involves the Equation (3-13). If δV=0, Equation (3-12) is tenable and the stationary exists, Equation (2-9) and Equation (3-13) are valid. According to this stationary, the value of h(x, y, z, t) can be given, which satisfies the both of Equation (2-9) and Equation (3-13).

3.2.3 Principle of virtual work

Virtual work on a system is the work resulting from either virtual forces acting through a real displacement or real forces acting through a virtual displacement. Figure 3-3 shows the virtual work on a system in 3D stress-strain fields.

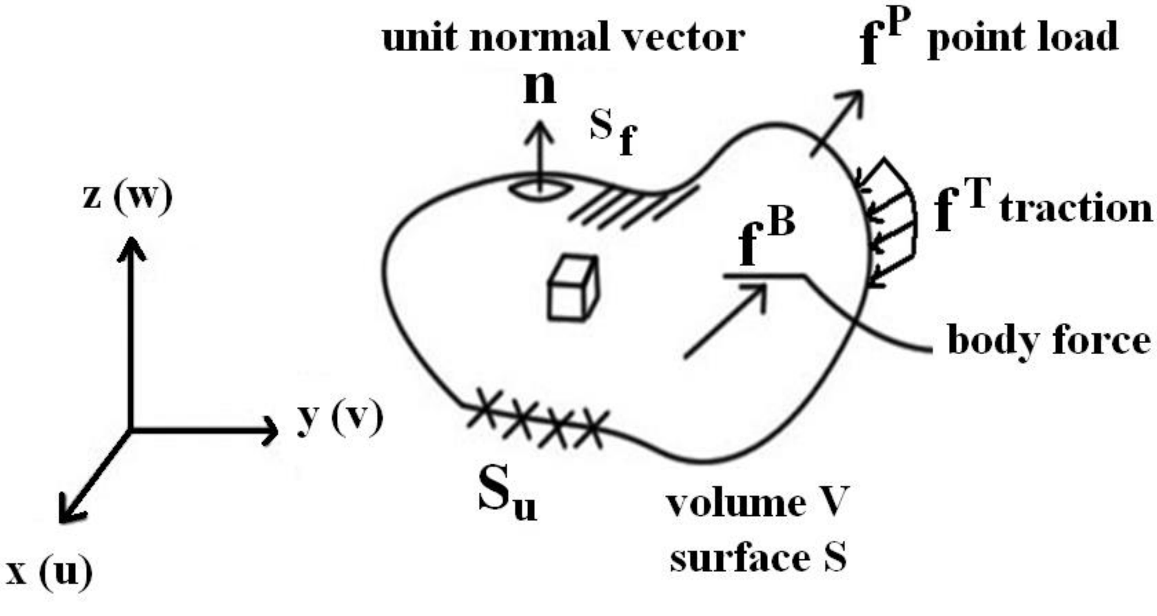

Figure 3-3 Virtual work on a system

where, Su is the surface on which displacements are prescribed, S_f is the surface on which loads are applied, f^P isa point load, f^T isa traction, f^B is a body force, and n is the unit normal vector.

The principle of virtual work states that for any compatible virtual displacement field imposed on the body in its state of equilibrium, the total internal virtual work is equal to the total external virtual work. According to the statement above, the matrix expression can be given in Equation (3-14). The relationship between total stress and effective stress has been introduced in section 2.3.1.4, and the stress in the Equation (3-14) is effective stress.

$$\int_V \lfloor \delta\Delta\varepsilon \rfloor \{\Delta\sigma\} = \int_S \lfloor \delta\Delta u \rfloor \{\Delta T\} dS + \int_V \lfloor \delta\Delta u \rfloor \{\Delta B\} dV + \int_\ell \lfloor \delta\Delta u \rfloor \{\Delta P\} d\ell \tag{3-14}$$

where, $\{\Delta P\}$ is vector concerning point load

$\{\Delta B\}$ is vector concerning point load

$\{\Delta T\}$ is vector concerning traction

3.2.4 Interpolation function and shape function

3.2.4.1 Interpolation function

In engineering and science applications, data collected from the field are usually discrete, which often come from a number of data points and the physical meanings of the data are not always well known. To estimate the outcomes and eventually to have a better understanding of the physical phenomenon, a more analytically controllable function that fits those data points is desirable. Interpolation is a specific case of curve fitting, in which the function must go exactly through the data points.

In finite element method, the polynomial interpolation function is generally employed to constitute the distribution function of desired variables, which is shown as

$$\Phi(x, y, z) = a_1 + a_2x + a_3y + a_4z + a_5x^2 + a_6xy + a_7yz + \cdots \quad (3\text{-}15)$$

Equation (3-15) shows the polynomial interpolation function in 3D coordinate system. In the axisymmetric coordinate system, the Equation (3-15) can be reduced to

$$\Phi(r, z) = a_1 + a_2r + a_3z + a_4r^2 + a_5rz + a_6z^2 + \cdots \quad (3\text{-}16)$$

3.2.4.2 Shape function

Distribution function of desired variables can be also shown as below:

$$\Phi(x, y, z) = \sum_{i=1}^{nod} N_i(x, y, z)\Phi_i \quad (3\text{-}17)$$

where, nod is the nodes number of element

N_i is shape function

Φ_i is the known head of nodes

The shape function should obey the following properties:

$$N_i(x, y, z) = \begin{cases} 1 & (x, y, z) = (x_i, y_i, z_i) \\ 0 & (x, y, z) \neq (x_i, y_i, z_i) \end{cases} \quad (3\text{-}18)$$

$$\sum_{i=1}^{nod} N_i = 1 \tag{3-19}$$

Because of the properties of shape function in Equation (3-18) and Equation (3-19), the distribution function of desired variables on the boundary of adjoining elements is compatibility.

3.3 Basic process of finite element solution

3.3.1 Axisymmetric seepage calculation

In case of six nodal triangular element, which is shown in Figure 3-4, the total head of arbitrary point in the element can be shown in Equation (3-20) according to the interpolation function.

$$\begin{aligned} h(r,z) &= a_1 + a_2 r + a_3 z + a_4 r^2 + a_5 rz + a_6 z^2 \\ &= \lfloor 1 \quad r \quad z \quad r^2 \quad rz \quad z^2 \rfloor \{a\} \end{aligned} \tag{3-20}$$

where, $a_1, a_2, a_3, a_4, a_5, a_6$ are undetermined coefficients.

The total head of nodes can be written as

$$\{h\} = [M]\{a\}$$

And $\{a\}$ can be shown as

$$\{a\} = [M^{-1}]\{h\}$$

$$\text{Where,}\{h\}=\begin{Bmatrix} h_i \\ h_j \\ h_k \\ h_l \\ h_m \\ h_n \end{Bmatrix}\quad \{a\}=\begin{Bmatrix} a_1 \\ a_2 \\ a_3 \\ a_4 \\ a_5 \\ a_6 \end{Bmatrix}$$

$[M^{-1}]$ is the inverse matrix of $[M]$, and matrix $[M]$ is shown as below

$$[M]=\begin{bmatrix} 1 & r_i & z_i & r_i^2 & r_i z_i & z_i^2 \\ 1 & r_j & z_j & r_j^2 & r_j z_j & z_j^2 \\ 1 & r_k & z_k & r_k^2 & r_k z_k & z_k^2 \\ 1 & r_l & z_l & r_l^2 & r_l z_l & z_l^2 \\ 1 & r_m & z_m & r_m^2 & r_m z_m & z_m^2 \\ 1 & r_n & z_n & r_n^2 & r_n z_n & z_n^2 \end{bmatrix}$$

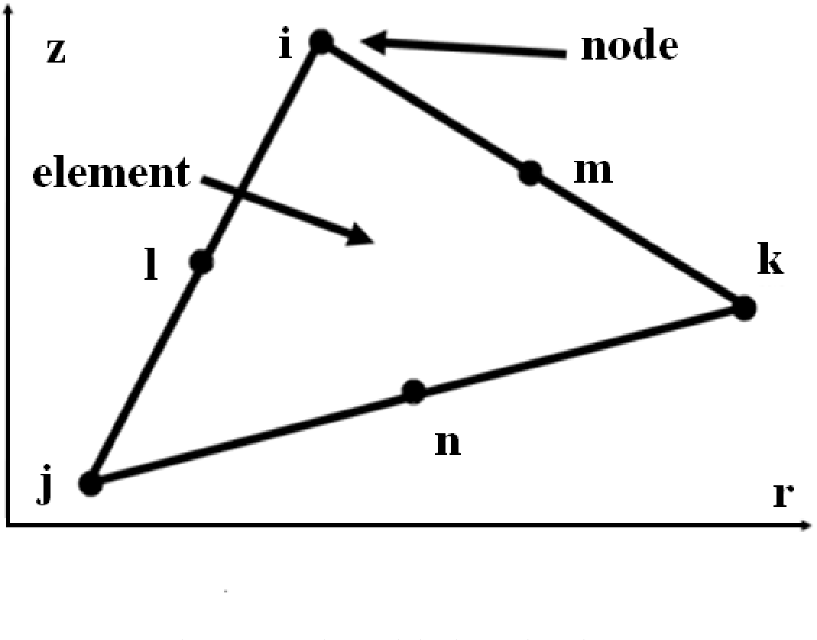

Figure 3-4 Six nodal triangular element

In this way, Equation (3-20) can be transformed to

$$h(r,z)=\lfloor 1 \;\; r \;\; z \;\; r^2 rz \;\; z^2 \rfloor [M^{-1}]\{h\}$$

And the according to the partial differentiation, we can also get the equations below

$$\begin{Bmatrix} \frac{\partial h}{\partial r} \\ \frac{\partial h}{\partial z} \end{Bmatrix} = \begin{bmatrix} 0 & 1 & 0 & 2r & z & 0 \\ 0 & 0 & 1 & 0 & r & 2z \end{bmatrix} [M^{-1}]\{h\}$$

$$\left\lfloor \frac{\partial h}{\partial r} \;\; \frac{\partial h}{\partial z} \right\rfloor = \lfloor h \rfloor [M^{-1}]^T \begin{bmatrix} 0 & 0 \\ 1 & 0 \\ 0 & 1 \\ 2r & 0 \\ z & r \\ 0 & 2z \end{bmatrix}$$

Based on the theories mentioned above, the matrix expression for Equation (3-4) is

$$V = \frac{1}{2} \lfloor h \rfloor [H]\{h\} + \lfloor h \rfloor [C] \left\{ \frac{dh}{dt} \right\} - \lfloor h \rfloor \{F_1\} + \lfloor h \rfloor \{F_2\} \tag{3-21}$$

where, $[H]$, $[C]$, $\{F_1\}$ and $\{F_2\}$ are shown as below

$$[H] = [M^{-1}]^T \int_A \begin{bmatrix} 0 & 0 \\ 1 & 0 \\ 0 & 1 \\ 2r & 0 \\ z & r \\ 0 & 2z \end{bmatrix} \begin{bmatrix} K_{Haxis} & 0 \\ 0 & K_{Vaxis} \end{bmatrix} \begin{bmatrix} 0 & 1 & 0 & 2r & z & 0 \\ 0 & 0 & 1 & 0 & r & 2z \end{bmatrix} dA [M^{-1}]$$

$$[C] = [M^{-1}]^T \int_A \begin{bmatrix} 1 \\ r \\ z \\ r^2 \\ rz \\ z^2 \end{bmatrix} C_{axis} [1 \quad r \quad z \quad r^2 \quad rz \quad z^2]\, dA [M^{-1}]$$

$$\{F_1\} = [M^{-1}]^T \int_A \; Q_{axis} \begin{Bmatrix} 1 \\ r \\ z \\ r^2 \\ rz \\ z^2 \end{Bmatrix} dA$$

$$\{F_2\} = [M^{-1}]^T \int_\ell \; \overline{V}_{axis} \begin{Bmatrix} 1 \\ r \\ z \\ r^2 \\ rz \\ z^2 \end{Bmatrix} d\ell$$

According to the variational principle, Equation (3-21) can be transformed as below

$$\delta V = \lfloor \delta h \rfloor \left([H]\{h\} + [C] \left\{ \frac{dh}{dt} \right\} - \{F_1\} + \{F_2\} \right) \tag{3-22}$$

If $\delta V=0$ is tenable, Equation (3-22) can be shown as

$$[H]\{h\} + [C] \left\{ \frac{dh}{dt} \right\} = \{F_1\} - \{F_2\} \tag{3-23}$$

When $\{F_1\} = 0$ and $\{F_2\} = 0$, Equation (3-23) reduced to

$$[H]\{h\} + [C]\left\{\frac{dh}{dt}\right\} = 0 \tag{3-24}$$

Based on the finite difference method, the Equation (3-24) can be written as

$$(1-\omega)\left[H_{ij}\right]^{k}\left\{h_j\right\}^{k} + \omega\left[H_{ij}\right]^{k+1}\left\{h_j\right\}^{k+1}$$
$$+\frac{1}{\Delta t}\left(\left[C_{ij}\right]^{k+1}\left\{h_j\right\}^{k+1} - \left[C_{ij}\right]^{k}\{h\}^{k}\right) = 0 \tag{3-25}$$

When ω=1 (receding difference), Equation (3-25) can be transformed as below

$$\left(\left[H_{ij}\right]^{k+1} + \frac{1}{\Delta t}\left[C_{ij}\right]^{k+1}\right)\left\{h_j\right\}^{k+1} = \frac{1}{\Delta t}\left[C_{ij}\right]^{k}\{h\}^{k} \tag{3-26}$$

In the Equation (3-26), for calculating the value of $\left[H_{ij}\right]^{k+1}$ and $\left[C_{ij}\right]^{k+1}$, a presumption of $\left\{h_j\right\}^{k+1}$ should be made. $\left\{h_j\right\}^{k+\frac{1}{2}}$ is used to calculate $\left[H_{ij}\right]^{k+\frac{1}{2}}$ and $\left[C_{ij}\right]^{k+\frac{1}{2}}$, which can approximatively replace the $\left[H_{ij}\right]^{k+1}$, $\left[C_{ij}\right]^{k+1}$ and $\left[C_{ij}\right]^{k}$. The presumption of the time steps k+1 and k+$\frac{1}{2}$ is shown in Figure 3-5. Here, k is the number of time step. In this way, Equation (3-26) can be transformed to

$$\left(\left[H_{ij}\right]^{k+\frac{1}{2}} + \frac{1}{\Delta t}\left[C_{ij}\right]^{k+\frac{1}{2}}\right)\left\{h_j\right\}^{k+1} = \frac{1}{\Delta t}\left[C_{ij}\right]^{k+\frac{1}{2}}\{h\}^{k} \tag{3-27}$$

Equation (3-28) is calculated for the first time loop computing, and Equation (3-29) is calculated for the inner of loop computing (i=1, 2, 3…).

$$h^{k+\frac{1}{2}} = h^k + \frac{\Delta t^k}{2\Delta t^{k-1}}\left(h^k - h^{k-1}\right) \tag{3-28}$$

$$h^{k+\frac{1}{2}} = \frac{1}{2}\left(h^i + h^{i+1}\right) \tag{3-29}$$

If $\left|h^{i+1} - h^i\right| < \varepsilon$, the result of h^{k+1} is convergent

where, ε is tolerance

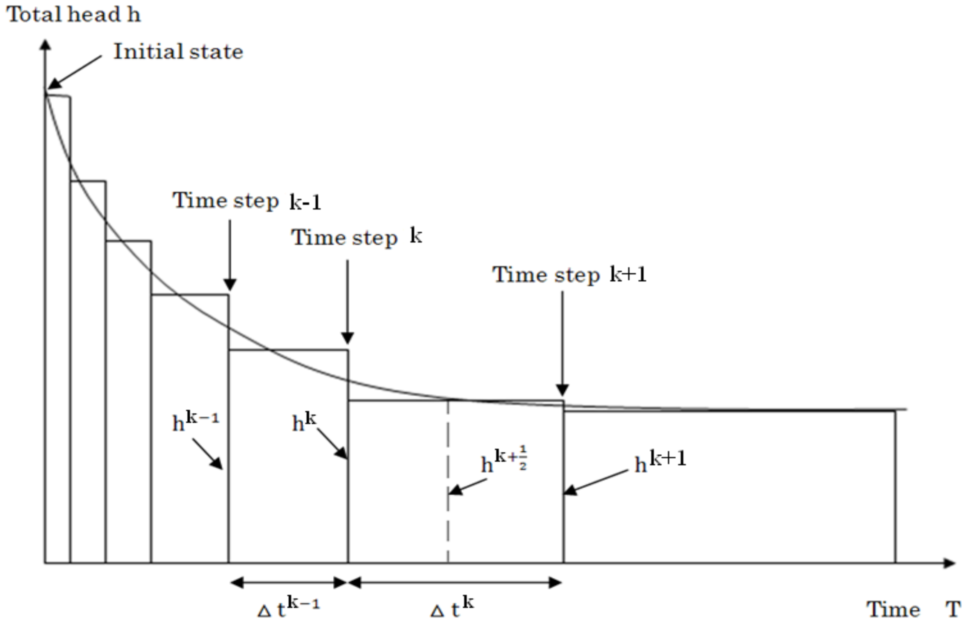

Figure 3-5 The presumption of time steps k+1 and k+$\frac{1}{2}$

For the first time step, there is on previous time step. So the initial state conditions is used to calculate h^1 in Equation (3-27), when h^1 is known,$\mathrm{h}^{\frac{1}{2}}$ can be given by $\frac{\mathrm{h}^0+\mathrm{h}^1}{2}$. And then loop computing can be done by using Equation (3-29). Under the steady state, $\frac{\mathrm{dh}}{\mathrm{dt}} = 0$, and Equation (3-23) reduce to

$$[\mathrm{H}]\{\mathrm{h}\} = \{\mathrm{F}_1\} - \{\mathrm{F}_2\} \tag{3-30}$$

Here, only $\{\mathrm{h}\}$ is unknown. By calculating Equation (3-30), the value of $\{\mathrm{h}\}$can be given in Figure 3-6 shows the flow chart of the programming.

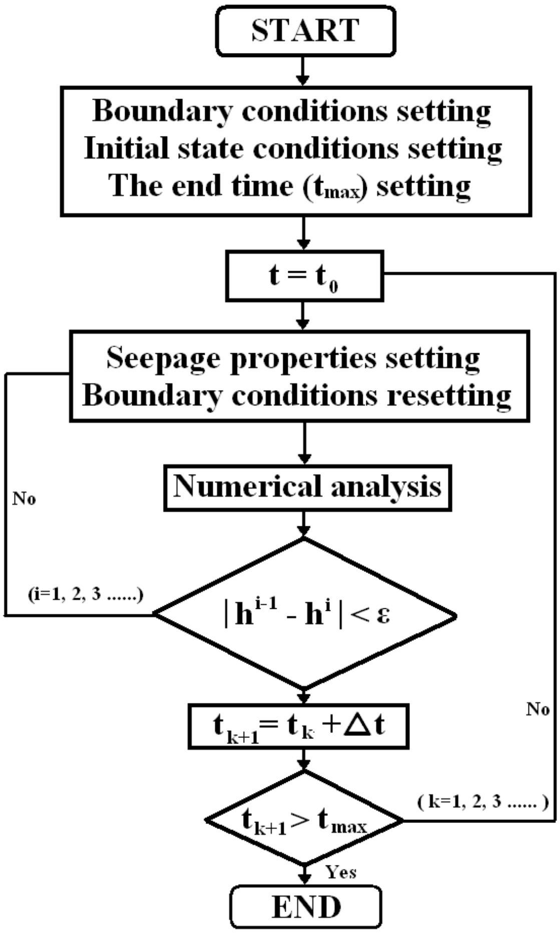

Figure 3-6 Flow chart of the programming

3.3.2 Axisymmetric deformation calculation

In case of deformation calculation, the displacement of arbitrary point in the six nodal triangular element can be shown in Equation (3-31) according to the interpolation function.

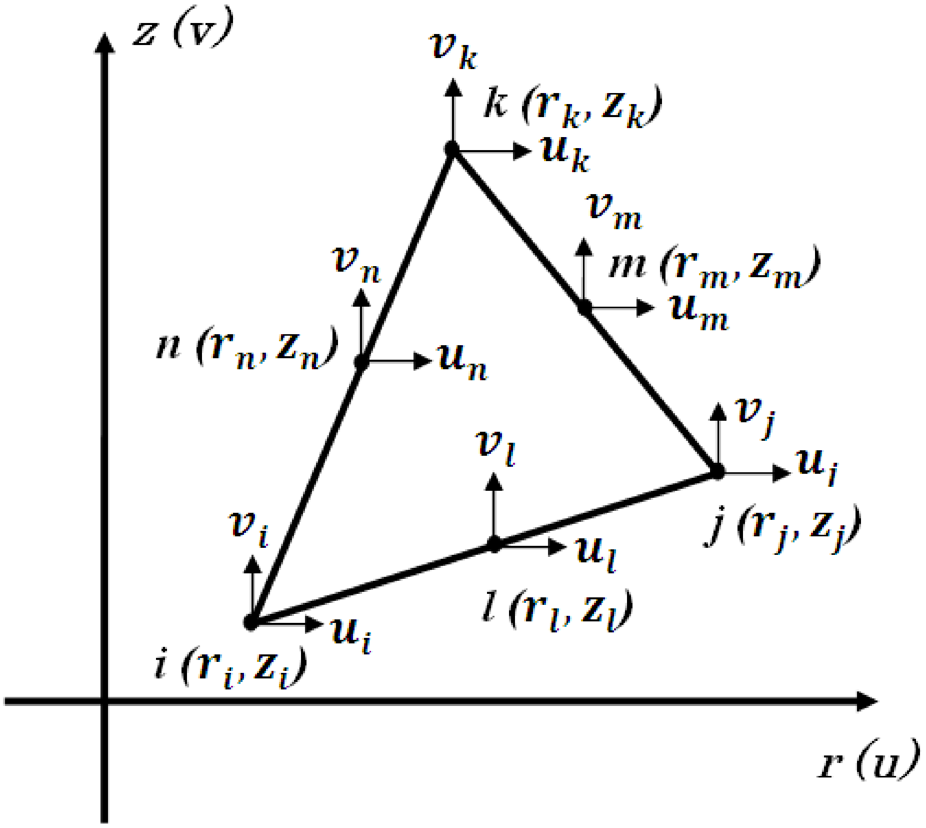

Figure 3-7 Displacements in the six nodal triangular element

$$\begin{cases} u = a_1 + a_2 r + a_3 z + a_4 r^2 + a_5 rz + a_6 z^2 \\ v = a_1 + a_2 r + a_3 z + a_4 r^2 + a_5 rz + a_6 z^2 \end{cases} \tag{3-31}$$

According to the theory of interpolation fuction mentioned before, the Equation (3-31) can be transformed to

$$\begin{cases}\{u\} = \lfloor 1 \ \ r \ \ z \ \ r^2 rz \ \ z^2 \rfloor [M^{-1}]\{u\} \\ \{v\} = \lfloor 1 \ \ r \ \ z \ \ r^2 rz \ \ z^2 \rfloor [M^{-1}]\{v\}\end{cases} \tag{3-32}$$

If we put Equation (3-32) into Equation (2-26), the equation can be changed as below.

$$\{\varepsilon\} = [A][M^{-1}]\{u\} \tag{3-33}$$

where, $\{\varepsilon\}$, $[A]$, $[M^{-1}]$ and $\{u\}$ are shown as below

$$\{\varepsilon\} = \begin{Bmatrix} \varepsilon_r \\ \varepsilon_z \\ \varepsilon_\theta \\ \gamma_{rz} \end{Bmatrix}$$

It is reseted as

$$[M^{-1}] = \begin{bmatrix} [M^{-1}] & 0 \\ 0 & [M^{-1}] \end{bmatrix} \{u\} = \begin{Bmatrix} \{u\} \\ \{v\} \end{Bmatrix}$$

$$[A] = \begin{bmatrix} \lfloor 0 \ \ 1 \ \ 0 \ \ 2r \ \ z \ \ 0 \rfloor \ , & \lfloor 0 \ \ 0 \ \ 0 \ \ 0 \ \ 0 \ \ 0 \rfloor \\ \lfloor 0 \ \ 0 \ \ 0 \ \ 0 \ \ 0 \ \ 0 \rfloor \ , & \lfloor 0 \ \ 0 \ \ 1 \ \ 0 \ \ r \ \ 2z \rfloor \\ \left\lfloor \frac{1}{r} \ \ 1 \ \ \frac{z}{r} \ \ r \ \ z \ \ \frac{z^2}{r} \right\rfloor \ , & \lfloor 0 \ \ 0 \ \ 0 \ \ 0 \ \ 0 \ \ 0 \rfloor \\ \lfloor 0 \ \ 0 \ \ 1 \ \ 0 \ \ r \ \ 2z \rfloor \ , & \lfloor 0 \ \ 1 \ \ 0 \ \ 2r \ \ z \ \ 0 \rfloor \end{bmatrix}$$

According to the Equation (2-26), the relationship of stress and strain can be shown in Equation (3-34) by considering primitive stress condition $\{\sigma_0\}$.

$$\begin{Bmatrix}\sigma_r\\ \sigma_z\\ \sigma_\theta\\ \tau_{rz}\end{Bmatrix} = [D]\begin{Bmatrix}\varepsilon_r\\ \varepsilon_z\\ \varepsilon_\theta\\ \gamma_{rz}\end{Bmatrix} + \{\sigma_0\} \qquad （3\text{-}34）$$

where, $[D]$ is shown below

$$[D] = \frac{E(1-\nu)}{(1+\nu)(1-2\nu)}\begin{bmatrix} 1 & \frac{1}{1-\nu} & \frac{1}{1-\nu} & 0 \\ \frac{1}{1-\nu} & 1 & \frac{1}{1-\nu} & 0 \\ \frac{1}{1-\nu} & \frac{1}{1-\nu} & 1 & 0 \\ 0 & 0 & 0 & \frac{1-2\nu}{2(1-\nu)} \end{bmatrix}$$

From the above, the incremental form of Equation（3-34）can be written in Equation（3-35）

$$\{\Delta\sigma\} = [D]\{\Delta\varepsilon\} + \{\Delta\ \sigma_0\} \qquad (3\text{-}35)$$

According to the principle of virtual work, the total internal virtual work is equal to the total external virtual work

The internal virtual work can be shown in Equation (3-36)

$$\int_V \lfloor \delta\Delta\varepsilon \rfloor \{\Delta\sigma\} dV \qquad (3\text{-}36)$$

Based on the Equation (3-33), the equation can be shown as below

$$\begin{cases} \{\Delta\ \varepsilon\} = [A][M^{-1}]\{\Delta\ u\} \\ \lfloor \delta\Delta\varepsilon \rfloor = \lfloor \delta\Delta u \rfloor [M^{-1}]^T [A]^T \end{cases} \tag{3-37}$$

The Equation（3-35）and Equation（3-37）be put into Equation（3-36）, the Equation can be given as below

$$\lfloor \delta\Delta u \rfloor \left([K]\lfloor \Delta u \rfloor + [M^{-1}]^T \int_A [A]^T \{\Delta\ \sigma_0\} r dA \times 2\pi \right) \tag{3-38}$$

where $[K]$ is elemental stiffness matrix, which is written as below

$$[K] = [M^{-1}]^T \int_A [A]^T [D][A] r dA \times 2\pi [M^{-1}]$$

The total external virtual work includes point load, traction force, body force, and seepage force.

The external virtual work of point load is shown in equation (3-39)

$$\int_\ell \lfloor \delta\Delta u \rfloor \begin{Bmatrix} P_{ir} \\ P_{jr} \\ P_{kr} \\ P_{\ell r} \\ P_{mr} \\ P_{nr} \\ P_{iz} \\ P_{jz} \\ P_{kz} \\ P_{\ell z} \\ P_{mz} \\ P_{nz} \end{Bmatrix} d\ell = \lfloor \delta\Delta u \rfloor \begin{Bmatrix} P_{ir} \\ P_{jr} \\ P_{kr} \\ P_{\ell r} \\ P_{mr} \\ P_{nr} \\ P_{iz} \\ P_{jz} \\ P_{kz} \\ P_{\ell z} \\ P_{mz} \\ P_{nz} \end{Bmatrix} 2\pi r \tag{3-39}$$

The external virtual work of traction force is given in Equation (3-40)

$$\int_S \lfloor \delta\Delta u, \delta\Delta v \rfloor \begin{Bmatrix} \overline{T}_r \\ \overline{T}_z \end{Bmatrix} dS \tag{3-40}$$

The external virtual work of body force can be written as below

$$\int_V \lfloor \delta\Delta u \quad \delta\Delta v \rfloor \begin{Bmatrix} \overline{B}_r \\ \overline{B}_z \end{Bmatrix} dV \tag{3-41}$$

where, $dV = 2\pi r dA$、$\overline{B_r} = b_r - \frac{\partial h}{\partial r}\gamma_w$,$\overline{B_z} = b_z - \frac{\partial h}{\partial z}\gamma_w$ b_r and $b_z$are real body force respectively in r and z directions, $-\frac{\partial h}{\partial r}\gamma_w$ and $-\frac{\partial h}{\partial z}\gamma_w$ are seepage force respectively in r and z directions

According to the principle of virtual work, which mentioned above, the global Equation (3-42) can be given by merging and superimposing the Equation (3-38), Equation (3-39), Equation (3-40) and Equation (3-41):

$$[K]\{\Delta U\} = \{\Delta F\} \tag{3-42}$$

where, $[K]$ is global stiffness matrix

$\{\Delta U\}$ is global nodal displacement matrix

$\{\Delta F\}$ is global nodal force matrix

Here, only $\{\Delta U\}$is unknown. By calculating Equation (3-42), we can get the value of $\{\Delta U\}$.

3.3.3 Three-dimensional seepage calculation under steady state

In case of eight nodal hexahedron element, which is shown in Figure 3-1 (e), the total head of arbitrary point in the element can be shown in Equation (3-43) according to the interpolation function.

$$\begin{aligned} h(x, y, z) &= a_1 + a_2x + a_3y + a_4z + a_5xy + a_6yz + a_7zx + a_8xyz \\ &= \lfloor 1 \quad x \quad y \quad z \quad xy \quad yz \quad zx \quad xyz \rfloor \{a\} \end{aligned} \tag{3-43}$$

where, $a_1, a_2, a_3, a_4, a_5, a_6, a_7, a_8$ are undetermined coefficients.

In the same way, the total head of nodes can be written as

$$\{h\} = [M]\{a\}$$

And $\{a\}$ can be shown as

$$\{a\} = [M^{-1}]\{h\}$$

where, $\{h\}=\begin{Bmatrix} h_i \\ h_j \\ h_k \\ h_l \\ h_m \\ h_n \\ h_o \\ h_p \end{Bmatrix}$ $\qquad \{a\} = \begin{Bmatrix} a_1 \\ a_2 \\ a_3 \\ a_4 \\ a_5 \\ a_6 \\ a_7 \\ a_8 \end{Bmatrix}$

In this way, Equation (3-43) can be transformed to

$$h(x, y, z) = \lfloor 1 \quad x \quad y \quad z \quad xy \quad yz \quad zx \quad xyz \rfloor [M^{-1}]\{h\}$$

And the according to the partial differentiation, the equations can be given as below

$$\begin{Bmatrix} \frac{\partial h}{\partial x} \\ \frac{\partial h}{\partial y} \\ \frac{\partial h}{\partial z} \end{Bmatrix} = \begin{bmatrix} 0 & 1 & 0 & 0 & y & 0 & z & yz \\ 0 & 0 & 1 & 0 & x & z & 0 & xz \\ 0 & 0 & 0 & 1 & 0 & y & x & xy \end{bmatrix} [M^{-1}]\{h\}$$

$$\left\lfloor \frac{\partial h}{\partial x} \quad \frac{\partial h}{\partial y} \quad \frac{\partial h}{\partial z} \right\rfloor = \lfloor h \rfloor [M^{-1}]^T \begin{bmatrix} 0 & 0 & 0 \\ 1 & 0 & 0 \\ 0 & 1 & 0 \\ 0 & 0 & 1 \\ y & x & 0 \\ 0 & z & y \\ z & 0 & x \\ yz & xz & xy \end{bmatrix}$$

where, $[M^{-1}]$ is the inverse matrix of $[M]$, and matrix $[M]$ is shown as below

$$[M] = \begin{bmatrix} 1 & x_i & y_i & z_i & x_i y_i & y_i z_i & z_i x_i & x_i y_i z_i \\ 1 & x_j & y_j & z_j & x_j y_j & y_j z_j & z_j x_j & x_j y_j z_j \\ 1 & x_k & y_k & z_k & x_k y_k & y_k z_k & z_k x_k & x_k y_k z_k \\ 1 & x_l & y_l & z_l & x_l y_l & y_l z_l & z_l x_l & x_l y_l z_l \\ 1 & x_m & y_m & z_m & x_m y_m & y_m z_m & z_m x_m & x_m y_m z_m \\ 1 & x_n & y_n & z_n & x_n y_n & y_n z_n & z_n x_n & x_n y_n z_n \\ 1 & x_o & y_o & z_o & x_o y_o & y_o z_o & z_o x_o & x_o y_o z_o \\ 1 & x_p & y_p & z_p & x_p y_p & y_p z_p & z_p x_p & x_p y_p z_p \end{bmatrix}$$

Based on the theories mentioned above, the matrix expression for Equation (3-10) is

$$V = \frac{1}{2} \lfloor h \rfloor [H] \{h\} - \lfloor h \rfloor \{F_1\} + \lfloor h \rfloor \{F_2\} \tag{3-44}$$

where, $[\mathrm{H}]$, $\{\mathrm{F}_1\}$ and $\{\mathrm{F}_2\}$ are shown as below

$$[\mathrm{H}] = [\mathrm{M}^{-1}]^{\mathrm{T}} \int_{\mathrm{V}} [\mathrm{W}]\, \mathrm{dV} [\mathrm{M}^{-1}]$$

$$\{\mathrm{F}_1\} = \mathrm{Q}[\mathrm{M}^{-1}]^{\mathrm{T}} \int_{\mathrm{V}} \begin{Bmatrix} 1 \\ \mathrm{x} \\ \mathrm{y} \\ \mathrm{z} \\ \mathrm{xy} \\ \mathrm{yz} \\ \mathrm{zx} \\ \mathrm{xyz} \end{Bmatrix} \mathrm{dv}$$

$$\{\mathrm{F}_2\} = \bar{\mathrm{v}}[\mathrm{M}^{-1}]^{\mathrm{T}} \int_{\mathrm{s2}} \begin{Bmatrix} 1 \\ \mathrm{x} \\ \mathrm{y} \\ \mathrm{z} \\ \mathrm{xy} \\ \mathrm{yz} \\ \mathrm{zx} \\ \mathrm{xyz} \end{Bmatrix} \mathrm{ds}$$

$$[\mathrm{W}] = \begin{bmatrix} 0 & 0 & 0 \\ 1 & 0 & 0 \\ 0 & 1 & 0 \\ 0 & 0 & 1 \\ \mathrm{y} & \mathrm{x} & 0 \\ 0 & \mathrm{z} & \mathrm{y} \\ \mathrm{z} & 0 & \mathrm{x} \\ \mathrm{yz} & \mathrm{xz} & \mathrm{xy} \end{bmatrix} \begin{bmatrix} \mathrm{Kx} & 0 & 0 \\ 0 & \mathrm{Ky} & 0 \\ 0 & 0 & \mathrm{Kz} \end{bmatrix} \begin{bmatrix} 0 & 1 & 0 & 0 & \mathrm{y} & 0 & \mathrm{z} & \mathrm{yz} \\ 0 & 0 & 1 & 0 & \mathrm{x} & \mathrm{z} & 0 & \mathrm{xz} \\ 0 & 0 & 0 & 1 & 0 & \mathrm{y} & \mathrm{x} & \mathrm{xy} \end{bmatrix}$$

According to the variational principle, Equation (3-44) can be transformed as below

$$\delta\mathrm{V} = \lfloor\delta\mathrm{h}\rfloor([\mathrm{H}]\{\mathrm{h}\} - \{\mathrm{F_1}\} + \{\mathrm{F_2}\}) \tag{3-45}$$

If δV=0 is tenable, Equation (3-45) can be shown as

$$[\mathrm{H}]\{\mathrm{h}\} = \{\mathrm{F_1}\} - \{\mathrm{F_2}\} \tag{3-46}$$

Here, only {h} is unknown. By calculating Equation (3-46), the value of {h} can be given.

3.3.4 Three-dimensional deformation calculation

In case of three-dimensional deformation calculation, the displacement of arbitrary point in the 20-nodal element can be shown in Equation (3-47) according to the interpolation function.

$$\begin{cases} u = \sum_{i=1}^{20} N_i u_i \\ v = \sum_{i=1}^{20} N_i v_i \\ w = \sum_{i=1}^{20} N_i w_i \end{cases} \tag{3-47}$$

$$\{\varepsilon\} = \begin{Bmatrix} \varepsilon_x \\ \varepsilon_y \\ \varepsilon_z \\ \gamma_{xy} \\ \gamma_{yz} \\ \gamma_{zx} \end{Bmatrix} = \begin{Bmatrix} \frac{\partial u}{\partial x} \\ \frac{\partial v}{\partial y} \\ \frac{\partial w}{\partial z} \\ \frac{\partial v}{\partial x} + \frac{\partial u}{\partial y} \\ \frac{\partial w}{\partial y} + \frac{\partial v}{\partial z} \\ \frac{\partial u}{\partial z} + \frac{\partial w}{\partial x} \end{Bmatrix} \tag{3-48}$$

$$\begin{cases} \frac{\partial u}{\partial x} = \sum_{i=1}^{20} \frac{\partial N_i}{\partial x} u_i \\ \frac{\partial v}{\partial y} = \sum_{i=1}^{20} \frac{\partial N_i}{\partial y} v_i \\ \frac{\partial w}{\partial z} = \sum_{i=1}^{20} \frac{\partial N_i}{\partial z} w_i \\ \frac{\partial u}{\partial y} = \sum_{i=1}^{20} \frac{\partial N_i}{\partial y} u_i \\ \frac{\partial v}{\partial x} = \sum_{i=1}^{20} \frac{\partial N_i}{\partial x} v_i \\ \frac{\partial w}{\partial x} = \sum_{i=1}^{20} \frac{\partial N_i}{\partial x} w_i \\ \frac{\partial u}{\partial z} = \sum_{i=1}^{20} \frac{\partial N_i}{\partial z} u_i \\ \frac{\partial v}{\partial z} = \sum_{i=1}^{20} \frac{\partial N_i}{\partial z} v_i \\ \frac{\partial w}{\partial y} = \sum_{i=1}^{20} \frac{\partial N_i}{\partial y} w_i \end{cases} \tag{3-49}$$

If we put Equation (3-49) into Equation (3-48), the equation can be changed as below.

$$\{\varepsilon\} = [B]\{u\} \tag{3-50}$$

where, $\{\varepsilon\}$, $[B]$, and $\{u\}$ are shown as below

$$[B] = \begin{bmatrix} \left\lfloor \frac{\partial N_1}{\partial x} \cdots \frac{\partial N_{20}}{\partial x} \right\rfloor, \cdots\cdots 0 \cdots\cdots, \cdots\cdots 0 \cdots\cdots \\ \cdots\cdots 0 \cdots\cdots, \left\lfloor \frac{\partial N_1}{\partial y} \cdots \frac{\partial N_{20}}{\partial y} \right\rfloor, \cdots\cdots 0 \cdots\cdots \\ \cdots\cdots 0 \cdots\cdots, \cdots\cdots 0 \cdots\cdots, \left\lfloor \frac{\partial N_1}{\partial z} \cdots \frac{\partial N_{20}}{\partial z} \right\rfloor \\ \left\lfloor \frac{\partial N_1}{\partial y} \cdots \frac{\partial N_{20}}{\partial y} \right\rfloor, \left\lfloor \frac{\partial N_1}{\partial x} \cdots \frac{\partial N_{20}}{\partial x} \right\rfloor, \cdots\cdots 0 \cdots\cdots \\ \cdots\cdots 0 \cdots\cdots, \left\lfloor \frac{\partial N_1}{\partial z} \cdots \frac{\partial N_{20}}{\partial z} \right\rfloor, \left\lfloor \frac{\partial N_1}{\partial y} \cdots \frac{\partial N_{20}}{\partial y} \right\rfloor \\ \left\lfloor \frac{\partial N_1}{\partial z} \cdots \frac{\partial N_{20}}{\partial z} \right\rfloor, \cdots\cdots 0 \cdots\cdots, \left\lfloor \frac{\partial N_1}{\partial x} \cdots \frac{\partial N_{20}}{\partial x} \right\rfloor \end{bmatrix}$$

$$\{\varepsilon\} = \begin{Bmatrix} \varepsilon_x \\ \varepsilon_y \\ \varepsilon_z \\ \gamma_{xy} \\ \gamma_{yz} \\ \gamma_{zx} \end{Bmatrix} \{u\} = \begin{Bmatrix} \{u\}_{1\sim20} \\ \{v\}_{1\sim20} \\ \{w\}_{1\sim20} \end{Bmatrix}$$

According to the Equation (3-48), the relationship of stress and strain can be shown in Equation (3-51) by considering primitive stress condition$\{\sigma_0\}$.

$$\begin{Bmatrix} \sigma_x \\ \sigma_y \\ \sigma_z \\ \tau_{xy} \\ \tau_{yz} \\ \tau_{zx} \end{Bmatrix} = [D] \begin{Bmatrix} \varepsilon_x \\ \varepsilon_y \\ \varepsilon_z \\ \gamma_{xy} \\ \gamma_{yz} \\ \gamma_{zx} \end{Bmatrix} + \{\sigma_0\} \tag{3-51}$$

where, [D] is shown below

$$[D] = \frac{E(1-\nu)}{(1+\nu)(1-2\nu)} \begin{bmatrix} 1 & \frac{\nu}{1-\nu} & \frac{\nu}{1-\nu} & & & \\ \frac{\nu}{1-\nu} & 1 & \frac{\nu}{1-\nu} & & 0 & \\ \frac{\nu}{1-\nu} & \frac{\nu}{1-\nu} & 1 & & & \\ & & & \frac{1-2\nu}{2(1-\nu)} & & \\ & 0 & & & \frac{1-2\nu}{2(1-\nu)} & \\ & & & & & \frac{1-2\nu}{2(1-\nu)} \end{bmatrix}$$

From the above, the incremental form of Equation（3-51）can be written in Equation (3-52)

$$\{\Delta\sigma\} = [D]\{\Delta\ \varepsilon\} + \{\Delta\ \sigma_0\} \tag{3-52}$$

According to the principle of virtual work, the total internal virtual work is equal to the total external virtual work

The internal virtual work can be shown in Equation (3-53)

$$\int_V \lfloor\delta\Delta\varepsilon\rfloor\{\Delta\sigma\}dV \tag{3-53}$$

Based on the Equation (3-50), the equation can be shown as below

$$\begin{cases} \{\Delta\ \varepsilon\}=[B]\{\Delta\ u\} \\ \lfloor\delta\Delta\varepsilon\rfloor=\lfloor\delta\Delta u\rfloor[B]^T \end{cases} \tag{3-54}$$

The Equation（3-52）and Equation（3-54）be put into Equation（3-53）, the equation can be given as below

$$\int_V \lfloor\delta\Delta u\rfloor[B]^T[D][B]\{\Delta\ u\}dv \tag{3-55}$$

The strain energy is introduced above and the work done by applied loads can be expressed as:

$$\int_S \lfloor\delta\Delta u\rfloor[N]^T\{\Delta T\}dS + \int_V \lfloor\delta\Delta u\rfloor[N]^T\{\Delta B\}dV + \lfloor\delta\Delta u\rfloor[N]^T\{\Delta P\}$$

where, $\{\Delta P\}$ is vector concerning point load

$\{\Delta B\}$ is vector concerning body force

$\{\Delta T\}$ is vector concerning traction

3.4 Special finite element

In geotechnical FEM analysis, special finite elements are usually used to simulate the soil-structure interaction situation and supporting structure.

3.4.1 Spring element 5)

In order to simulate the horizontal bracing, spring element is employed in this analysis. Figure3-8 gives the schematic of spring element. On the left end, the origin of local coordinates is set. The displacement in y and z directions are ignored, the displacement in x direction is considered only.

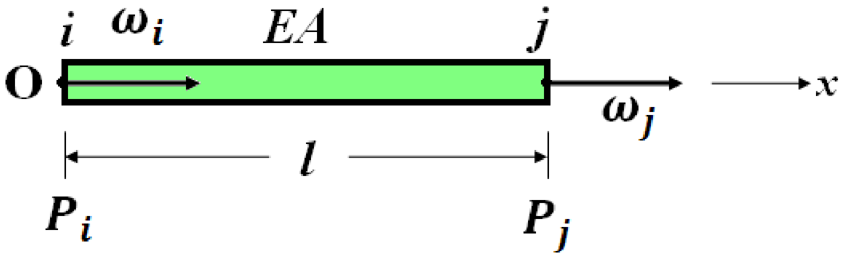

Figure 3-8 Spring element

$$U(x,\ y,\ z) = \omega(x) \tag{3-56}$$

The assumption of $\omega(x)$ is given in Equation (3-56) in the element.

$$\omega(x) = a_1 + a_2 x \tag{3-57}$$

The nodes at each end are points i and j, and the length of the element is *l*, the indeterminate coefficients in Equation (3-57) could be shown as below:

$$\begin{Bmatrix} \omega_i \\ \omega_j \end{Bmatrix} = \begin{bmatrix} 1 & 0 \\ 1 & l \end{bmatrix} \begin{Bmatrix} a_1 \\ a_2 \end{Bmatrix} = [A]\{a\} \tag{3-58}$$

$$\{a\} = [A]^{-1}\{\omega\} = \begin{bmatrix} 1 & 0 \\ -\frac{1}{l} & \frac{1}{l} \end{bmatrix} \{\omega\} \tag{3-59}$$

where, $\{a\}$ is indeterminate coefficients vector, and $\{\omega\}$ is nodal displacement vector. In this way Equation (3-57) can be transform into Equation (3-61).

$$\{a\}^T = \lfloor a_1 \quad a_2 \rfloor \{\omega\}^T = \lfloor \omega_i \quad \omega_j \rfloor \tag{3-60}$$

$$\omega(x) = \lfloor 1 \quad x \rfloor [A]^{-1}\{\omega\} \tag{3-61}$$

Strain in x direction is shown as below:

$$\varepsilon_x = \frac{\partial U}{\partial x} = \lfloor 0 \quad 1 \rfloor [A]^{-1}\{\omega\} = \left\lfloor -\frac{1}{l} \quad \frac{1}{l} \right\rfloor \{\omega\} = \lfloor B \rfloor \{\omega\}$$

The element stiffness matrix is given in Equation (3-62) and the integrating result is shown in Equation (3-63).

$$[k_w] = \iiint \{B\}[D]\lfloor B \rfloor \, dxdydz \tag{3-62}$$

$$[k_w] = \{B\}E\lfloor B \rfloor lA = \frac{EA}{l}\begin{bmatrix} 1 & -1 \\ -1 & 1 \end{bmatrix} \tag{3-63}$$

where, the stress-strain matrix $[D]$is represented by elastic modulus E.

Stress calculation methods are given in Equation (3-64) and Equation (3-65).

$$\{\sigma\} = \sigma_x = [S]\{\omega\} \tag{3-64}$$

$$[S] = [D][B] = \frac{E}{l}\lfloor -1 \quad 1 \rfloor \tag{3-65}$$

$$\begin{Bmatrix} \omega_i \\ \omega_j \end{Bmatrix} = \begin{bmatrix} \cos\alpha & \cos\beta & \cos\gamma & 0 & 0 & 0 \\ 0 & 0 & 0 & \cos\alpha & \cos\beta & \cos\gamma \end{bmatrix} \begin{Bmatrix} u_i \\ v_i \\ w_i \\ u_j \\ v_j \\ w_j \end{Bmatrix}$$

$$= [T][u] \tag{3-66}$$

Figure 3-9 shows the transformation of global coordinate and local coordinate. Equation (3-66) gives the transfer equation according to the Figure 3-9

In this way, the element stiffness matrix in global coordinate is shown as below:

$$[k_w^*] = [T]^T[k_w][T] = \frac{EA}{l}[M] \tag{3-67}$$

$$[M] = [\mathrm{M1}, \mathrm{M2}]$$

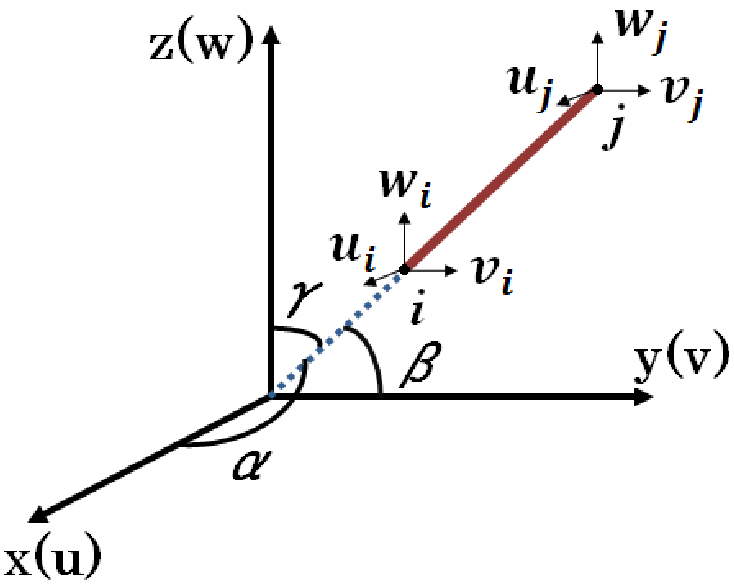

Figure 3-9 Transformation of global coordinate and local coordinate

$$[M1] = \begin{bmatrix} \cos^2\alpha & \cos\alpha\cos\beta & \cos\alpha\cos\gamma \\ \cos\beta\cos\alpha & \cos^2\beta & \cos\beta\cos\gamma \\ \cos\gamma\cos\alpha & \cos\gamma\cos\beta & \cos^2\gamma \\ -\cos^2\alpha & -\cos\alpha\cos\beta & -\cos\alpha\cos\gamma \\ -\cos\beta\cos\alpha & -\cos^2\beta & -\cos\beta\cos\gamma \\ -\cos\gamma\cos\alpha & -\cos\gamma\cos\beta & -\cos^2\gamma \end{bmatrix}$$

$$[M2] = \begin{bmatrix} -\cos^2\alpha & -\cos\alpha\cos\beta & -\cos\alpha\cos\gamma \\ -\cos\beta\cos\alpha & -\cos^2\beta & -\cos\beta\cos\gamma \\ -\cos\gamma\cos\alpha & -\cos\gamma\cos\beta & -\cos^2\gamma \\ \cos^2\alpha & \cos\alpha\cos\beta & \cos\alpha\cos\gamma \\ \cos\beta\cos\alpha & \cos^2\beta & \cos\beta\cos\gamma \\ \cos\gamma\cos\alpha & \cos\gamma\cos\beta & \cos^2\gamma \end{bmatrix}$$

The stress calculation method in global coordinate is given in Equation (3-68)

$$[S^*] = [S][T'] = \frac{E}{l}\lfloor -cos\,\alpha \quad -cos\,\beta \quad -cos\,\gamma \quad cos\,\alpha \quad cos\,\beta \quad cos\,\gamma \rfloor \qquad (3\text{-}68)$$

3.4.2 Interface element

The relative movement of the structure with respect to the soil may occur in any soil-structure interaction situation. Interface, or joint elements as they are sometimes called, can be used to simulate the soil-structure boundary such as the sides of the underground wall. Particular advantages are the ability to vary the constitutive behavior of the soil-structure interface and to allow differential displacement of the soil and the structure, slip and separation. Many methods have been proposed to model discontinuous behavior at the soil-structure interface 6)-13). Among these alternatives, the use of zero thickness interface elements is probably the most popular.

3.4.2.1 Two-dimensional theory

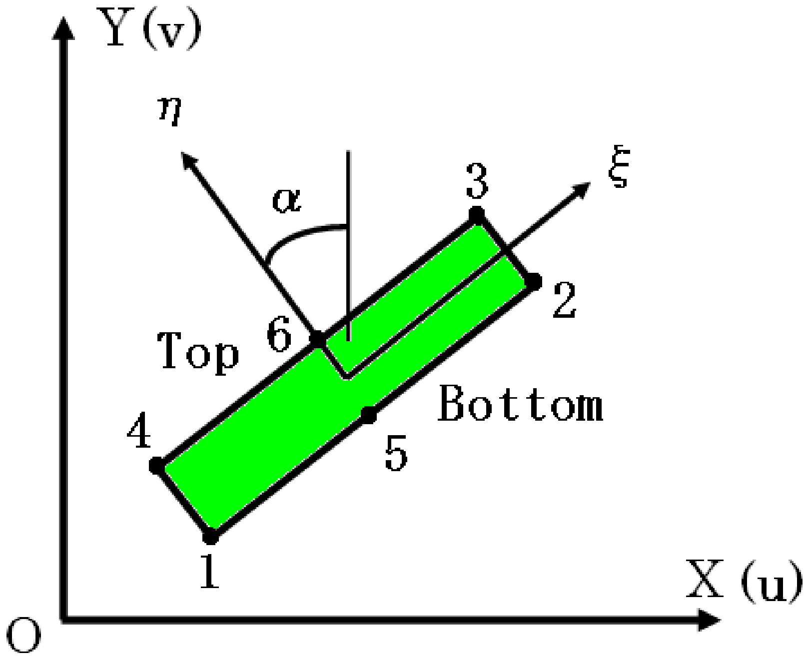

Figure 3-10 Six-nodal element

The element (see Figure 3-10) with six nodes is fully compatible with eight-nodal quadrilateral 2D element.

The interface stress consists of the normal and shear components. The normal stress σ and the shear stress τ are related by the constitutive equation to the normal and tangential element strains, ε and γ:

$$\begin{Bmatrix} \Delta\tau \\ \Delta\sigma \end{Bmatrix} = [\mathrm{D}] \begin{Bmatrix} \Delta\gamma \\ \Delta\varepsilon \end{Bmatrix} \tag{3-69}$$

For isotropic linear elastic behavior, the [D] matrix takes the form:

$$[\mathrm{D}] = \begin{bmatrix} \mathrm{K_s} & 0 \\ 0 & \mathrm{K_n} \end{bmatrix} \tag{3-70}$$

where, K_s and K_n are the elastic shear stiffness and normal stiffness respectively.

The interface element strain is defined as the relative displacement of the top and bottom of the interface element.

$$\gamma = \Delta \mathrm{u}_l = \mathrm{u}_l^{\mathrm{bot}} - \mathrm{u}_l^{\mathrm{top}} \tag{3-71}$$

$$\varepsilon = \Delta \mathrm{v}_l = \mathrm{v}_l^{\mathrm{bot}} - \mathrm{v}_l^{\mathrm{top}} \tag{3-72}$$

where:

$$\begin{Bmatrix} \mathrm{u}_l \\ \mathrm{v}_l \end{Bmatrix} = \begin{bmatrix} \cos\alpha & \sin\alpha \\ -\sin\alpha & \cos\alpha \end{bmatrix} \begin{Bmatrix} \mathrm{u} \\ \mathrm{v} \end{Bmatrix} \tag{3-73}$$

$$\begin{cases} \mathrm{u}_l^{\mathrm{bot}} = \mathrm{v}^{\mathrm{bot}}\ \sin\alpha + \mathrm{u}^{\mathrm{bot}}\cos\alpha \\ \mathrm{u}_l^{\mathrm{top}} = \mathrm{v}^{\mathrm{top}}\ \sin\alpha + \mathrm{u}^{\mathrm{top}}\cos\alpha \\ \mathrm{v}_l^{\mathrm{bot}} = \mathrm{v}^{\mathrm{bot}}\ \sin\alpha - \mathrm{u}^{\mathrm{bot}}\cos\alpha \\ \mathrm{v}_l^{\mathrm{top}} = \mathrm{v}^{\mathrm{top}}\ \sin\alpha - \mathrm{u}^{\mathrm{top}}\cos\alpha \end{cases} \tag{3-74}$$

$$\begin{aligned} \gamma = \Delta \mathrm{u}_l = \mathrm{u}_l^{\mathrm{bot}} - \mathrm{u}_l^{\mathrm{top}} \\ = (\mathrm{v}^{\mathrm{bot}} - \mathrm{v}^{\mathrm{top}})\ \sin\alpha + (\mathrm{u}^{\mathrm{bot}} - \mathrm{u}^{\mathrm{top}})\cos\alpha \end{aligned}$$

$$\begin{aligned} \varepsilon = \Delta \mathrm{v}_l = \mathrm{v}_l^{\mathrm{bot}} - \mathrm{v}_l^{\mathrm{top}} \\ = (\mathrm{v}^{\mathrm{bot}} - \mathrm{v}^{\mathrm{top}})\cos\alpha - (\mathrm{u}^{\mathrm{bot}} - \mathrm{u}^{\mathrm{top}})\ \sin\alpha \end{aligned}$$

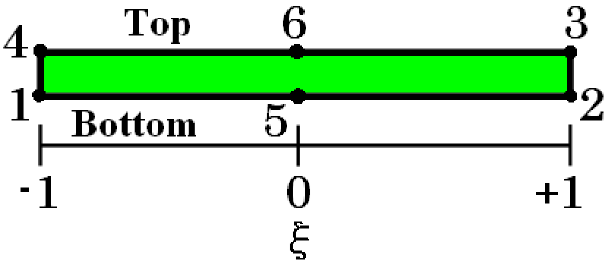

Figure 3-11 Six-nodal element in local ordinate

Figure 3-11 shows a six-nodal interface element. The strains are defined as:

$$\begin{Bmatrix} \gamma \\ \varepsilon \end{Bmatrix} = \begin{Bmatrix} \mathrm{u}_l^{\mathrm{bot}} - \mathrm{u}_l^{\mathrm{top}} \\ \mathrm{v}_l^{\mathrm{bot}} - \mathrm{v}_l^{\mathrm{top}} \end{Bmatrix} \tag{3-75}$$

The transformation of local to global displacement is written in matrix form as Equation (3-73), and the substitution into Equation (3-75) gives:

$$\begin{Bmatrix} \gamma \\ \varepsilon \end{Bmatrix} = \begin{bmatrix} \cos\alpha & \sin\alpha \\ -\sin\alpha & \cos\alpha \end{bmatrix} \begin{Bmatrix} u^{bot} - u^{top} \\ v^{bot} - v^{top} \end{Bmatrix} \tag{3-76}$$

The global displacement (u, v) at any point in the element can be expressed in terms of the nodal displacements, using the isoparametric shape functions N_i:

$$\begin{cases} u^{top} = N_3 u_3 + N_4 u_4 + N_6 u_6 \\ u^{bot} = N_1 u_1 + N_2 u_2 + N_5 u_5 \\ v^{top} = N_3 v_3 + N_4 v_4 + N_6 v_6 \\ v^{bot} = N_1 v_1 + N_2 v_2 + N_5 v_5 \end{cases} \tag{3-77}$$

where the subscript refers to the node number.

The isoparametric shape functions, Ni, are defined as:

$$\begin{gathered} N_1 = N_4 = \frac{1}{2}\xi(\xi - 1) \\ N_2 = N_3 = \frac{1}{2}\xi(\xi + 1) \\ N_5 = N_6 = 1 - \xi^2 \end{gathered} \tag{3-78}$$

where ξ is the natural ordinate that varies from -1 to +1 over the element length. Substitution of Equation (3-77) into Equation (3-76) gives:

$$\begin{Bmatrix} \gamma \\ \varepsilon \end{Bmatrix} = [B]\{\delta\}$$

where δ is the vector of nodal displacements defined as:

$$\{\delta\} = \lfloor u_1 \quad v_1 \quad u_2 \quad v_2 \quad u_3 \quad v_3 \quad u_4 \quad v_4 \quad u_5 \quad v_5 \quad u_6 \quad u_6 \rfloor$$

$$[B] = \begin{bmatrix} \cos\alpha & \sin\alpha \\ -\sin\alpha & \cos\alpha \end{bmatrix} [N]$$

$$[N] = \begin{bmatrix} N_1 & 0 & N_2 & 0 & -N_3 & 0 & -N_4 & 0 & N_5 & 0 & -N_6 & 0 \\ 0 & N_1 & 0 & N_2 & 0 & -N_3 & 0 & -N_4 & 0 & N_5 & 0 & -N_6 \end{bmatrix}$$

The element stiffness matrix, $[K_E]$, gives

$$[K_E] = \int_0^l [B]^T [D][B]\, dl \tag{3-79}$$

where l is the length of the element and the constitutive matrix $[D]$ is given by Equation.(3-70). The integral is evaluated in the natural ordinate system, see Figure 3-11, giving:

$$[K_E] = \int_{-1}^{1} [B]^T [D][B]\, |J| ds \tag{3-80}$$

where $|J|$ is Jacobian determinant:

$$|J| = \left[\left(\frac{dx}{d\xi}\right)^2 + \left(\frac{dy}{d\xi}\right)^2\right]^{\frac{1}{2}}$$

3.4.2.2 Three-dimensional theory

The element (see Figure 3-12) with 16 nodes is fully compatible with 20-nodal quadrilateral 3D elements.

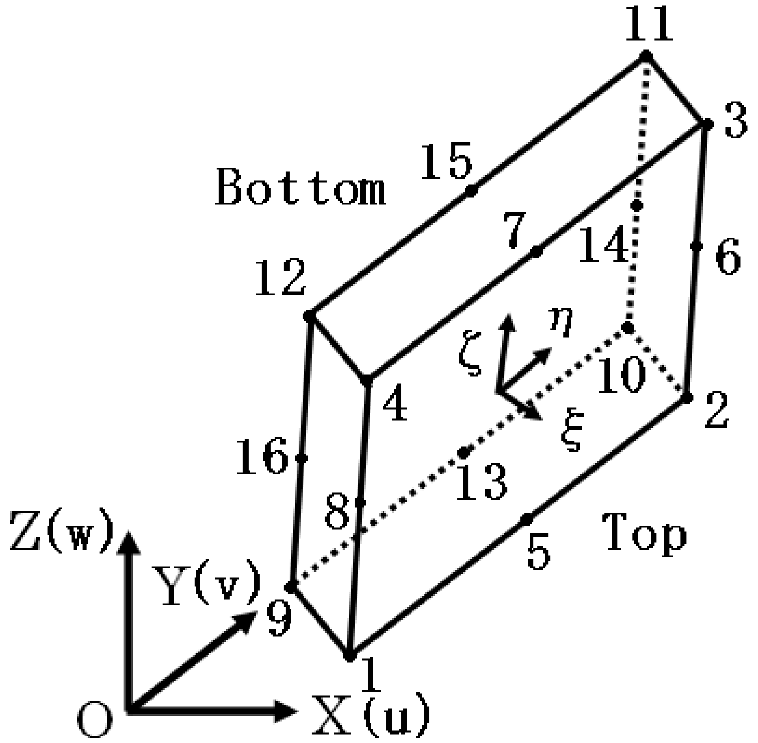

Figure 3-12 16-nodal element

The interface stress consists of the normal and shear components. The normal stress σ_x and the shear stress τ_y, τ_z are related by the constitutive Equation to the normal and tangential element strains, ε_x, γ_y and γ_z:

$$\begin{Bmatrix} \Delta\sigma_x \\ \Delta\tau_y \\ \Delta\tau_z \end{Bmatrix} = [D] \begin{Bmatrix} \Delta\varepsilon_x \\ \Delta\gamma_y \\ \Delta\gamma_z \end{Bmatrix} \tag{3-81}$$

For isotropic linear elastic behavior, the [D]matrix takes the form:

$$[\mathrm{D}] = \begin{bmatrix} \mathrm{K_{nx}} & 0 & 0 \\ 0 & \mathrm{K_{sy}} & 0 \\ 0 & 0 & \mathrm{K_{sz}} \end{bmatrix} \tag{3-82}$$

where, Ksy, Ksz and Knx are the elastic shear stiffness and normal stiffness respectively.

The interface element strain is defined as the relative displacement of the top and bottom of the interface element.

$$\varepsilon_{\mathrm{x}} = \Delta \mathrm{u_s} = \mathrm{u}_s^{\mathrm{bot}} - \mathrm{u}_s^{\mathrm{top}} \tag{3-83}$$

$$\gamma_{\mathrm{y}} = \Delta \mathrm{v}_s = \mathrm{v}_s^{\mathrm{bot}} - \mathrm{v}_s^{\mathrm{top}} \tag{3-84}$$

$$\gamma_{\mathrm{z}} = \Delta \mathrm{w}_s = \mathrm{w}_s^{\mathrm{bot}} - \mathrm{w}_s^{\mathrm{top}} \tag{3-85}$$

where:

$$\begin{Bmatrix} \mathrm{u}_s \\ \mathrm{v}_s \\ \mathrm{w}_s \end{Bmatrix} = \begin{bmatrix} \cos\alpha & \cos\beta & \cos\gamma \\ \cos\gamma & \cos\alpha & \cos\beta \\ \cos\beta & \cos\gamma & \cos\alpha \end{bmatrix} \begin{Bmatrix} \mathrm{u} \\ \mathrm{v} \\ \mathrm{w} \end{Bmatrix} \tag{3-86}$$

$$\begin{cases} \mathrm{u}_s^{\mathrm{bot}} = \mathrm{u}^{\mathrm{bot}}\cos\alpha + \mathrm{v}^{\mathrm{bot}}\cos\beta + \mathrm{w}^{\mathrm{bot}}\cos\gamma \\ \mathrm{u}_s^{\mathrm{top}} = \mathrm{u}^{\mathrm{top}}\cos\alpha + \mathrm{v}^{\mathrm{top}}\cos\beta + \mathrm{w}^{\mathrm{top}}\cos\gamma \\ \mathrm{v}_s^{\mathrm{bot}} = \mathrm{u}^{\mathrm{bot}}\cos\gamma + \mathrm{v}^{\mathrm{bot}}\cos\alpha + \mathrm{w}^{\mathrm{bot}}\cos\beta \\ \mathrm{v}_s^{\mathrm{top}} = \mathrm{u}^{\mathrm{top}}\cos\gamma + \mathrm{v}^{\mathrm{top}}\cos\alpha + \mathrm{w}^{\mathrm{top}}\cos\beta \\ \mathrm{w}_s^{\mathrm{bot}} = \mathrm{u}^{\mathrm{bot}}\cos\beta + \mathrm{v}^{\mathrm{bot}}\cos\gamma + \mathrm{w}^{\mathrm{bot}}\cos\alpha \\ \mathrm{w}_s^{\mathrm{top}} = \mathrm{u}^{\mathrm{top}}\cos\beta + \mathrm{v}^{\mathrm{top}}\cos\gamma + \mathrm{w}^{\mathrm{top}}\cos\alpha \end{cases} \tag{3-87}$$

$$\varepsilon_x = \Delta u_s = u_s^{bot} - u_s^{top}$$
$$= (u^{bot} - u^{top}) \cos\alpha + (v^{bot} - v^{top}) \cos\beta + (w^{bot} - w^{top}) \cos\gamma$$

$$\gamma_y = \Delta v_s = v_s^{bot} - v_s^{top}$$
$$= (u^{bot} - u^{top}) \cos\gamma + (v^{bot} - v^{top}) \cos\alpha + (w^{bot} - w^{top}) \cos\beta$$

$$\gamma_z = \Delta u_s = u_s^{bot} - u_s^{top}$$
$$= (u^{bot} - u^{top}) \cos\beta + (v^{bot} - v^{top}) \cos\gamma + (w^{bot} - w^{top}) \cos\alpha$$

Figure 3-12 shows a 16-nodal interface element. The strains are defined as:

$$\begin{Bmatrix} \varepsilon_x \\ \gamma_y \\ \gamma_z \end{Bmatrix} = \begin{Bmatrix} u_s^{bot} - u_s^{top} \\ v_s^{bot} - v_s^{top} \\ w_s^{bot} - w_s^{top} \end{Bmatrix} \tag{3-88}$$

The transformation of local to global displacement is written in matrix form as Equation (3-86), and the substitution into Equation (3-88) gives:

$$\begin{Bmatrix} \varepsilon_x \\ \gamma_y \\ \gamma_z \end{Bmatrix} = \begin{bmatrix} \cos\alpha & \cos\beta & \cos\gamma \\ \cos\gamma & \cos\alpha & \cos\beta \\ \cos\beta & \cos\gamma & \cos\alpha \end{bmatrix} \begin{Bmatrix} u^{bot} - u^{top} \\ v^{bot} - v^{top} \\ w^{bot} - w^{top} \end{Bmatrix} \tag{3-89}$$

The global displacement (u, v, w) at any point in the element can be expressed in terms of the nodal displacements, using the isoparametric shape functions N_i:

$$\begin{cases} u^{top} = N_1u_1 + N_2u_2 + N_3u_3 + N_4u_4 + N_5u_5 + N_6u_6 + N_7u_7 + N_8u_8 \\ u^{bot} = N_9u_9 + N_{10}u_{10} + N_{11}u_{11} + N_{12}u_{12} + N_{13}u_{13} + N_{14}u_{14}+N_{15}u_{15}+N_{16}u_{16} \\ v^{top} = N_1v_1 + N_2v_2 + N_3v_3 + N_4v_4 + N_5v_5 + N_6v_6 + N_7v_7 + N_8v_8 \\ v^{bot} = N_9v_9 + N_{10}v_{10} + N_{11}v_{11} + N_{12}v_{12} + N_{13}v_{13} + N_{14}v_{14}+N_{15}v_{15}+N_{16}v_{16} \\ w^{top} = N_1w_1 + N_2w_2 + N_3w_3 + N_4w_4 + N_5w_5 + N_6w_6 + N_7w_7 + N_8w_8 \\ w^{bot} = N_9w_9 + N_{10}w_{10} + N_{11}w_{11} + N_{12}w_{12} + N_{13}w_{13} + N_{14}w_{14}+N_{15}w_{15}+N_{16}w_{16} \end{cases} \tag{3-90}$$

where the subscript refers to the node number.

The isoparametric shape functions, Ni, are defined as:

$$N_1 = N_9 = \frac{1}{4}(1-\eta)(1-\zeta)(-\eta-\zeta-1) \tag{3-91}$$

$$N_2 = N_{10} = \frac{1}{4}(1+\eta)(1-\zeta)(\eta-\zeta-1) \tag{3-92}$$

$$N_3 = N_{11} = \frac{1}{4}(1+\eta)(1+\zeta)(\eta+\zeta-1) \tag{3-93}$$

$$N_4 = N_{12} = \frac{1}{4}(1-\eta)(1+\zeta)(-\eta+\zeta-1) \tag{3-94}$$

$$N_5 = N_{13} = \frac{1}{2}(1-\eta^2)(1-\zeta) \tag{3-95}$$

$$N_6 = N_{14} = \frac{1}{2}(1+\eta)(1-\zeta^2) \tag{3-96}$$

$$N_7 = N_{15} = \frac{1}{2}(1-\eta^2)(1+\zeta) \tag{3-97}$$

$$N_8 = N_{16} = \frac{1}{2}(1-\eta)(1-\zeta^2) \tag{3-98}$$

where η, ζ are the natural ordinate that varies from -1 to +1 over the element each length. Substitution of Equation (3-91)-(3-98) into Equation (3-89) gives:

$$\begin{Bmatrix} \varepsilon_{\mathrm{x}} \\ \gamma_y \\ \gamma_z \end{Bmatrix} = [\mathrm{B}]\{\delta\}$$

where δ is the vector of nodal displacements defined as:

$$\{\delta\} = \lfloor \mathrm{u}_1 \quad \mathrm{v}_1 \quad \mathrm{w} \quad \mathrm{u}_2 \quad \mathrm{v}_2 \quad \mathrm{w}_2 \quad \ldots \quad \mathrm{u}_{16} \quad \mathrm{v}_{16} \quad \mathrm{w}_{16} \rfloor$$

and

$$[\mathrm{B}] = \begin{bmatrix} \cos\alpha & \cos\beta & \cos\gamma \\ \cos\gamma & \cos\alpha & \cos\beta \\ \cos\beta & \cos\gamma & \cos\alpha \end{bmatrix} [\mathrm{N}]$$

$$[\mathrm{N}] = [-\mathrm{NN1} \quad -\mathrm{NN2} \quad \mathrm{NN3} \quad \mathrm{NN4}]$$

$$[\mathrm{NN1}] = \begin{bmatrix} \mathrm{N}_1 & 0 & 0 & \mathrm{N}_2 & 0 & 0 & \mathrm{N}_3 & 0 & 0 & \mathrm{N}_4 & 0 & 0 \\ 0 & \mathrm{N}_1 & 0 & 0 & \mathrm{N}_2 & 0 & 0 & \mathrm{N}_3 & 0 & 0 & \mathrm{N}_4 & 0 \\ 0 & 0 & \mathrm{N}_1 & 0 & 0 & \mathrm{N}_2 & 0 & 0 & \mathrm{N}_3 & 0 & 0 & \mathrm{N}_4 \end{bmatrix}$$

$$[\mathrm{NN2}] = \begin{bmatrix} \mathrm{N}_5 & 0 & 0 & \mathrm{N}_6 & 0 & 0 & \mathrm{N}_7 & 0 & 0 & \mathrm{N}_8 & 0 & 0 \\ 0 & \mathrm{N}_5 & 0 & 0 & \mathrm{N}_6 & 0 & 0 & \mathrm{N}_7 & 0 & 0 & \mathrm{N}_8 & 0 \\ 0 & 0 & \mathrm{N}_5 & 0 & 0 & \mathrm{N}_6 & 0 & 0 & \mathrm{N}_7 & 0 & 0 & \mathrm{N}_8 \end{bmatrix}$$

$$[\mathrm{NN3}] = \begin{bmatrix} \mathrm{N}_9 & 0 & 0 & \mathrm{N}_{10} & 0 & 0 & \mathrm{N}_{11} & 0 & 0 & \mathrm{N}_{12} & 0 & 0 \\ 0 & \mathrm{N}_9 & 0 & 0 & \mathrm{N}_{10} & 0 & 0 & \mathrm{N}_{11} & 0 & 0 & \mathrm{N}_{12} & 0 \\ 0 & 0 & \mathrm{N}_9 & 0 & 0 & \mathrm{N}_{10} & 0 & 0 & \mathrm{N}_{11} & 0 & 0 & \mathrm{N}_{12} \end{bmatrix}$$

$$[\mathrm{NN4}] = \begin{bmatrix} \mathrm{N}_{13} & 0 & 0 & \mathrm{N}_{14} & 0 & 0 & \mathrm{N}_{15} & 0 & 0 & \mathrm{N}_{16} & 0 & 0 \\ 0 & \mathrm{N}_{13} & 0 & 0 & \mathrm{N}_{14} & 0 & 0 & \mathrm{N}_{15} & 0 & 0 & \mathrm{N}_{16} & 0 \\ 0 & 0 & \mathrm{N}_{13} & 0 & 0 & \mathrm{N}_{14} & 0 & 0 & \mathrm{N}_{15} & 0 & 0 & \mathrm{N}_{16} \end{bmatrix}$$

The element stiffness matrix, $[K_E]$, gives

$$[K_E] = \iint_s [B]^T[D][B]\,dA \tag{3-99}$$

The constitutive matrix [D] is given by Equation(3-82). The global derivatives $\frac{\partial N_i}{\partial x}$, $\frac{\partial N_i}{\partial y}$ can't be determined directly. However, using the chain rule which relates the x, y derivatives to the ξ, η derivatives gives:

$$\left\{\frac{\partial N_i}{\partial \xi} \quad \frac{\partial N_i}{\partial \eta}\right\}^T = [J]\left\{\frac{\partial N_i}{\partial x} \quad \frac{\partial N_i}{\partial y}\right\}^T$$

where $[J]$ is the Jacobian matrix:

$$[J] = \begin{bmatrix} \frac{dx}{d\xi} & \frac{dx}{d\eta} \\ \frac{dy}{d\xi} & \frac{dy}{d\eta} \end{bmatrix}$$

The integral is evaluated in the natural ordinate system, see Figure 3-12, giving:

$$[K_E] = \iint_{-1}^{1} [B]^T[D][B]\,|J|\,d\eta\, d\zeta \tag{3-100}$$

where $|J|$ is Jacobian determination:

$$|J| = \begin{bmatrix} \frac{dx}{d\xi} & \frac{dx}{d\eta} \\ \frac{dy}{d\xi} & \frac{dy}{d\eta} \end{bmatrix}$$

3.5 Summary

This chapter introduces basic theory of finite element method. An comprehensive and detailed introduction of the history and basic concepts of FEM for seepage and deformation are described, respectively. Chapter 4 will deal with a single pumping well models and numerical prediction by using axi-symmetrical theory mentioned in this chapter.

Reference

1) Hrennikoff, A.: Solution of problems of elasticity by the framework method. ASME J.,Vol. 8, 1941, pp. 169-175.

2) Courant. R., Variational method for solution of problem of equilibrium and vibration, Bull. Am. Math. Soc., Vol.49, 1-23, 1943.

3) David M. P. and Lidija Z., Finite element analysis in geotechnical engineering (Theory), Tomas Telford press, 1999.

4) David M. P. and Lidija Z., Finite element analysis in geotechnical engineering (Application), Tomas Telford press, 1999.

5) M. P. David and Z. Lidija, Finite element analysis in geotechnical engineering (Application), Tomas Telford press, 1999, pp.78-80

6) G. Beer, An isoparametric joint/ interface element for finite element analysis, Int. Jnl. Num. Meth. Eng., vol. 21, pp. 585-600, 1985.

7) I. Caro and E. E. Alonso, A new joint element for the analysis of fractured rock, 5th Int. Congr. Rock Mech., Melbourne, vol. F, pp 147-151, 1983.

8) C. S. Desai et al., Thin-layer element for interfaces and joints, Int. Jnl. Num. Anal. Meth. Gemech. , vol 8, pp 19-43, 1984.

9) A. Francavilla and O.C. Zienkieviczs, A note on numerical computation of elastic contact problems, Int. Jnl. Num. Meth, Eng., vol.9, pp. 913-924, 1975.

10) R. Frank et al., Numerical analysis of contacts in geomechanics, Proc. 4th Int. Conf. Num. Meth. Geomech., Rotterdam, vol. 9, pp. 37-42, 1982.

11) R. E. Goodman et al., A model for the mechanics of jointed rock, ASCE, SM3, vol, 94, pp. 637-659, 1968.

12) D. V. Griffiths, Numerical modelling of interfaces using conventional finite element,

Proc. 5thInt. Conf. Num. Meth. Geomech., Nagoya, pp. 837-844, 1985.

13) L. R. Hermann, Finite element analysis of contact problems, ASCE, EM5, vol. 104, pp. 1043-1057, 1978.

CHAPTER 4

SINGLE PUMPING WELL MODELS AND NUMERICAL PREDICTION

4.1 Model overview

In hydraulic engineering, single well drainage is a complicated axisymmetrical problem, and time effect is often considered. When these issues were considered, unconfined seepage problem with free surface is often confronted. Because the position of free surface and overflow boundaries are both unknown in advance, an iterative process is consequently required, it is a boundary nonlinear problem.

At all times, how to locate the free surface and overflow boundaries reliably and efficiently is the key of the matter for the unconfined seepage field analysis.

Currently, Finite Element Method (FEM) is the primary means for numerical analysis of seepage. Fixed Mesh Method (FMM), one of the FEM, owing to advantages of itself, has a very application, and is taking the place gradually of the Altered Mesh Method (AMM), the traditional finite element method in this realm which needs to modify the mesh when the free surface changes during the iteration process.1)

In this chapter, several methods common in use were introduced, including Dupuit assumption, Bathe method, and Saturated-unsaturated theory.

The Dupuit assumption holds that groundwater moves horizontally in an unconfined aquifer, and the groundwater discharge is proportional to the saturated aquifer thickness. It was first designed by Jules Dupuit in 1863 to simplify the groundwater flow equation for analytical solutions.

The Bathe method suggests divide the whole domain by free surface into two parts, saturated region and unsaturated region under and beyond the free surface, the element coefficient of permeability within the unsaturated region is discounted to a very small value (1/1000) while keeps unchanged within the saturated region.

In the Saturated-unsaturated theory, the effect of the zone of capillarity has been taken into account, which is much more realistic manner to simulate the groundwater seepage flow.

4.2 Driven well model

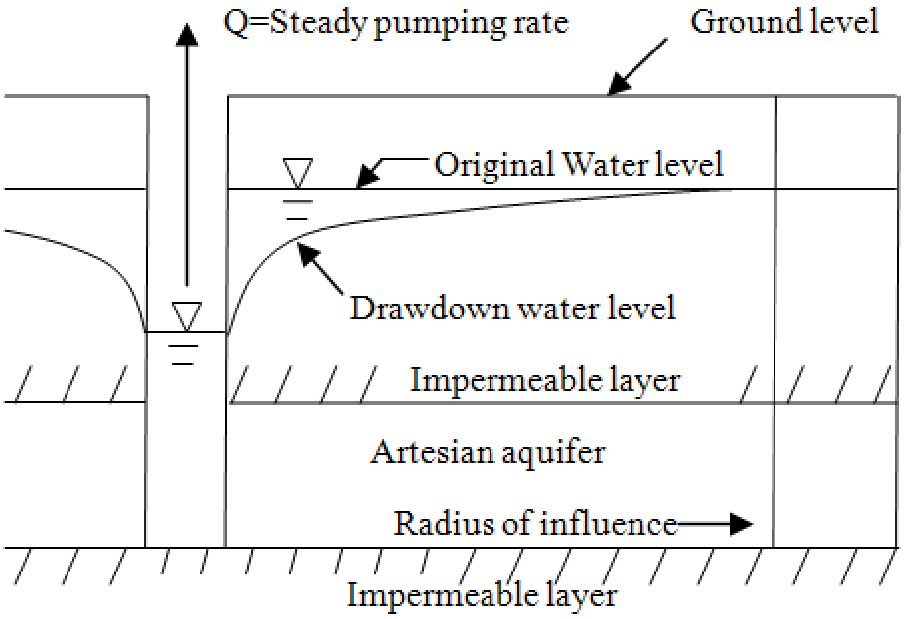

Figure 4-1 Schematic of driven well

An aquifer is a geologic layer of porous and permeable material such as sand and limestone, gravel or sandstone, through which water flows and is stored. An artesian aquifer is confined between impermeable rocks or clay, which is a confined aquifer containing groundwater under positive pressure. This causes the water level in the well to rise to a point where hydrostatic equilibrium has been reached. This type of well is called a driven well. Water may even reach the ground surface if the natural pressure is high enough, in which case the well is called a flowing driven well. Figure 4-1 shows the schematic of a driven well.

4.2.1 Outline of the model

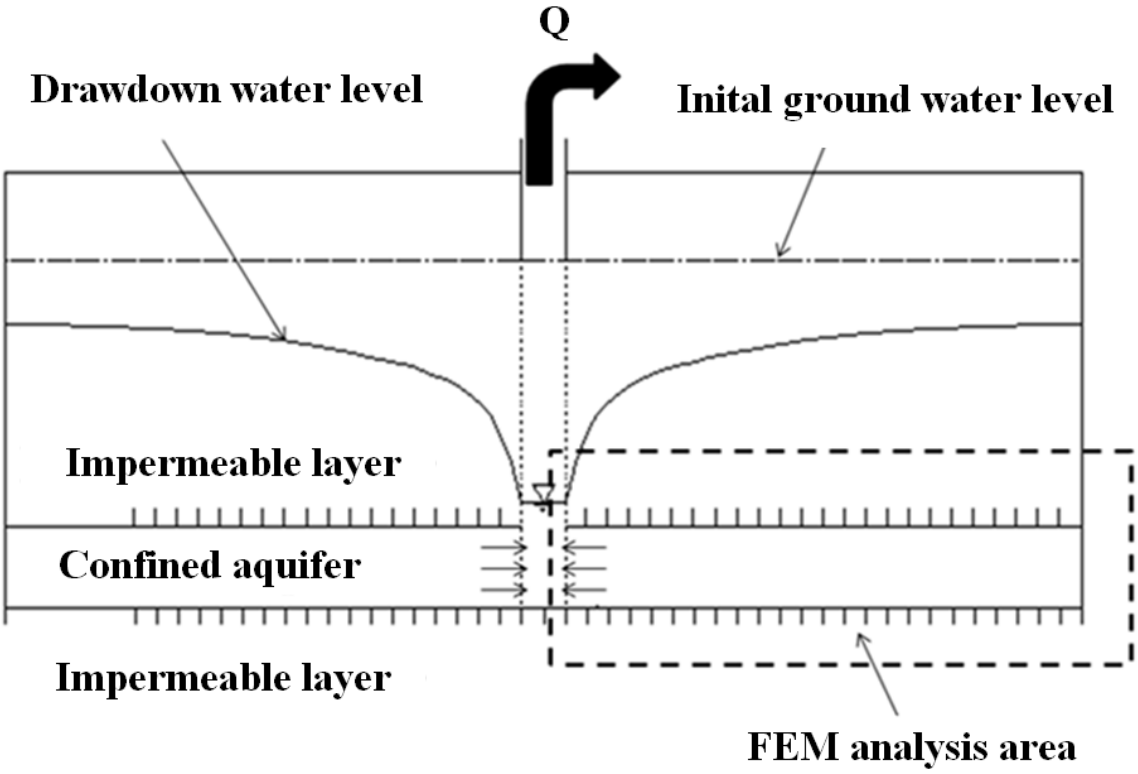

Figure 4-2 A simple driven well model

In order to validate the correctness of the programming, a simple driven well model has been tested which is shown in Figure 4-2.

According to the Figure 4-2, the FEM analysis area has been chosen. In case of six nodal triangular element, the finite element mesh has been plotted which is given in Figure 4-3. As shown in the figure, the height of the analysis area is 10 meters and the width is 50 meters.

For this model, the following basic assumptions are introduced into the analysis:

(1) The ground water flow is laminar and governed by Darcy's law.

(2) Behaviors around the pumping well are assumed to be axisymmetrical, therefore cylindrical coordinates can be used, and the problem can be considered as a 2D one.

(3) The water molecules and soil particles can't be compressed and the stress-strain relationship of the soil is linear.

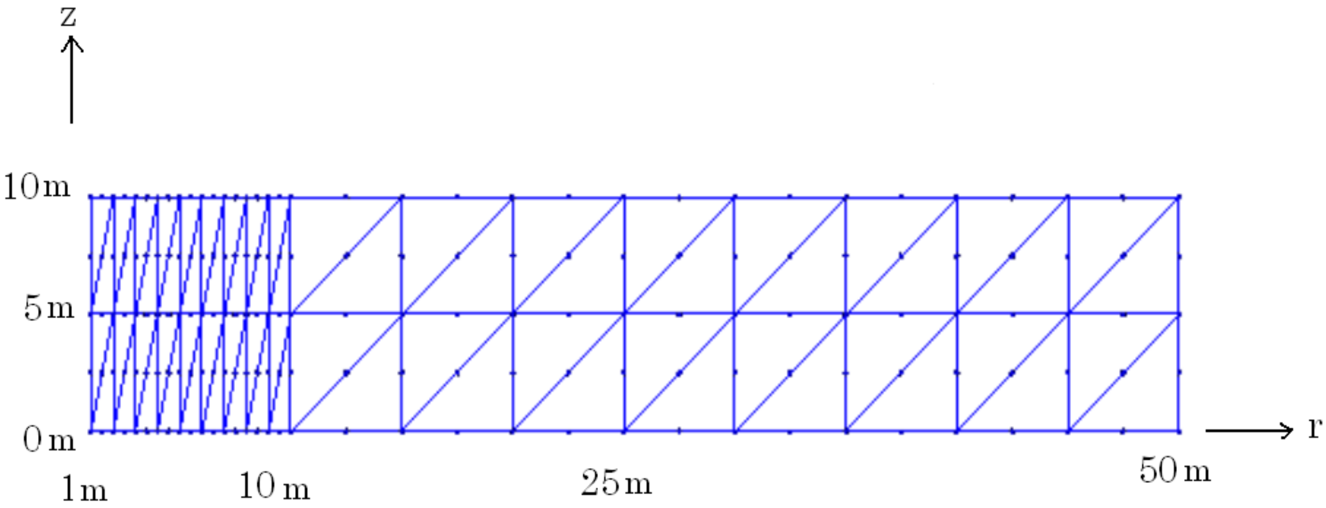

Figure 4-3 Finite element mesh of driven well

4.2.1.1 Case 1 test

In the case 1, it assumed that the total head H=10m on the boundary r=1m and the total head H=20m on the boundary r=50m, which is shown in the Figure 4-4.In this model, the coefficient of permeability K=0.036 m/h is assumed.

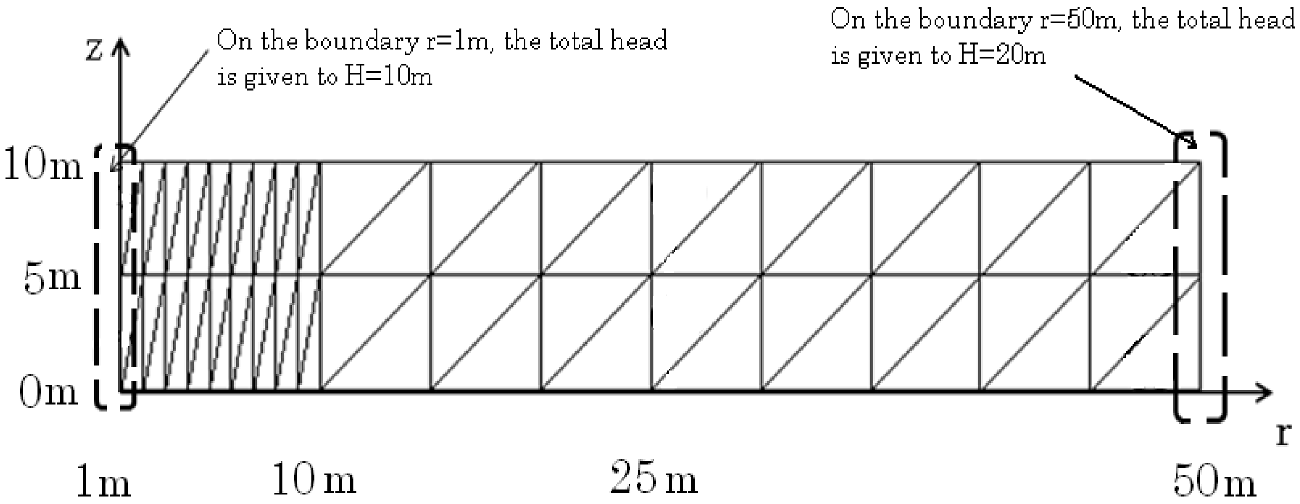

Figure 4-4 Case 1 test

Numerical prediction of Case 1

For the case 1, Figure 4-5 shows the numerical prediction results, the longer the arrows are, the larger the seepage velocity. The numerical prediction results and theoretical values have been given on Table 4-1. Here, R is the distance from the axis of the pumping well, V is the velocity of seepage flow of the data points and the similarity is the ratio of numerical prediction results and theoretical values.

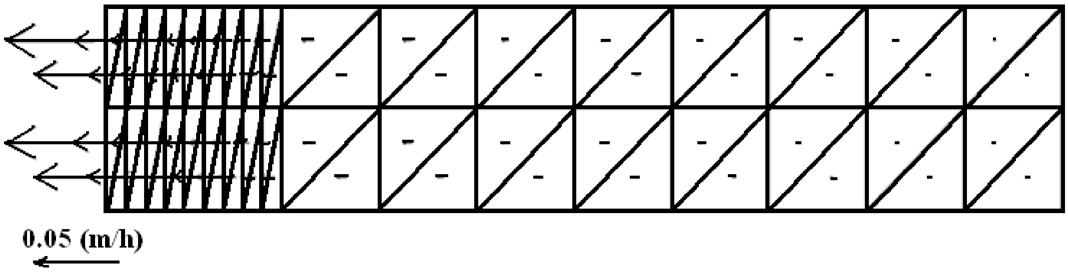

Figure 4-5 Numerical prediction results of case 1

Table 4-1 Theoretical values and numerical prediction results in case 1

R (Distance) m	V (Theoretical values) m/h	V (Numerical prediction) m/h	Similarity(C/T)
1.05971586	0.086838881	0.083195	95.8039%
2.05971585	0.04467827	0.043965	98.4035%
3.05971584	0.030076172	0.02983	99.1815%
5.05971582	0.018187689	0.018135	99.7103%
10.29857925	0.008935654	0.0087975	98.4539%
20.29857915	0.004533546	0.004513	99.5468%
30.29857905	0.003037256	0.003031	99.7940%
40.29857895	0.002283568	0.002281	99.8876%
49.70142015	0.001851547	0.00185	99.9164%

As shown in the Table 4-1, the similarity increases with the increases of radius R. Here the similarity is the ratio of calculation value of numerical prediction and theoretical value (C/T). When R is larger than 3m, the similarity is larger than 0.99. But the similarity decreases relatively quickly from R=1m to R=3m where the seepage velocity increases quickly.

4.2.1.2 Case 2 test

In the case 2, it assumed that the total head H=10m on the boundary z=0m and the total head H=20m on the boundary z=10m, which is shown in the Figure 4-6. In this model, coefficient of permeability K=0.036 m/his assumed.

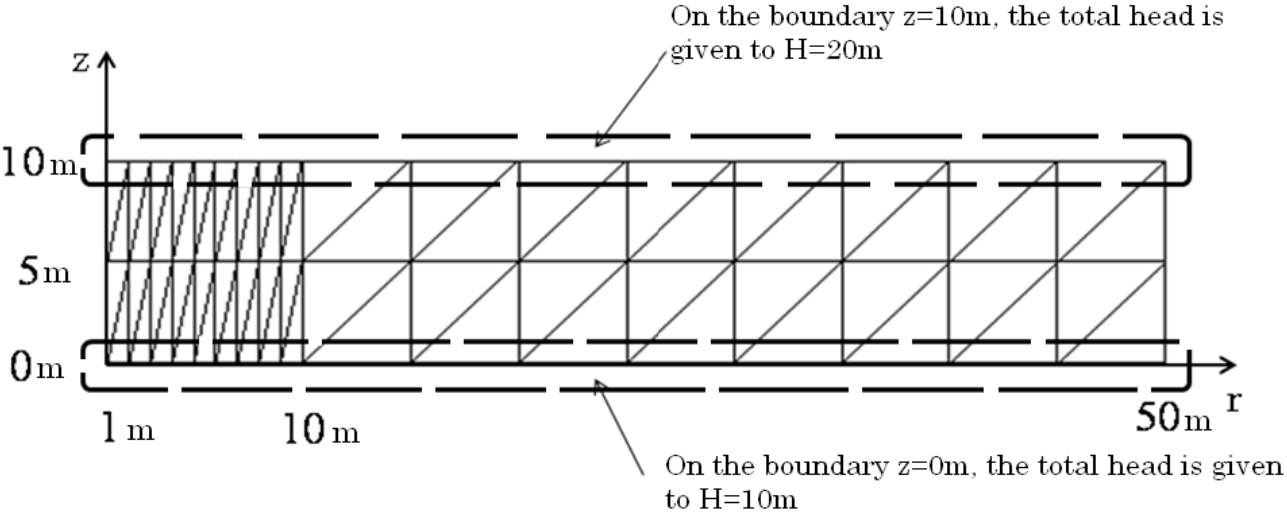

Figure 4-6 Case 2 test

Numerical prediction of Case 2

For the case 2, the numerical prediction results and theoretical values has been given on Table 4-2. Here, Z is the elevation of the data points and the similarity is the ratio of numerical prediction results and theoretical values.

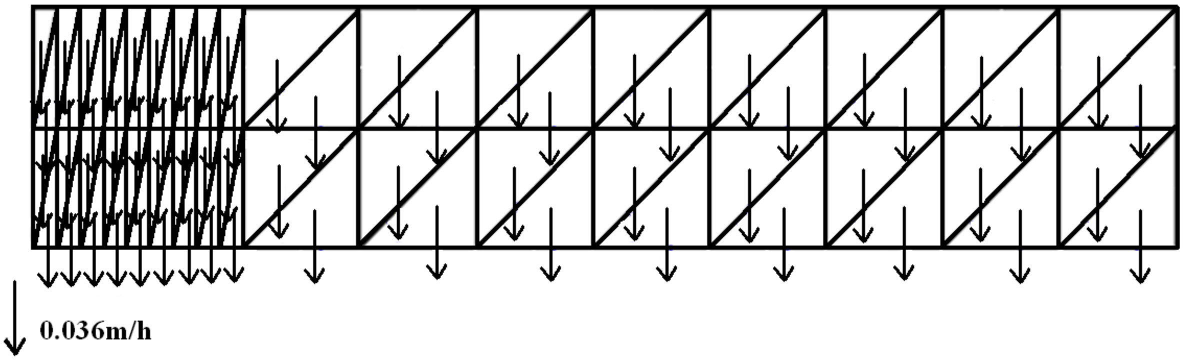

Figure 4-7 Numerical prediction results of case 2

Table 4-2 Theoretical values and numerical prediction results in case 2

Z (hight) m	V (Theoretical values) m/h	V (Numerical prediction) m/h	Similarity(C/T)
2	0.036	0.036	100%
4	0.036	0.036	100%

As shown in the Table 4-2, the numerical prediction results match well with the theoretical values.

4.2.1.3 Case 3 test

In the case 3, it assumed that the traction is given to Tr=1 kN/m on the boundary r=50m and the other boundary conditions of soil deformations are also given, which is shown in the Figure 4-8. In this model, elastic modulus E=1000Kpa, and Poisson’s ratio ν =0.3 are assumed.

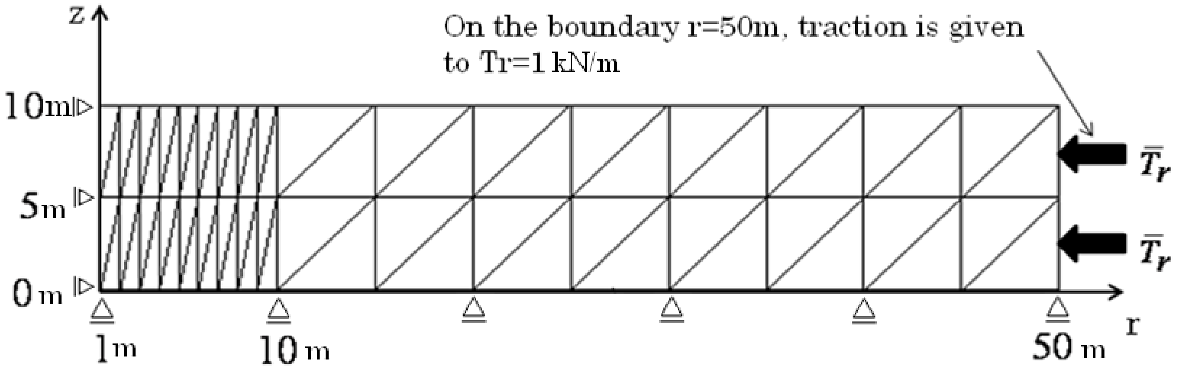

Figure 4-8 Case 3 test

Numerical prediction of Case 3

Table 4-3 Theoretical values and numerical prediction results in case 3

R (Distance) m	U (Numerical prediction) m	U (Theoretical values) m	Similarity (C/T)
3	0.0018524	0.001866265	99.2571%
5	0.0033478	0.003359276	99.6584%
10	0.0069248	0.006928508	99.9465%
20	0.01396	0.013961993	99.9857%
30	0.02097	0.02097215	99.9898%
40	0.02798	0.027976474	100.0126%
50	0.03498	0.034978466	100.0044%

For the case 3, the numerical prediction results and theoretical values has been given on Table 4-3. Here, U is the horizontal displacement due to the traction at the data points and the similarity is the ratio of numerical prediction results and theoretical values.

As shown in the Table 4-3, the similarity increases with the increases of radius R. the numerical prediction results match well with the theoretical values.

4.2.1.4 Case 4 test

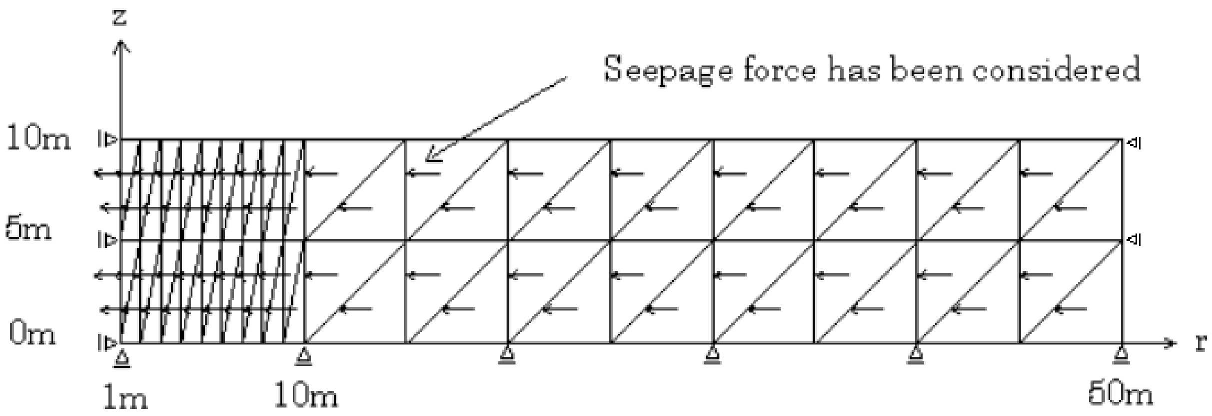

Figure 4-9 Case 4 test

In the case 4, the seepage force due to ground water flow has been considered and the boundary conditions of soil deformations are also given, which is shown in the Figure 4-9.In this model, the coefficient of permeability K=0.036 m/h, elastic modulus E=1000Kpa, and Poisson's ratio ν =0.3 are assumed.

Theoretical values of case 4

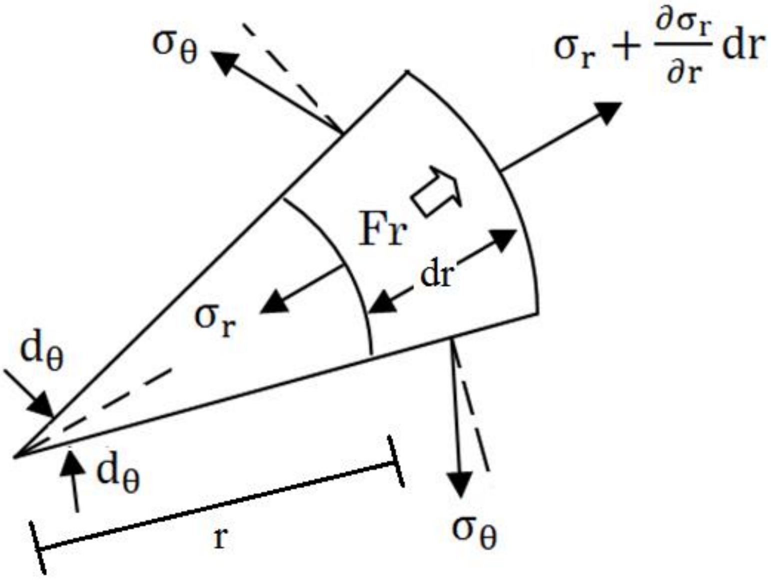

Figure 4-10 Axisymmetric deformation theory

According to the axisymmetric deformation theory, which is shown in the Figure 4-10, the equations of equilibrium is given in Equation (4-1)

$$2(\sigma_\theta \, L \, dr)\frac{d\theta}{2} = \left(\sigma_r + \frac{d\sigma_r}{dr} dr\right) L(r + dr)d\theta - \sigma_r \, L \, r \, d\theta + F_r \, L \, dr \left(r + \frac{dr}{2}\right) d\theta \qquad (4\text{-}1)$$

Here, L is the thickness of the representative elementary volume, Fr is the seepage force.

If the higher order terms in the Equation (4-1) were ignored, the equation can be reduced to

$$\sigma_\theta - \sigma_r - r\frac{d\sigma_r}{dr} = F_r r \tag{4-2}$$

In the driven well conditions, the rate of flow Q through the cross section can be shown below, here Hb is the thickness of permeable layer.

$$Q = k\frac{dh}{dr}\,2\pi r\,H_b \tag{4-3}$$

And the seepage force F_r can be given in Equation (4-4)

$$F_r = -\frac{dh}{dr}\gamma_w = -\frac{Q\,\gamma_W}{2\pi k H_b}\frac{1}{r} = \frac{A}{r} \tag{4-4}$$

$$\text{Here, } A = -\frac{Q\,\gamma_W}{2\pi k H_b}$$

To sum up, the Equation (4-2) can be written as

$$\sigma_\theta - \sigma_r - r\frac{d\sigma_r}{dr} = A \tag{4-5}$$

According to the axisymmetric deformation theory, the equations of compatibility are given below:

$$\begin{cases} \varepsilon_r = \dfrac{\partial u}{\partial r} \\ \varepsilon_\theta = \dfrac{u}{r} \end{cases} \tag{4-6}$$

The relation equations between stress and strain are shown in Equation (4-7)

$$\begin{cases} \sigma_r = \frac{E}{1-\nu^2}\left(\frac{du}{dr} + \nu\frac{u}{r}\right) \\ \sigma_\theta = \frac{E}{1-\nu^2}\left(\frac{u}{r} + \nu\frac{du}{dr}\right) \end{cases} \tag{4-7}$$

According to the Equations (4-5) and (4-7), the Equation (4-8) can be given

$$\frac{d^2u}{dr^2} + \frac{1}{r}\frac{du}{dr} - \frac{u}{r^2} = \frac{B}{r} \tag{4-8}$$

here, $B = -A\,\frac{1-\nu^2}{E} = \frac{Q\,\gamma_W(1-\nu^2)}{2\pi k H_b E}$

The general solution of Equation (4-8) is shown below, and the boundary conditions are shown in the Figure 4-11

$$u = B\,\frac{r}{2}\left(\ln r - \frac{1}{2}\right) + C_1 r + \frac{C_2}{r} \tag{4-9}$$

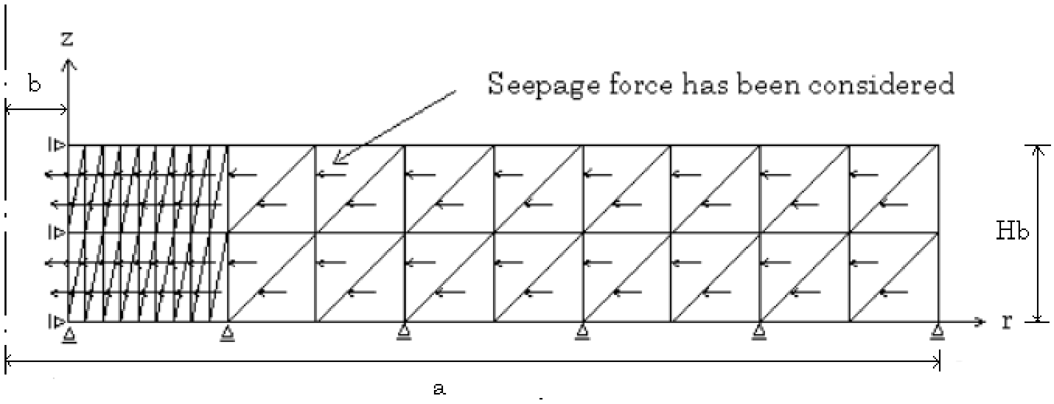

Figure 4-11 Boundary conditions for the case 4

When r=b, u=0, the Equation (4-9) can be written as

$$u = B\,\frac{b}{2}\left(\ln(b) - \frac{1}{2}\right) + C_1 b + \frac{C_2}{b} = 0 \qquad (4\text{-}10)$$

When r=a, $\sigma_r = 0$, the Equation (4-11) can be given below

$$\frac{B}{2}\left\{(1+\nu)\ln(a) + \frac{1-\nu}{2}\right\} + C_1(1+\nu) - \frac{C_2(1-\nu)}{a^2} = 0 \qquad (4\text{-}11)$$

According to the Equations (4-10) and (4-11), the Equation (4-12) can be given

$$\frac{B}{2}\left(\ln(a) - \ln(b) + \frac{1-\nu}{2(1+\nu)} + \frac{1}{2}\right) = C_2\left(\frac{1}{a^2}\frac{1-\nu}{1+\nu} + \frac{1}{b^2}\right) \qquad (4\text{-}12)$$

In this way, the C_1 and C_2 can be derived, which is shown in Equation (4-13) and (4-14)

$$C_1 = -\frac{B}{2}\left(\ln b - \frac{1}{2}\right) - \frac{C_2}{b^2} \qquad (4\text{-}13)$$

$$C_2 = \frac{\frac{B}{2}\left(\ln\left(\frac{a}{b}\right) + \frac{1}{1+\nu}\right)a^2 b^2 (1+\nu)}{a^2(1+\nu) + b^2(1-\nu)} \qquad (4\text{-}14)$$

Numerical prediction of Case 4

For the case 4, the numerical prediction results and theoretical values has been given on Table 4-4. Here, R is the distance from the axis of the driven well, U is the horizontal displacement due to the seepage flow and the similarity is the ratio of numerical prediction results and theoretical values.

Table 4-4 Theoretical values and numerical prediction results in case 4

R（Distance） m	U (Numerical prediction) m	U (Theoretical values) m	Similarity(C/T)
1	0.000000	0	
3	0.010186	0.010677118	95.40402%
5	0.016256	0.016760219	96.99157%
10	0.026782	0.027091452	98.85775%
15	0.033860	0.034016822	99.53899%
20	0.038798	0.038877863	99.79458%
25	0.042196	0.042230259	99.91888%
30	0.044388	0.044395695	99.98267%
35	0.045588	0.045578496	100.02085%
40	0.045944	0.045916295	100.06034%
45	0.045566	0.045522898	100.09468%
50	0.044530	0.044483338	100.10490%

As shown in the Table 4-4, the similarity increases with the increases of radius R. When R is larger than 10m, the similarity is larger than 0.99. But the similarity decreases relatively quickly from R=10m to R=3m where the seepage velocity increases quickly. Because the seepage velocity data used in case 4 comes from case 1, the similarity in case 4 is smaller when the data points near the boundary of pumping, which match with the similarity of case 1.

Figure 4-12 shows the relationship of the horizontal displacement and the radius. The peak value comes from around R=40m and is more than 0.045m. From the 4 cases test results, it can make sure that the programming is validity.

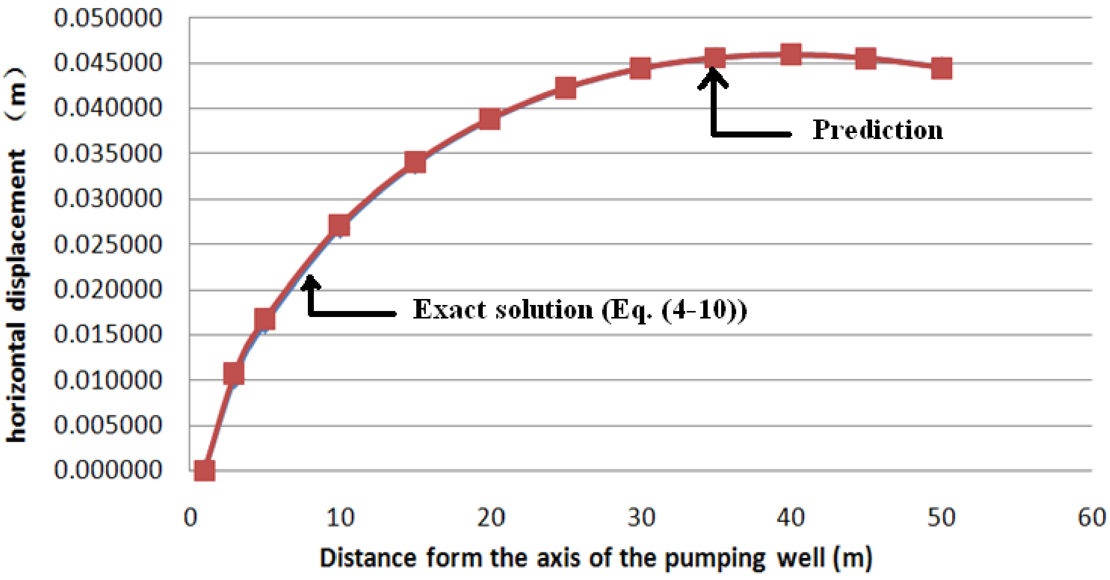

Figure 4-12 Numerical prediction results of case 4

4.3 Gravity well model

Gravity well is an unconfined seepage problem. Because the phreatic surface and seepage face are both unknown, at all times, how to locate the free surface and overflow boundaries reliably and efficiently is the key of the matter for the unconfined seepage field analysis.

4.3.1 Dupuit's steady seepage model

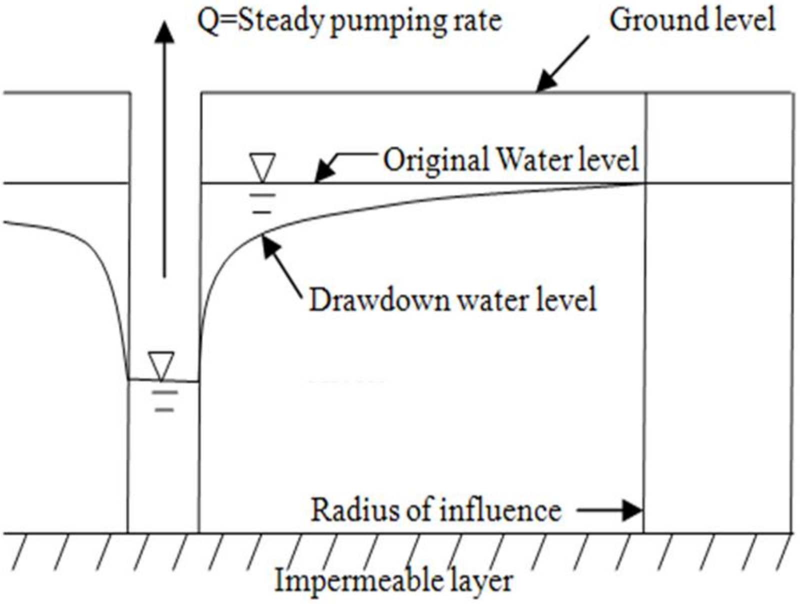

Figure 4-13 Dupuit’s assumption

It was first designed by Jules Dupuit in 1863 to simplify the groundwater flow equation for analytical solutions. The Dupuit assumption holds that groundwater moves horizontally in an unconfined aquifer, and the groundwater discharge is proportional to the saturated aquifer thickness. Figure 4-13 shows the schematic of Dupuit’s assumption.

4.3.1.1 Outline of the model

For this model, the following basic assumptions are introduced into the analysis:

(1) The ground water flow is laminar and governed by Darcy’s law.

(2) Behaviors around the pumping well are assumed to be axisymmetrical, therefore cylindrical coordinates can be used, and the problem can be considered as a 2D one.

(3) The water molecules and soil particals can't be compressed and the stress-strain relationship of the soil is linear.

(4) The Dupuit's assumption is used for theoretical solution, so the leaking face and vertical flow are ignored, which is shown in Figure 4-13

In this numerical model, soil deformation is calculated from the changes in the body forces. In period of water level lowering in foundation pit, it is impossible for an evident consolidation settlement to appear in the soil layer beneath the water lowering level, whereas greater settlement may be produced in the soil layer between water lowering level and the original ground water level at the action of the added self-weight stress due to the drainage solidifying. So in this numerical model, the deformations caused by both seepage force and added self-weight stress had been considered.

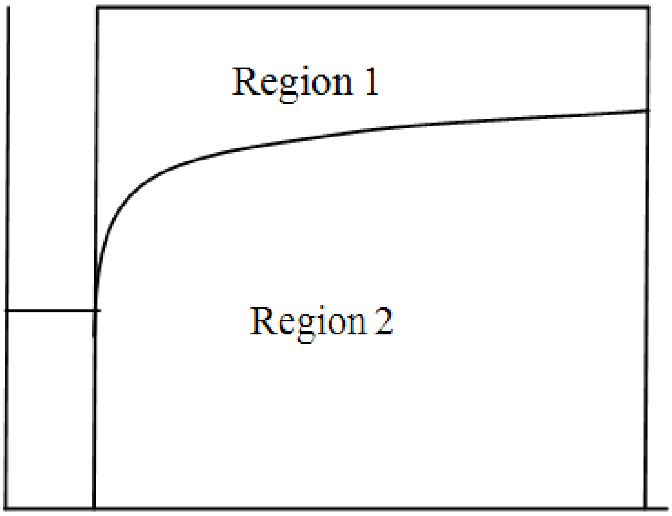

Figure 4-14 Regions of body force

For the calculation of body forces, the affected area is divided into two regions which are shown in Figure 4-14 and the changes in body force for region 1 and region 2 are shown below:

Region 1: saturated before pumping and unsaturated after pumping.

Region 2: saturated before and after pumping.

For saturated areas, it is only considered the seepage force as body force.

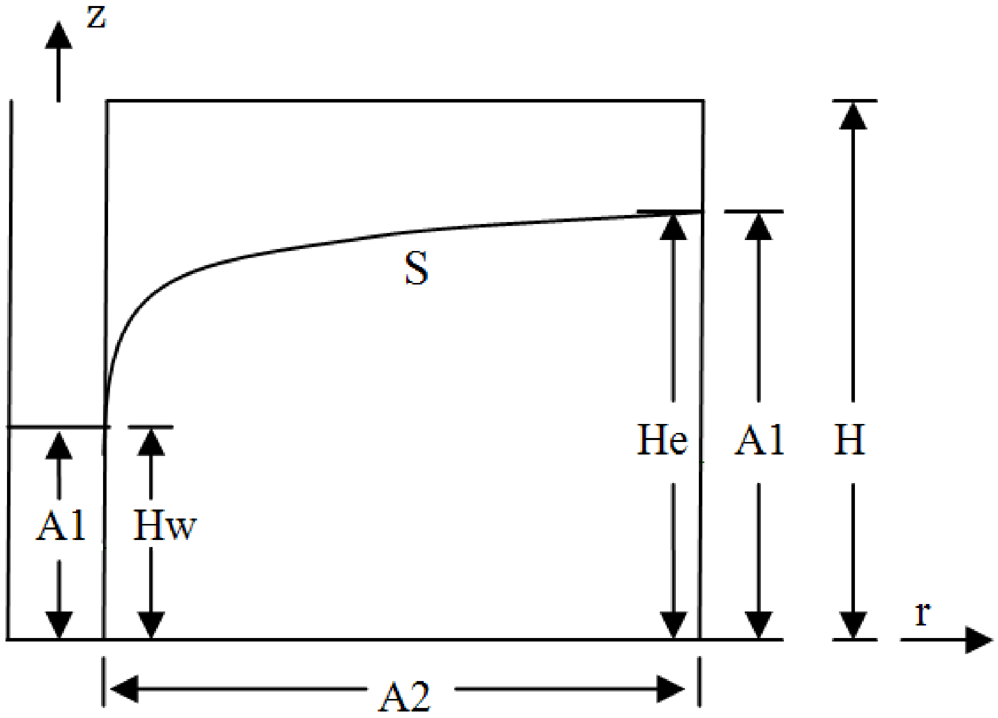

Figure 4-15 Boundary conditions for seepage

For the unsaturated areas, flow can be simplified if it influence in soil weight is taking into account rather than in flow pattern, so the body force is only in the z direction.

As shown in Figure 4-15:

Border with constant water level, A1

At well border h=Hw

At radius influence h=He

where, H is original water level, Hw is the water level of well.

Impervious layer, A2

$$\frac{\partial h}{\partial z} = 0$$

Phreatic surface, S

$$Qs = 0$$

where, Qs is seepage flow across surface

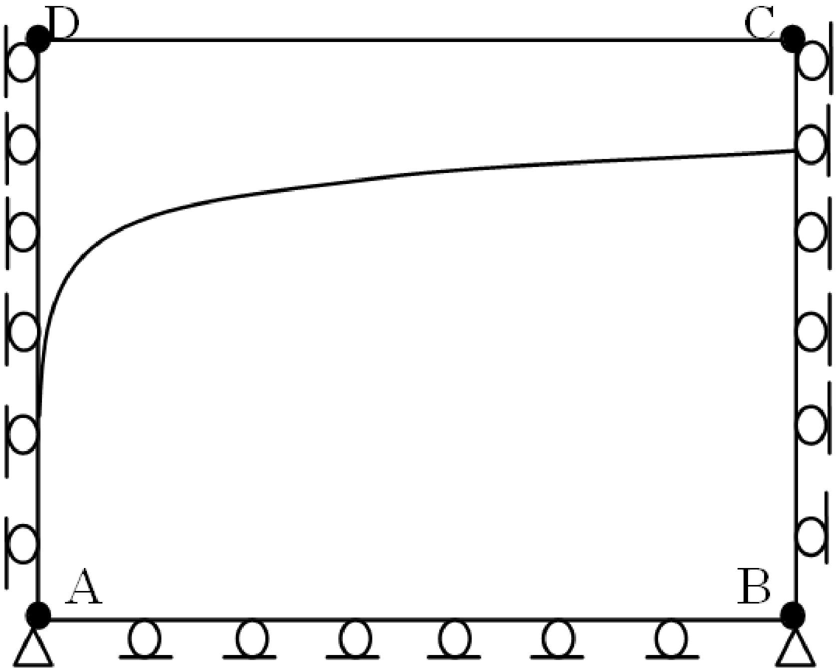

Figure 4-16 Boundary conditions for soil deformations

In Figure 4-16, the boundary conditions used to calculate soil deformation are given. At the border of the well and radius influence (boundary AD and BC), only vertical deformations are permitted. At the bottom layer, (boundary AB), only horizontal deformation is allowed. And the point A and B are restricted in both vertical and horizontal directions.

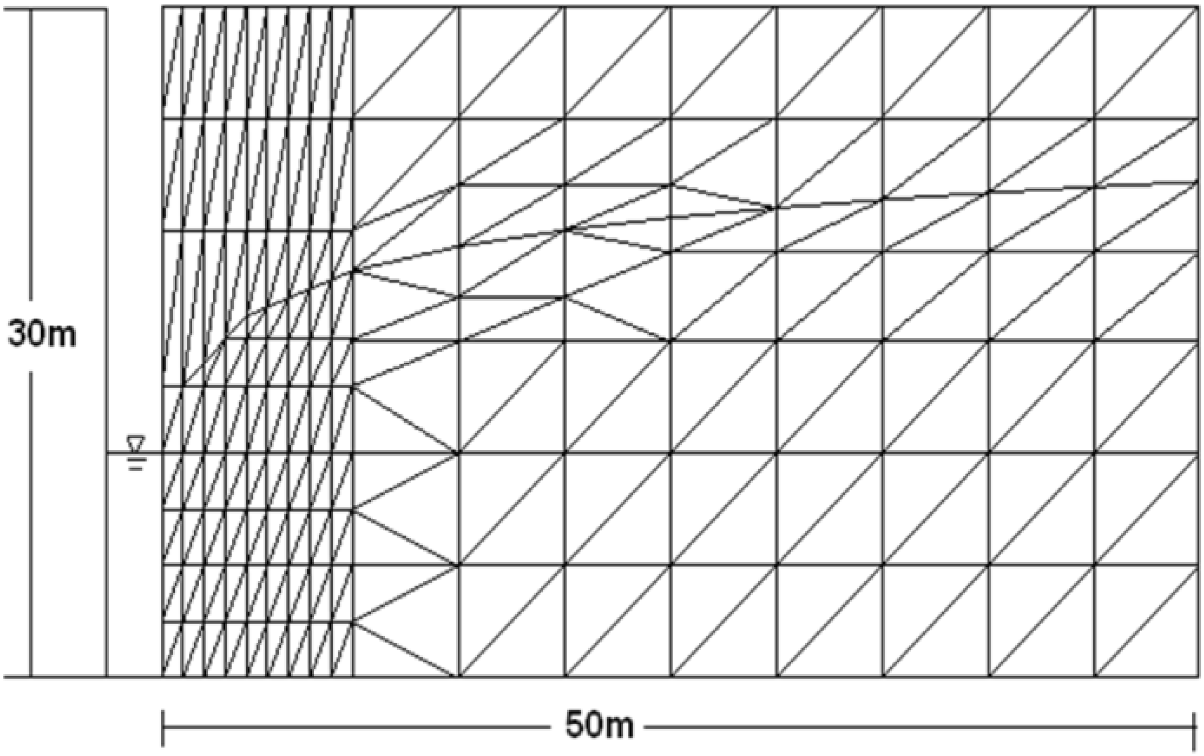

Figure 4-17 Cross-section for finite element mesh

The seepage flow due to single pumping well can be considered an axisymmetrical flow, and the domain is divided into a network of concentric rings of triangular cross-section elements. The finite element mesh is shown in Figure 4-17. The Drawdown water level can be calculated by using Dupuit assumption. And the Dupuit surface was taken into account when the mesh was made. The elements near the well had been divided smaller in order to imporve the accuracy of calculation.

4.3.1.2 Numerical prediction

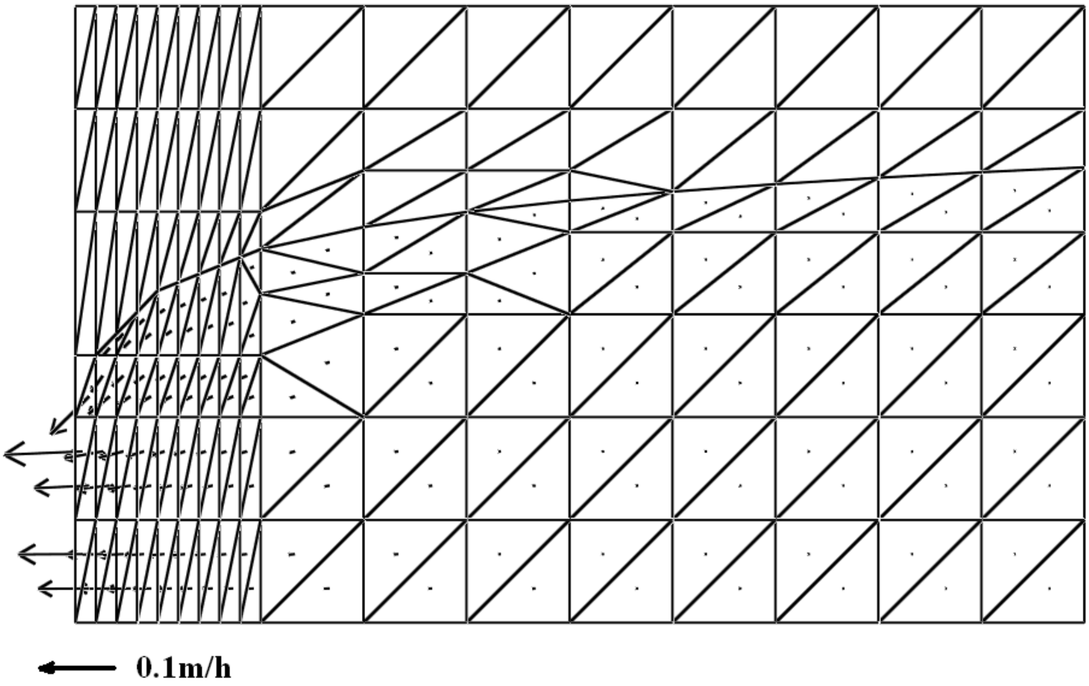

Figure 4-18 Flow velocity distribution

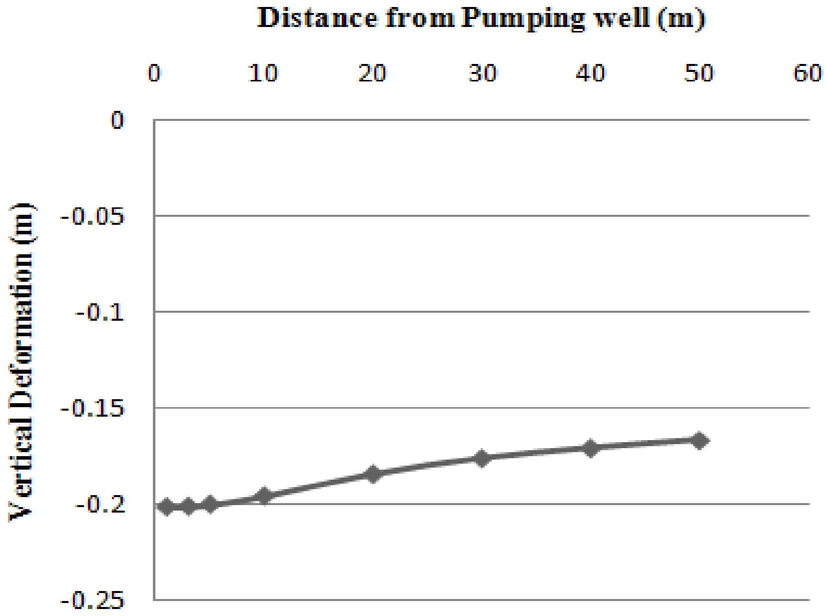

Figure 4-19 Vertical deformation results

Calculated result of water flow from the numerical modeling is basically matched with theoretical value and the flow velocity distribution is shown in Figure 4-18. As it can be seen, flow rate near the pumping well is larger than 0.1m/h. And the flow rate decreases gradually with increasing distance from the well. In this model, the coefficient of permeability K=0.036 m/h, elastic modulus E=1000Kpa, and Poisson's ratio ν =0.3 are assumed.

The effective stress in the soil will be increased by lowering the ground water level which causes deformation. The vertical displacement of ground from the numerical results is shown in Figure 4-19. As shown, the average displacement exceeds 0.15m, and the value of displacement near the well is relatively larger. The tendency of the displacement curve is found to be related to the drawdown water level. The lower the drawdown water level, the larger displacement occurs. This tendency of simulation results is in accord with the actual condition well.

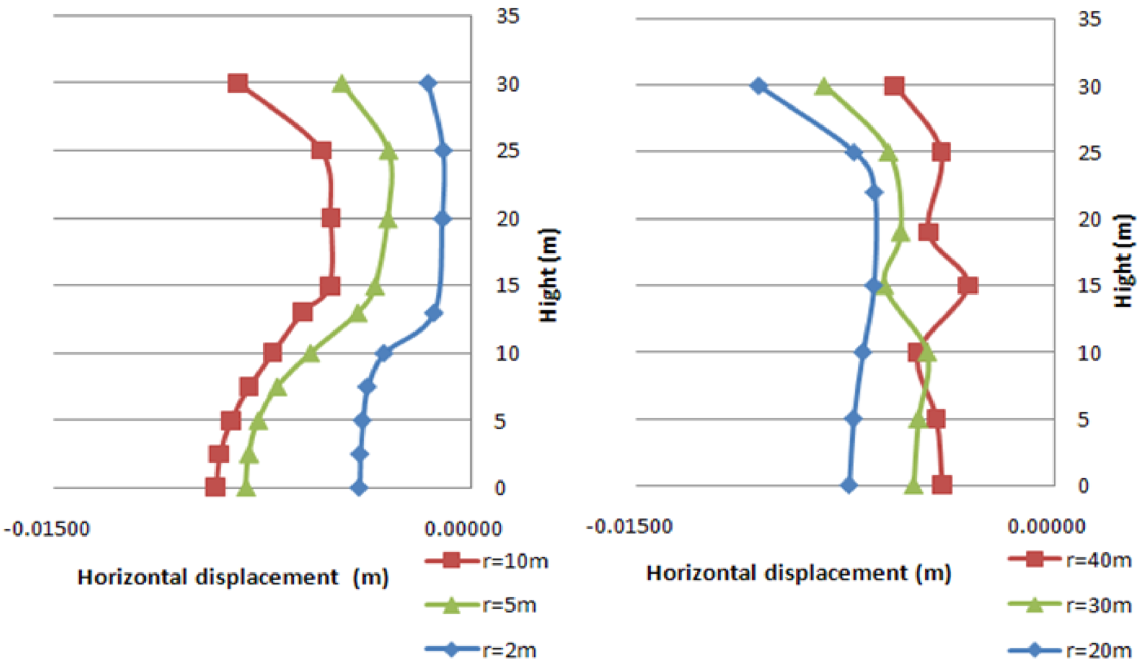

Figure 4-20 Horizontal displacement results

In this model, the seepage force is taken into consideration, so the lateral seepage flow causes deformation in horizontal direction. The results are shown in the Figure 4-20.

As shown, when r is smaller than 10m, the horizontal displacement of the points under the phreatic surface is obviously larger than the points' which are above the phreatic surface, whereas when r is larger than 20m, the displacement curves become smoothly. The main reason is the change of seepage velocity. When r is small, the seepage velocity is large which cause relatively larger seepage force. On the contrary, when r becomes larger, the seepage velocity decreases and the seepage force become smaller. It can also see that the horizontal displacement near the ground level tends to increase firstly(r is less than 10m) and then decrease(r is larger than 20m) with increase of radius. The vertical displacement of one element can lead to the horizontal displacement of adjacent elements when the domain assumed to be a continuous body. The lager the vertical displacement of one element occurs, the bigger the horizontal displacement of adjacent elements get. Referring to vertical displacement results in Figure 4-19, the change rate of vertical displacement is relatively larger when r is between 10m and 20m, which matches with horizontal displacement results in Figure 4-20, in which the peak values come from r=10m and r=20m.

4.3.2 Bathe's steady seepage model

The solution algorithm employs a non-linear permeability description of the material and avoids iteration with the finite element mesh. It was first designed by Bathe in 1979, and the schematic of Bathe's model was shown in Figure 4-21.

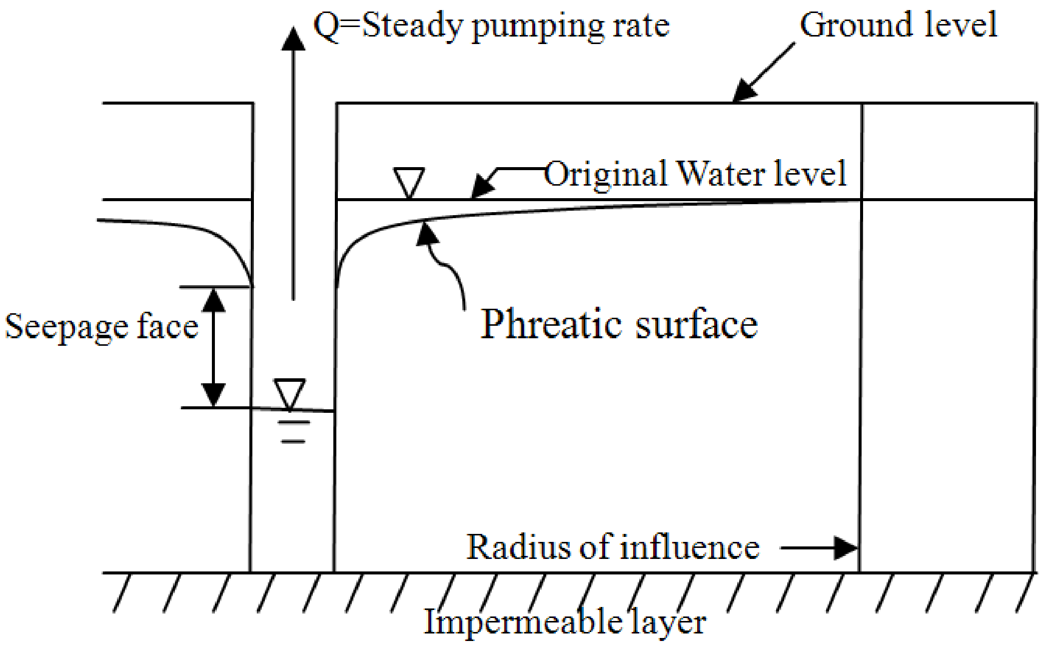

Figure 4-21 Schematic of Bathe's model

The Bathe method divides the whole domain by free surface into two parts, saturated region and unsaturated region under and beyond the free surface. Because the phreatic surface and seepage face are both unknown at first, an iteration process for locating the phreatic surface and seepage face is needed. The element coefficient of permeability within the unsaturated region is discounted to a very small value ($k \times \frac{1}{1000}$) while keeps unchanged within the saturated region.

4.3.2.1 Outline of the model

For this model, the following basic assumptions are introduced into analysis:

(1) The ground water flow is laminar and governed by Darcy'slaw.

(2) Behaviors around the pumping well are assumed to be axisymmetrical, therefore cylindrical coordinates can be used, and the problem can be

considered as a 2D one.

(3) The water molecules and soil particals can't be compressed and the stress-strain relationship of the soil is linear.

(4) The element coefficient of permeability within the unsaturated region is discounted to a very small value ($k \times \frac{1}{1000}$) while keeps unchanged within the saturated region.

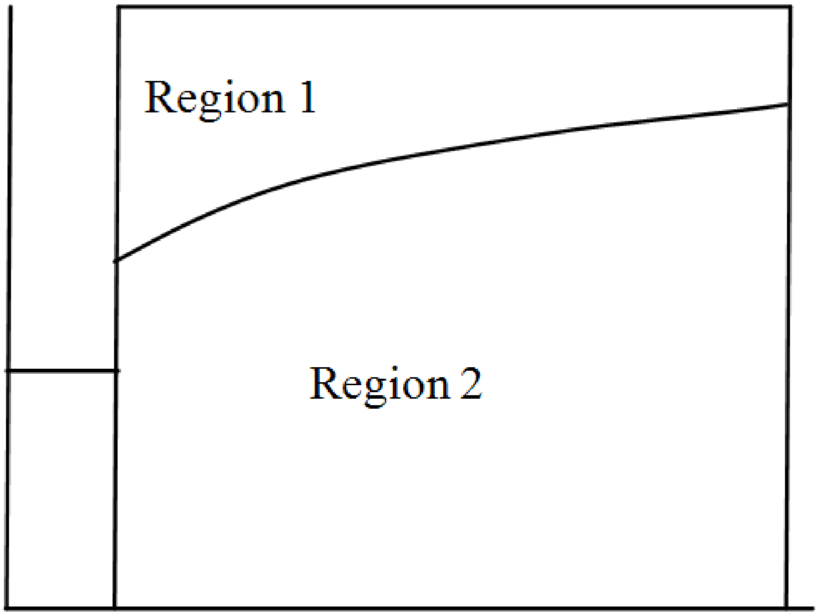

Figure 4-22 Regions for coefficient of permeability

For the calculation of coefficient of permeability, it was divided the affected area into two regions which is shown in Figure 4-22 and the changes of coefficient of permeability for region 1 and region 2 are shown below:

Region 1: saturated before pumping and unsaturated after pumping.

Region 2: saturated before and after pumping.

For saturated areas, the coefficient of permeability keeps unchanged ($\mathrm{K} = \mathrm{K}_0$), K_0 is the initial coefficeient of permeability.

For the unsaturated areas, the coefficient of permeability is discounted to a very small value ($\mathrm{K} = \frac{\mathrm{K}_0}{1000}$).

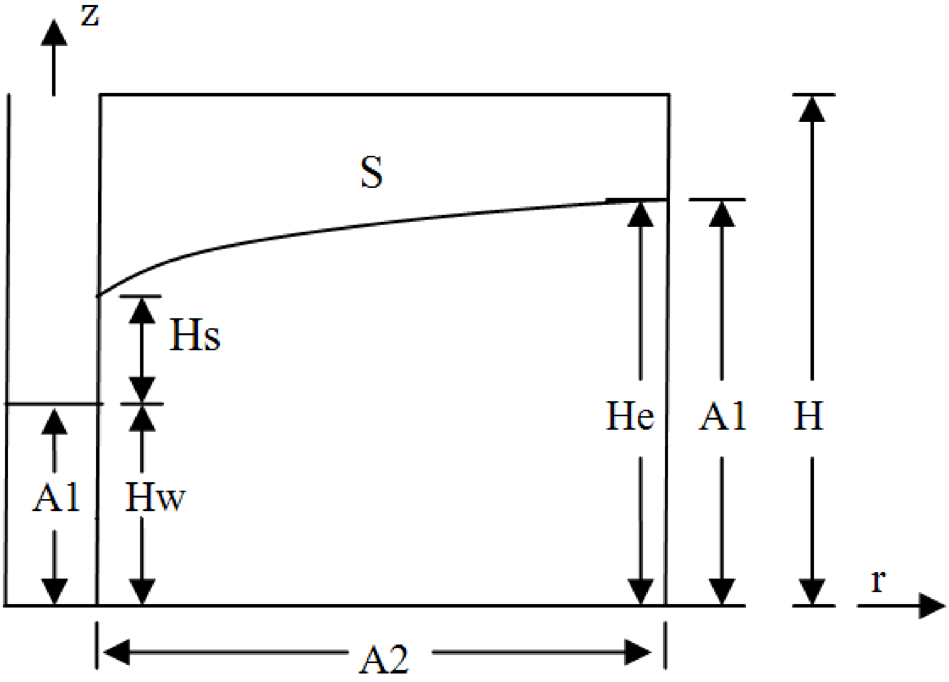

Figure 4-23 Boundary conditions for seepage

Boundary conditions for water flow was shown in Figure 4-23, there are three kinds of boundary conditions.

(1) Border with constant water level, A1

At well border h=Hw

At radius influence h=He

where, H is original water level, Hw is the water table in the well.

(2) Impervious layer, A2

$$\frac{\partial h}{\partial z} = 0$$

(3) Leaking face at the well border, Hs

At well border h=Z, here Z is elevation

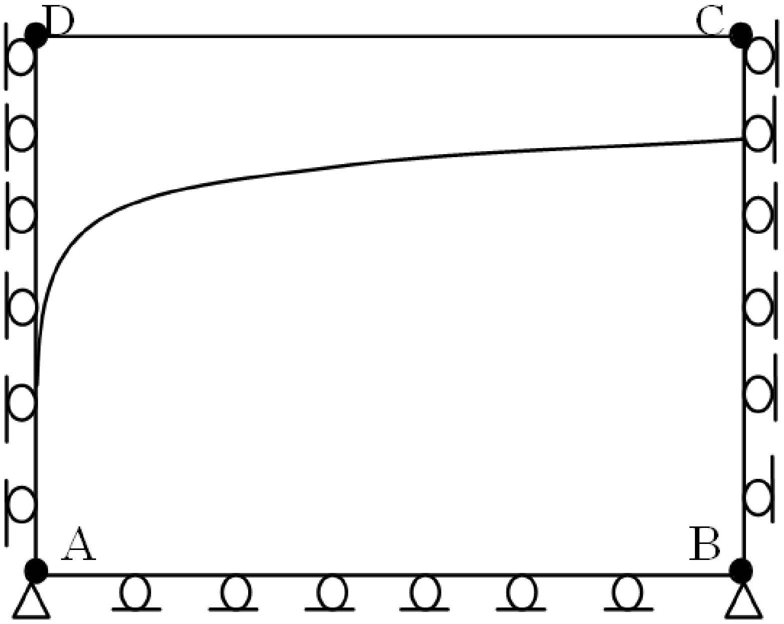

Figure 4-24 Boundary conditions for soil deformations

In Figure 4-24, the boundary conditions used to calculate soil deformation are given. At the border of the well and radius influence (boundary AD and BC), only vertical deformations are permitted. At the bottom layer, (boundary AB), only horizontal deformation is allowed. And the point A and B are restricted in both vertical and horizontal directions.

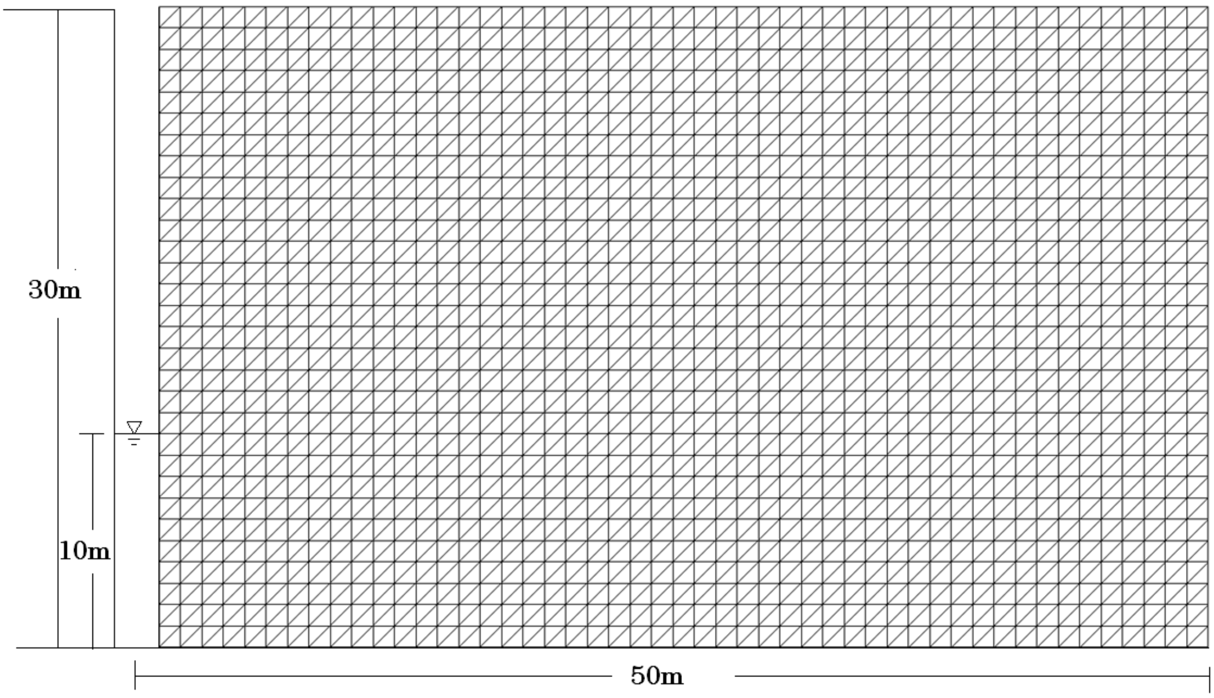

Figure 4-25 Cross-section for finite element mesh

The seepage flow due to single pumping well can be considered an axisymmetrical flow, and the domain is divided into a network of concentric rings of triangular cross-section elements. The finite element mesh is shown in Figure 4-25. The phreatic surface and seepage face are both unknown at first, so an iteration process for locating the phreatic surface and seepage face is needed. The elements had been divided smaller in order to improve the accuracy of calculation.

4.3.2.2 Numerical prediction

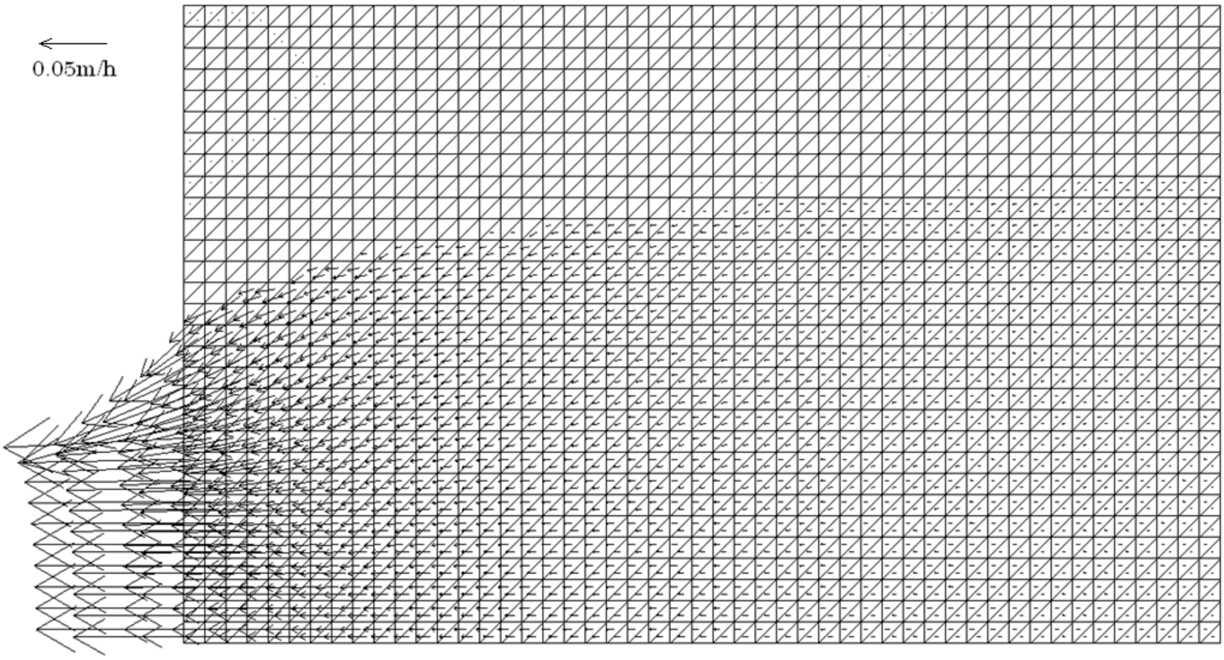

Figure 4-26 Flow velocity distribution

Calculated result of water flow from the numerical modeling is basically matched with theoretical value and the flow velocity distribution is shown in Figure 4-26. As shown, flow rate near the pumping well is larger than 0.1m/h, which is match with the Dupuit's steady seepage model. And the flow rate decreases gradually with increasing distance from the well. In this model, the coefficient of permeability K=0.036 m/h, elastic modulus E=1000Kpa, and Poisson’s ratio ν =0.3 are assumed.

Figure 4-27 shows the flow velocity distribution of the elements, the black zone is the unsaturated zone. The white zone and the gray zone are saturated zone. The color becomes darker when the seepage velocity of the element decreases and the boundary of unsaturated zone and saturated zone is also shown clearly.

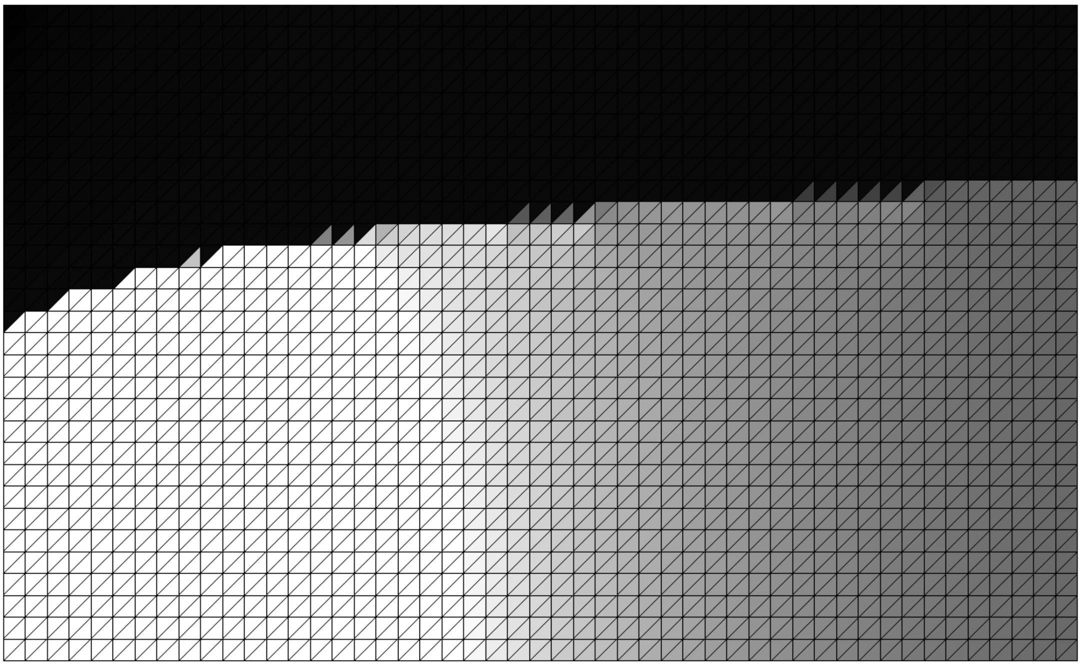

Figure 4-27 Flow velocity distribution of the elements

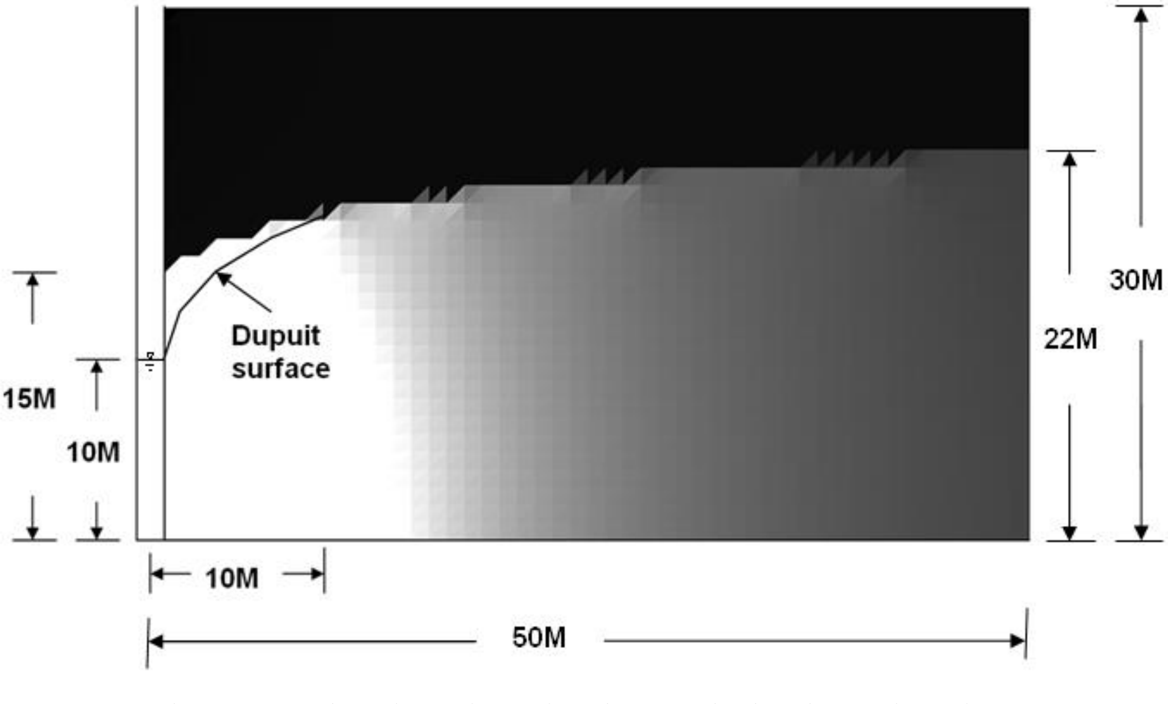

Figure 4-28 Phreatic surface of Bathe's method and Dupuit surface

Figure 4-28 gives the comparison of phreatic surface of Bathe's method and Dupuit surface, when radius r is larger than 10 meters, phreatic surface of Bathe's method and Dupuit surface are coincident. But when radius r is smaller than 10 meters, there is significant difference. On the boundary of the pumping well, Dupuit's surface connect with the water level in the well, but for the Bathe's method, there is leaking face on the boundary of the well, the height of which is 5 meters. In actual, the leaking face is formed along the free boundary surface.

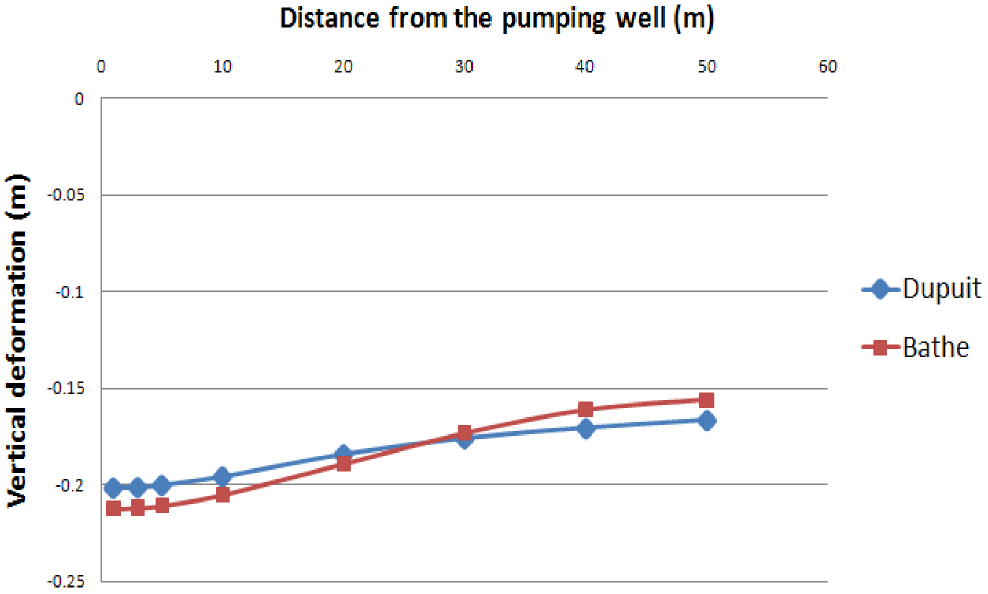

Figure 4-29 Deformation results of Dupuit's assumption and Bathe's method

The comparison of vertical deformation results from Dupuit's assumption and Bathe's method are shown in Figure 4-29. The two curves' changing trends are basically same. The average displacement of two curves exceeds 0.15m, and the values of displacement near the well are relatively larger. The tendency of the displacement curve is found to be related to the drawdown water level. The lower the drawdown water level, the larger displacement occurs. This tendency of simulation results is in accord with the actual condition well. But the curve of Dupuit's assumption is more smoothly.

4.3.3 Unsteady seepage model

In the unsteady seepage model, the Saturated-unsaturated theory has been considered. The effect of the capillary zone has been taken into account, which is much more realistic manner to simulate the groundwater seepage flow. The schematic of unsteady seepage model is shown in Figure 4-30. According to unsteady seepage theory, the position of free surface and overflow boundaries are also changed with time.

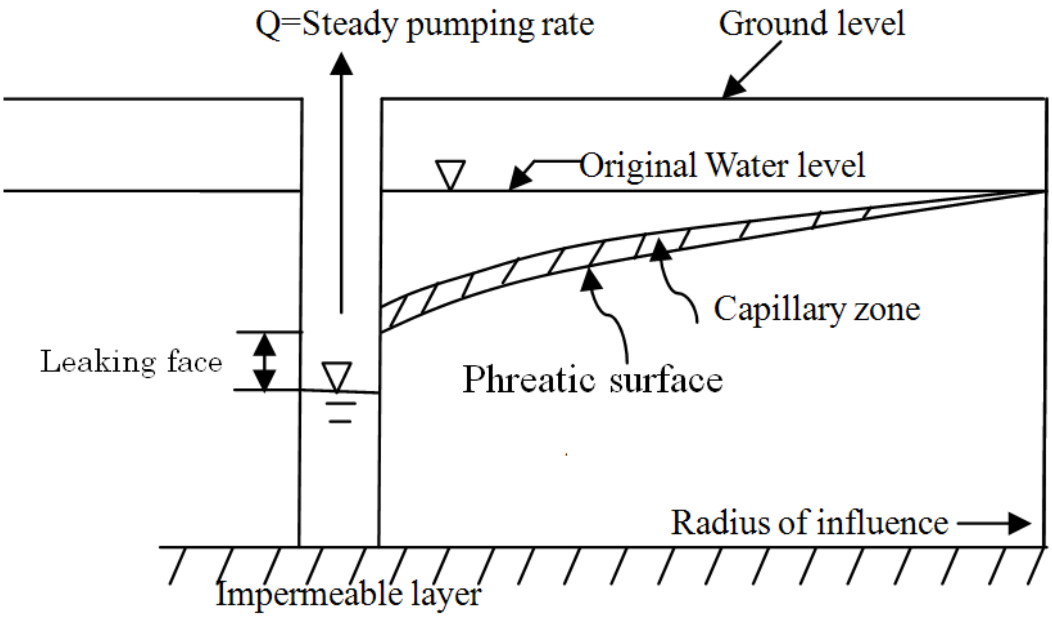

Figure 4-30 Schematic of unsteady seepage model

Because the position of phreatic surface and overflow boundaries are both unknown in advance, an iterative process is consequently required on each time step, it is a boundary nonlinear problem.

The Saturated-unsaturated theory divides the whole domain by phreatic surface into two parts, saturated region and unsaturated region. Because the phreatic surface and leaking face are both unknown at first, an iteration process for locating the phreatic surface and leaking face is needed on each time step.

According to the Van Genuchten model, the element coefficient of permeability in the unsaturated region has a relationship with the capillary pressure while keeps unchanged within the saturated region.

$$\mathrm{S_e} = \frac{\theta-\theta_r}{\theta_s-\theta_r} = (1 + |\alpha\Phi|^n)^{-m} \tag{5-1}$$

$$\mathrm{C}(\theta) = \alpha(n-1)(\theta_s-\theta_r)\mathrm{S_e}^{\frac{1}{m}}\left(1-\mathrm{S_e}^{\frac{1}{m}}\right)^m \tag{5-2}$$

$$\mathrm{K}(\theta) = \mathrm{K_s K_r} = \mathrm{K_s S_e}^{\frac{1}{2}}\left[1-\left(1-\mathrm{S_e}^{\frac{1}{m}}\right)^m\right]^2 \tag{5-3}$$

$$m = 1 - \frac{1}{n} \tag{5-4}$$

The relational expressions of Van Genuchten model $^{2)}$ are shown in Equation (5-1), (5-2), (5-3) and (5-4).

Where, Se is effective saturation

C(θ) is specific capacity

Φ is capillary pressure

K(θ) is coefficient of permeability in the unsaturated region

Ks is saturated permeable coefficient

Kr is relative permeable coefficient

$\theta$is volumetric moisture content ($\frac{V_w}{V}$)

$\theta_s$is residual volumetric moisture content

$\theta_r$is saturated volumetric moisture content

$\alpha, n, \theta_r, \theta_s, K_s$ are material parameters of Van Genuchten model

In this model, the coefficient of permeability Ks=0.036 m/h, elastic modulus E=1000Kpa, Poisson's ratio ν =0.3, $\alpha = 0.0079$, $\theta_s = 0.25$, $\theta_r = 0.153$, $n = 10.4$ are assumed 3)-4).

4.3.3.1 Outline of the model

For this model, the following basic assumptions are introduced into analysis:

(1) The ground water flow is laminar and governed by Darcy's law.

(2) Behaviors around the pumping well are assumed to be axisymmetrical, therefore cylindrical coordinates can be used, and the problem can be considered as a 2D one.

(3) The water molecules and soil particles can't be compressed and the stress-strain relationship of the soil is linear.

(4) The element coefficient of permeability variation in the unsaturated region obeys the Van Genuchten model while keeps unchanged within the saturated region.

For the calculation of coefficient of permeability, it is divided the affected area into two regions which is shown in Figure 4-31 and the changes of coefficient of permeability for region 1 and region 2 are shown below:

Region 1: saturated before pumping and unsaturated after pumping.

Region 2: saturated before and after pumping.

For saturated areas, the coefficient of permeability keeps unchanged ($K = K_S$), K_S is the saturated permeable coefficient.

For the unsaturated areas, the coefficient of permeability obeys the Van Genuchten model.

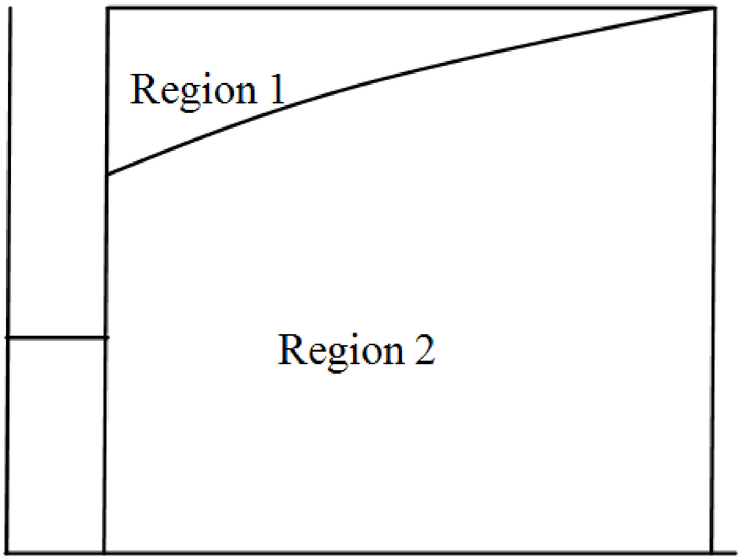

Figure 4-31 Regions for coefficient of permeability

Boundary conditions for water flow was shown in Figure 4-32, there are three kinds of boundary conditions.

(1) Border with constant water level, A1

At well border h=Hw

At radius influence h=He

where, He is original water level, Hw is the water table in the well.

(2) Impervious layer, A2

$$\frac{\partial h}{\partial z} = 0$$

(3) Leaking face at the well border, Hs

At well border h=Z

where, Z is elevation.

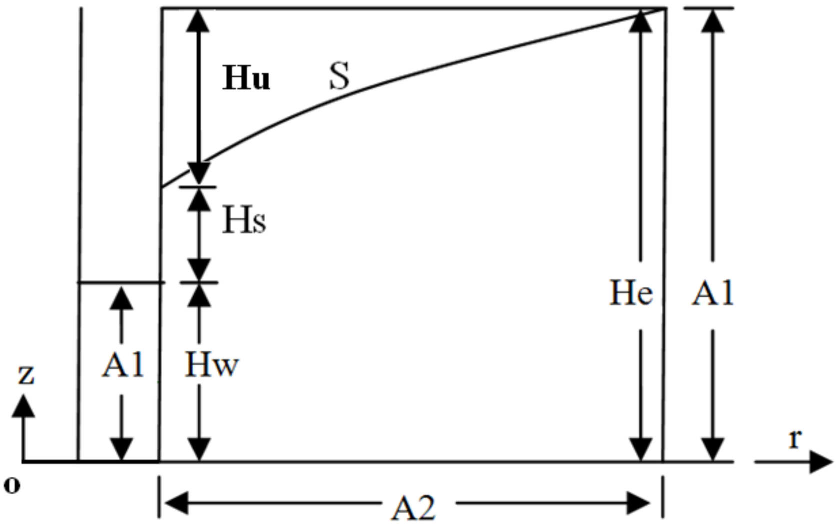

Figure 4-32 Boundary conditions for seepage

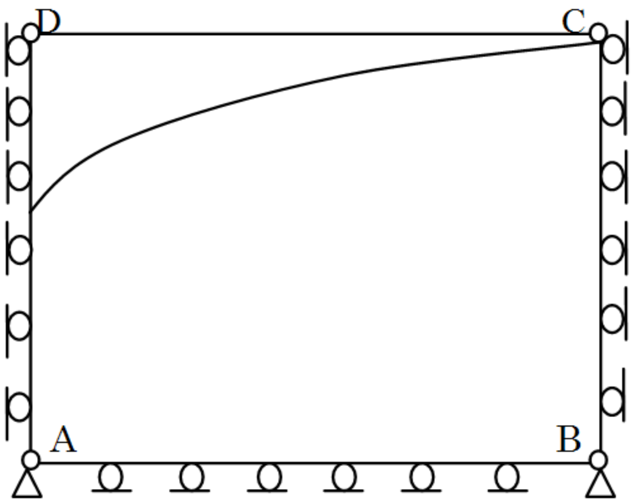

Figure 4-33 Boundary conditions for soil deformations

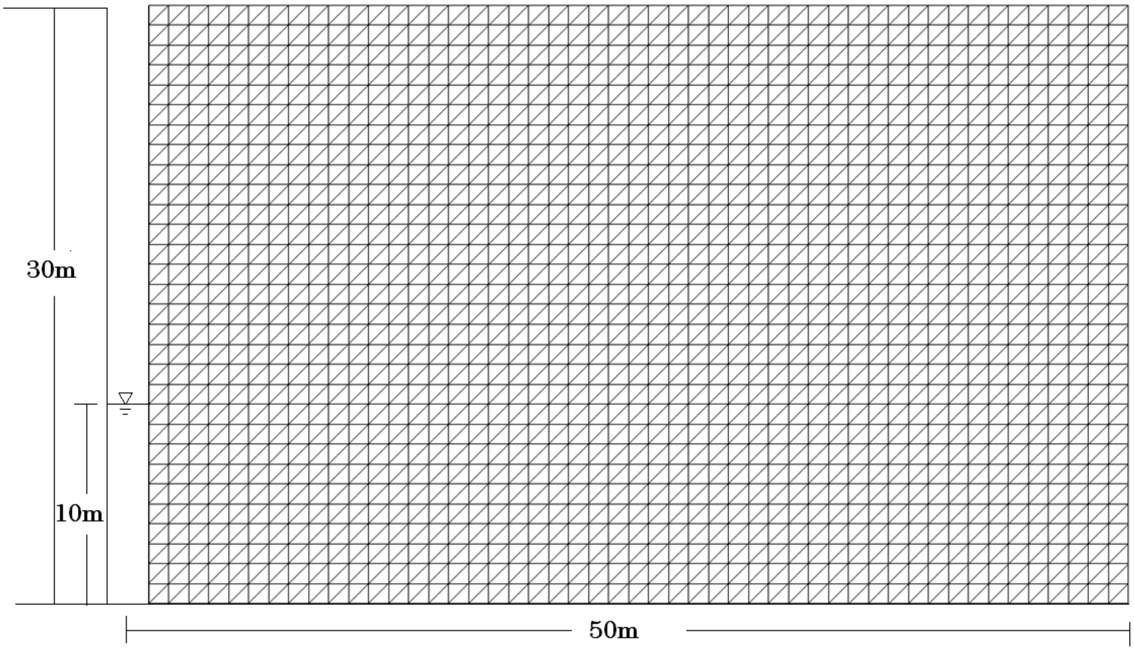

Figure 4-34 Cross-section for finite element mesh

In Figure 4-33, the boundary conditions used to calculate soil deformation are given. At the border of the well and radius influence (boundary AD and BC), only vertical deformations are permitted. At the bottom layer, (boundary AB), only horizontal deformation is allowed. And the point A and B are restricted in both vertical and horizontal directions.

The seepage flow due to single pumping well can be considered an axisymmetrical flow, and the domain is divided into a network of concentric rings of triangular cross-section elements. The elements had been divided smaller in order to improve the accuracy of calculation. The finite element mesh is shown in Figure 4-34. The phreatic surface and leaking face are both unknown at first, so an iteration process for locating the phreatic surface and leaking face is needed on each time step, which is shown in section 3.3.1(Equation 3-28 and Equation 3-29). In the iteration process, the boundary of leaking face is variable in the loop computing. The nodes on the boundary are divided into two parts, permeable boundary (Hs and Hw) and impermeable boundary (Hu), which is shown in the Figure 4-32. If the head h of node is smaller than its elevation z, the node will be considered as impermeable boundary (Hu) in the next iteration step. On the contrary, if the head h is larger than elevation z, the node will be considered as permeable boundary (Hs) in the next iteration step, this process is continually conducted until convergent result get. When the result is convergent, the phreatic surface (Curve S in Figure 4-32) can be fixed with the condition of h=z.

4.3.3.2 Numerical prediction

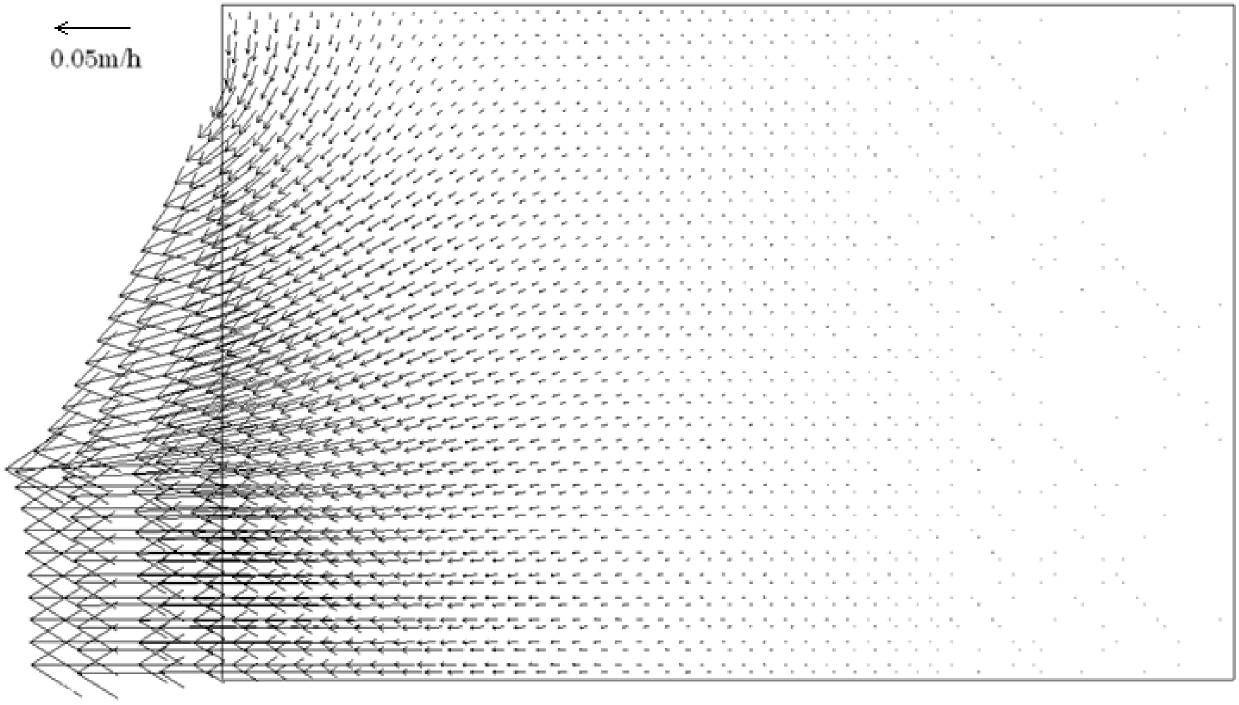

Figure 4-35 (a) Flow velocity distribution when T=0.5 hour

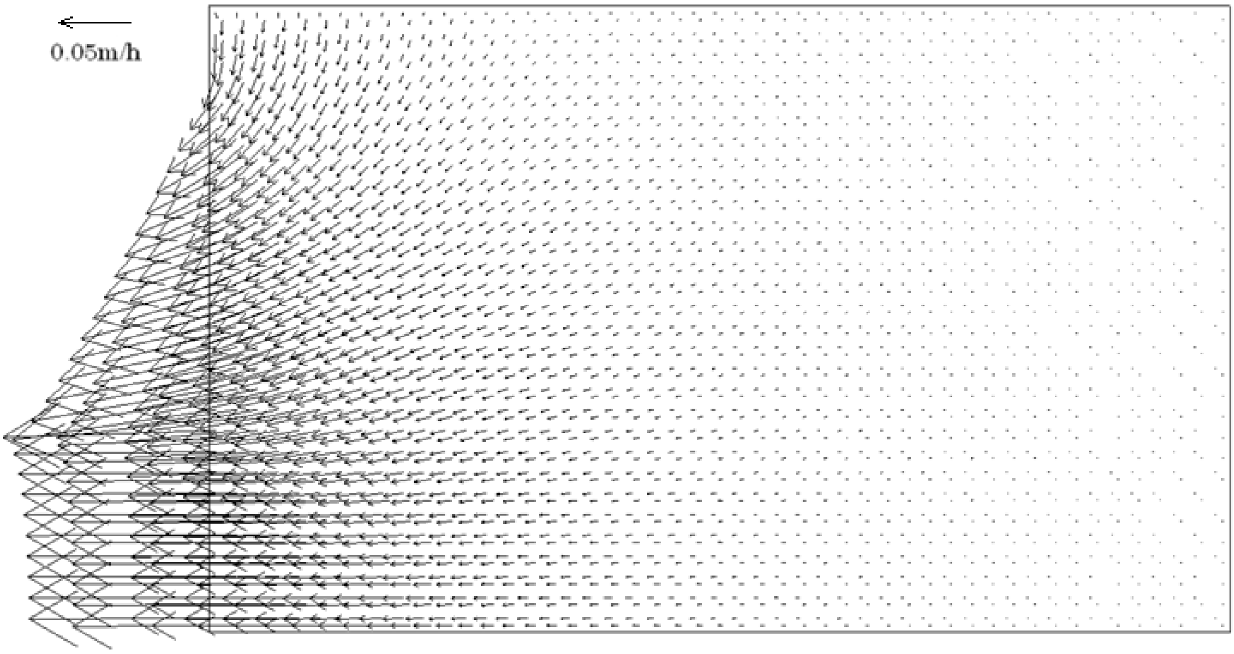

Figure 4-35 (b) Flow velocity distribution when T=1 hour

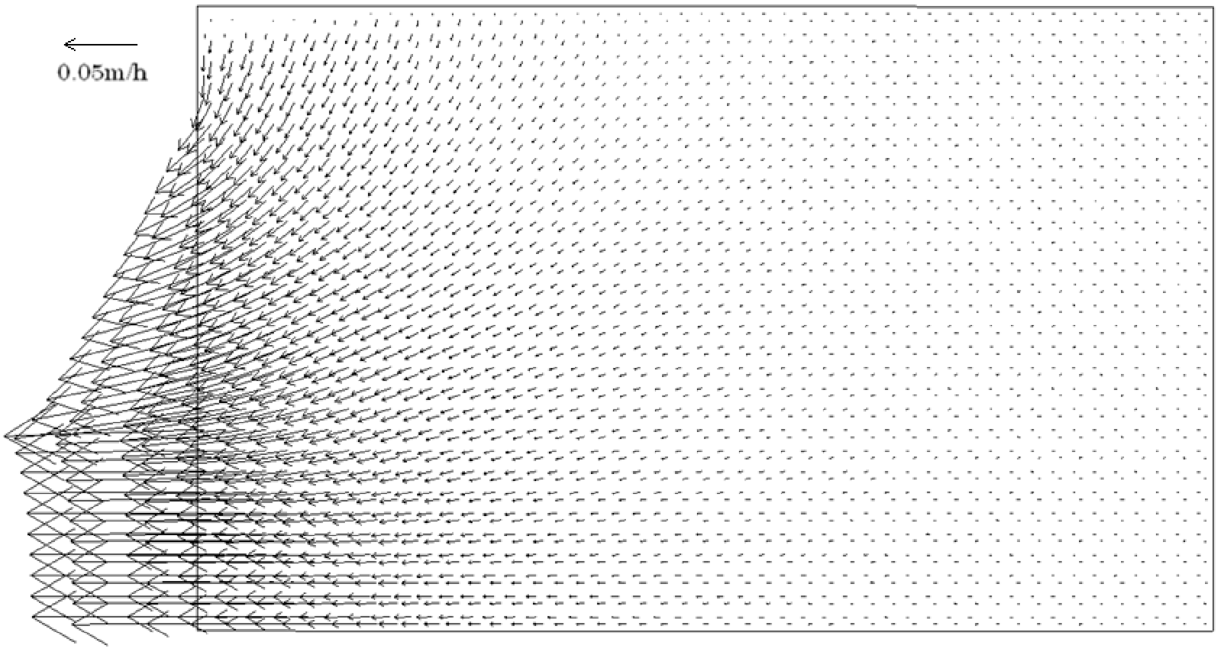

Figure 4-35 (c) Flow velocity distribution when T=5 hour

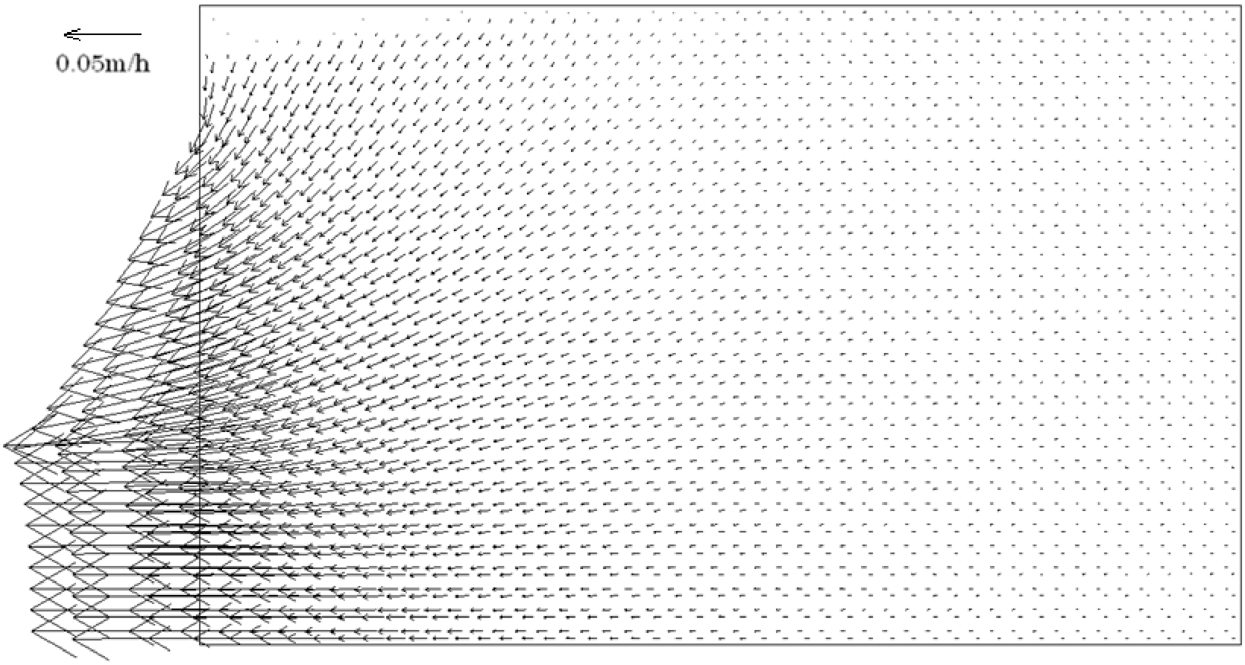

Figure 4-35 (d) Flow velocity distribution when T=10 hour

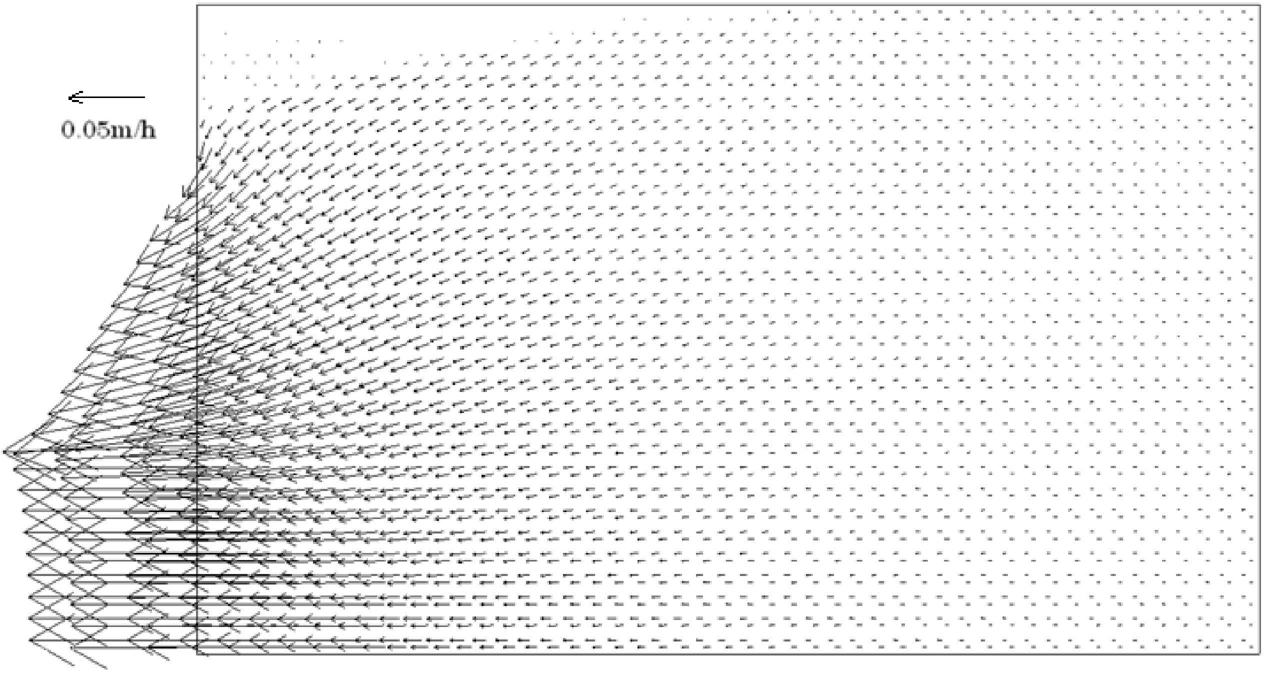

Figure 4-35 (e) Flow velocity distribution when T=50 hour

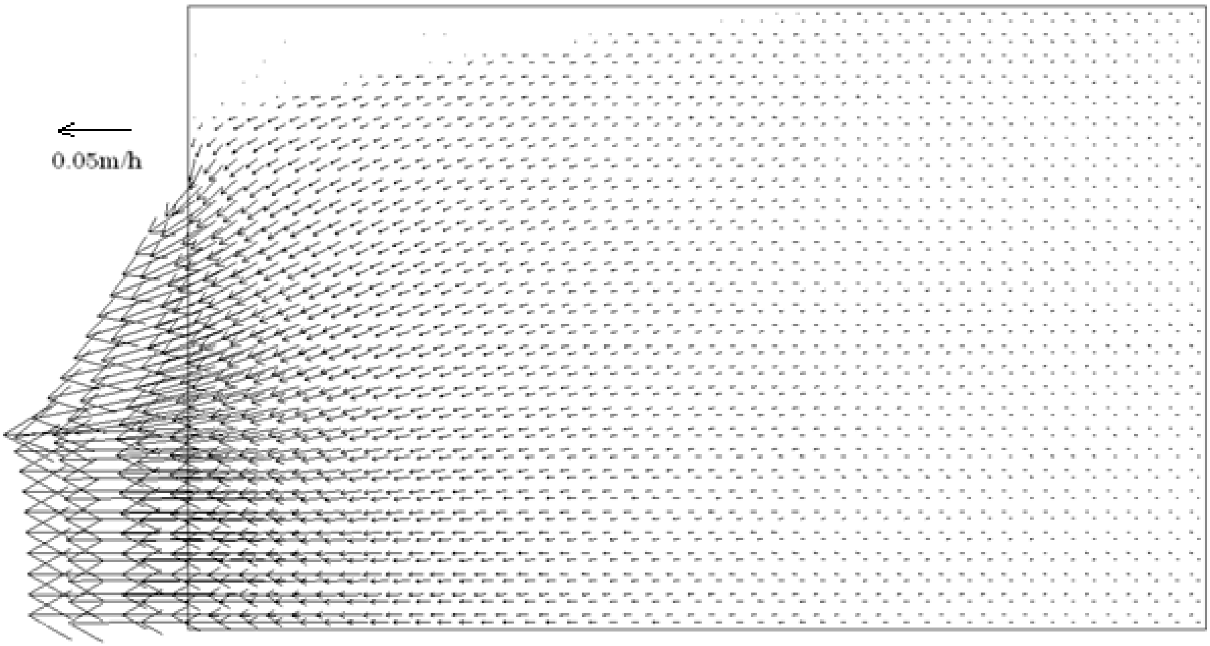

Figure 4-35 (f) Flow velocity distribution when T=100 hour

Calculated result of water flow from the numerical modeling is basically matched with theoretical value and the flow velocity distribution is shown in Figure 4-35(a)-(f). As shown, flow rate near the pumping well is larger than 0.1m/h, which is match with the Dupuit's steady seepage model and Bathe’s method. And the flow rate decreases gradually with increasing distance from the well.

Figure 4-35 (a)-(f) gives the flow velocity distributions from T=0.5 hour to T=100 hours. With the time proceeding, unsaturated zone becomes larger and the flow velocity distribution in unsaturated zone becomes smaller. When T=100 hour, the seepage flow becomes almost steady flow.

Here, a numerical prediction of the Bathe’s model under the same boundary conditions has been conducted for comparing with the numerical prediction of the unsteady seepage model.

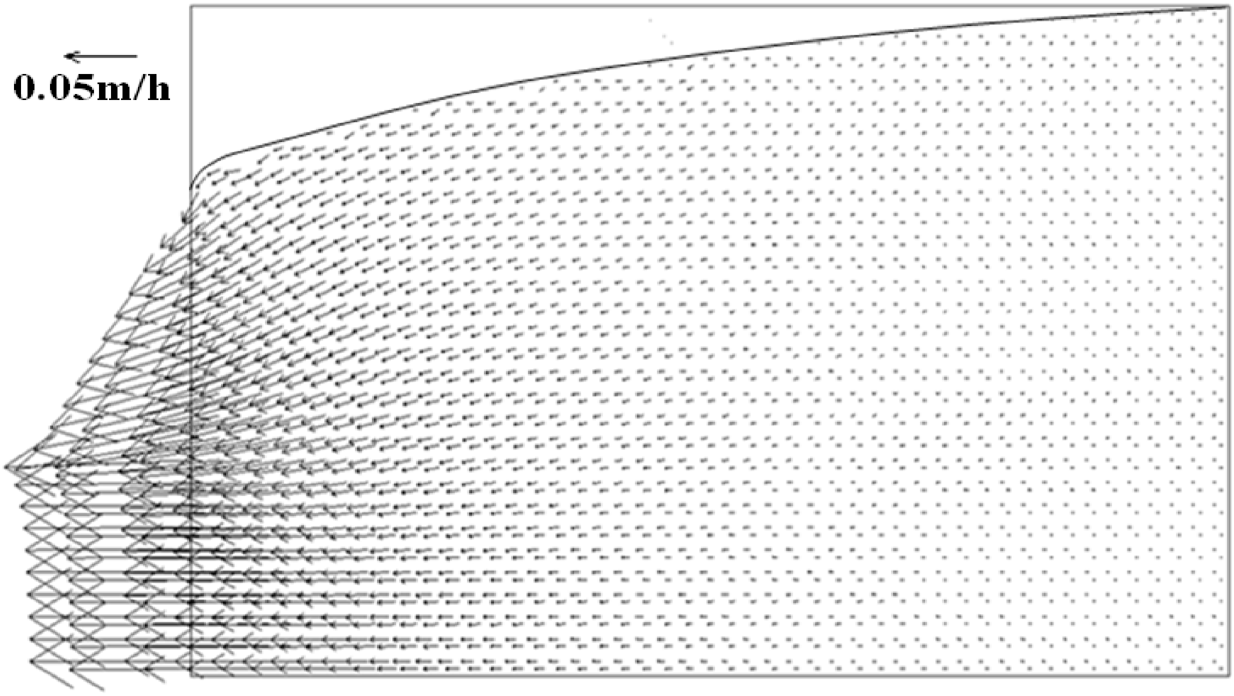

Figure 4-36 (a) Flow velocity distribution of Bathe’s method

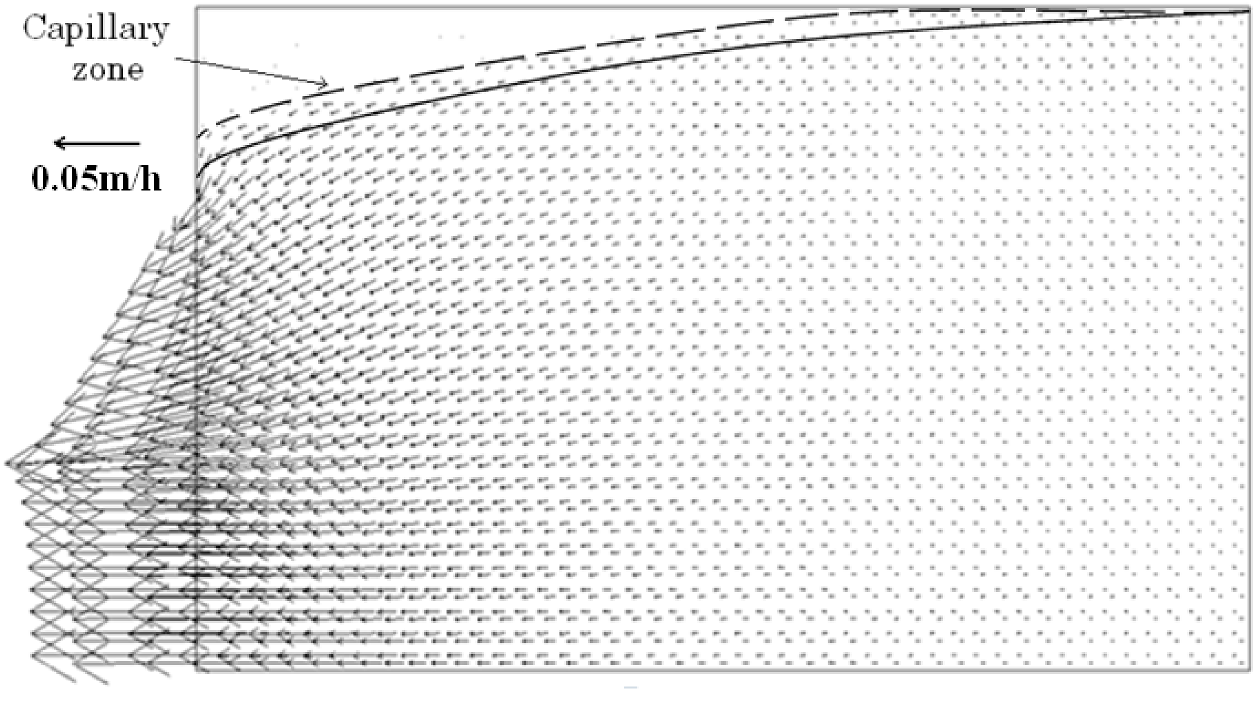

Figure 4-36 (b) Flow velocity distribution of unsteady seepage when T=100h

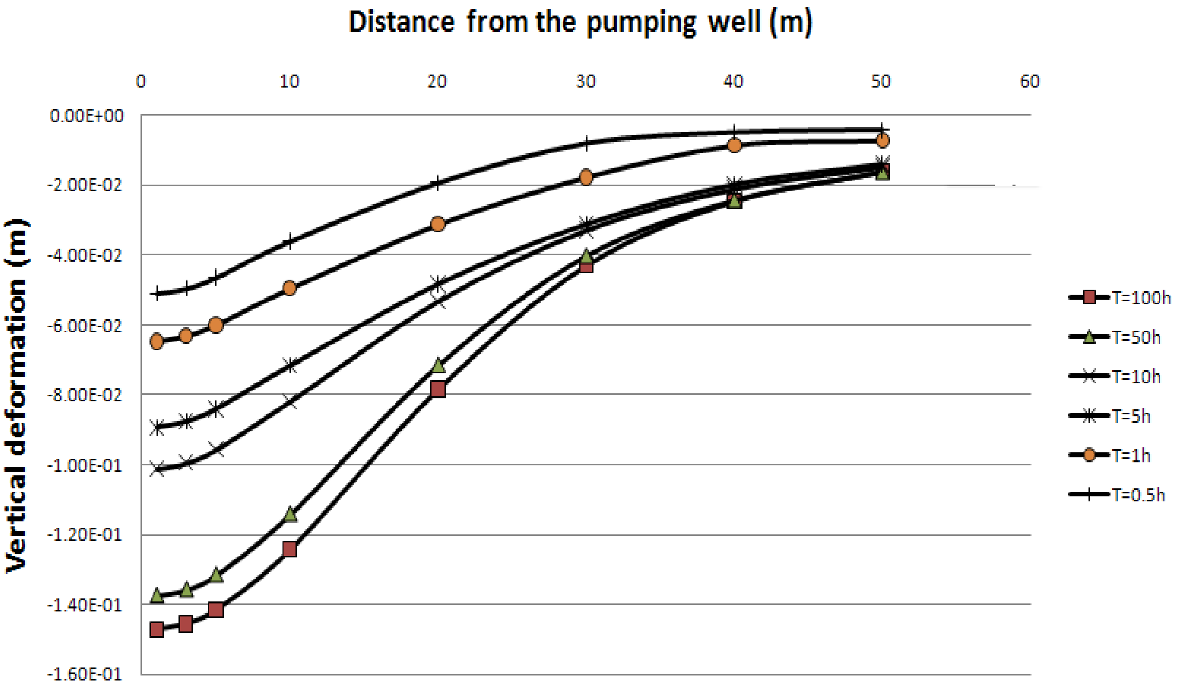

Figure 4-37 Vertical deformation results of unsteady seepage model

Figure 4-36 gives the flow velocity distribution of two models. For the unsteady seepage model, when T=100 hours, the seepage flow becomes almost steady flow. The results shows that the locations of phreatic surface from two models are basically same and the velocity distribution of two models are essential consistent. But for the unsteady seepage model, there isa capillary zone, the height of which is approximately 2 meters and the seepage flow in the unsaturated zone obviously existed, which is shows that the effect of capillary zone plays an extremely important role in the seepage field.

The vertical deformation results of unsteady seepage model have been shown in the Figure 4-37. The settlement rate is relatively quicker when pumping time is smaller than 10 hours and gradually got slower when pumping time is larger than 10 hours, which match well with the dropping rate of the phreatic surface.

The deformation results of Bathe's model and unsteady seepage model have been given in Figure 4-38. Here, the deformation result of unsteady seepage model comes form at T=100 hours.

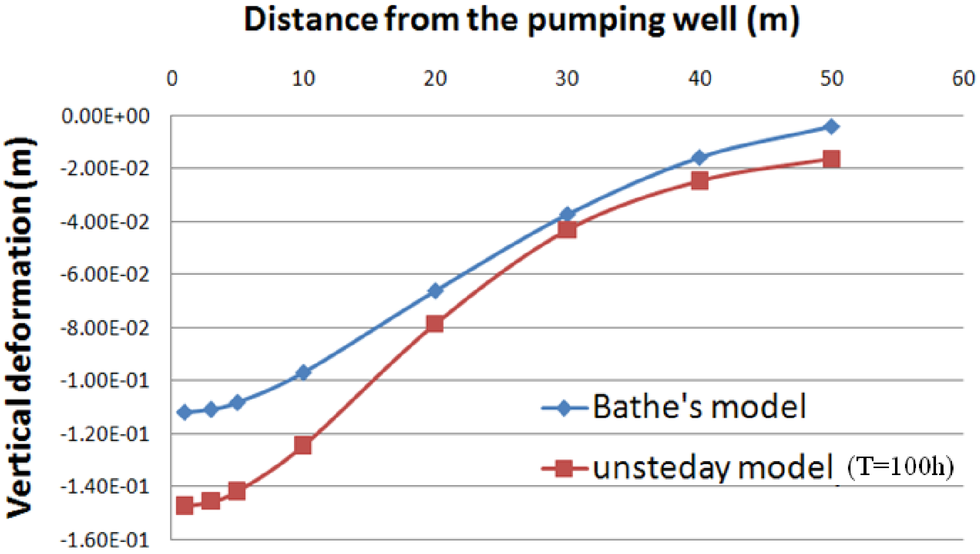

Figure 4-38 Vertical deformations of bathe model and unsteady model

The two curves' changing trends are nearly same and the values of displacement by unsteady model are relatively larger. The tendency of the displacement curve is found to be related to the drawdown water level. The lower the drawdown water level, the larger displacement occurs. This tendency of simulation results is in accord with the actual condition well.

But the deformation result of unsteady seepage model is generally larger the Bathe's model's, especially when radius r is smaller than 10 meters. This is because the effect of capillary zone wasn't considered in the Bathe's model. The results of unsteady seepage model shows that the height of capillary zone is approximately 2 meters and the seepage flow in the unsaturated zone obviously is existed. When the radius r is smaller than 10 meters, the effect of seepage force in the capillary zone becomes larger because of the higher seepage velocity, which leads to the higher vertical deformation. The comparison of Bathe's model and unsteady seepage model shows that the effect of capillary zone plays an extremely important role in the seepage field.

4.4 Summary and discussions

This chapter discusses the developing process of seepage numerical analysis in detail and several methods common in use were introduced, including Dupuit's assumption, Bathe method, and Saturated-unsaturated theory. Numerical predictions which correspond to the single pumping well models by using different methods have been compared under axi-symmetrical FEM theory mentioned in previous chapter.

Comparison of phreatic surface of Bathe's method and Dupuit surface were conducted. Results shows that when radius r is larger than 10 meters, phreatic surface of Bathe's method and Dupuit surface are coincident, but when radius r is smaller than 10 meters, there is significant difference. On the boundary of the pumping well, Dupuit's surface connect with the water level in the well, but for the Bathe's method, there is leaking face on the boundary of the well. In actual, the leaking face is formed along the free boundary surface.

The prediction results of Bathe's method and Saturated-unsaturated method are also been discussed. The results shows that the locations of phreatic surface from two models are nearly same and the velocity distribution of two models are essential consistent. But for the unsteady seepage model, there is a capillary zone, the height of which is approximately 2 meters and the seepage flow in the unsaturated zone obviously existed, which is shows that the effect of capillary zone plays an extremely important role in the seepage field. The deformation result of Saturated-unsaturated seepage model is generally larger the Bathe's model's, especially when radius r is smaller than 10 meters. This is because the effect of capillary zone isn't considered in the Bathe's model, and the seepage velocity is relatively larger in the unsaturated zone near the pumping well. Chapter 5 will deal with excavation models and numerical prediction by using three-dimensional theory.

Reference

1) GUAN Ming-fang: Review of solution methods of seepage free surface of slope, Journal of Chongqing Jiaotong University, (2005). (In Chinese)

2) M. TH. Van Genuchten: A Closed-from Equation for Predicting the Hydraulic Conductivity of Unsaturated Soils, (1980) Soil Sci. Soc. Am. J. 44:892-898.

3) Takeshi KODAKA: Estimation of the safety of river embankment using an unsaturated seepage-deformation coupled analysis, (2005) The 50th Geotechnical Engineering Symposium. (In Japanese)

4) Mssahiko SAITO: Numerical Study on Fingering Flow in Non-uniform Porous Media. (In Japanese)

CHAPTER 5

EXCAVATION MODELS AND NUMERICAL PREDICTION

5.1 Introduction

Excavation is one of the most common engineering works in ancient construction as well as in today's civil engineering projects. One of the major concerns for many excavation projects is the ground displacement generated around the excavated zone. By the groundwater surface lowering, the effective stress in the soil increases and this causes an additional ground settlement. Furthermore, it is necessary to consider the effects of seepage force in calculating ground displacement field, especially under unsteady seepage flow condition. In recent years, with the rapid development of computer technology and FEM, ground behavior due to seepage flow of groundwater has been more emphasized heavily 1-3). In this chapter, several cases of 3D analysis are made on the ground behavior around the excavation due to seepage of groundwater.

5.2 Elastic deformation model under steady seepage condition

In the last two decades, with the economy growing at a fast pace, utilizing underground space has become a new focus for municipal development, since tall buildings, underground stores and subways are concentrated in the downtown of the city, roads, structures, underground pipelines and etc. are crowded around the excavation work. During the deep excavation of foundation pit, due to the great variation of groundwater level, the huge head fall could result in drastic seepage flow of the ground water, which will bring about a full influence on the deformation on the surrounding structures in a large-scale area, buildings, pipes and roads tend to buckle and crack because of the displacement of the ground, therefore, the circumjacent environment conditions of deep excavation are growing severe [4,5)].

5.2.1 Outline of the model

This analysis shows that horizontal deformation caused by seepage flow plays a very important role in deformation field, which may lead to toppling behavior to the foundation of high-rise buildings.

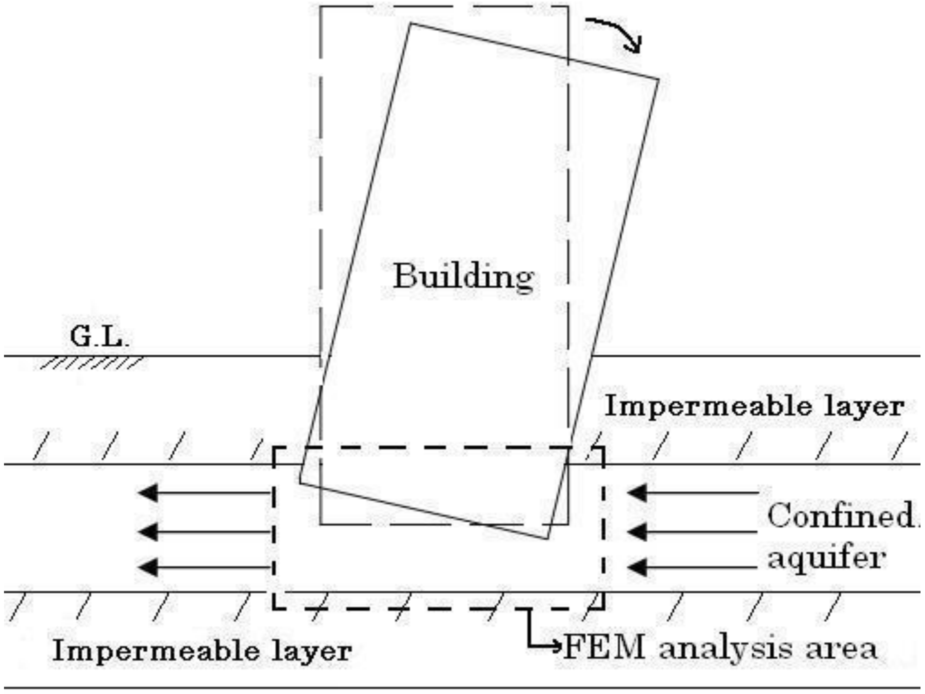

Figure 5-1 Schematic of toppling behavior due to seepage flow

Figure 5-1 shows the schematic of foundation behavior due to seepage flow in two dimensions. The FEM analysis area is shown in the figure. In this model, the following basic assumptions are introduced into analysis:

1. The ground water flow is laminar and governed by Darcy's law.
2. The water molecules and soil particles can't be compressed and the stress-strain relationship of the soil is linear.
3. The coefficient of permeability K, elastic modulus E and Poisson's ratio ν are shown in Table 5-1 for common sand.

Table 5-1 Material constants

K	E	ν
0.036[m/h]	1000 [KN/m^2]	0.3

5.2.2 Simple test model

In order to validate the correctness of the programming, a simple test model under considering seepage force has been tested which is shown in Figure 5-2. The size of the model is 20m×10m×10m with two 20-nodal cubic elements.

Boundary conditions for seepage flow are given as below:

On plan ABCD: total head H=10m

On plan EFGH: total head H=20m

Boundary conditions for displacement are given as below:

On plan ABCD: displacement in X direction has been restricted. On plan BCGF: displacement in Y direction has been restricted.

On plan DCGH: displacement in Z direction has been restricted.

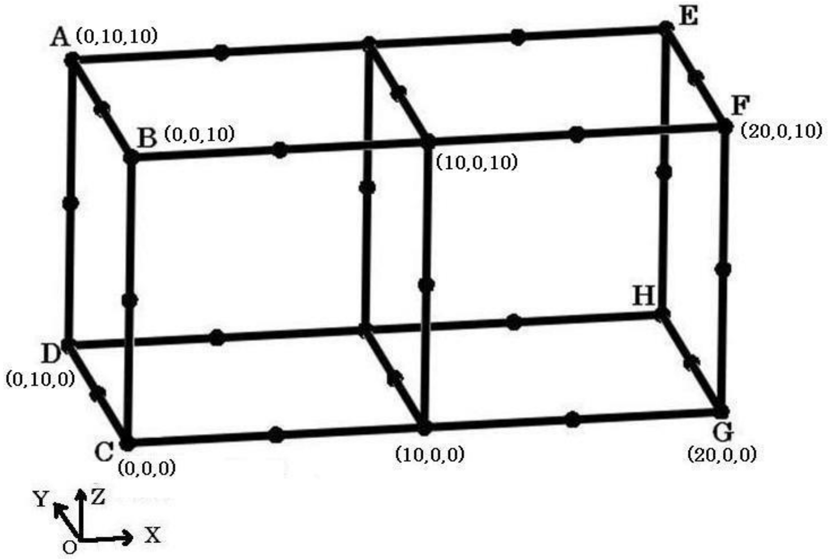

Figure 5-2 Schematic of test model

According to the deformation theory, Equation (5-1) can be given as below, and the general solution of Equation (5-1) is shown in Equation (5-2). Here *Fx* is the seepage force due to groundwater in X direction, *i* is the hydraulic gradient, *L* is the distance of the model in X direction and γ_w is the unit weight of groundwater.

$$\frac{d^2u}{dx^2}E + Fx = 0 \tag{5-1}$$

$$Fx = i\,\gamma_w = -\frac{\partial h}{\partial x}\gamma_w$$

$$u + \frac{i\gamma_w}{2E}x^2 + C_1x + C_2 = 0 \tag{5-2}$$

$$C_1 = \frac{i\gamma_w}{2E}L\,,\quad C_2 = 0 \qquad (5\text{-}3)$$

According to the boundary conditions, C_1 and C_2 can be derived which are shown in Equation (5-3)

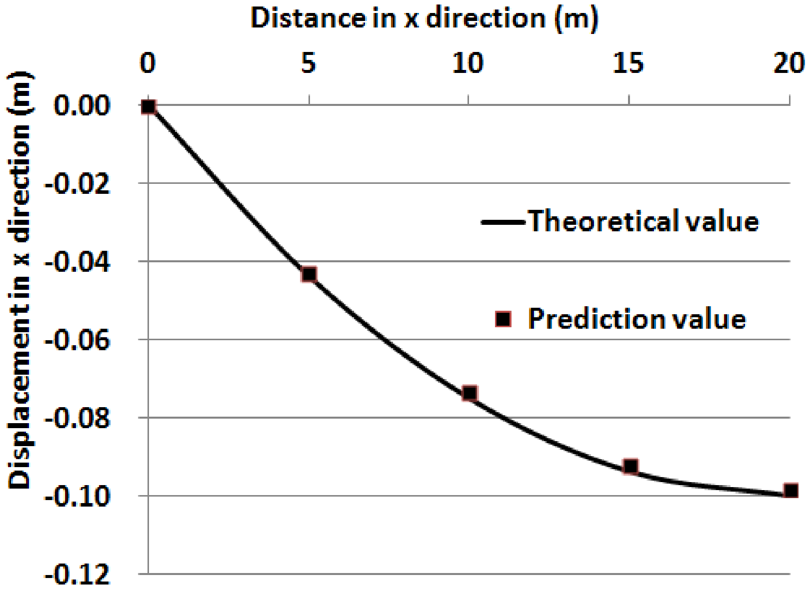

Figure 5-3 Theoretical and predication values

The numerical prediction results and theoretical displacement values had been given in Figure 5-3. From the test model results, it can make sure that the programming is valid.

5.2.3 Numerical prediction of the toppling behavior model

Half of the domain has been selected for calculating easily, which is shown in Figure 5-4. ABFE is the center section of the whole domain. The size of the model is

50m×20m×20m and the size of foundation is 10m×6m×10m. The simulated domain is divided into 2500 cubic elements. The foundation has been considered as a rigid body and elastic modulus E of which has been given a very large value.

Boundary conditions for seepage flow are given as below:

On plan ABCD: total head H=10m

On plan EFGH: total head H=20m

Boundary conditions for displacement are given as below:

On plan ABCD: displacement in X direction has been restricted.

On plan ABFE: displacement in Y direction has been restricted.

On plan ADHE: displacement in Z direction has been restricted.

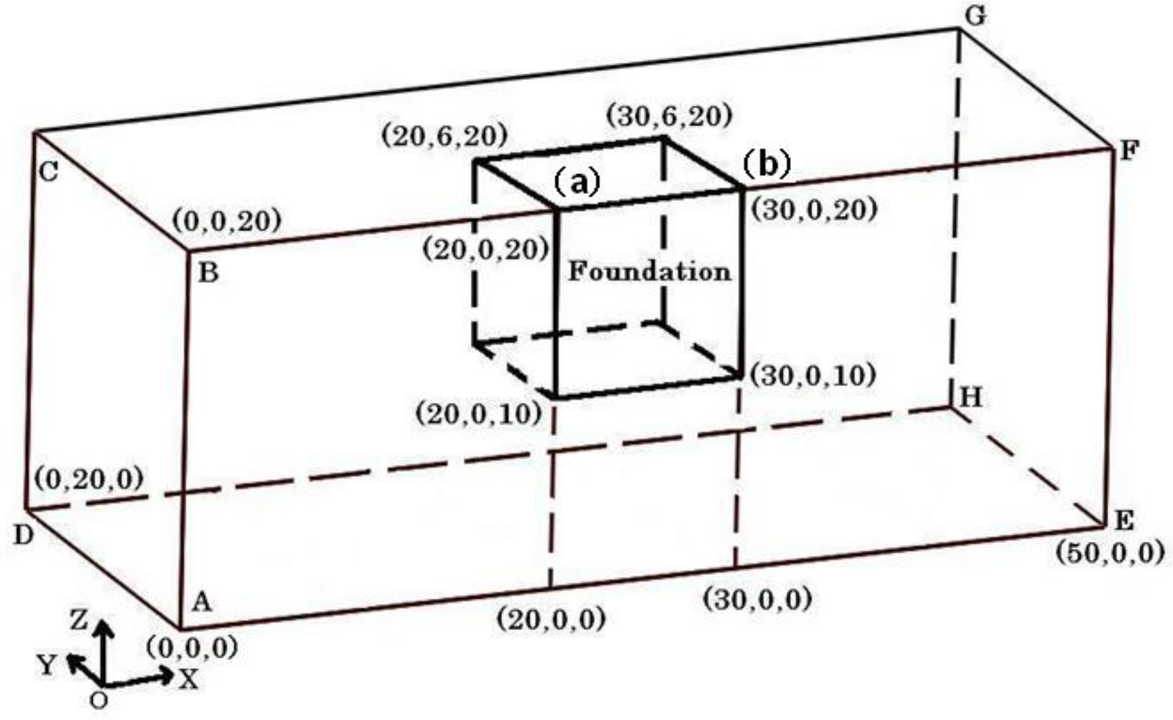

Figure 5-4 Schematic of toppling behavior model

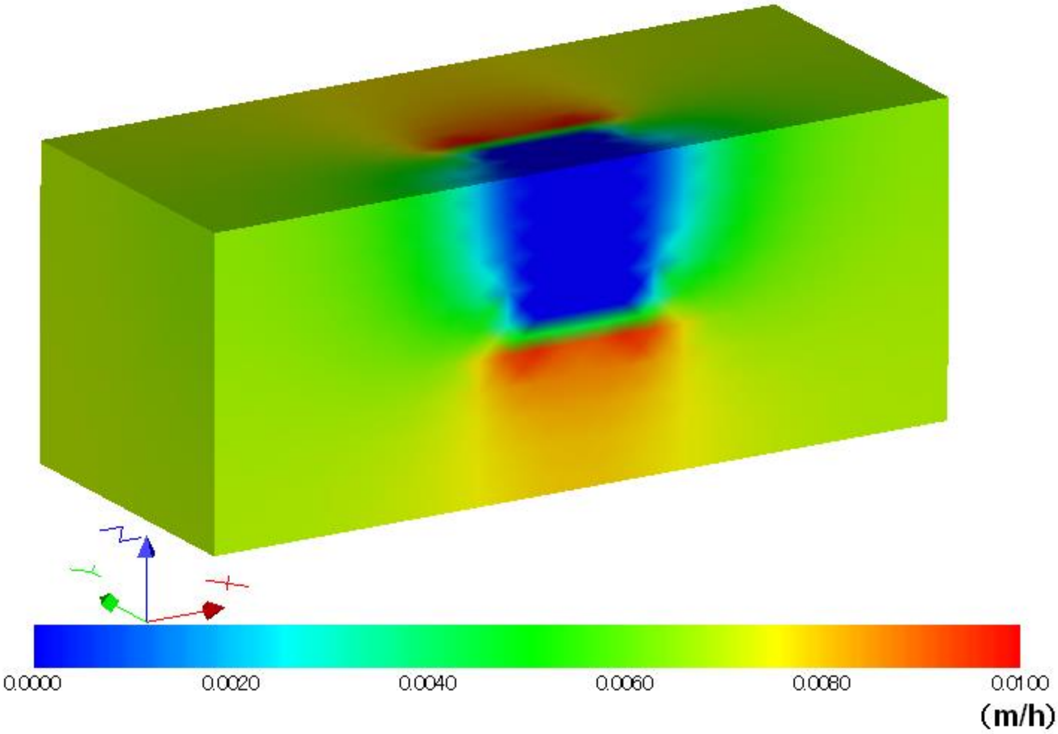

Figure 5-5 Composite flow velocity distribution

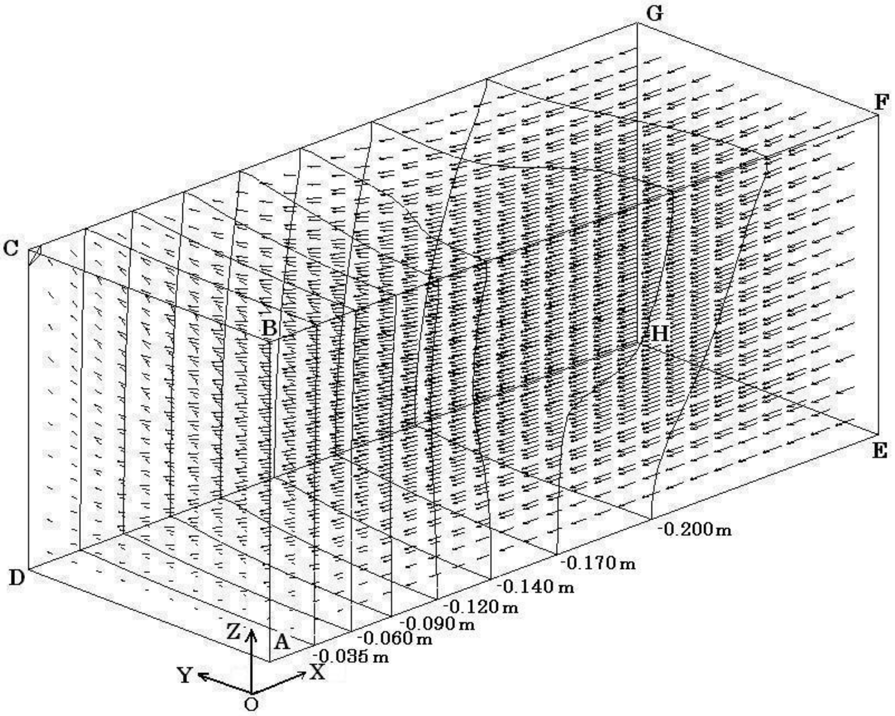

Figure 5-6 Displacement distribution

The numerical prediction results of flow velocity distribution are shown in Figure 5-5. The seepage velocity near the bottom and the back side of the foundation is quite larger than the other area, where the value of seepage velocity is near 0.01 m/h. At near the two sides of the foundation in X direction, the flow velocity is quite small due to the effect of the foundation which is impermeable.

The numerical prediction results of displacement distribution are shown in Figure 5-6 and Figure 5-7. As shown in Figure 5-6, the arrows represent the directions of the displacement and the longer of the arrow is the larger displacement it represents.

The equi-displacement surfaces in X direction also be given in the Figure 5-6, the changing rates of equi-displacement surfaces is larger when X is smaller than 20m and becomes smaller when X is larger than 30m. The equi-displacement surfaces seem regular when X is smaller than 20m and have been seriously twisted when X is larger than 20m.

The phenomenon of differential displacement occurs around the foundation, and the displacement of ground near the foundation bottom is quite larger than other parts on the parallel section of YOZ plan. As shown in Figure 5-7, when X is larger than 25m, the displacement values become larger with decreasing of elevation Z on each parallel section of YOZ plan. The differential settlement comes from both sides ((a) and (b) in Figure 5-4) of foundation is 0.01244m, and the rotation angle of foundation is 1.2/1000 rad.

This numerical prediction shows that the distribution of seepage velocity around foundation is quite different. The seepage velocity near the bottom and the back side of the foundation is quite larger than the other zones, whereas velocity is quite small at near the two sides of the foundation in x direction which are impermeable. The changing rates of seepage velocity become smaller with increasing distance from the zone of foundation.

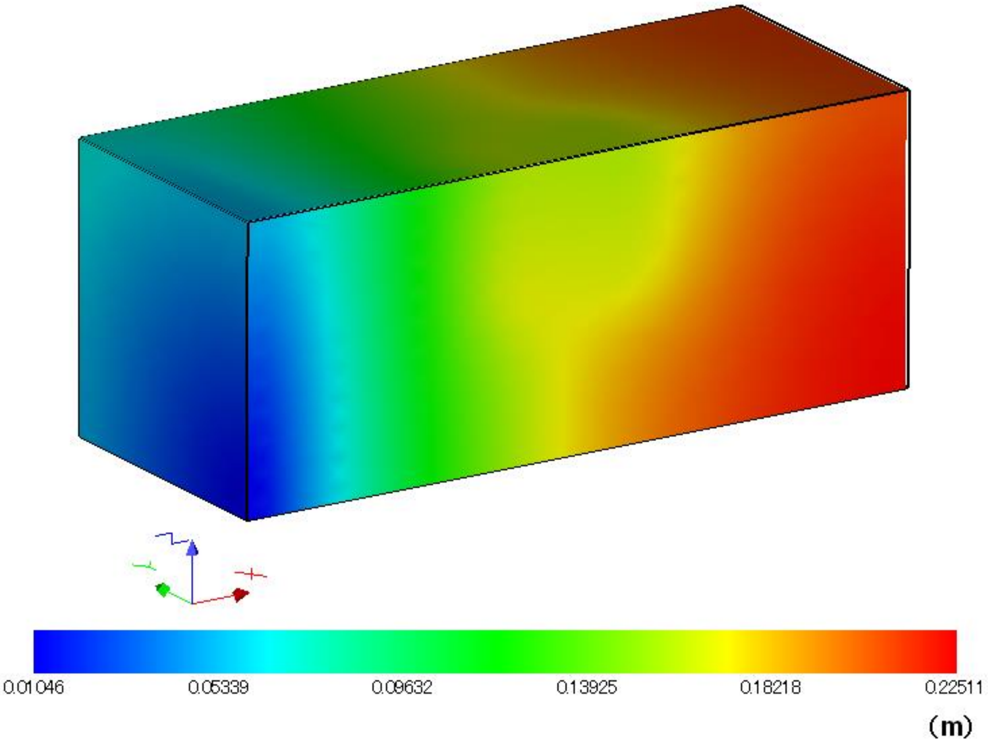

Figure 5-7 Composite displacement distribution

The phenomenon of differential displacement occurs around the foundation. The displacement of ground near the foundation bottom is quite larger than other parts on the parallel section of YOZ plan.

The analysis shows that horizontal deformation caused by seepage flow plays a very important role in deformation field around the foundation. The differential displacement may occur around foundation, which can lead to toppling behavior to the foundation and the pipes and roads near the foundation may tend to buckle and crack because of the displacement of the ground. Therefore it is necessary to consider the effect of the seepage flow of groundwater when the dewatering of excavation design is made, especially in the case of high-rise buildings surrounded.

5.3 Elastic deformation model under unsteady seepage condition

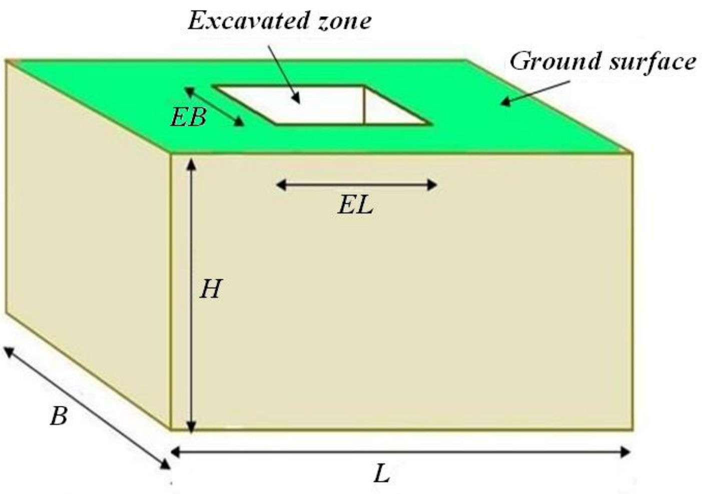

Figure 5-8 Schematic of 3D excavation

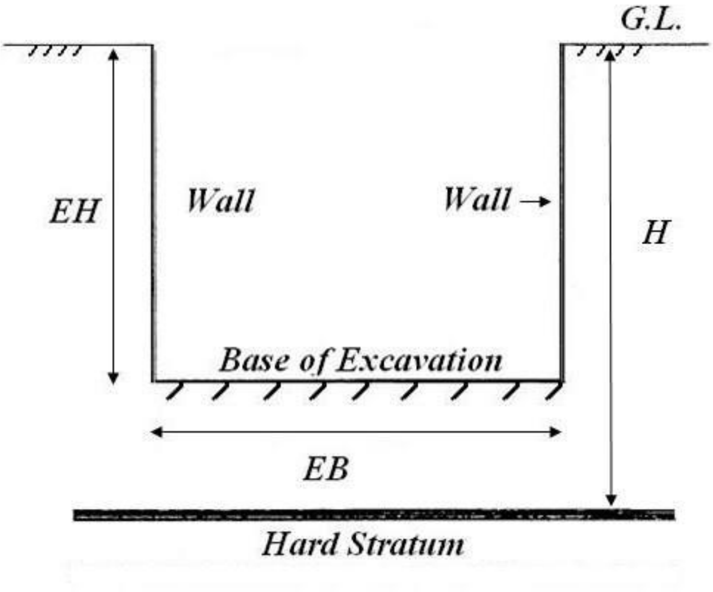

Figure 5-9 Elevation

Figure 5-8 shows the schematic of 3D excavation and Figure 5-9 gives the elevation of the excavation, where EL, EB and EH are the length, width and depth of the excavation respectively. In this analysis case for the purpose of saving computing time and storage space, a quarter of the whole field has been selected as analytical field because of symmetry, which is shown in Figure 5-10.

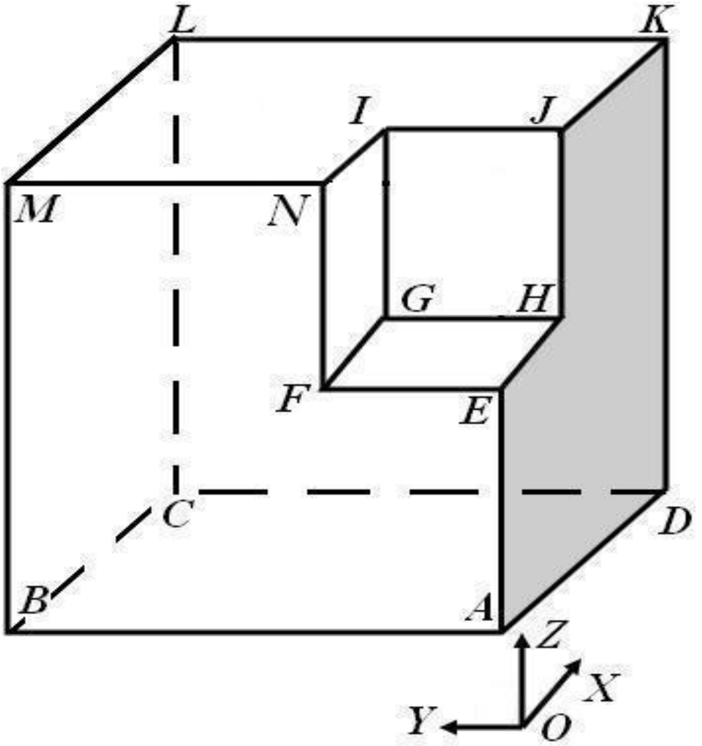

Figure 5-10 FEM analytical field

5.3.1 Outline of the model

In this model, the following basic assumptions are introduced into analysis:

(1) The ground water flow is laminar and governed by Darcy's law.

(2) The water molecules and soil particles can't be compressed and the stress-strain relationship of the soil is linear.

(3) The coefficient of permeability variation in the unsaturated region obeys the VG model [6), while keeps unchanged within the saturated region. The coefficient of permeability K, elastic modulus E and Poisson's ratio υ, and the material parameters of VG model α, θs, θr, n are shown in Table 5-2 for common sand.

Table 5-2 Material constants

K (m/h)	E (kN/m^2)	ν	α	θs	θr	n
0.036	1000	0.3	0.0079	0.25	0.153	10.4

The size of the model is 15m×15m×8m and the size of excavation is 5m×5m×5m. A quarter of the whole field has been selected as analytical field for the purpose of saving computing time and storage space which is shown in Figure 5-10.

Boundary conditions for seepage flow are given as below:

On plan EFGH: total head H=3m, on plan CDKL: total head H=8m and on the plan CBML: total head H=8m.

Boundary conditions for displacement are given as below:

On plan ABCD: displacement in Z direction has been fixed, on plan IJHG and ABMNFE: displacement in X direction has been fixed, on plan IGFN and ADKJHE: displacement in Y direction has been fixed.

5.3.2 Numerical prediction

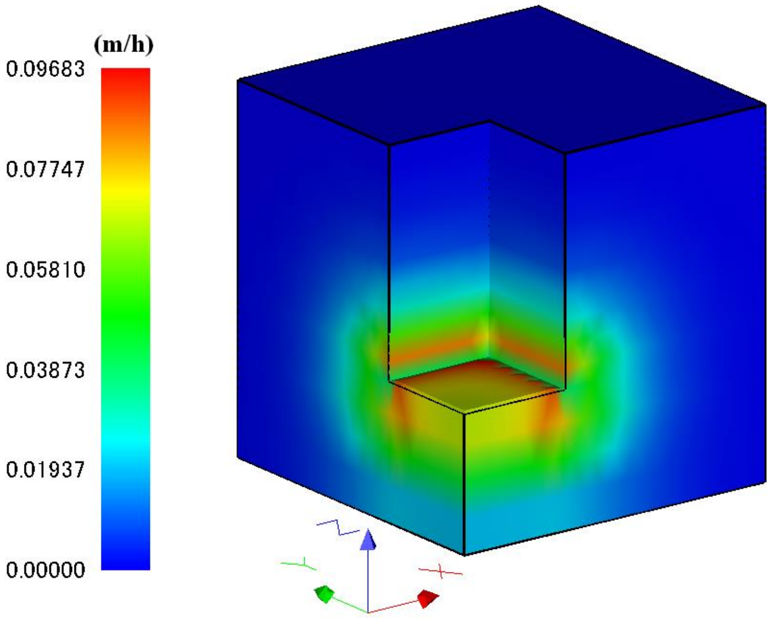

Figure 5-11 Composite Flow velocity distribution (T=0.5h)

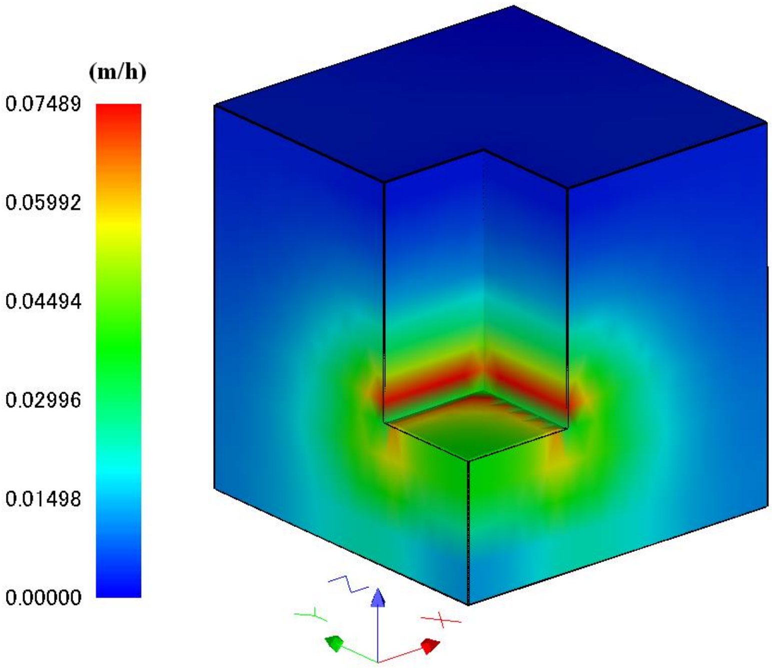

Figure 5-12 Composite Flow velocity distribution (T=2h)

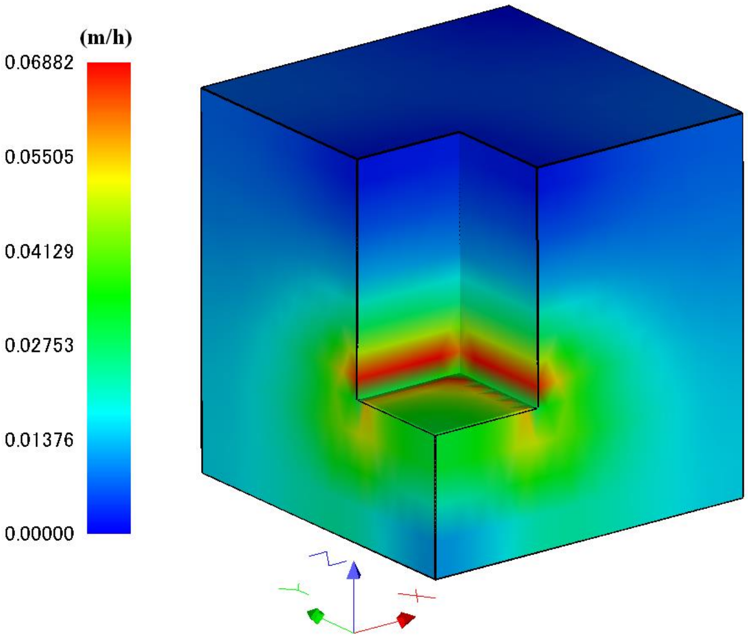

Figure 5-13 Composite Flow velocity distribution (T=15h)

Calculated results of seepage flow are shown in Figure 5-11 (T=0.5 hour), Figure 5-12 (T=2 hours) and Figure 5-13 (T=15 hours). The maximum velocity zone appears around the bottom of the excavation in all the time. The peak value of velocity near the excavation bottom is almost 0.1m/h in Figure 5-11 (T=0.5h), and decreases gradually with time proceeding in Figure 5-12 (T=2h) and Figure 5-13(T=15h). In the early stage of seepage field, when T=0.5 hour, the seepage-affected area is not full-field. The seepage flow is unsteady, the seepage flow far from the excavation is nearly zero, and high velocity zone comes from the bottom of the excavation (Face EFGH in Figure 5-10), especially below the lines G-F and G-H, the red zones (high velocity zones) appears.

With the time proceeding, seepage-affected area becomes larger gradually, seepage flow becomes steady nearly when T=15 hours which is shown in Figure 5-13. The high velocity zones below the lines G-F and G-H simply fade away, at the same time, the high velocity areas appear around the sole of face IGFN and face IJGH in Figure 5-10. The maximum velocity zone appears at the corner of the pit (around point G in Figure 5-10).

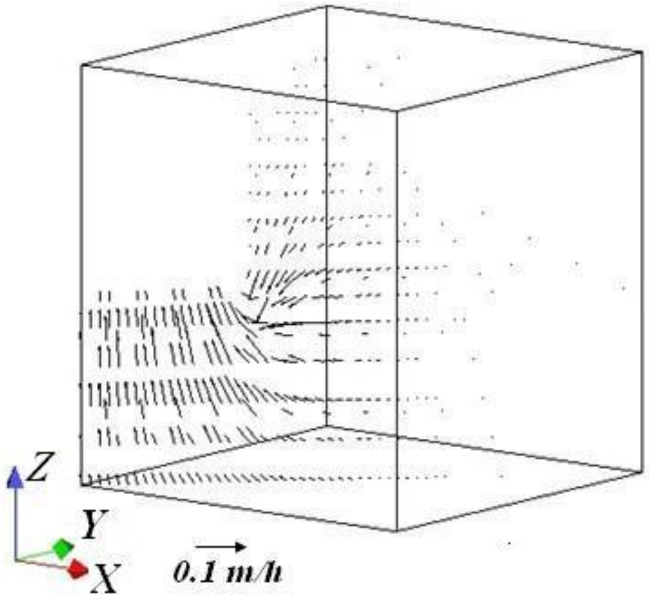

Figure 5-14 Flow velocity distribution (T=0.5h)

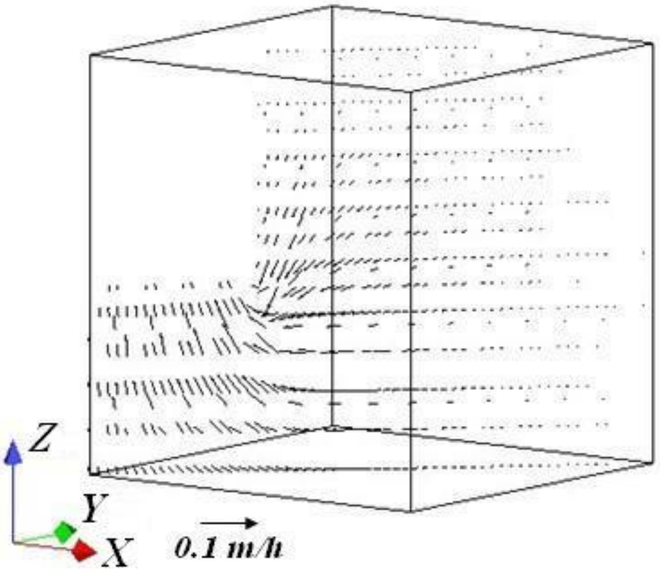

Figure 5-15 Flow velocity distribution (T=2h)

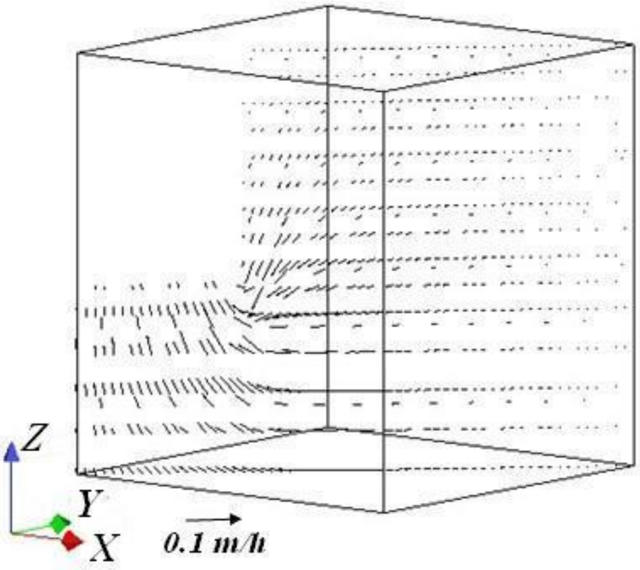

Figure 5-16 Flow velocity distribution (T=15h)

The results of flow velocity distributions on the diagonal plan (ILCAEG plan in Figure 5-10) are shown in the Figure 5-14, Figure 5-15 and Figure5-16. In these figures, the maximum velocity zone appears at the corner of the pit (around point G in Figure 5-10) in all time, and the seepage streamline takes a shape of an arc on the whole. The seepage velocity near the bottom of excavation come from unsteady stage (Figure 5-14) is notably larger the steady stage's (Figure 5-16).

Calculated results of displacement (mesh distortion) on the plan Y=0 (ADKJHE plan in Figure 5-10) are shown in Figure 17 (T=0.5 hour), Figure 18 (T=2 hours) and Figure 19 (T=15 hours). The solid lines are deformed mesh and the broken lines are original mesh. The maximum vertical displacement zone appears at the bottom of the pit, the maximum of upheaval is point E in the Figure 5-10. The maximum horizontal displacement zone appears at the bottom of the analytical domain (above the hard stratum) and becomes larger gradually with time proceeding.

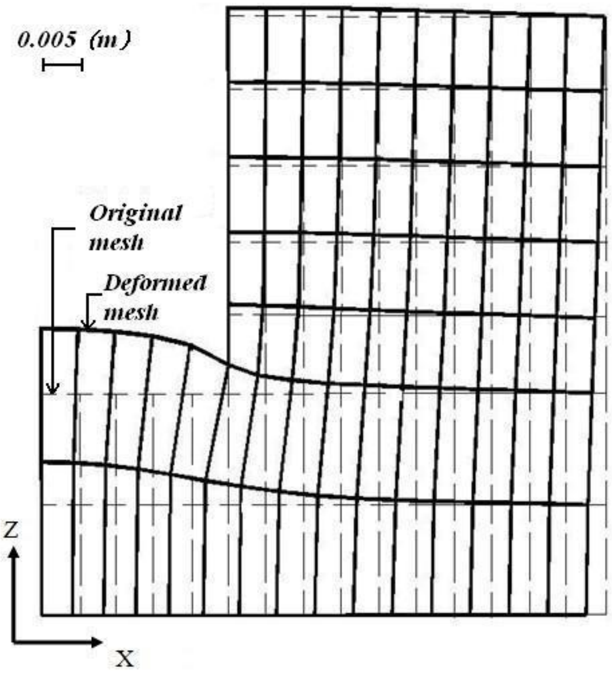

Figure 5-17 Displacement distribution (T=0.5h)

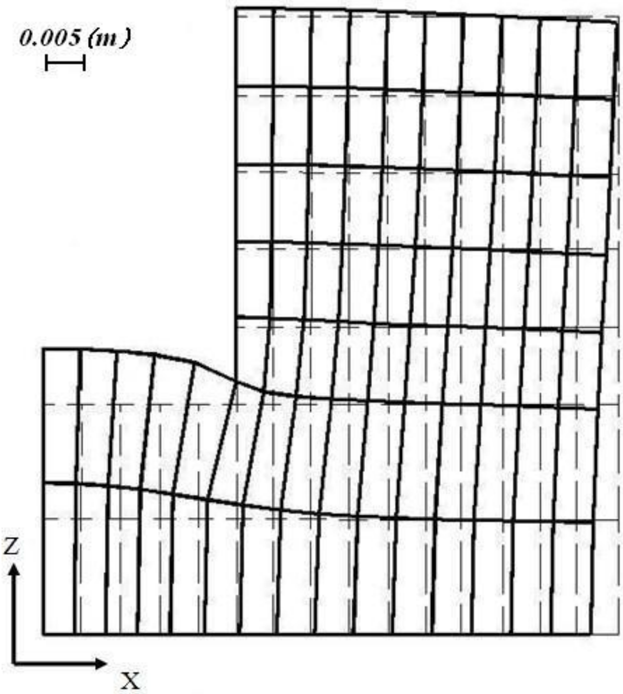

Figure 5-18 Displacement distribution (T=2h)

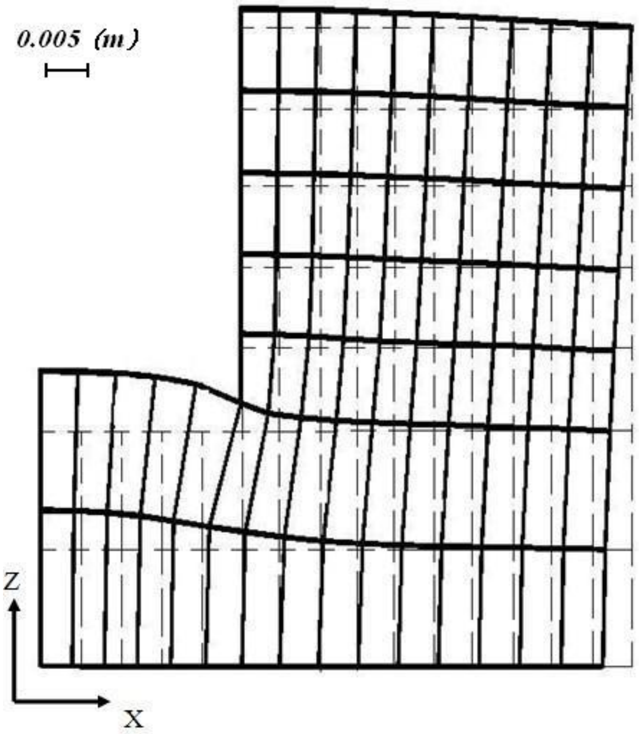

Figure 5-19 Displacement distribution (T=15h)

Composite displacement distributions are shown in Figure 5-20, Figure 5-21 and Figure 5-22. The peak value of displacement at the excavation bottom is almost 0.008 m in the early stage (Figure 5-20) and decreases slightly with time proceeding (Figure 5-21and Figure 5-22). This is because the seepage velocity under the bottom of the pit is relatively large during the initial period of unsteady seepage which can lead to a larger seepage force, and the seepage velocity decreases in the process after.

Two large horizontal displacement regions (red areas) appears above the hard stratum in Figure 5-22, which is mainly caused by horizontal seepage flow and the large vertical displacement region under the bottom of the pit is due to upward vertical seepage flow. The interface of high-displacement zone and low-displacement zone takes a Spoon-shaped space gradually in three-dimensional space when time passes enough, which is shown in Figure 5-22.

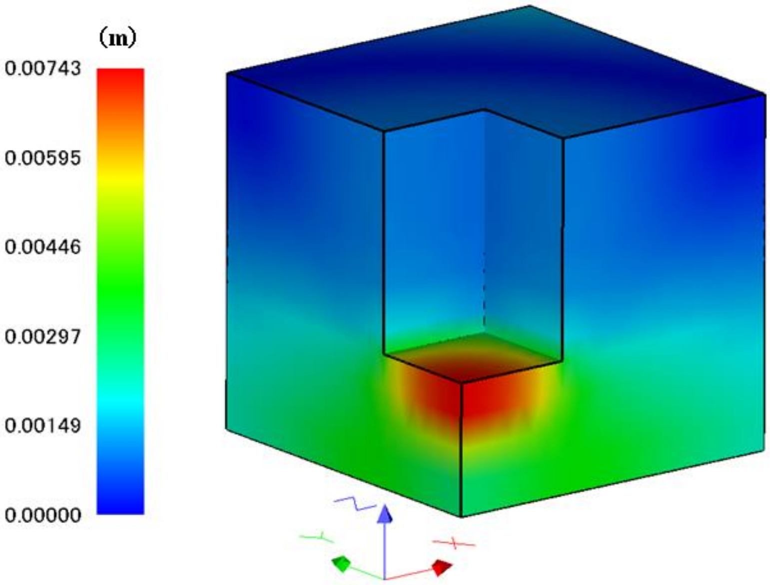

Figure 5-20 Composite displacement distribution (T=0.5h)

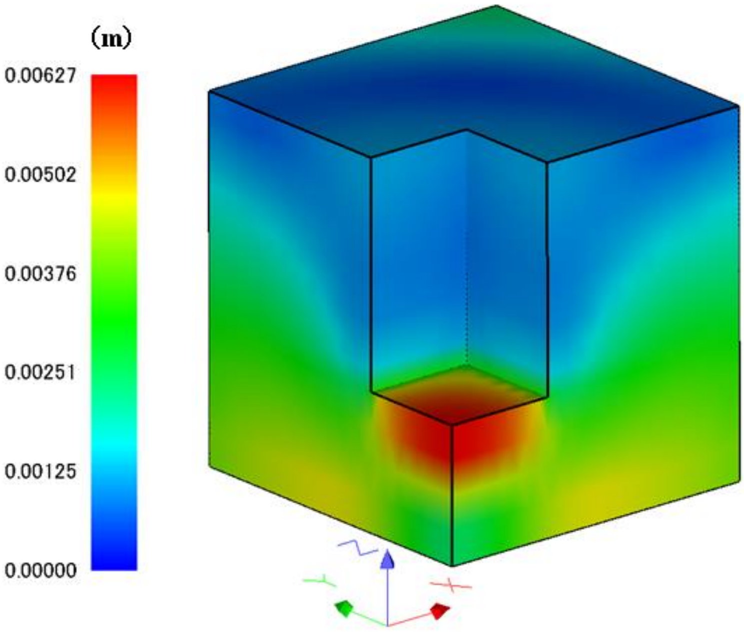

Figure 5-21 Composite displacement distribution (T=2h)

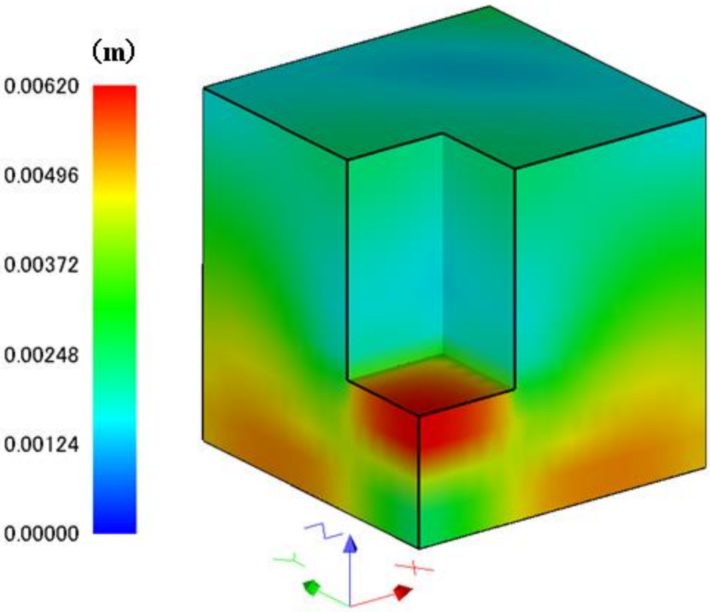

Figure 5-22 Composite displacement distribution (T=15h)

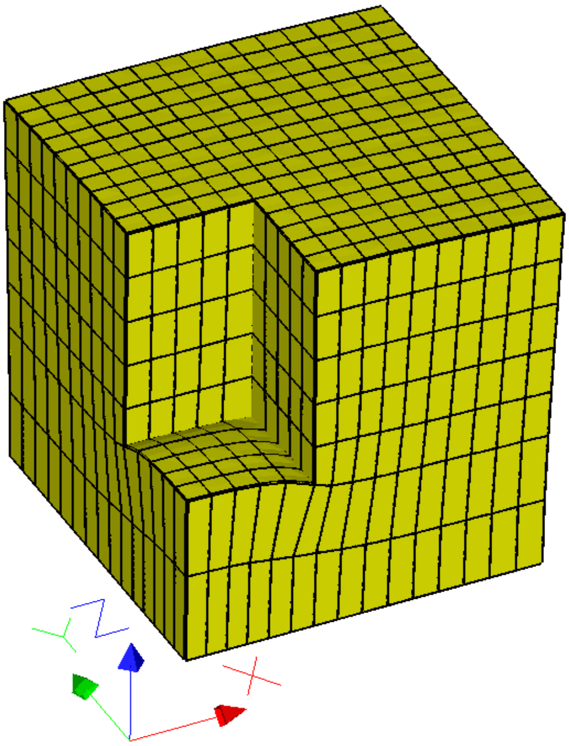

Figure 5-23 Schematic of 3D displacement field (T=15h)

Figure 5-23 gives the schematic of 3D displacement field (T=15h), from which the shape of upheaval surface due to seepage force could be observed apparently.

In this analysis, a numerical model test was performed on ground behavior around the excavation due to unsteady seepage of groundwater by proposed FEM-FDM program. The numerical prediction shows that the vertical upward seepage velocity below the bottom of pit is relative larger at the early stage of seepage field and decreases gradually with time proceeding. The maximum velocity zone appears at the foot of the excavation all the time where the potential seepage failure such as quicksand and piping maybe happen. The maximum displacement zone appears at the bottom of the pit and extends gradually with time proceeding, which matches well with the results of seepage field. The horizontal displacement caused by seepage flow plays a very important role in displacement field and a 3D sliding surface may appears when time passes enough.

5.4 Non-linear deformation model under unsteady seepage condition

In this analysis, a 2-dimensional small model analysis is made on the non-linear ground behavior around the excavation due to unsteady seepage of groundwater under considering the saturated-unsaturated theory.

5.4.1 Outline of the model

Figure 5-9 shows the elevation of the excavation, where EB is the width and EH is the depth of the excavation area respectively. In the analysis, half of the whole area has been selected as analytical area because of symmetry, which is shown in Figure 5-24. In this model, the following basic assumptions are introduced into analysis: The ground water flow is laminar and governed by Darcy's law. The water molecules and soil particles can't be compressed and the stress-strain relationship of the soil is ruled by Duncan-Chang model7). The coefficient of permeability variation in the unsaturated region obeys the V-G model, while keeps unchanged within the saturated region. The material coefficients of V-G model8) for Toyoura sand are shown in Table 5-3 and material parameters of D-C model for Toyoura sand are shown in Table 5-4.

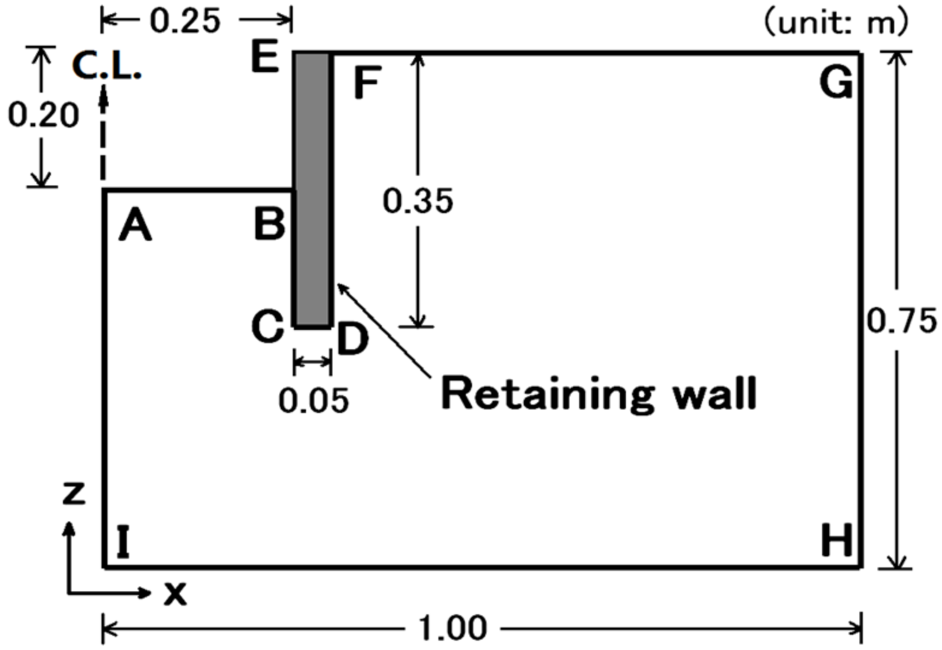

Figure 5-24 FEM analytical area

Table 5-3 Material constants for V-G model

Ksat (m/s)	α	θs	θr	n
0.00025	5.52	0.41	0.00	12.96

Table 5-4 Material constants for D-C model

K	Rf	ν	Φ (deg.)	n	c
397	0.9	0.3	41°	0.7	0

The size of the model is 2m×0.75m and the size of excavation is 0.5m×0.2m, the size of retaining wall is 0.05m×0.35m. Half of the whole area has been selected as analytical area for the purpose of saving computing time and storage space, which is shown in Figure 5-24.

Boundary conditions for seepage flow are given as below:

On AB: total head H=0.55m, on GH: total head H=0.75m.

Boundary conditions for displacement are given as below:

On AI, BC, FD and GH: displacement in X direction has been fixed, on IH: displacement in Z direction has been fixed.

5.4.2 Numerical prediction

In order to validate the correctness of the programming, a simple model has been tested for comparing with the tri-axial test data. The sample was made of Toyoura sand with relative density of 90%, which was implemented by Yamamoto 9).

Figure 5-25 gives the schematic of tri-axial test apparatus, the confining (lateral) pressure varies from 50KPa, 100KPa, 150KPa, 200KPa, 250KPa to 300KPa. The loading is acted on the specimen until the failure happens. Figure 5-26 shows the comparison of numerical prediction and experimental data under loading condition with different confining pressure. Numerical prediction results match well with the tri-axial test data, which can make sure that the programming is validity.

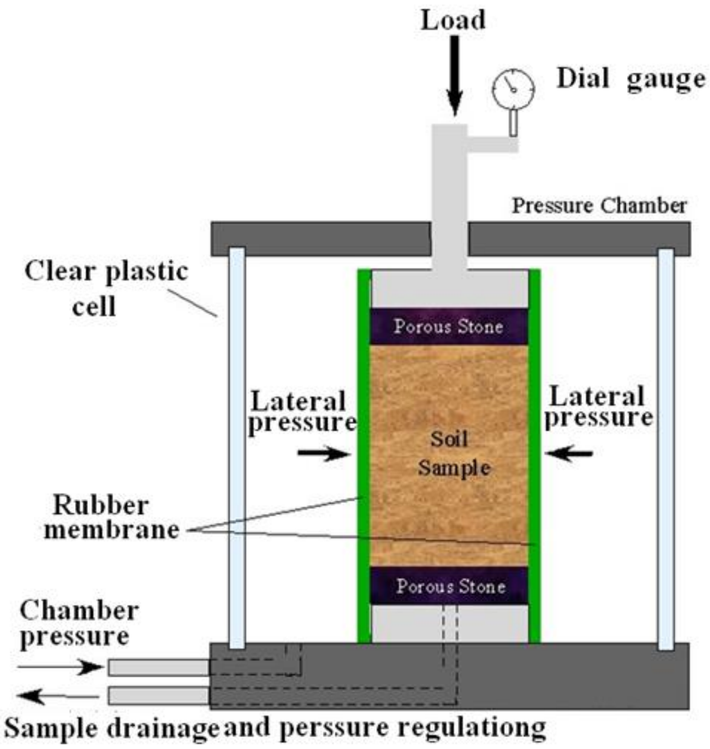

Figure 5-25 Schematic of triaxial testing model

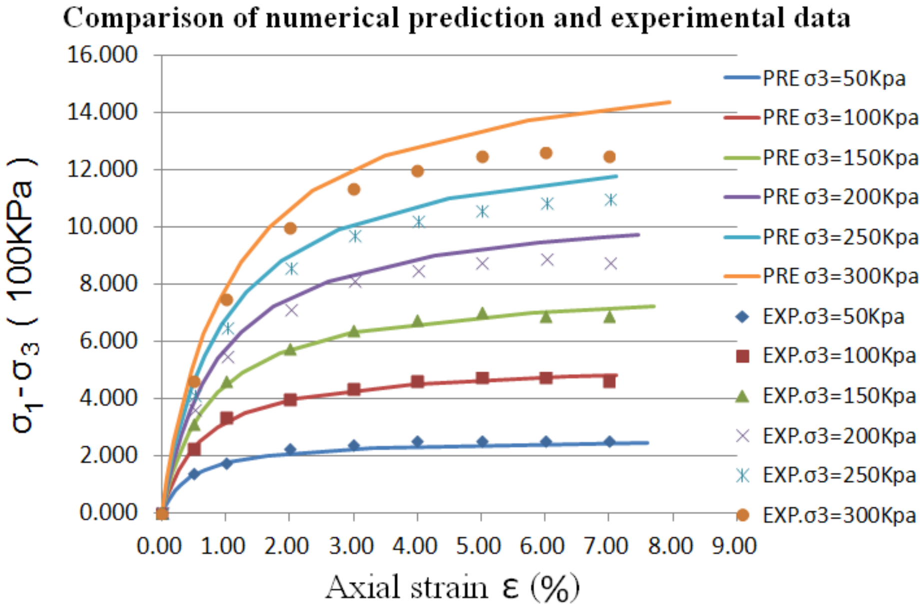

Figure 5-26 Comparison of numerical prediction and experimental data under monotone loading condition

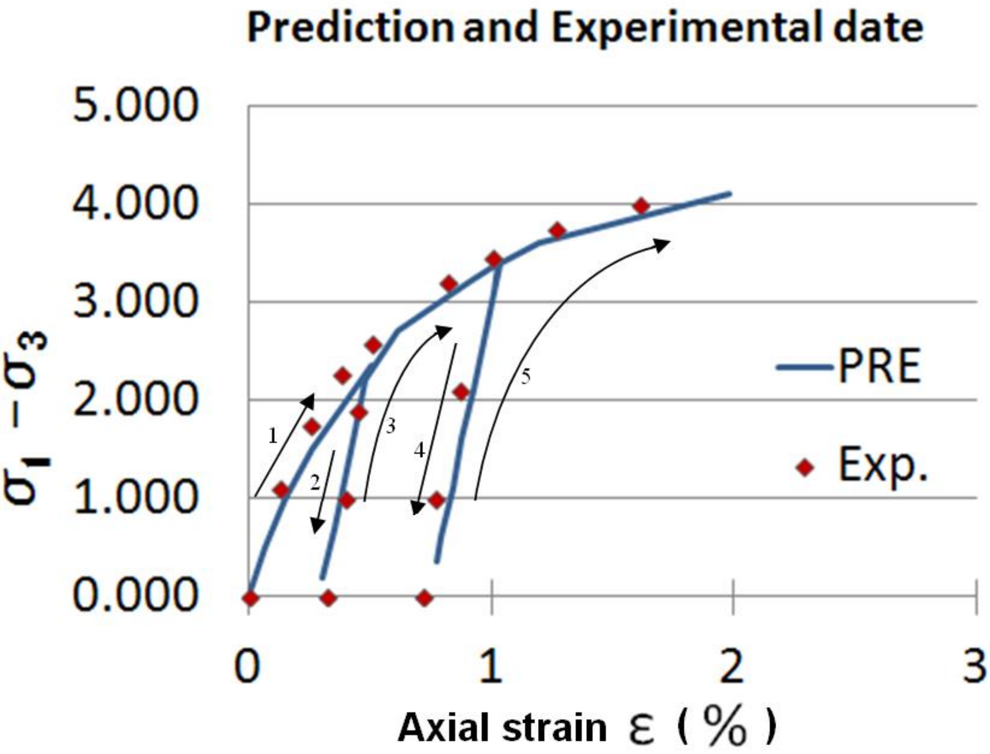

Figure 5-27 Comparison of numerical prediction results and tri-axial test data under unloading-reloading condition

The influence of the soil resilience of deep pit excavation's bottom due to dewatering is inevitable during the excavation. Therefore, it is necessary to consider the unloading phenomenon when numerical prediction is implemented. Figure 5-27 shows the comparison of numerical prediction results and tri-axial test data under unloading-reloading condition with confining pressure equal to 100Kpa. By comparing the prediction results with tri-axial test, the numerical prediction results match well with the test data, the correctness of the analysis programming under unloading-reloading condition has been confirmed.

5.4.3 Prediction results

Calculated results of seepage flow are shown in Figure 5-28 (T=36s), Figure 5-29 (T=180s) and Figure 5-30 (T=360s) at different points in time. When time equal to 360s, the seepage flow becomes almost steady flow.

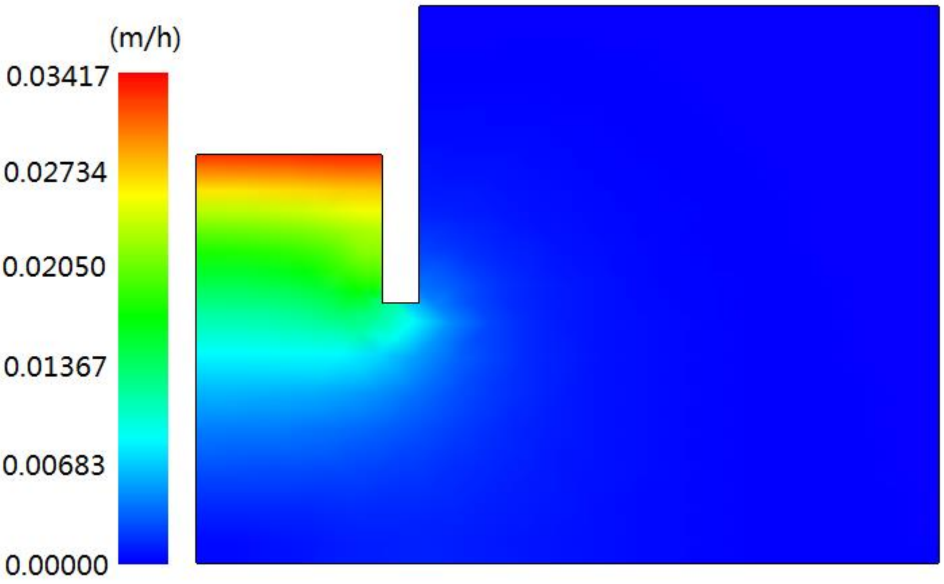

Figure 5-28 Composite flow velocity distribution (T= 36s)

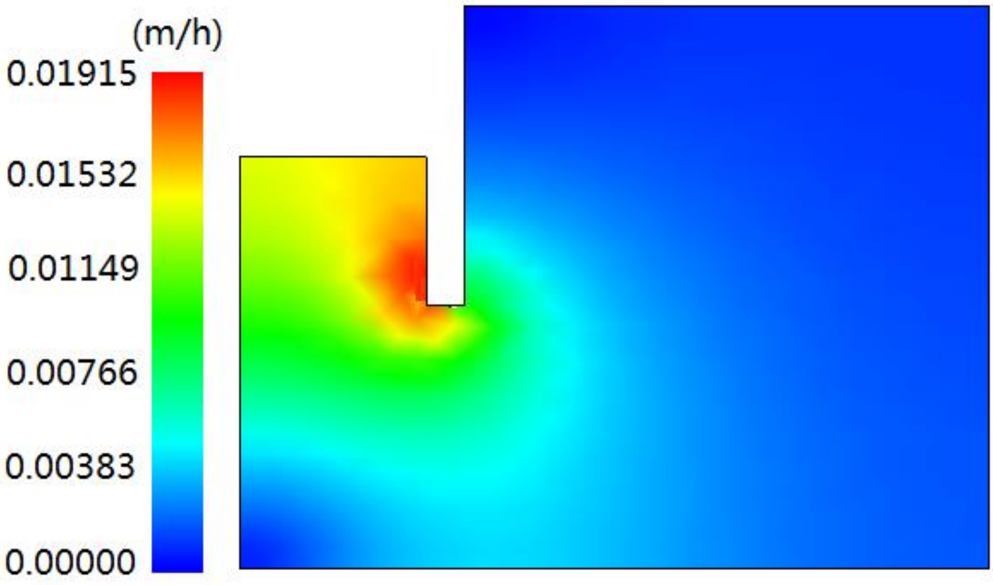

Figure 5-29 Composite flow velocity distribution (T= 180s)

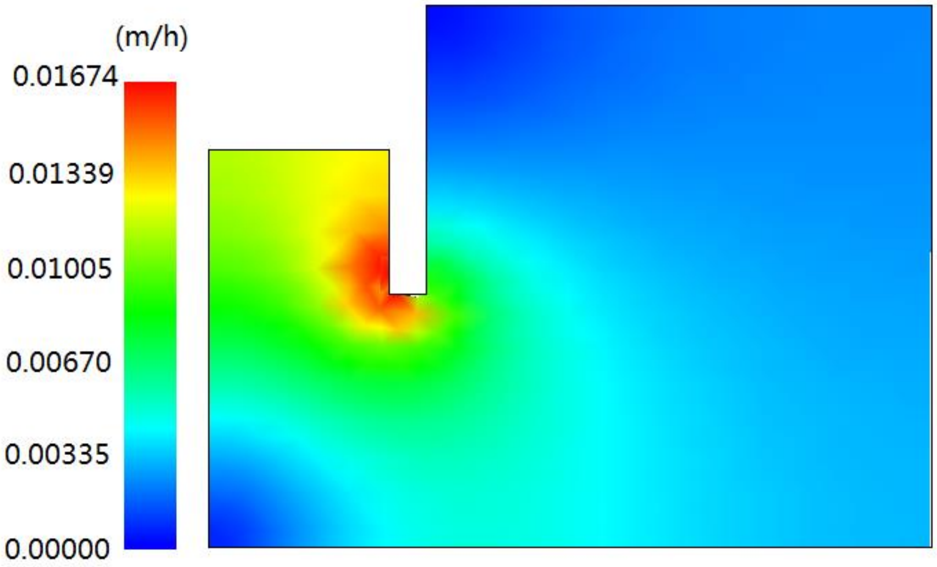

Figure 5-30 Composite flow velocity distribution (T= 360s)

The maximum velocity zone appears around the bottom of the excavation at early stage (T=36s), the peak value of composite velocity near the excavation bottom is almost 0.035m/h in Figure 5-28, and after that the velocity decreases gradually with time proceeding in Figure 5-29 (0.01915 m/h) and Figure 5-30 (0.01674 m/h).

When T=36s, the seepage is unsteady flow, the affected area of seepage is not full-area, the seepage flow behind the retaining wall is nearly zero. With the time proceeding, affected area of seepage becomes larger and larger which is shown in Figure 5-29 (T=180s), and the seepage flow becomes steady nearly when T=360s which is shown in Figure 5-30. The high velocity zone mainly appears around the bottom of the excavation in at early stage which is shown in Figure 5-28, with the time proceeding the seepage velocity around the bottom begins to decrease until reduces by half, and the high velocity zone comes from the corner of the retaining wall (around points C in the Figure 5-24) which is shown in Figure 5-30.

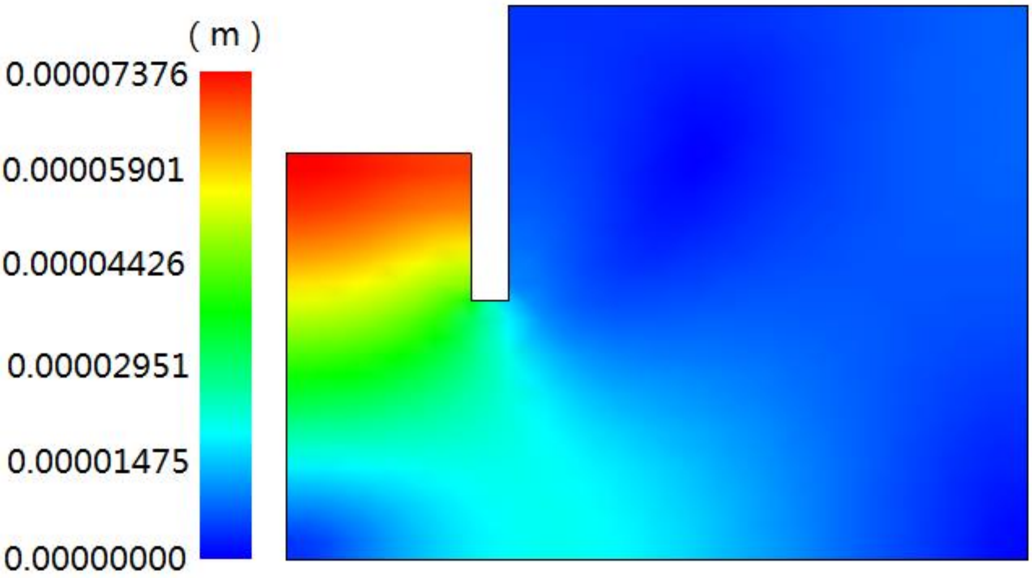

Figure 5-31 Composite displacement distribution (T= 36s)

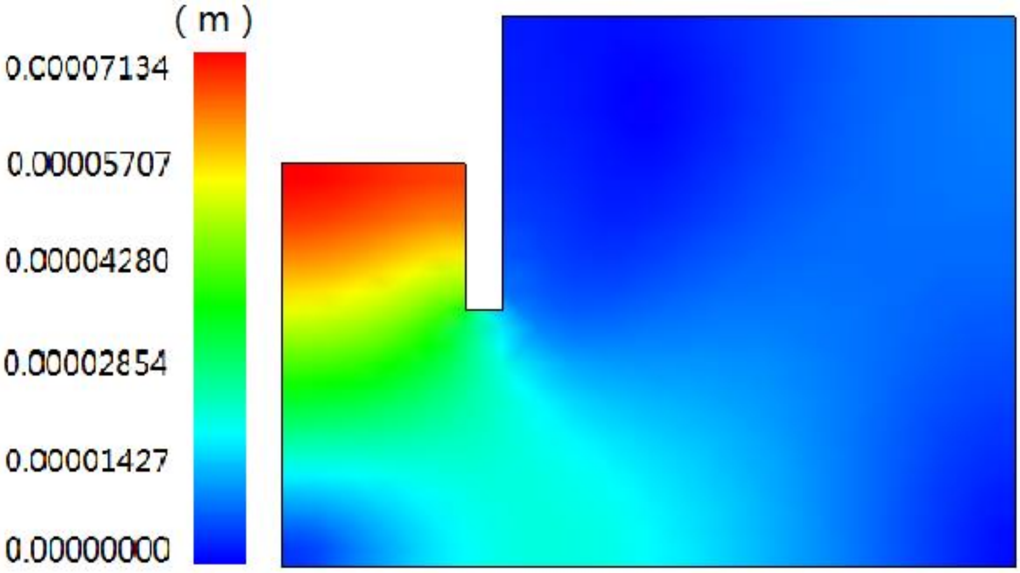

Figure 5-32 Composite displacement distribution (T= 180s)

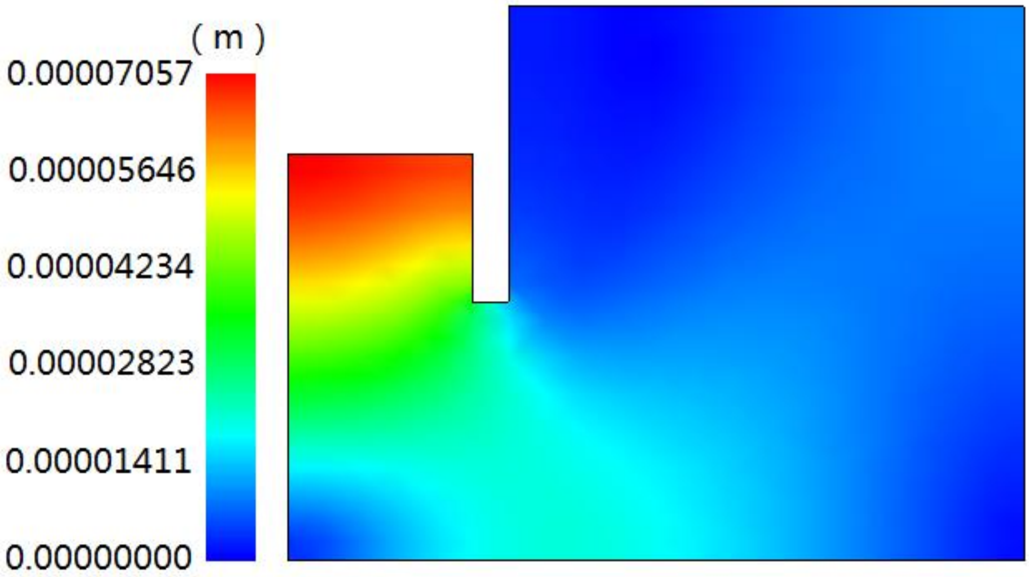

Figure 5-33 Composite displacement distribution (T= 360s)

Calculated results of composite displacement are shown in Figure 5-31 (T=36s), Figure 5-32 (T=180s) and Figure 5-33 (T=360s) at different points in time. The maximum vertical displacement zone appears at the bottom of the pit all the time. The peak value of displacement at the excavation bottom is almost 0.000074m in the Figure 5-31, and decreases slightly with time proceeding which are shown in Figure 5-32 (0.00007134m) and Figure 5-33 (0.00007057m). This is because the seepage velocity under the bottom of the pit is relatively larger during the initial period of unsteady seepage flow, which can lead to a larger seepage force and causes relatively larger vertical displacement. Comparing with the early stage (T=36s), the final displacement (T=360s) only decreases 5% when seepage flow is reduced by half, this is because that D-C model is a nonlinear-elastic model, the modulus for loading and the modulus for unloading is different, which can describe the elasto-plasticity of soil approximately. A relatively larger horizontal displacement area appears above the hard stratum all the time, which is mainly caused by horizontal seepage flow. The large vertical displacement region under the bottom of the pit is due to vertical seepage flow. The large-displacement zones create a Spoon-shaped zone gradually behind the retaining wall when time passes enough, which is shown in Figure 5-33.

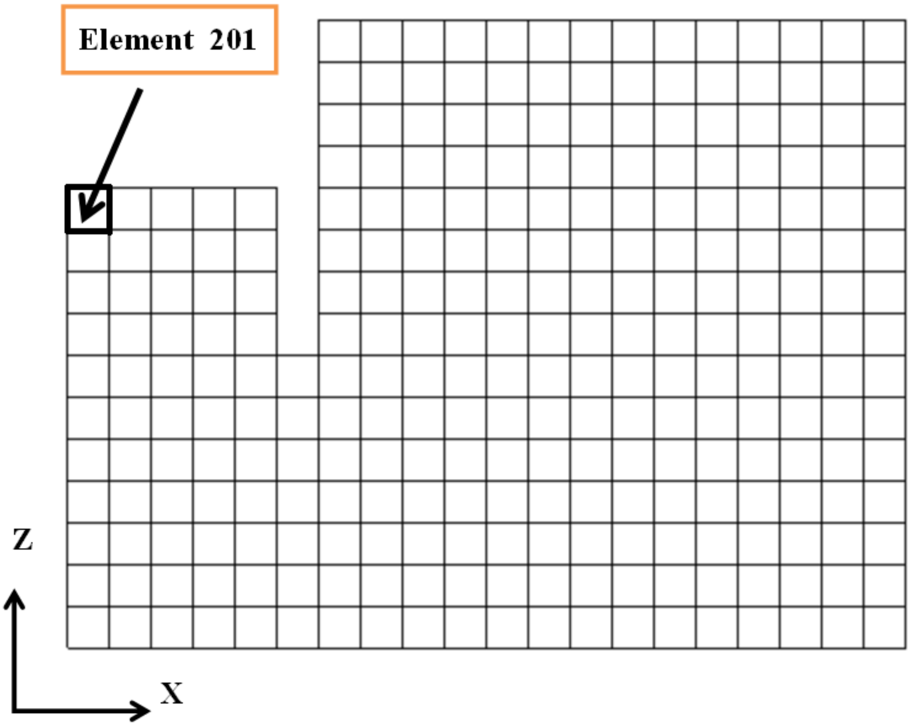

Figure 5-34 Element selection for stress path analysis

To investigate the stress path of the soil due to seepage force inside of pit, the element on symmetrical face is selected for stress path analysis, which is shown in Figure 5-34. Figure 5-35 gives the stress path and critical state line. The detail of the stress path is given (A-B-C) in Figure 5-36, point A is original state, point B is the starting of dewatering and point C is steady state of seepage field.

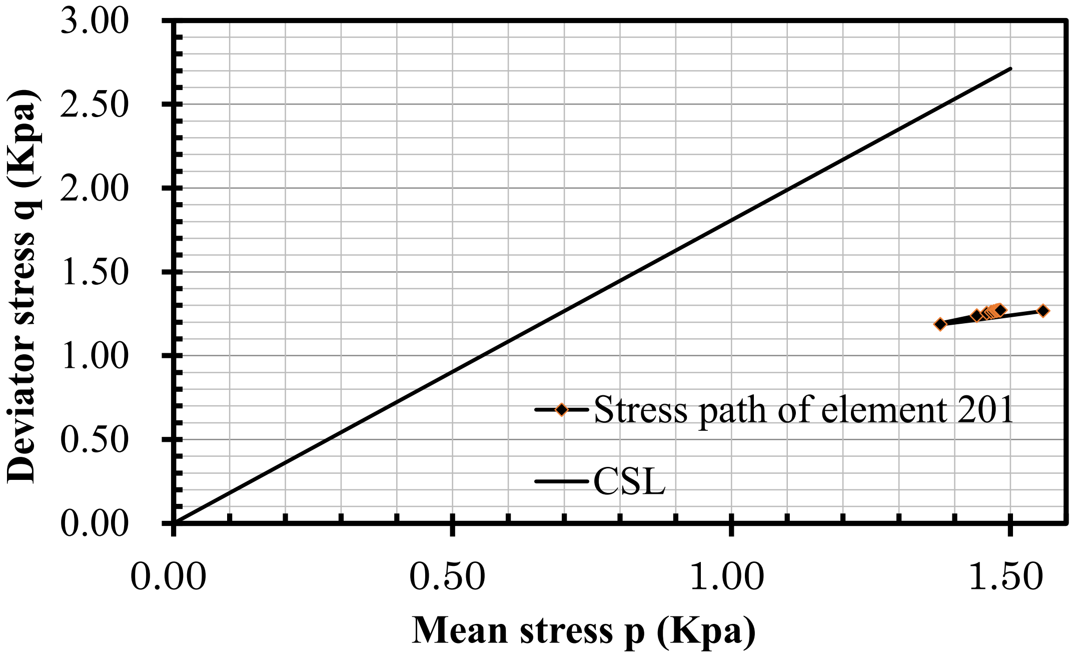

Figure 5-35 Stress path and critical state line

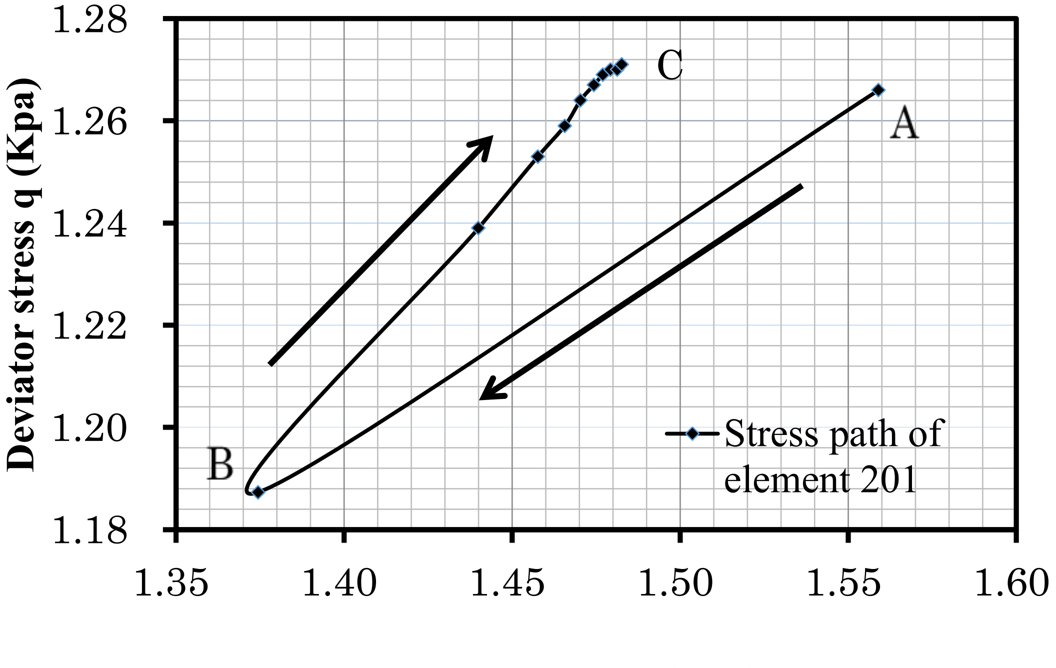

Figure 5-36 Stress path in detail

Because of upward seepage force due to dewatering, the mean stress p and deviator q are both decreases, stress path change from A to B, which is coming close to CSL. The seepage field becomes steady with time proceeding, upward seepage force reduces and tends to be stable finally, which moves away from the CSL gradually. In conclusion, in the early stage of dewatering, soil failure is easy to happen and soil tents to be safer with time proceeding.

In this analysis, a 2-dimensional small model analysis is made on the non-linear ground behavior around the excavation due to unsteady seepage of groundwater under considering the saturated-unsaturated theory. The numerical prediction shows that the vertical upward seepage velocity below the bottom of pit is relative larger at the early stage of seepage field and decreases gradually with time proceeding. The maximum velocity zone appears at the foot of the excavation at the early time where the potential seepage failure such as quicksand and piping maybe happen. The maximum displacement zone appears at the bottom of the pit and extends gradually with time proceeding, which matches well with the results of seepage field. The influence of the soil resilience of deep pit excavation's bottom due to dewatering is inevitable during the excavation. Therefore, it is necessary to consider the unloading phenomenon in non-linear analysis when numerical prediction is implemented.

5.5 Summary and discussions

In this chapter, several cases of 3D analysis are made on the ground behavior around the excavation site due to seepage of groundwater under different conditions.

The analysis in 5.2 shows that horizontal deformation caused by seepage flow plays a very important role in deformation field around the excavation site, especially in the case of high-rise buildings surrounded. The differential displacement may occur around foundation adjacent buildings, which can lead to toppling behavior to the foundation and the pipes and roads near the foundation may tend to buckle and crack because of the displacement of the ground.

The numerical prediction in 5.3 shows that the vertical upward seepage velocity below the bottom of pit is relative larger at the early stage of seepage field and decreases gradually with time proceeding. The maximum velocity zone appears at the foot of the excavation all the time where the potential seepage failure such as quicksand and piping maybe happen. The maximum velocity zone appears at the corner of the pit with time passing enough, which points out the importance and necessity of the 3D analysis. The maximum horizontal displacement zone appears at the bottom of the pit and extends gradually with time proceeding, which matches well with the results of seepage field. The horizontal displacement caused by seepage flow plays a very important role in displacement field and a 3D sliding surface may appears when time passes enough.

In 5.4, a 2-dimensional model analysis is made on the non-linear ground behavior around the excavation site due to unsteady seepage of groundwater under considering the saturated-unsaturated theory. The influence of the soil resilience of deep pit excavation's bottom due to dewatering has been shown in the analysis, which proves the importance and necessity of considering the unloading phenomenon in non-linear analysis. In seepage analysis of 5.2, high velocity area appears at outside of the excavation’s bottom (Around G point in Figure 5-10), but in seepage analysis of 5.3, high velocity area appears under the bottom of retaining wall (Around C point in Figure 5-24), which proves that the retaining wall affects the seepage field significantly.

Reference

1) Debidin. F. and Lee. C. F., Groundwater and Drawdown in a Large Earth Excavation, National Research Council of Canada, 17(2), pp.185-202, May, 1980.

2) Holt. D. A. and Griffiths. D. V., Transient Analysis of Excavations in Soil, Computer and Geotechnics, 13, pp.159-174, 1992.

3) Hsi. J. P. and Small. J. C., Analysis of Excavation in an Elasto-plastic Soil Involving Drawdown of the Water Table, Computer and Geotechnics, 13, pp.1-19, 1992.

4) ZHOU Hui, XIONG Ju-hua: QI Hong-xiang: Influence analysis underground water to foundation background, Jiangxi Hydraulic Science and Technology, pp. 54, 2001 (In Chinese)

5) Wu Lingao, Yao Ying: The Characteristics of the Groundwater Seepage around Barrier-wall and its Numerical Modeling, Shanghai Geology 55, pp. 8, 1995. (In Chinese)

6) Van Genuchten. M. TH., A Closed-from Equation for Predicting the Hydraulic Conductivity of Unsaturated Soils, Soil Sci. Soc, pp. 892-898, 1980.

7) D. A. Sun, Estimate of Initial Modulus of Hyperbolic Stress-Strain Relation from Result of Consolidation Tests, Thirteenth Southeast Asian Geotechnical Conference, pp.171-176, 1998.

8) Y. KIYOHARA et al., The Applicability of Hachinohe Shirasu as Material of Capillary Barrier, Japanese Geotechnical Journal, pp.329-337, 2007. (In Japanese)

9) H. Yamamoto et al., Model Tests of Friction Piles in Sand by Means of the Hydraulic Gradient Similarity Method, Journal of Structural Engineering, Vol.37B,

pp. 11-22, 1991. (In Japanese)

CHAPTER 6

EXAMPLE OF APPLICATIONS

6.1 General situation of the excavation project of the Zhujiang Road metro station

Zhujiang Road metro station is located in the north-east of the node of Zhongshan road and Zhujiang road in Nanjing, which is shown in the Figure 6-1. The length of excavation is 124 m, the width is 22.9 m and the depth of the excavation is 15.68m. The groundwater table around the excavation site is from -1m to -1.5m.1)-3)

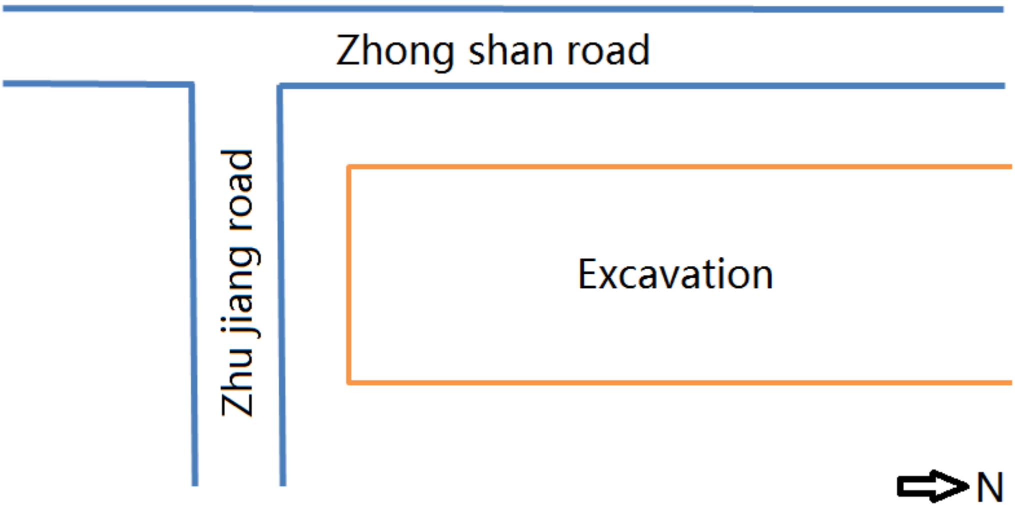

Figure 6-1 Plan of the excavation

The project is situated in the downtown of the city, roads, structures, underground pipelines and etc. are crowded around the excavation work, therefore controlling the subsidence around the excavation is particularly important. Excavation project have 5 stages, dewatering project should be completed in advance before every excavation stage start, and detailed information is shown in Table 6-1.

Table6-1 Information of excavation and dewatering of every stage

Number of stage	Increment deepth of excavation (m)	Accumulated deepth of excavation (m)	Increment deepth of dewatering (m)	Accumulated deepth of dewatering (m)
1	-1.1	-1.1	-2.2	-2.2
2	-4.68	-5.78	-4.38	-6.58
3	-4.3	-10.08	-4.6	-11.18
4	-3.3	-13.38	-3	-14.18
5	-2.3	-15.68	-2.1	-16.28

Figure 6-2 gives the section of the excavation, the thickness of the retaining wall is 0.85m, bottom elevation of the retaining wall is 12.32m, and the bottom elevation of the excavation is 24.32 m. Because the water and earth pressure are key factors to the stability of excavation, four sets of support structure have been set up above the bottom of excavation. Below the surface of the ground, there are mainly 7 kinds of soil. The types of the soil are Plain fill (Artficial backfill), loam, silty sand, muddy-silty clay, and silty clay, respectively.

For simulating the actual project, the construction loading due to machines, temporary building and materials pilling is necessary to consider for the safety of excavation design. Generally speaking, the overloading around the excavation is given

15-30 KPa. In Nanjing road station project, 20 KPa has been added by considering the ground overload around the excavation site.

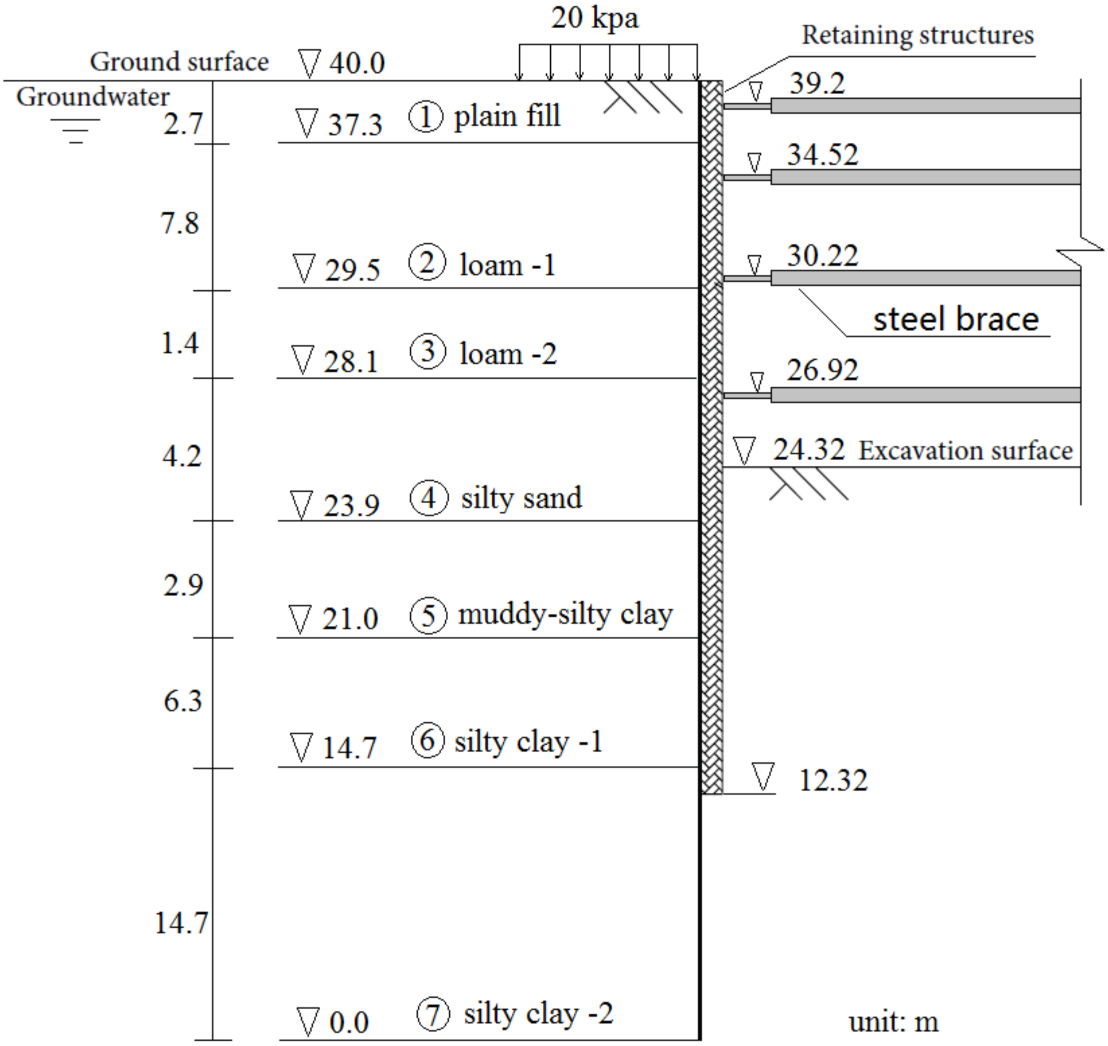

Figure 6-2 The soil profile

The soil distribution is shown in the Table 6-2, and the bottom elevation, moist unit weight and submerged unit weight of soil also given.The D-C model parameters of soils for FEM calculation is shown in the Table 6-3, and V-G model parameters are given in the Table 6-4.

Table 6-2 Soil distribution1)

Soil layer	Bottom elevation （m）	Depth of stratum (m)	Moist unit weight γ (KN/m^3)	Submerged unit weight of soil γ' (KN/m^3)
Plain fill	-2.7	2.7	19.3	9.59
Loam-1	-10.5	7.8	20.1	9.89
Loam-2	-11.9	1.4	19.4	9.25
Silty sand	-16.1	4.2	19	9.21
Muddy-silty clay	-19	2.9	18.5	8.29
Silty clay-1	-25.3	6.3	20.3	9.93
Silty clay-2	-40	14.7	20	10

Table 6-3 D-C model parameter1)

Material	K	Kur	G	F	n	D	C (kPa)	Φ (°)	Rf
Plain fill	190.3	380.6	0.20	0.03	0.22	3.5	17.7	14.0	0.80
Loam-1	199.2	398.4	0.21	0.06	0.53	5.1	42.9	20.2	0.89
Loam-2	190.2	380.4	0.22	0.05	0.53	4.0	24.8	20.0	0.89
Silty sand	200.2	300.4	0.21	0.08	0.24	2.3	13.7	25.6	0.70
Muddy-silty clay	156.3	312.6	0.24	0.03	0.25	1.5	17.8	15.1	0.90
Silty clay-1	213.4	426.8	0.27	0.00	0.23	2.2	24.7	17.5	0.75
Silty clay-2	213.8	427.6	0.27	0.00	0.28	2.3	22.5	23.6	0.73

Table 6-4 V-G model parameters

Material	Kh（10^{-4} m/d）	Kv（10^{-4} m/d）	θs	θr	α	n	Ss
Plain fill	2.7475	10.6272	0.4629	0.034	0.016	1.37	0.0015
Loam-1	1.4947	0.6998	0.4457	0.078	0.036	1.56	0.0015
Loam-2	2.3414	1.6243	0.4457	0.078	0.036	1.56	0.0015
Silty sand	101.952	68.6016	0.4544	0.034	0.016	1.37	0.00015
Muddy-silty clay	2.0563	2.7043	0.5236	0.07	0.005	1.09	0.0015
Silty clay-1	6.3158	14.5152	0.4401	0.07	0.005	1.09	0.0015
Silty clay-2	2.6006	1.7194	0.4401	0.07	0.005	1.09	0.0015

6.2 Finite element analysis model for simulation

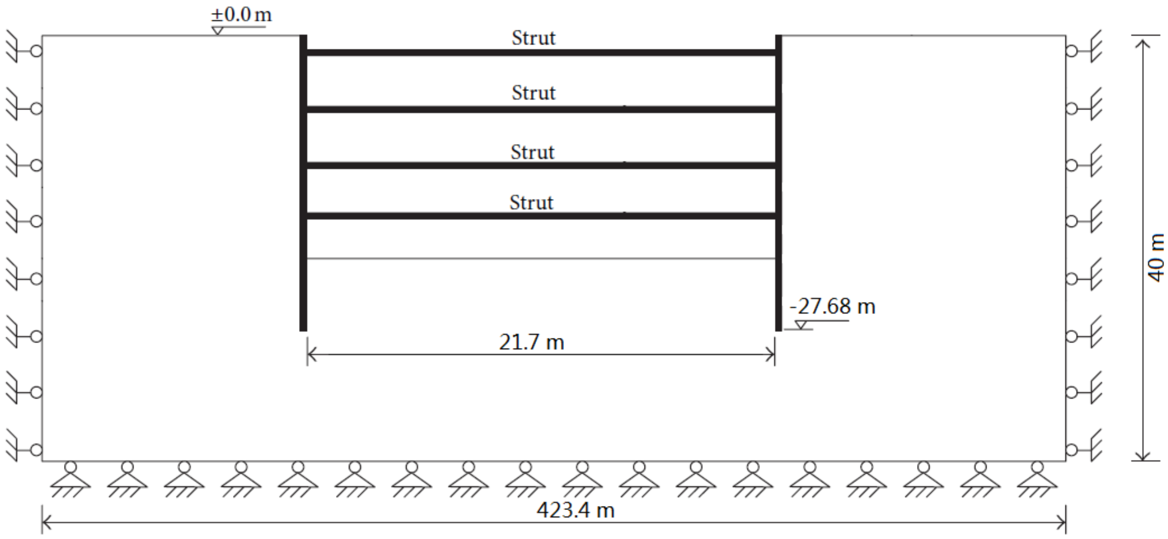

Figure 6-3 Elevation

According to the introduction of excavation in 6.1, the Length/Width>4, therefore the excavation could be considered as a two dimension problem. The size of the model is 423.4m×40m and the size of excavation is 21.7m×15.68m and the size of retaining wall is 0.85m×27.68m. Four inner supports are employed in the project, which are shown in Figure 6-3. In the analysis, half of the whole area has been selected as analytical area because of symmetry.

6.2.1 Simulation of excavation

Excavation of soil is involved in many geotehnical problems. Simulation of a stage of excavation involves determination of the nodal forces which are equivalent to the tractions T (T are equal to the internal stresses in the soil mass that act on the excavated surface before soil mass is removed) act on the excavated surface. These nodal forces could be calculated from the excavated elements adjacent to the excavation boundary by using:

$$\{\mathrm{F}\} = \int_{Vol} [\mathrm{B}]^{\mathrm{T}} \{\sigma\} \mathrm{d}Vol - \int_{Vol} [\mathrm{N}]^{\mathrm{T}} \gamma \mathrm{d}Vol \tag{6-1}$$

Where γ is the bulk unit weight, $\{\sigma\}$is the stress vector in the element and Vol is the volume of the excavated element. Only the forces appropriate to the nodes on the excavated surface are placed in$\{\mathrm{F}\}$. This procedure is based on Brown and Booker$^{4)}$

In this analysis, structual elements, supports are added as excavation proceeds, and nonlinear constitutive model for soil are used, it is therefore necessary to split the analysis in the a sequence of increments. The procedure in the analysis is as follows:

(1) Label the elements to be excavation for a particular increment.

(2) Using Equation (6-1) determine the equivalent nodal forces to be applied to the excavated surface boundary to simulate removal of the elements. Tag the elements to be excavated as deactivated elements and remove them from the active mesh.

(3) Assemble the new boundary conditions and the global stiffness matrix by using the active mesh. Solve the finite element equations to give the new incremental changes in displacements, stresses and strains.

(4) Add the incremental changes of stresses and strains to the accumulated values existing before the increment for giving the updated accumulated values.

(5) Conduct the next increment calculation of the analysis.

6.2.2 Simulation of foundation pit fencing structures

Table 6-5 Material coefficients of steel pipe1)

External diameter (mm)	Thickness (mm)	Length (m)	Sectional area (m^2)	E (Gpa)
609	16	21.9	0.0151	210

SMW (Soil mixing wall) method plus steel support are used as foundation pit enclosures in Zhujiang Road metro station project. The thickness of the SMW wall is 0.85m, the buried depth is 27.68m and ø-609×t-16mm steel pipe is used for the horizontal bracing. The elevations of every horizontal bracing are shown in the Figure 6-2. The material coefficients of steel pipe are given in the Table 6-5 and the elastic modules of SMW wall is 11.64 Gpa.1)

6.2.3 Simulation of interfaces

The relative movement of the structure with respect to the soil may occur in any soil-structure interaction situation. Interface, or joint elements as they are sometimes called, can be used to simulate the soil-structure boundary such as the sides of the wall. Particular advantages are the ability to vary the constitutive behavior of the soil-structure interface and to allow differential displacement of the soil and the structure, slip and separation.

Many methods have been proposed to model discontinuous behavior at the soil-structure interface, which have been introduced in the chapter 3. Among these alternatives, the use of zero thickness interface elements is probably the most popular. In this analysis, 16-nodel elastic perfectly plastic friction Goodman element is employed to simulate relative movement between the soil body and structure. The parameters of the joint element are given in Table 6-6.

Table 6-6 The parameters of joint element

Shear coefficient Ks (kpa/m)	Compression coefficient Kc (kpa/m)	Friction coefficient μ
10^7	10^7	0.6

6.2.4 Modeling

In this analysis, the Length/Width>4, therefore the excavation could be considered as a two dimension problem, the FEM analytical area is shown in the Figure 6-4, half of the whole area has been selected as analytical area because of symmetry. For deep excavation work, the excavation should be conducted step by step, and the supporting structure would be also employed in excavation. Dewatering project should be completed in advance before every excavation stage start. In general, construction sequence for each stage is dewatering, excavation and supporting. Excavation project of Nanjing road station have 5 stages (E1-E5 in Figure 6-4).

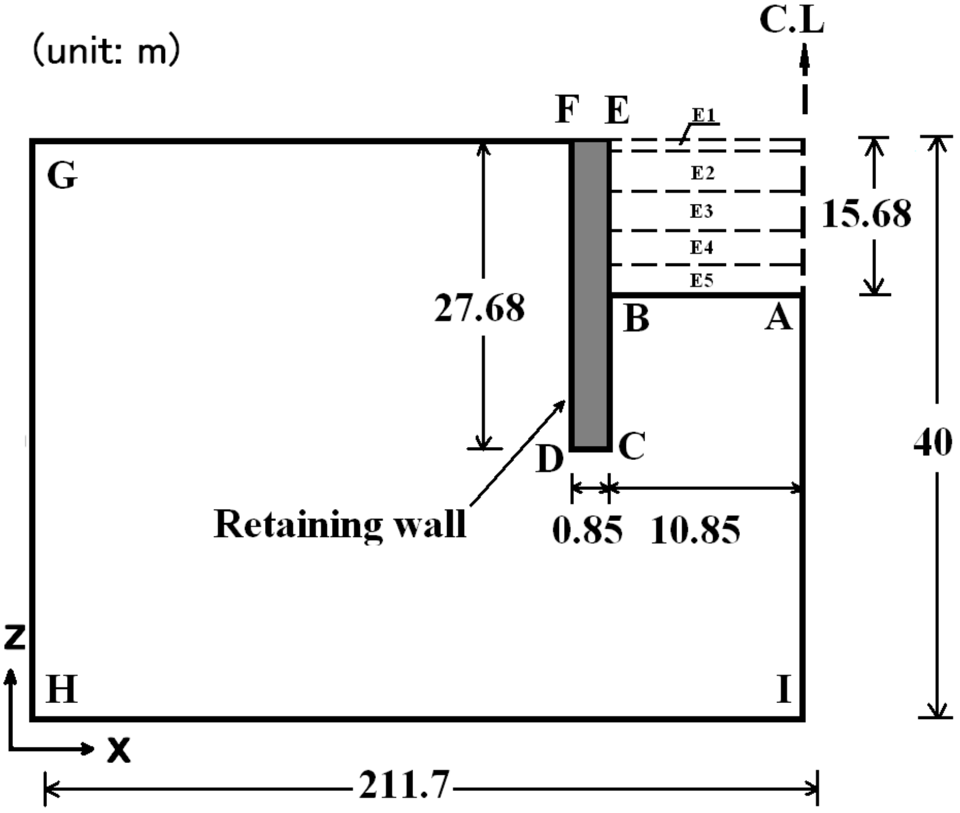

Figure 6-4 FEM analytical area for deformation

Dewatering project should be accomplished in advance before every excavation stage start. For every stage calculation of dewatering, the boundary condition for inner excavation is different (D1-D5 in Figure 6-5), which could simulate the variation of the boundary condition.

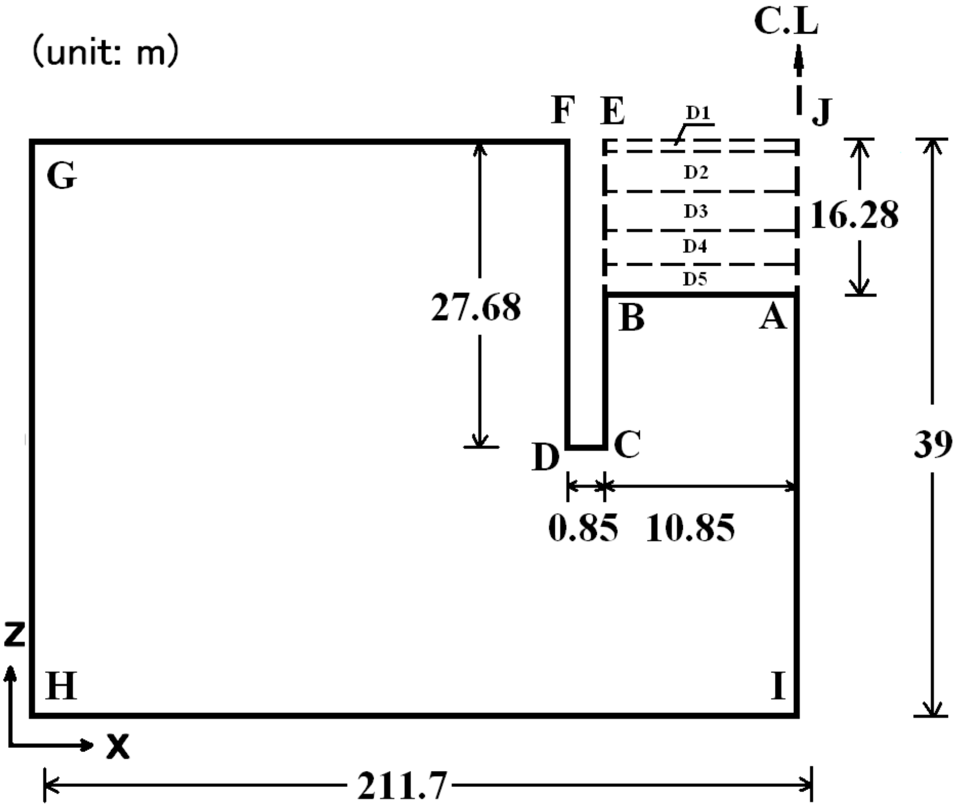

Figure 6-5 FEM analytical area for seepage

Boundary conditions for displacement are given in Figure 6-4:

On AI and GH: displacement in X direction has been fixed, on IH: displacement in Z direction has been fixed.

Boundary conditions for seepage flow are given in Figure 6-5:

The Boundary condition for inner excavation is different from EJ to AB in every dewatering step (From 37.8m to 23.72m, which can obtain from Table 6-1), on GH: total head is constant, H=39m.

The relative movement of the structure with respect to the soil in this analysis has been simulated by 16-nodel friction Goodman element to match 20-nodel hexahedron element, the detail drawing is shown in Figure 6-6.

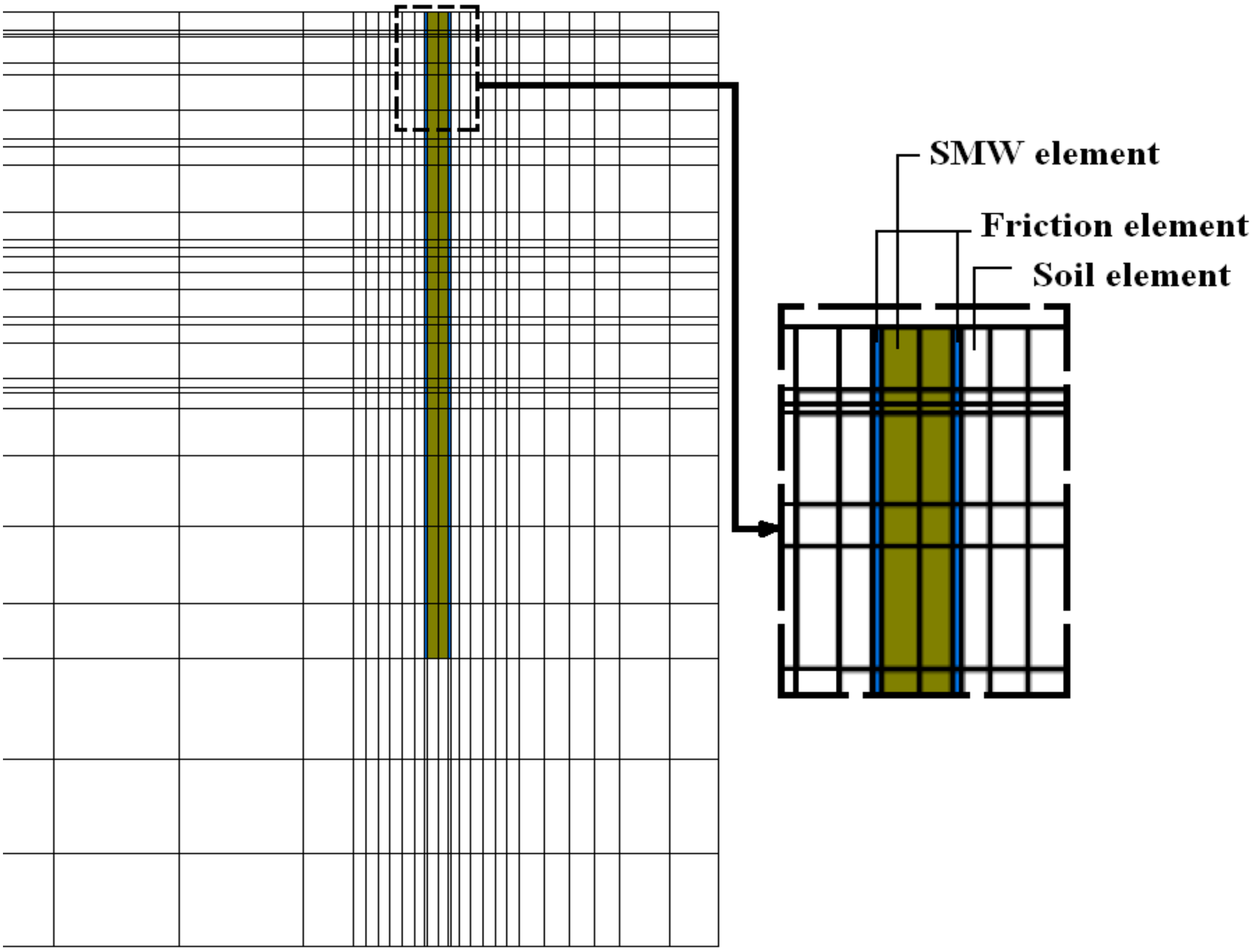

Figure 6-6 Friction element modeling

The variation of the load can be mainly divided into 16 parts, which are shown below:

1. Gravity stress
2. 20kpa overloading behind the SMW
3. Dewatering for the first stage (-2.2m)
4. Excavation for the first stage (-1.1m)
5. Support structure for the first stage (-0.8m)

6. Dewatering for the second stage (-6.58m)
7. Excavation for the second stage (-5.78m)
8. Support structure for the second stage (-5.48m)
9. Dewatering for the third stage (-11.18m)
10. Excavation for the third stage (-10.08m)
11. Support structure for the third stage (-9.78m)
12. Dewatering for the fourth stage (-14.18m)
13. Excavation for the fourth stage (-13.38m)
14. Support structure for the fourth stage (-13.08m)
15. Dewatering for the fifth stage (-16.28m)
16. Excavation for the fifth stage (-15.68m)

6.3 Comparison of observed results and prediction results

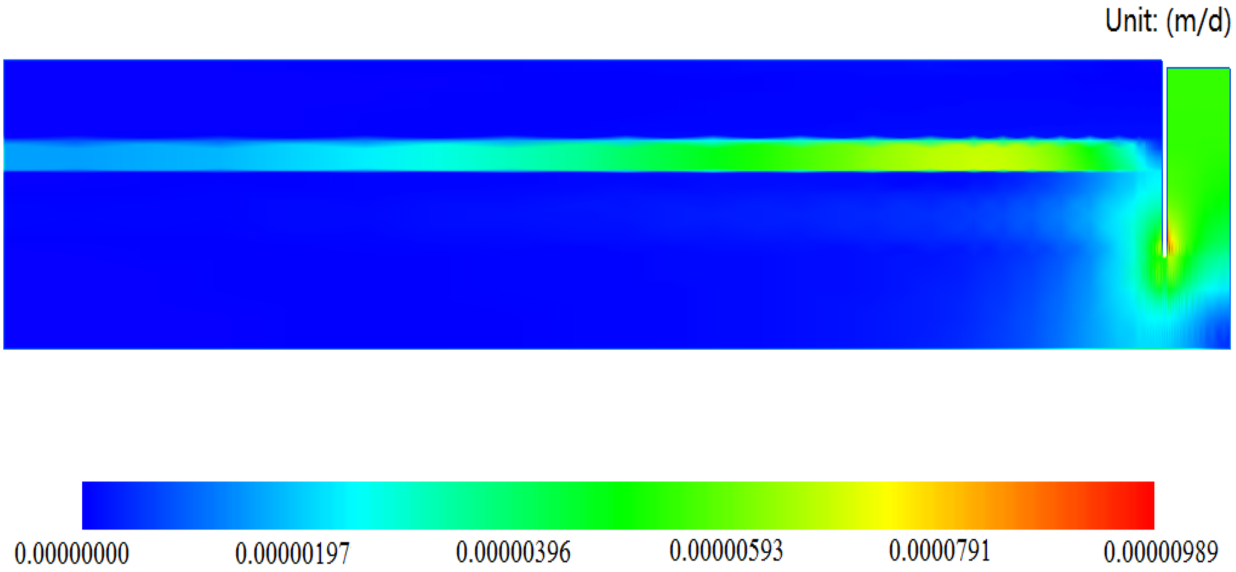

Figure 6-7 Composite velocity distribution in the first stage

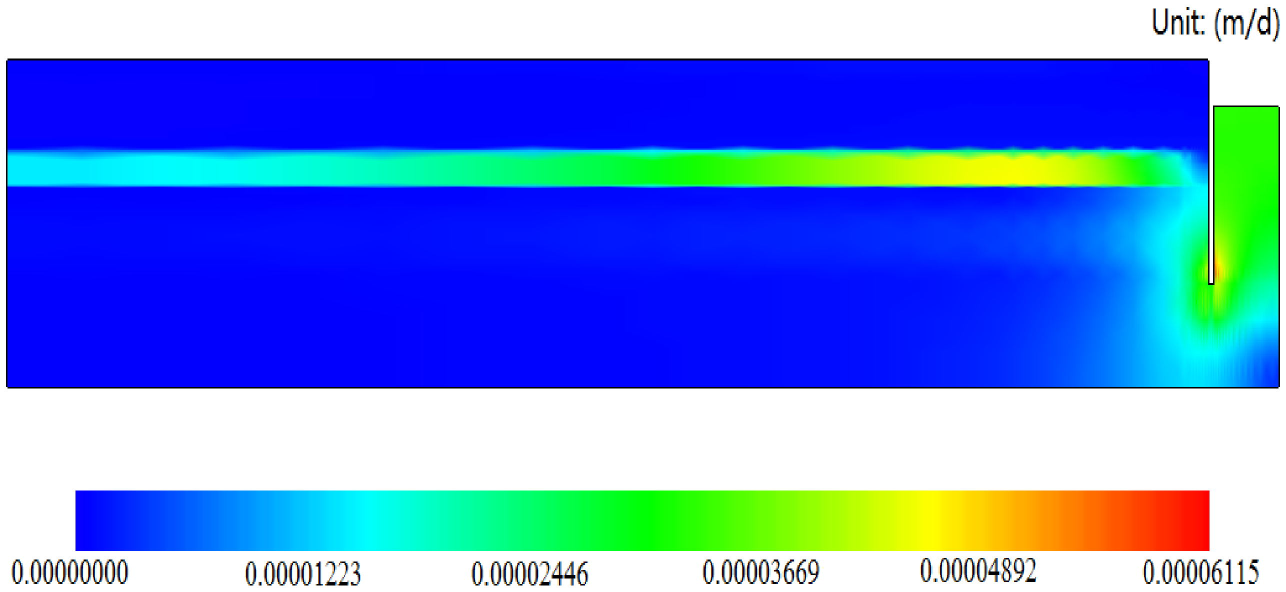

Figure 6-8 Composite velocity distribution in the second stage

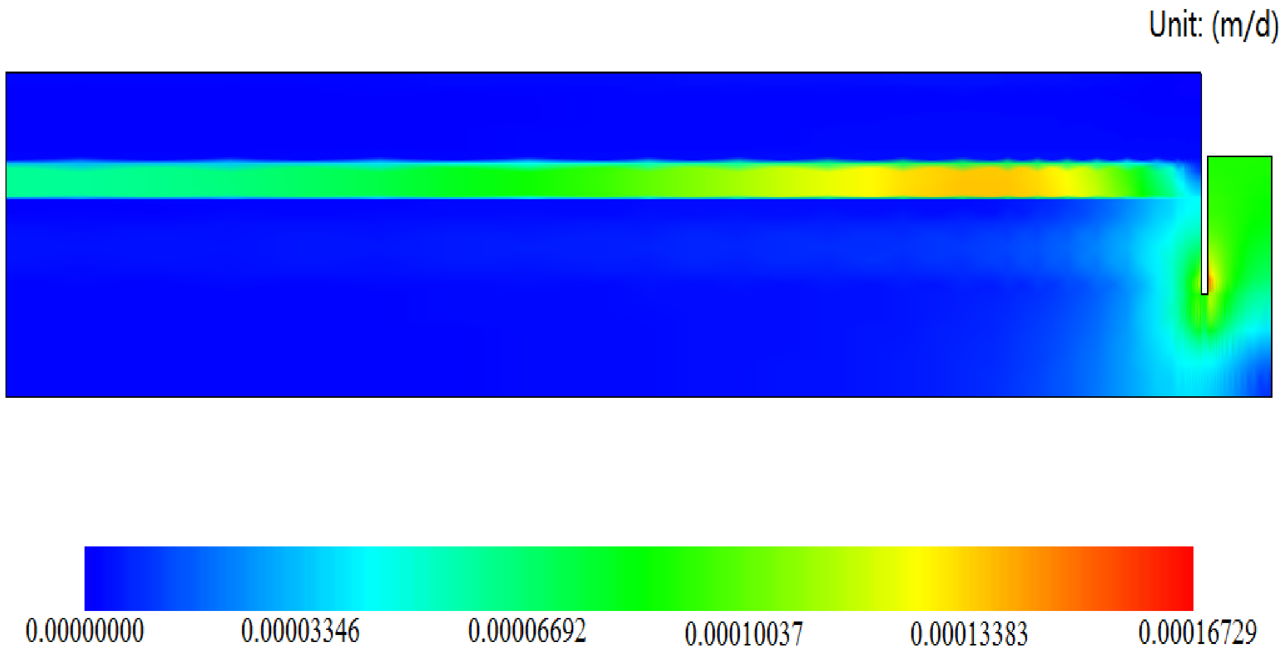

Figure 6-9 Composite velocity distribution in the third stage

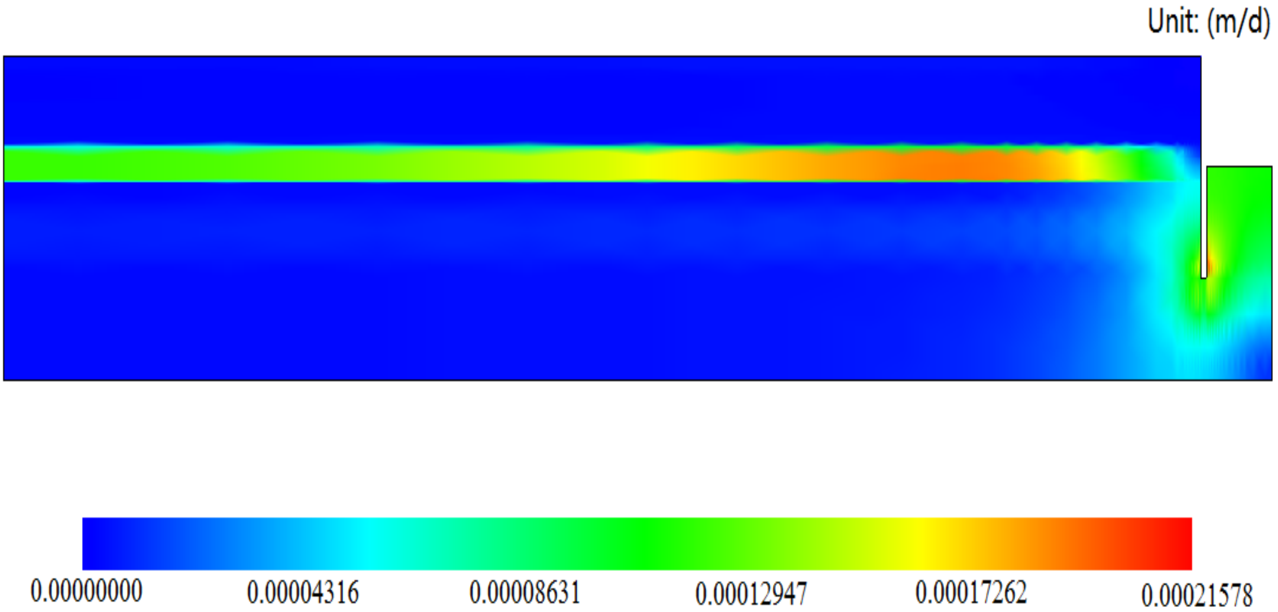

Figure 6-10 Composite velocity distribution in the fourth stage

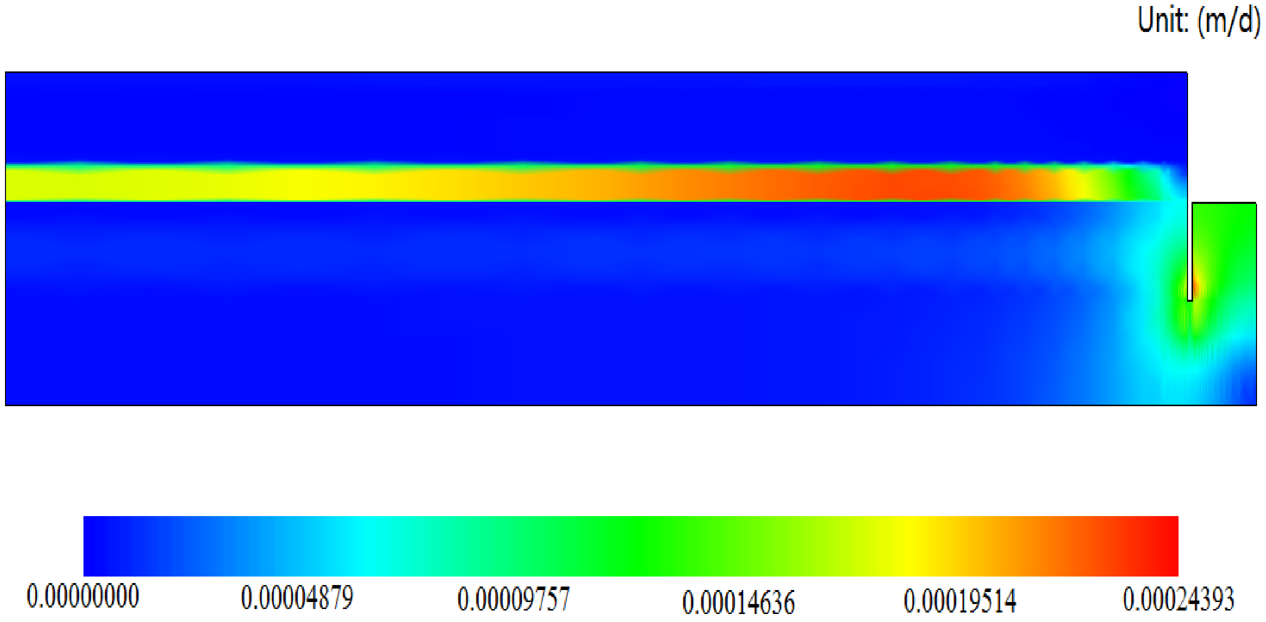

Figure 6-11 Composite velocity distribution in the fifth stage

Calculated results of seepage flow are shown in Figure 6-7(The first stage dewatering), Figure 6-8 (The second stage dewatering), Figure 6-9 (The third stage dewatering), Figure 6-10 (The fourth stage dewatering) and Figure 6-11 (The fifth stage dewatering).With increasing of dewatering depth for inner excavation, the head difference between the inside and the outside of pit increases dramatically, which lead to a big difference of high seepage velocity zone in every dewatering stage, for instance, the maximum seepage velocity value around the bottom of the SMW (Around point C in Figure 6-5) is nearly 0.00001m/d in the first dewatering stage in Figure 6-7, and the value changes to 0.00025m/din the fifth dewatering stage under the same conditions in Figure 6-11.

In these figures above, the high velocity zone appears under the bottom of pit in all time, and there is a zonal high flow velocity region behind the SMW, the seepage velocity of which is significantly higher than that of the upper and lower soil layer. The reason is that the layer with high seepage velocity is sand layer, the permeability coefficient of which is much higher than other soil layers. When the dewatering depth is not large (Stage 1 and stage 2), the high seepage velocity zone appears under the bottom of the pit, especially around the bottom of the SMW (Around point C in Figure 6-5), but when dewatering depth becomes larger (Stage 4 and stage 5) the high seepage velocity zone changes to the sand layer behind the SMW.

Velocity distribution in the final dewatering stage is shown in the Figure 6-12. The arrow represents the seepage velocity. The larger arrow is the higher the velocity. The detail drawing of seepage flow around the two sides of the SMW is also given in the figure. The seepage flow inner pit is mainly upwards, the seepage flow outer pit is mainly downwards. High velocity zones come from around the bottom of the SMW and sand layer behind SMW, which matches well with Figure 6-11.

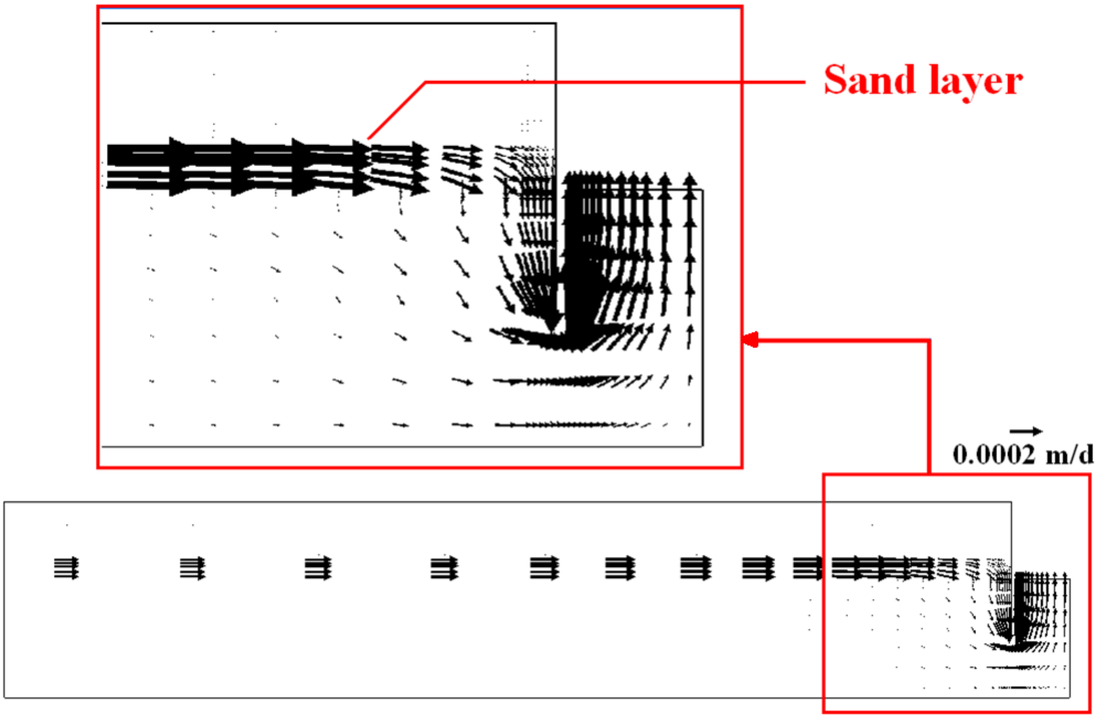

Figure 6-12 Velocity distribution in the final dewatering stage

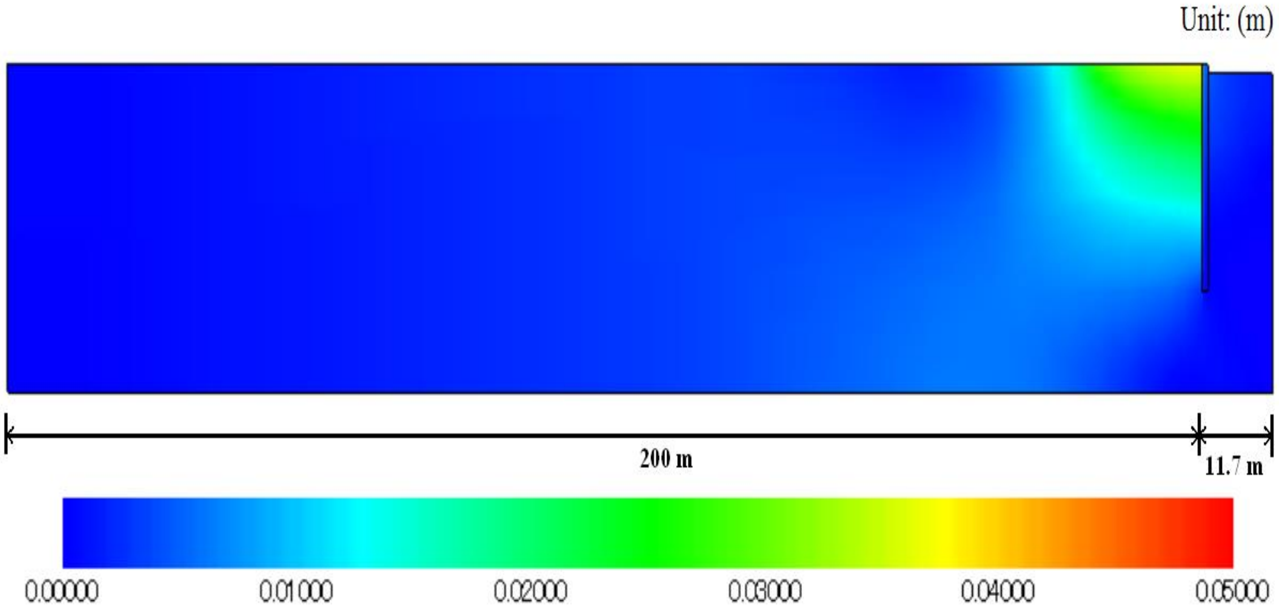

Figure 6-13 Composite displacement distribution in the first stage

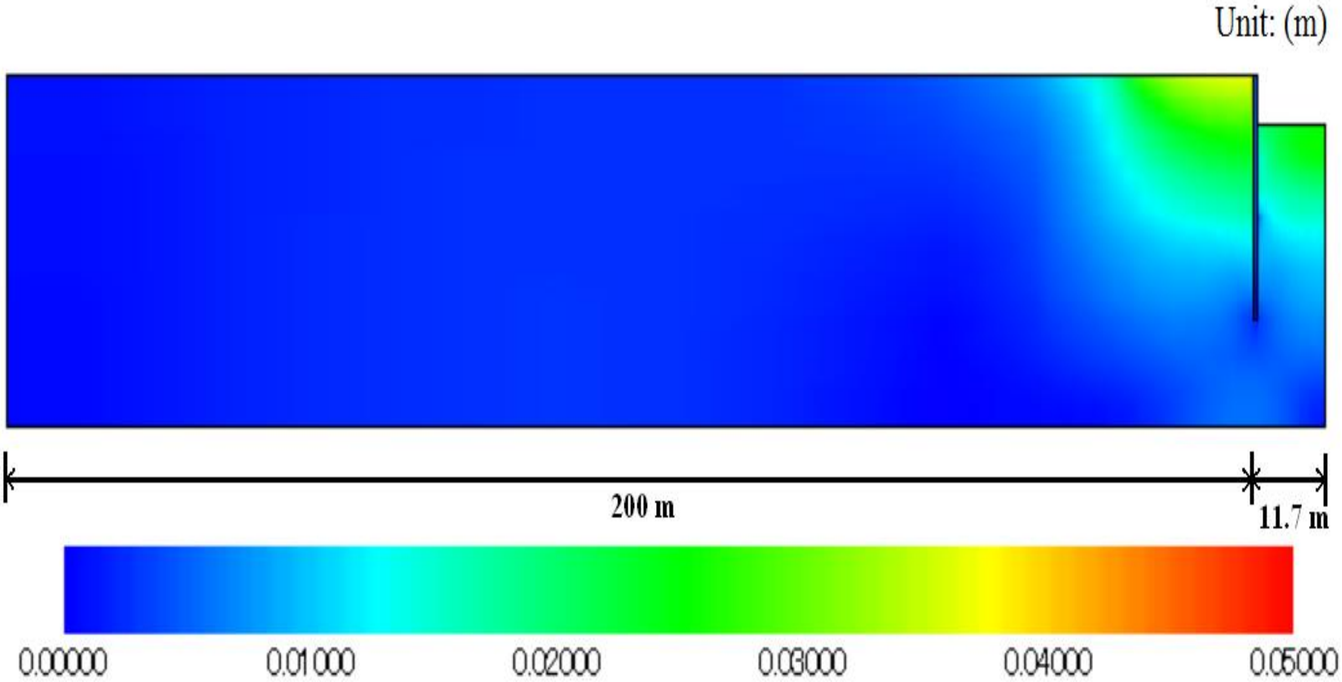

Figure 6-14 Composite displacement distribution in the second stage

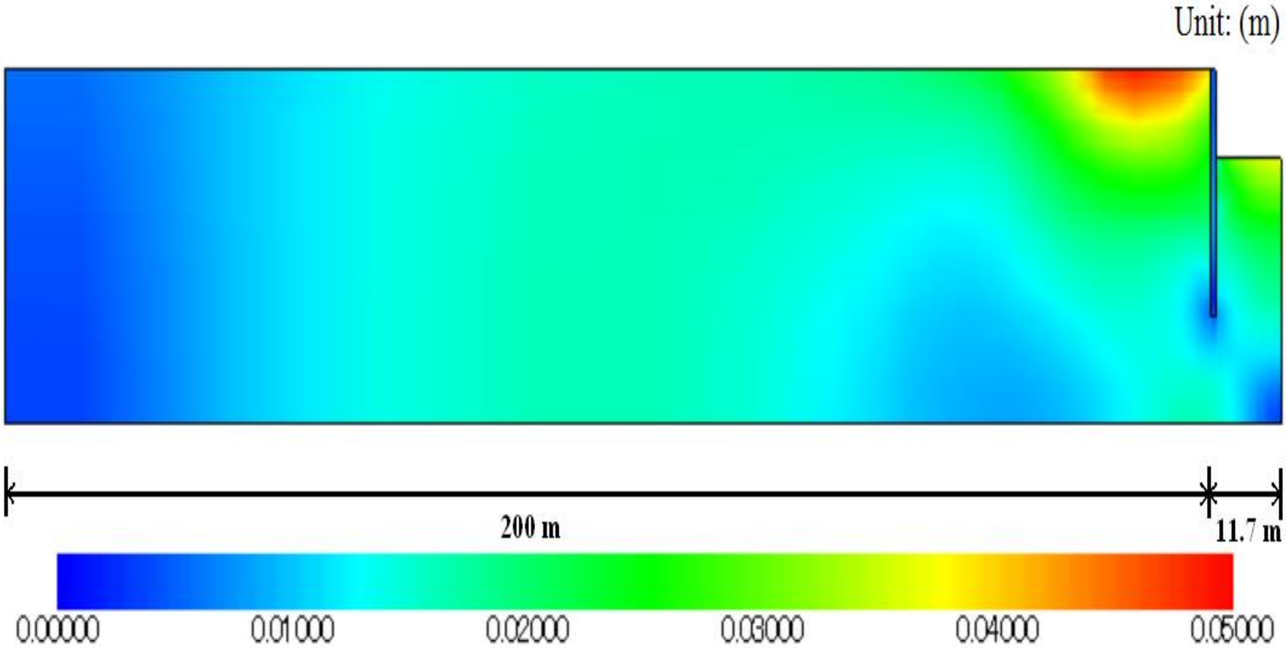

Figure 6-15 Composite displacement distribution in the third stage

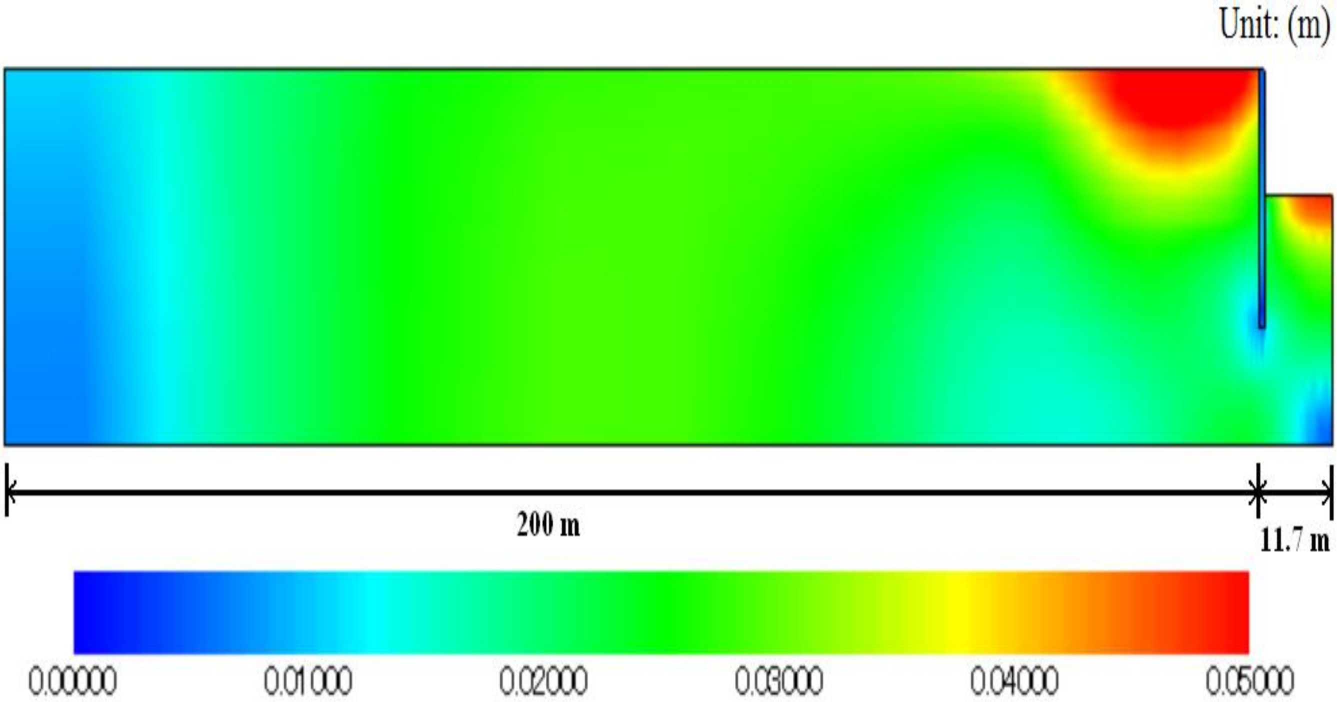

Figure 6-16 Composite displacement distribution in the fourth stage

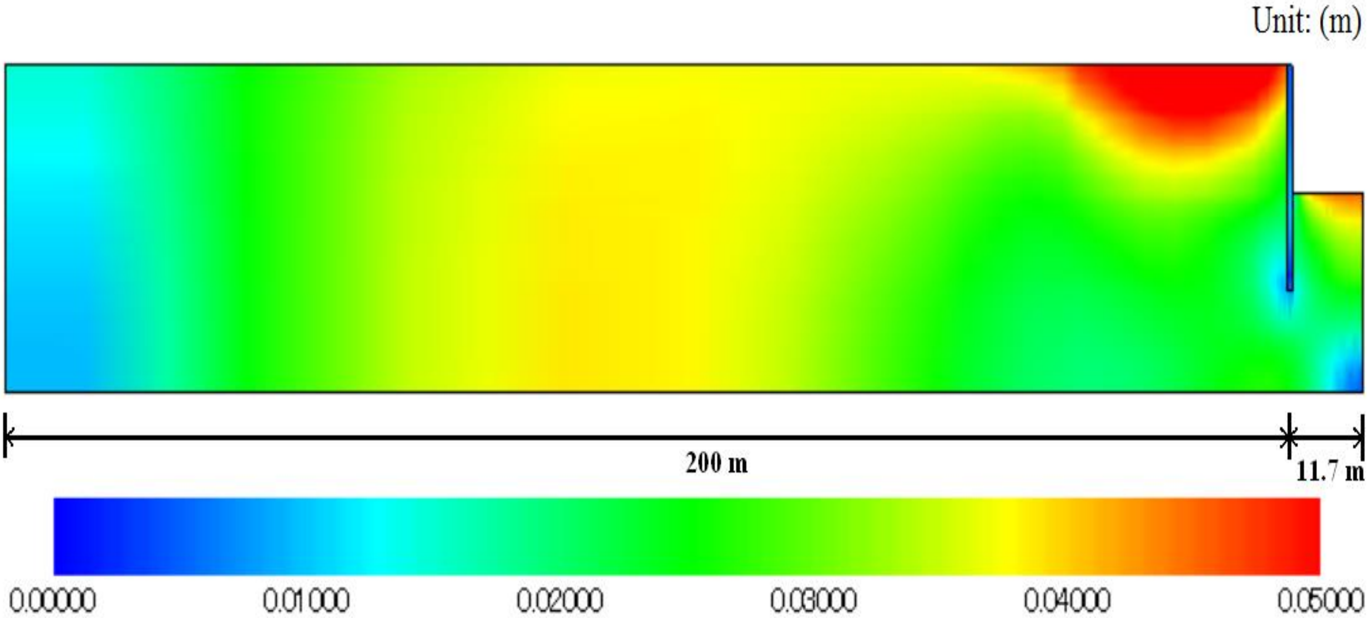

Figure 6-17 Composite displacement distribution in the fifth stage

Calculated results of displacement distribution are shown in Figure 6-13 (The first stage excavation), Figure 6-14 (The second stage excavation), Figure 6-15 (The third stage excavation), Figure 6-15 (The fourth stage excavation) and Figure 6-17 (The fifth stage excavation).

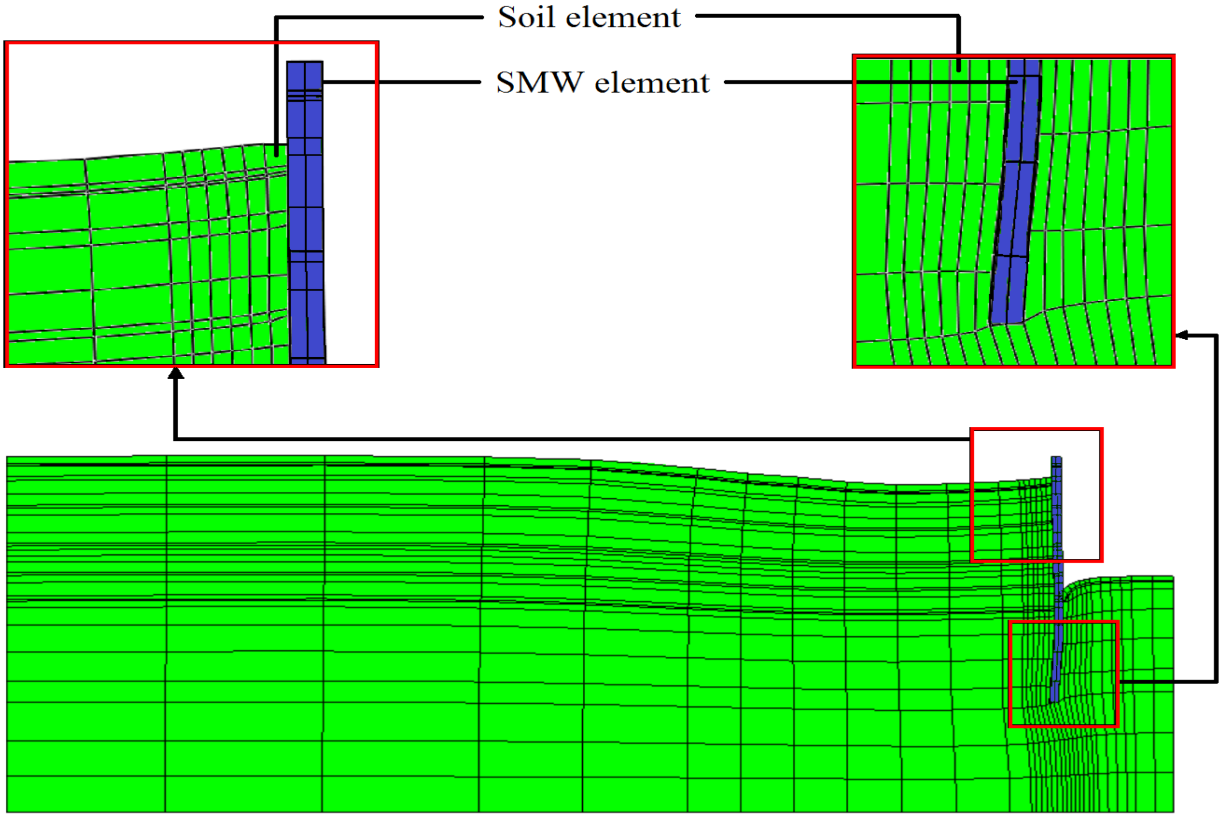

Figure 6-18 Mesh deformation of final stage excavation

Figure 6-18 gives the mesh deformation of final stage excavation, the differential settlement behind the SMW and uneven heave inner pit can be clearly observed. The detail drawing of relative movements between the SMW and soil mass is also shown in the Figure 6-18, relative to SMW, the displacement of soil mass behind SMW is downwards on one hand, but the displacement of soil mass in front of SMW is upwards on the other hand. Displacement discontinuity is evident between the SMW and soil mass, which illustrates that it is reasonable to employ friction element in this analysis.

The numerical prediction of ground settlement behind SMW and heave inner excavation pit for every excavation stage are given in the Figure 6-19 and Figure 6-20 respectively. In the first and second stages of excavation, depth of dewatering in the pit is relatively shallow. The head difference between the inside and the outside of pit is not obvious. The effect of downward seepage force behind SMW is not apparent yet. The influence of excavation is also limited, because the depth of digging in the pit is not deep, which is not enough to cause displacement behind SMW. Therefore, large displacement regions appear behind SMW is mainly caused by 20Kpa external load and the settlement difference behind SMW from stage 1 and stage 2 is negative, which is shown in Figure 6-19. With the increasing depth of digging, the heave inner pit becomes more apparent, which can be observed in stage 3, stage 4 and stage 5. In addition, on account of the head difference between the inside and the outside of pit increases with excavation process step by step, the head difference between the inside and the outside of pit increase gradually. The displacement behind SMW gradually increases and the large displacement region is expanding due to downward seepage flow and the effect of buoyancy disappearing. So in conclusion, the early settlement behind SMW mainly comes from overburden pressure, and afterward settlement is caused by seepage flow and the effect of buoyancy disappearance.

The depth of digging in the first stage is relatively shallow, for this reason, the heave due to excavation inner pit is negative found, which is shown in Figure 6-20. Comparing with the first stage, the second stage excavation causes greater rebound of excavated surface, apart from the reason of digging depth, the effect of soil properties from different soil layer could also be another factor.

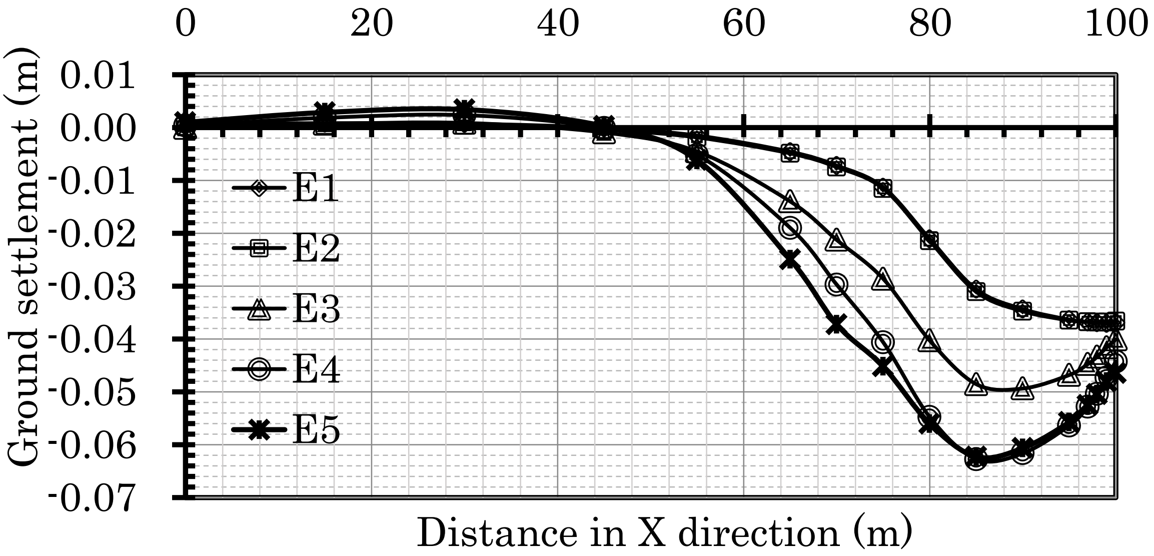

Figure 6-19 Ground settlement behind SMW

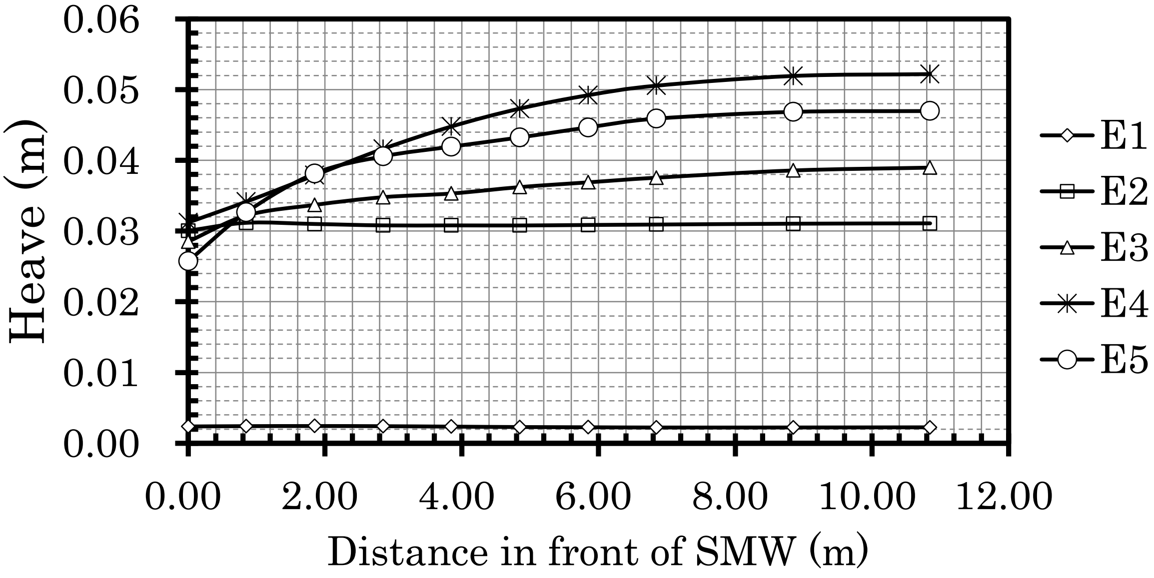

Figure 6-20 Heave inner excavation pit

With the increase of excavation depth, horizontal seepage force in the sand layer behind the SMW becomes larger and larger in stage 4 and stage 5 (Figure 6-10 and Figure 6-11), which gives upward force to the soil layer above the sand layer and the ground settlement behind the SMW due to downward seepage force and effect of buoyancy disappearing are partly counterbalanced. In addition to these reasons, because of the horizontal seepage force in the sand layer, the confining pressure of soil body behind the SMW significantly increases, which could improve strength of soil and the settlement becomes hard to occur. In consequence, the settlements from stage 4 and stage 5 are nearly identical.

With the increasing depth of digging, the heave inner pit becomes more apparent. In stage one and stage two, the depth of digging is relatively shallow, the initial horizontal stress σ_h of soil due to gravity is small, and the relative movements between the SMW and soil mass is easy to occur, therefore, the heaves in stage one and stage two are uniform. When digging depth, with initial horizontal stress σ_h increasing, relative movements become difficult to happen, and uneven heaves appear in the stage three, stage four and stage fifth. The maximum of heave point comes from the plane of symmetry.

The comparison of numerical predication results (final stage) and field observed data are given in the Figure 6-21 and Figure 6-22. The numerical results (Case 1) agree well with the field observed data, which indicates that the hydro-mechanical numerical model is reasonable and right.

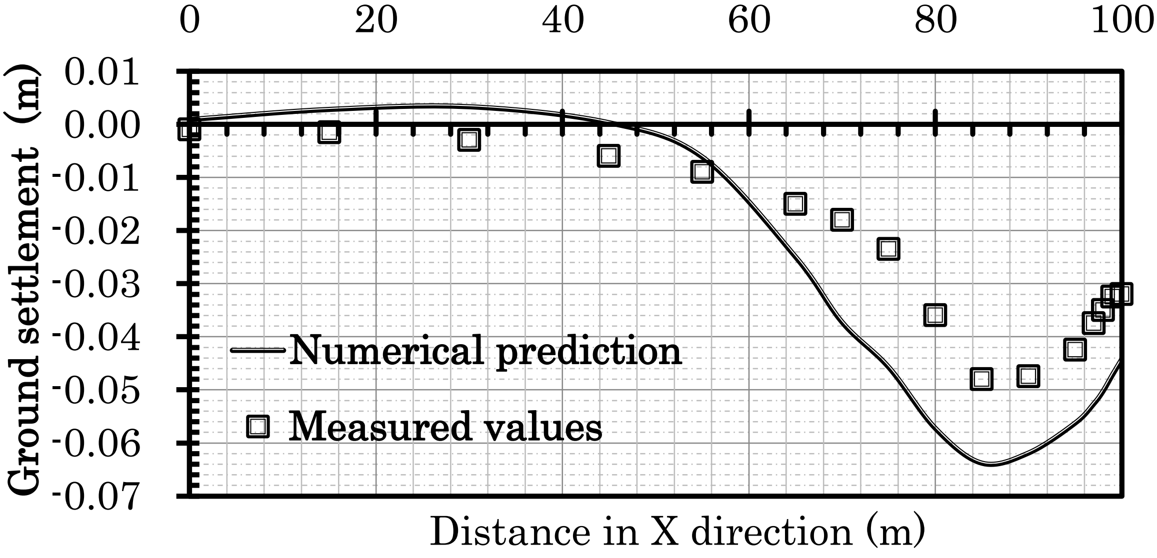

Figure 6-21 Ground settlement behind SMW

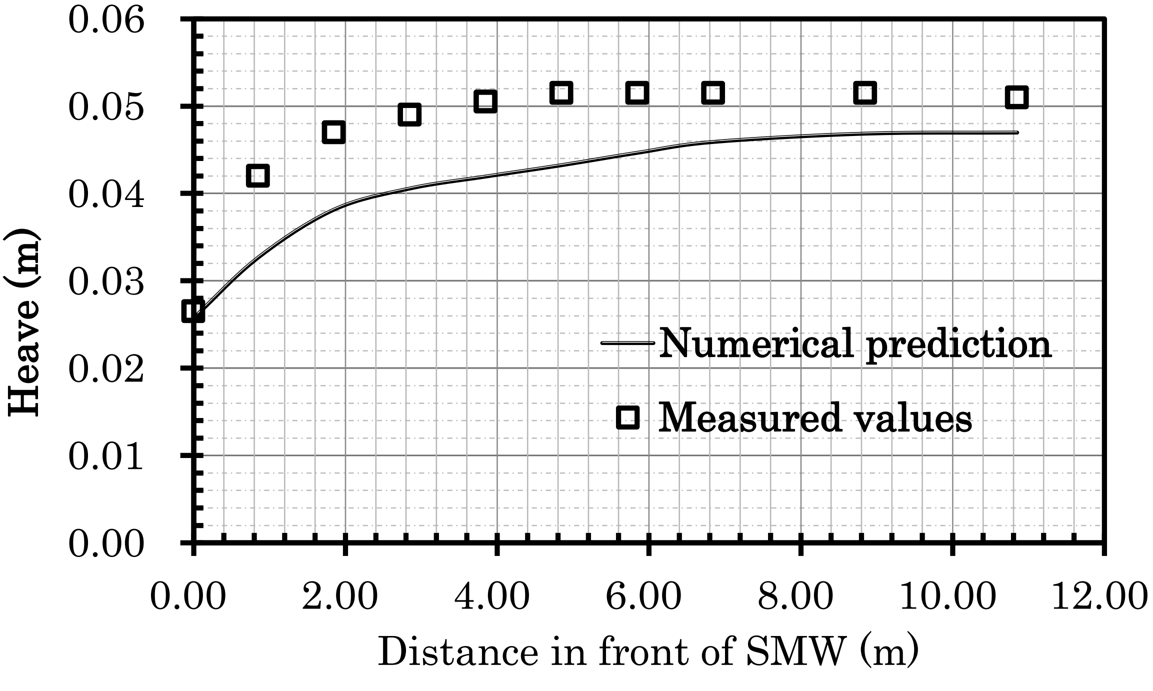

Figure 6-22 Heave inner excavation pit

Four numerical cases have been compared for further study of rule of pit deformation, which are given in Table 6-7.

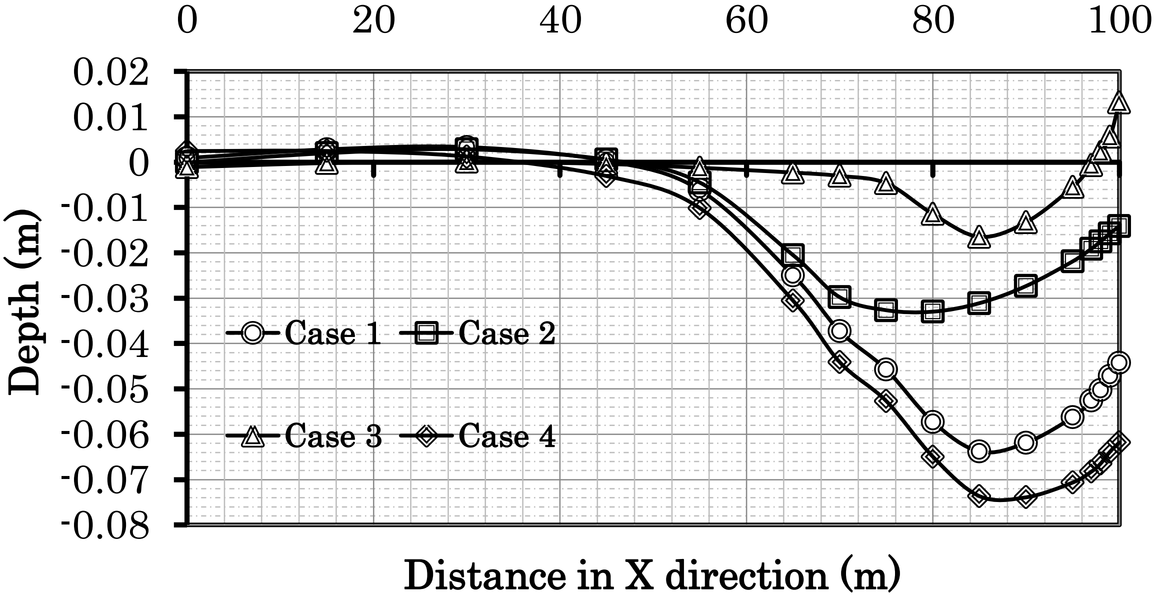

Figure 6-23 Ground settlement behind SMW for different cases

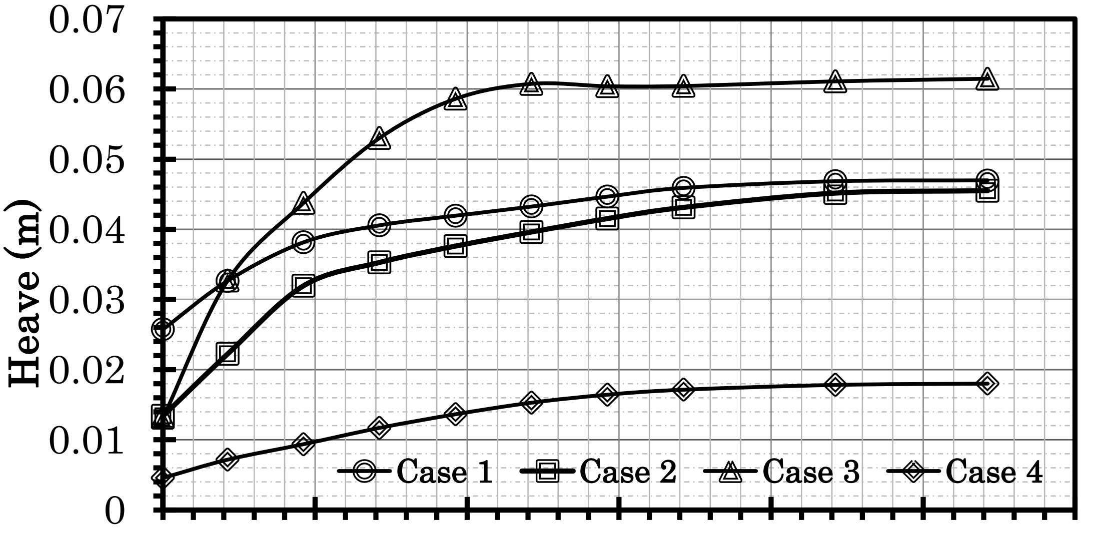

Figure 6-24 Heave inner excavation pit for different cases

Case 1 is the model by considering external load behind the SMW and friction element is employed. External load effect behind the SMW is not considered in case 2, friction element is not employed in the case 3 and seepage force is not considering in the case 4.

Table 6-7 Numerical prediction of different cases

Case name	External load behind the SMW	Friction element is employed	Seepage force active
Case1	○	○	○
Case2	×	○	○
Case3	○	×	○
Case4	○	○	×

The results of ground settlement and heave are given in Figure 6-23 and Figure 6-24.

By comparing with case 1, the deformation behind SMW in case 2 is significantly reduced (50%), but the effect of reduced heave inner pit is unobvious, which indicates that lighten external load around the pit can effectively reduce the differential settlement behind the SMW.

In case 3, friction element is not employed and the relative movements between the SMW and soil mass couldn’t occur. As shown in Figure 6-23, The upwards movement of SMW due to bottom ground heave inner pit greatly limits the settlement behind the SMW, which incompatible with field measured data. The curve of heave inner pit in case 3 is not smooth by comparing with case 1, especially at the joint of SMW and soil, the upheaval values in case 3 is only as half as field observed data. This illustrates that it is necessary and reasonable to employ friction element in this analysis project.

In In case 4 (seepage force is not considered), the heave of which on the excavated surface is distinctly reduced (60%) by comparing with case 1 (seepage force is considered), which indicates that vertical seepage force inside pit plays a very important role in the displacement field. By comparing with the vertical seepage force behind SMW, horizontal seepage force in the sand layer is much larger, which could give upward force to the soil layer above the sand layer and the ground settlement behind the SMW is partly counterbalanced. In case 4, seepage force is not considered, therefore, the deformation behind SMW in case 4 is slightly larger than case1, which illustrates that the effect of horizontal seepage force is more significant than vertical seepage force behind the SMW.

6.4 Summary and discussion

In this chapter, a hydro-mechanical numerical model was presented to describe the seepage and deformation behaviors of the excavation site of the Zhujiang Road metro station in China. The Van-Genuchten saturated-unsaturated model was used to model for the seepage of the groundwater and the Duncan-Chang nonlinear elastic model was employed to model the deformation behavior of the soil mass. The interaction between the structure and the soil was characterized with the Goodman's zero thickness elements.

The numerical results (Case 1) agree well with the field observed data, which indicates that the hydro-mechanical numerical model in this analysis is reasonable and right.

In the early stage of excavation, the effect of seepage force due to seepage flow is not obvious, and the settlement behind SMW is mainly caused by external load. With the increasing depth of dewatering inner pit, the head difference between the inside and the outside of pit increases, the effect of seepage force behind SMW becomes more apparent.

A roughly 40m-wide large differential settlement region behind the SMW is appeared after excavation accomplished, which may leads to destroy of roads, structures and underground pipelines crowded around the excavation work, therefore controlling the subsidence around the excavation site is particularly important.

The external load has a great impact on the deformation behind the SMW, but has small influence on the heave inner pit, which indicates that lighten external load around the pit can effectively reduce the differential settlement behind the SMW.

Seepage force inside the pit plays a very important role in the displacement field. However, due to the effect of high permeability sand layer, horizontal seepage force in the sand layer behind the SMW is much larger than vertical seepage force, which decreases the effect of downward seepage force. The early settlement behind SMW mainly comes from overburden pressure, and afterward settlement is principally caused by the effect of buoyancy disappearing.

The relative movements between the SMW and soil mass should not be ignored in numerical analysis, otherwise, the correct prediction results may not be obtained.

Consequently, it is vital to integrate various factors are in numerical analysis to model as closely as possible the true “in the field” behavior.

Reference

1) Fuhua GAO, Analysis of seepage and deformation of deep excavation of foundation pit, Academic dissertation of Hohaiuniversity, pp.37-62, 2004. (In Chinese)

2) Xiang WANG, Deformation of foundation pit considering coupled effects of seepage and stress, Academic dissertation of Hohaiuniversity, pp.48-64, 2007.(In Chinese)

3) Caihong JIA, Research on the deformation of foundation pit considering couple effect of seepage and stress, Journal of Wuhan university of technology, pp.119-122, 2010. (In Chinese)

4) P. T. Brown and J.R. Booker, Finite element analysis of excavation, Computers in geotechnics, vol.1, pp. 207-220, 1985.

Chapter 7

Conclusion and future developments

7.1 Summary and conclusions

Since tall buildings, underground stores and subways are concentrated in the downtown of the city, the environment conditions around project site are growing severe when dewatering projects are conducted. Roads, structures, underground pipelines and etc. are crowded around the excavation work, therefore, the design of deep excavation controlled by strength has switched to the one controlled by deformation step by step. To minimize both the risk of catastrophic failure of deep excavation construction and of structural damage around the project site, the design of deep excavation should be carried out by detailed deformation analysis.

The innovation of current research is that various factors are considered in numerical analysis to model as closely as possible the true behavior in the field. Joint element, spring element, and non-liner model in displacement analysis are employed to represent the ground behaviors around the excavation site. The finite element analysis incorporating excavating theory is utilized to simulate heave of excavated surface and saturated-unsaturated model for seepage analysis is implemented in consideration of seepage force.

This thesis addresses the problem of predicting ground displacement around dewatering project firstly by comparing results from Dupuit's assumption, Bath's seepage method and Saturated-unsaturated method under effect of single pumping well, secondly by analysis results of 2D and 3D excavation dewatering cases respectively, and thirdly by making comparison analysis of field observed and numerical predictions.

7.1.1 Conclusion of single pumping well prediction

Comparison of phreatic surface of Bathe’s method and Dupuit surface were conducted. Results shows that when radius r is larger, phreatic surface of Bathe’s method and Dupuit surface are coincident, but when radius r is smaller (smaller 10 meters in the prediction case), there is significant difference. On the boundary of the pumping well, Dupuit’s surface connect with the water level in the well, but for the Bathe’s method, there is leaking face on the boundary of the well. In actual, the leaking face is formed along the free boundary surface.

The prediction results of Bathe’s method and saturated-unsaturated method are also been compared. The results shows that the locations of phreatic surface from two models are nearly same and the velocity distribution of two models are essential consistent. But in the saturated-unsaturated model (T=100 hr in the prediction case), there is a obvious capillary zone, the height of which is approximately 2 meters and the seepage flow in the unsaturated zone is obviously observed, which is encouraging that the effect of capillary zone can be considerable in the seepage field. It is further observed that the deformation result of saturated-unsaturated seepage model (T=100 hr in the prediction case) is generally larger than Bathe’s model’s. The closer the distance from the well, the more obvious phenomenon is because of the effect of unsaturated zone near the pumping well. In the unsteady analysis, the settlement rate of ground surface matches well with the dropping rate of the phreatic surface.

7.1.2 Conclusion of 3D cases prediction

The unsteady numerical prediction shows that the vertical upward seepage velocity below the bottom of pit is relative larger at the early stage of seepage field and decreases gradually with time proceeding. The maximum velocity zone appears at the foot of the excavation all the time where the potential seepage failure such as quicksand and piping maybe happen. The maximum velocity zone appears at the corner of the pit with time passing enough, which points out the importance and necessity of the 3D analysis. The maximum horizontal displacement zone appears at the bottom of the pit and extends gradually with time proceeding, which matches well with the results of seepage field. The horizontal displacement caused by seepage flow is considerable in displacement field and a 3D sliding surface may appears when time passes enough.

Horizontal deformation caused by seepage flow plays a very important role in deformation field around the excavation site, especially in the case of high-rise buildings surrounded. The differential displacement may occur around foundation adjacent buildings, which can lead to toppling behavior to the foundation, and the pipes and roads near the foundation may tend to buckle and crack because of the displacement of the ground.

7.1.3 Conclusion of non-linear ground behavior due to unsteady seepage model

It is encouraging that the predicted values are well agreeable with tri-axial test in both monotone loading and unloading-reloading conditions, which validates the correctness of the programming. In the excavation prediction, the influence of the soil resilience of deep pit excavation's bottom due to dewatering has been observed in the analysis, which illustrates the importance and necessity of considering the unloading phenomenon in non-linear excavation analysis. In seepage analysis, high velocity area appears at outside of the excavation’s bottom, which is found that the retaining wall affects the seepage field significantly by comparing with 3D excavation case (without retaining wall).

7.1.4 Conclusion of example of application

The numerical analysis on ground behavior around excavation site of the Zhujiang Road metro station in China incorporating excavating theory with spring element implemented. The Van-Genuchten saturated-unsaturated model is used to model for the seepage of the groundwater and the Duncan-Chang non-linear model is employed to model the deformation behavior of the soil mass. The interaction between the structure and the soil was characterized with the Goodman’s zero thickness elements.

The numerical results (Case 1) agree well with the field observed data, which indicates that the hydro-mechanical numerical model in this analysis is reasonable and right.

In the early stage of excavation (step1 and step2), the effect of seepage force due to seepage flow is not obvious, and the settlement behind SMW is mainly caused by external load. With the increasing depth of dewatering inner pit (step3 and step4), the head difference between the inside and the outside of pit increases, the effects of buoyancy disappearing and downwards seepage force behind SMW become more apparent. The early settlement behind SMW mainly comes from overburden pressure, and afterward settlement is principally caused by the effect of buoyancy disappearing.

A roughly 40m-wide area of large differential settlement region behind the SMW is appeared after excavation accomplished, which may leads to destroy of roads, structures and underground pipelines crowded around the excavation work, therefore controlling the subsidence around the excavation site is particularly important.

Four numerical cases have been compared, the prediction accuracy by the external load and joint element is more agreeable with the field observed data. It is found that external load has a great impact on the deformation behind the SMW, but it has small influence on the heave inner pit, which indicates that lighten external load around the pit can effectively reduce the differential settlement behind the SMW. Relative movements between the SMW and soil mass should not be ignored in numerical prediction, otherwise, the correct prediction results may not be obtained. Consequently, it is vital to integrate various factors in numerical analysis to model as closely as possible the true ground behaviors in the field and hydro-mechanical model analysis is necessary to present useful reference to the excavation stability and excavation disaster predication.

7.2 Recommendation for further developments

7.2.1 More reasonable coupling model

In this research, seepage field is calculated in advance and seepage force is considered as an external force acted on the soil mass in the following displacement calculation. A more advantageous coupling model that is capable of considering synchronicity of seepage field and displacement field should be incorporated in the numerical analysis in further work.

7.2.2 Comparison analysis of Three-dimensional application

In the analysis of Zhujiang Road metro station, the length of excavation is 124 m, the width is 22.9 m, the Length/Width>4, therefore, the excavation could be considered as a two dimension problem. However, three-dimensional problem will be faced more often in actual project. Therefore three-dimensional field experiment may be test the feasibility of this numerical modeling. A further improvement of model should be made according to the experimental feedback data.

Publication list regarding this study

Journal paper (refereed)

1) Lingyu Meng, Haruyuki Yamamoto: Study on Foundation Behavior due to Seepage Force of Groundwater, Applied Mechanics and Materials, Vols. 170-173, pp 199-204, May, 2012

2) Lingyu Meng, Haruyuki Yamamoto: Ground Behaviors Due to Seepage Force of Groundwater, Advanced Materials Research, Vols. 594-597, pp 516-521, Nov., 2012

Conference paper (refereed)

3) Lingyu Meng, Haruyuki Yamamoto (2013): Numerical Simulation of Ground Displacement Behaviors due to Unsteady Seepage flow, The Seventh International Structural Engineering and Construction Conference (ISEC-7), New Developments in Structural Engineering and Construction, Vols.1, pp. 729-734, Honolulu, USA, June 18-23, 2013.

4) Haruyuki Yamamoto, Lingyu Meng (2014): Ground Displacement Behaviors considering Unsteady Seepage Flow and Non-liner Deformation, The Second Australasia and South-East Asia Structural Engineering and Construction Conference (ASEA-SEC-2), Bangkok, Thailand, November 3–7, 2014. (Accepted)

Oral presentation (No-refereed)

5) Lingyu Meng, Haruyuki Yamamoto: Study on Ground Behaviors due to Seepage Force of Groundwater, In Proceedings of Annual Research Meeting (Vol. 34). Presented at the Chugoku Chapter, Architectural Institute of Japan (AIJ), Mar 5-6, 2011, Tokuyama, Japan.

6) Lingyu Meng, Haruyuki Yamamoto: Ground Behaviors due to Unsteady Seepage Force of Groundwater, In Proceedings of Annual Research Meeting (Vol. 36). Presented at the Chugoku Chapter, Architectural Institute of Japan (AIJ), Mar 2-3, 2012, Hiroshima, Japan.

7) Lingyu Meng, Haruyuki Yamamoto: Numerical Simulation of Three-dimensional Ground Behaviors due to Unsteady Seepage Flow, In Proceedings of Annual Research Meeting (Vol. 35). Presented at the Chugoku Chapter, Architectural Institute of Japan (AIJ), Mar 3-4, 2013, Okayama, Japan.

8) Lingyu Meng, Haruyuki Yamamoto: Numerical Simulation of Unsteady Seepage Flow and Non-linear Deformation for Ground Displacement Behaviors, In Proceedings of Annual Research Meeting (Vol. 37). Presented at the Chugoku Chapter, Architectural Institute of Japan (AIJ), Mar 1-2, 2014, Hiroshima, Japan.